LAST ICE SHEET RECESSION AND SUBMARINE SLOPE FAILURES IN A COMPLEX ARCTIC INLET, INNER FROBISHER BAY, BAFFIN ISLAND, NUNAVUT

A Thesis submitted to the School of Graduate Studies in partial fulfillment of the requirements for the degree of

Doctor of Philosophy

Department of Geography

Memorial University of Newfoundland

October 2022

St. John's, Newfoundland and Labrador

Abstract

The Cockburn Substage readvance marks the last major late-glacial advance of the northeast sector of the Laurentide Ice Sheet, but has been examined at only a handful of sites on Baffin Island. The causes of this abrupt, late reversal of retreat are still unclear, but greater chronological control may provide some insight. To date, the literature has focused on the large terminal moraines common in the region, providing a singular date of readvance (prior to c. 9.5-8.5 ka cal BP). In Frobisher Bay, the Cockburn Substage readvance and recession are marked by a series of end moraines spanning ~20 km on either side of the inner bay. New acoustic marine mapping reported here from inner Frobisher Bay (IFB) reveals five distinct seafloor ridges that roughly correspond to the onshore moraines, as well as two fields of DeGeer moraines. These differing types of ridges indicate that the style of ice retreat changed over time from an episodic recession to a more regular tidewater ice front retreat. Radiocarbon dated shells from cored glaciomarine and postglacial sediments adjacent to and between the moraines indicate that ice readvanced prior to 9.4 ka cal BP and did not retreat from IFB before 7.6 ka cal BP. Sedimentary characteristics indicate changes in provenance and deposition rate as ice retreated. This paper describes the final retreat of Laurentide ice out of IFB, showing how style of deglaciation and depositional environments changed from the end of the Cockburn Readvance until recently.

Inner Frobisher Bay is home to an abnormally high density of submarine slope failures (SSF; at least 246; ~1/20 km^2). Understanding the causes of such an abundance of failure products and their chronology contributes to hazard reduction in the capital region of Nunavut. SSFs have the potential to destroy seafloor and coastal infrastructure directly and, when sufficiently large, can be tsunamigenic. Morphometric analysis of SSFs provides an insight into their spatial distribution, relative chronology, triggers, and preconditioning factors. SSFs in IFB are asynchronous and have

been occurring in IFB since at least 5.7 ka cal BP, with some features dated to within the last 500 years, indicating the possibility of SSFs being an active process in the basin. Factors preconditioning these events in the basin appear to be connected to the geotechnical properties of deglacial sediments and the complex bathymetry of IFB. Triggering mechanisms appear to act asynchronously, suggesting probable triggers include small seismic events or cyclic tidal loading.

Acknowledgements

This work would not have been possible without the unending support of my family. My parents have been with me on this journey since the beginning, have seen the highs and lows, and supported me all the way through. Laura has put up with long nights and weird schedules with much patience and grace. Jack, Figgy, and Foster have provided many distractions to pull me away from this when it was needed most. Without all of you, this never would have come together.

My supervisors, Drs. Trevor Bell and Don Forbes, have had more patience in the past eight years than could be reasonably expected (though at times that went both ways). They've spent long evenings and weekends to try to make me into a better scientist and pushed me to make my work the best it could be. Even though I took longer than expected to get this thing out, they haven't given up.

My supervisory committee members, Drs. Evan Edinger and Calvin Campbell, have been a font of ideas through all of this. Their ideas have pushed me to broaden my perspective and made me a more well-rounded scientist.

A special thanks to the late Alice Telka. Her work identifying mollusc species for radiocarbon dating has materially strengthened the quality of the work. Without her efforts, this work would have gone down a rabbit hole that would have been very difficult to escape.

It turns out you meet a lot of people over the course of nearly a decade. In fact, too many to list them all out by name. A big thanks to everybody in the Department of Geography at MUNL. Whether it was commiserating over coffee or bouncing around ideas over beers, grad students in the department provided an understanding community to lean on.

I would like to acknowledge the support of the following organizations for this work: ArcticNet, Canada-Nunavut Geoscience Office (Tommy Tremblay), Government of Nunavut, Memorial University of Newfoundland and Labrador, Marine Institute, NSERC, and the Geological Survey of Canada. I thank the captains and crew of the CCGS *Amundsen* and RV *Nuliajuk* (Cecil and Bob) over the years and everybody who had a hand in laboratory analysis.

It may be my name on the cover, but this work could not have been completed (certainly not to the quality it is now) without all of you. Thank you all.

Table of Contents

List of Tables

List of Figures

List of Abbreviations

AMS	Accelerator Mass Spectrometry
BIO	Bedford Institute of Oceanography
Cal BP	Calibrated years before present
CHS	Canadian Hydrographic Service
CNGO	Canada-Nunavut Geoscience Office
GEBCO	The General Bathymetric Chart of the Oceans
GSC	Geological Survey of Canada
GSC-A	Geological Survey of Canada – Atlantic
IFB	Inner Frobisher Bay
IRD	Ice rafted debris
LGM	Last Glacial Maximum
LIS	Laurentide Ice Sheet
MBES	Multibeam echo-sounding
NRCan	Natural Resources Canada
RSL	Relative Sea Level
SSF	Submarine Slope Failure

List of Appendices

1. Introduction and Overview

1.1 Background

Marine geohazards pose a risk to seabed infrastructure and coastal communities worldwide, with 10% of the global population living less than 10 m above sea level (masl; McGranahan et al. 2007) and much of our essential shipping and communications infrastructure being located there. It is estimated that there are more than 1.1 million km of seafloor telecommunications cables (and more being laid every year), accounting for most of all data transferred globally (Telegeography 2017). The coast and seabed comprise areas of intense economic, cultural, and political activity that are vulnerable to the impacts of marine geohazards. Potentially hazardous events commonly occur unseen on the seabed, lacking the same visual impact as terrestrial geohazards, leaving many unaware of the threat they pose (Vanneste et al. 2014; Yonggang et al. 2016). Typically, only large-scale events, such as the 2004 Indian Ocean tsunami, receive broad recognition (Cochard et al. 2008). The scale of that disaster (up to 280,000 dead; widespread destruction) brought global media coverage, bringing marine geohazards and their destructive force into the public eye. Less well known are small-scale marine geohazards, such as the 2007 Aysén Fjord tsunamis (Chile) which killed 10 (Lastras et al. 2013; Van Daele et al. 2013) or the 2017 Nuugaatsiaq tsunami which killed 4 (Nunatsiaq News 2021). These small-scale marine geohazards are recognized as threats locally, but are not publicized on a global scale, even though these events could significantly impact coastal communities worldwide (Canals et al. 2004; Leynaud et al. 2009).

In Canadian Arctic coastal communities, this threat is amplified both by their typically low-lying infrastructure and their remoteness. In recent years, significant effort has begun to map marine geohazards and assess their prevalence in the region (e.g., Gosse et al. 2020; Normandeau et al.

2020). Understandably, early focus has been on areas of scientific, navigational, or economic interest, including inner Frobisher Bay (IFB), one of the few areas in northern Canada with comprehensive acoustic bathymetric mapping coverage (Figure 1.1). This dissertation represents the first survey of the marine geohazards, specifically submarine slope failures (SSFs), and seafloor glacial features in that embayment.

The research presented here is part of a larger Frobisher Bay marine geoscience project. Starting in 2014, the ArcticNet-funded, GSC-supported, and CNGO-partnered project "Integrated Marine Geoscience to Guide Environmental Impact Assessment and Sustainable Development in Frobisher Bay, Nunavut" began a systematic and integrated investigation of the seabed in Frobisher Bay, with the purpose of generating geoscience knowledge to inform decision-making for infrastructure planning in the region (Hughes Clarke et al. 2015; Mate et al. 2015; Todd et al. 2016; Deering et al. 2018a, b).

Integrated marine geoscience draws upon knowledge and methods from a variety of fields to gain a more comprehensive understanding of a region (Vanneste et al. 2014). These methods include geological and hydroacoustic techniques, such as bathymetric mapping, sub-bottom profiling, substrate sampling and comprehensive analyses of materials, but also incorporate aspects of other disciplines such as habitat mapping. This robust approach is necessary to develop a better understanding of past and present seabed processes in a basin such as IFB. The focus of this dissertation is the analysis and interpretation of the post-glacial stratigraphy and seafloor geomorphology of IFB, with an emphasis on marine geohazards.

IFB is an area where increasing demands for coastal and seabed infrastructure intersect with a complex seafloor geomorphology. Near its head, the City of Iqaluit (Capital of Nunavut; 2016

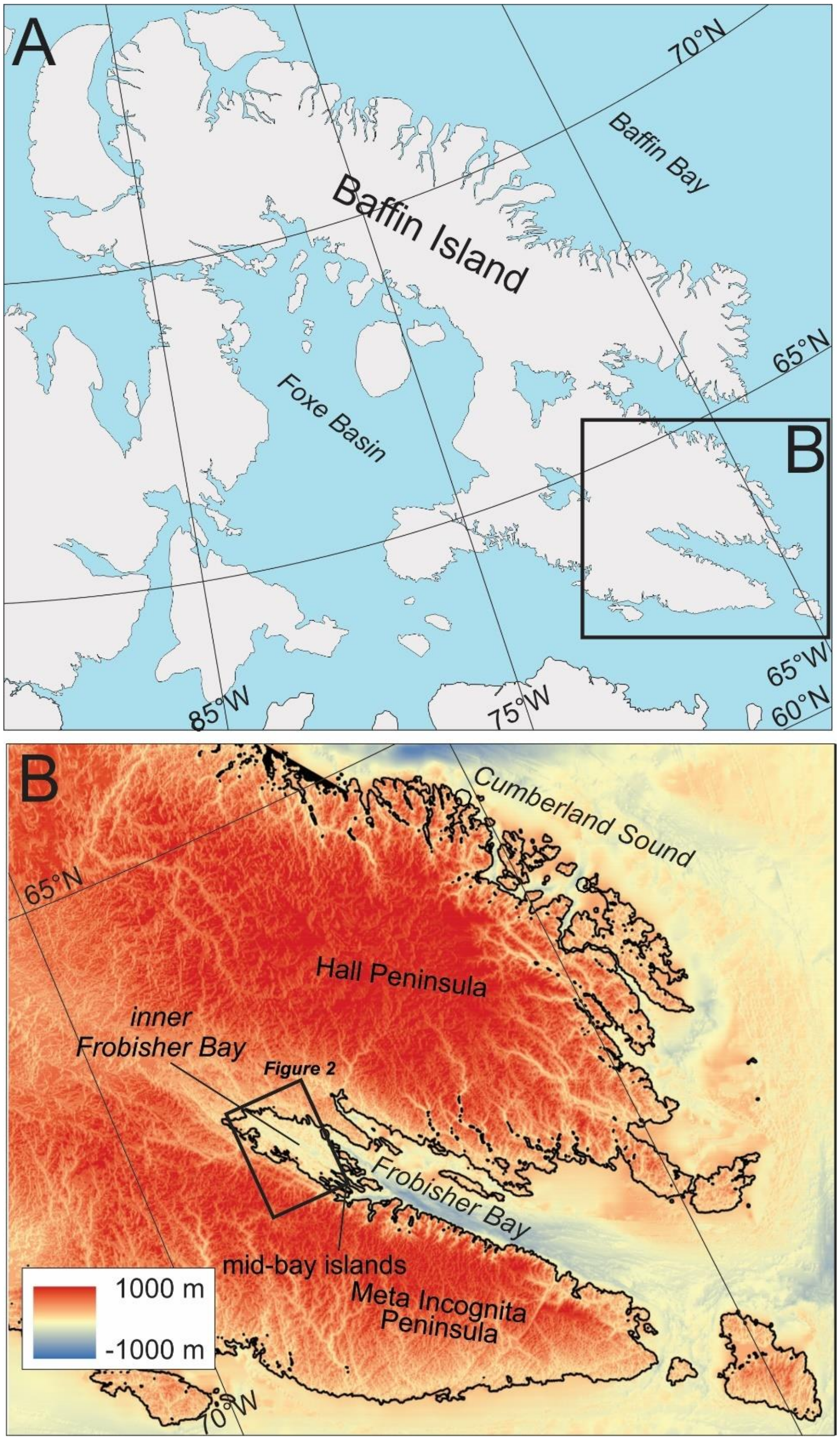

Figure 1.1 (A) Baffin Island showing regional place names and the location of Frobisher Bay (base map ESRI 2021). (B) Southeastern Baffin Island showing place names and outlining area shown in Figure 1.2. Background is GEBCO bathymetric and topographic data (GEBCO Compilation Group 2020).

population approx. 7740), is facing increased infrastructure demands, sparking the development of necessary upgrades to transportation, shipping, and communications infrastructure. This is culminating in two major projects: the deep-water Port of Iqaluit and a submarine fibre-optic connection to Greenland (funding announced 2019; projected online in 2023). Both projects will increase the economic capacity of Iqaluit and support its growing needs in the coming years, but the long-term sustainability of both is contingent on informed decision-making, including an understanding of seafloor processes in IFB.

1.2 Research Purpose and Questions

Until this study, the seafloor of IFB remained largely unknown. Little comprehensive bathymetric mapping had occurred, only what was required for navigation in and out of the port of Iqaluit. No sub-bottom surveying had occurred there. Minimal seafloor sampling, mostly for biological research, had taken place (e.g., Wacasey et al. 1980). First and foremost, this dissertation fills a geographically-defined research gap and generates a geoscience foundation on which future seafloor investigations can build. Baseline knowledge of the structure of the basin, the timing and style of deglaciation, and its underlying stratigraphy is a necessary precursor for understanding the processes that have acted on it since deglaciation began. The following research questions were addressed in this thesis and are accompanied by short introductory rationales.

Research Question 1: *How do the character and distribution of seafloor landforms and sediments augment our understanding of Laurentide ice retreat in IFB and in bathymetrically complex shallow basins?*

The previous understanding of deglaciation in IFB was based solely on terrestrial records. The extensive new marine morphological and stratigraphic records provided in this thesis allow us to augment our knowledge of local deglaciation processes and depositional environments. This understanding of ancient deglaciation may be useful for understanding deglacial processes occurring in marine environments today. Further knowledge of deglacial landforms and sediments provides context for research on post-glacial seafloor processes in IFB.

Research Question 2: *What was the deglacial chronology for IFB?*

Previous work to establish the timing of deglaciation in IFB relied on terrestrial glacial and raised glaciomarine features along the coast of the bay (Hodgson 2005). Those studies used primarily bulk radiocarbon dating and lacked the resolution required to establish a chronostratigraphy of marine sediments for IFB. The present work uses calibrated AMS radiocarbon dating of samples from seafloor sediment cores to establish marine chronostratigraphy and to refine the date of final continental ice withdrawal from IFB.

Research Question 3: *Do the large moraines in IFB coincide with the timing of the Cockburn Substage readvance as seen elsewhere on Baffin Island?*

In IFB, a series of large moraines mark both the northeast and southwest coasts. These are thought to have been the result of the Cockburn Substage readvance (and subsequent retreat) in IFB. Their connection has been surmised, but until now uproven. Understanding the timing of the formation of these features provides insight into the Cockburn Substage readvance on southern Baffin Island.

Research Question 4: *What is the basin setting and morphological character of SSFs in IFB and how do they compare with other populations in similar marine settings?*

Submarine slope failures may present a widespread marine geohazard in IFB. Based on multibeam echo-sounding (MBES) data, there are at least 246 of these features in the inner bay, a greater concentration than has been noted in any other embayment of the Canadian Arctic (Figure 1.2). The large number of SSF features mapped in high-resolution in IFB also allows for the measurement of a suite of morphometric parameters. Such morphometric measurements in relation to SSFs have not yet been standardized (Haflidason et al. 2005; Clare et al. 2018). This dissertation presents a set of measurements applied to 246 SSFs and suggests several new metrics not previously published in the literature.

Research Question 5: *Is there a suite of diagnostic features that help to identify relatively small SSFs in the bathymetric, sub-bottom acoustic and sedimentary records?*

The extensive record of SSFs in IFB provides an opportunity to illustrate how small SSFs can be recognized in bathymetric, acoustic sub-bottom, and sediment coring records. Identification of these features can aid in seafloor geoscientific hazard assessment both for research and engineering purposes. Practically, this can help to inform the sustainability of future seafloor and coastal infrastructure projects, both in IFB and in similar embayments.

Research Question 6: *What were the timing, triggering mechanism(s) and preconditioning factor(s) for SSFs in IFB?*

Until recently, small scale SSFs have, understandably, garnered less attention in the literature than their larger (typically more destructive) counterparts. Nevertheless, these features represent a localized marine geohazard. This dissertation examines the preconditioning factors, triggering mechanisms, and chronology of SSFs in IFB. This information can be applied to identify areas of the seafloor at risk of failing in IFB. Further, this could aid in future, regional marine geohazard assessments.

1.3 Study Area

Frobisher Bay is a large, partially enclosed embayment in southeastern Baffin Island. Approximately 265 km in length, it is widest at its mouth (~66 km), tapering toward its head. The bay can be divided into three physiographic sectors: outer and inner bay, and mid-bay islands. The outer bay (180 km long), open to the North Atlantic, is a half graben, with depths exceeding 800 m along the fault bounded southwestern coast. The mid-bay islands and the shallow channels that separate them divide the outer and inner bays. The inner bay is relatively shallow (<350 m deep), with two-thirds of it <100 m deep.

Frobisher Bay is bounded to the northeast and southwest by the Hall and Meta Incognita peninsulas, respectively. These peninsulas are composed of Paleoproterozoic metamorphic and igneous rocks from the Trans-Hudson Orogen (St-Onge et al. 2006; Steenkamp and St-Onge 2014). Minor outcrops of Paleoproterozoic marble occur north of Frobisher Bay, especially around Iqaluit. To the northwest of the bay (near Sylvia Grinnell Lake, approximately 50 km from the head of the bay) is an area of Ordovician carbonate rocks. A minor outlier of Paleozoic carbonate rocks also occurs near Foul Inlet. Based on the occurrence of Paleozoic carbonate materials in the till (Miller 1980) and observations from multibeam bathymetry data, carbonate-rich bedrock is thought to extend below the seabed of the outer bay (MacLean et al. 2014).

During the last glacial maximum (LGM), Frobisher Bay was covered predominantly by continental ice originating from the Foxe and Amadjuak domes to the northwest, with alpine glaciation occurring on local highlands (500–600 m elevation; Hodgson 2005; Miller et al. 2005; Tremblay et al. 2015). This LGM Foxe–Amadjuak ice extended beyond the inner bay to cover much of the outer bay. At c. 9800 cal BP, continental ice receded to the northwest of the mid-bay islands,

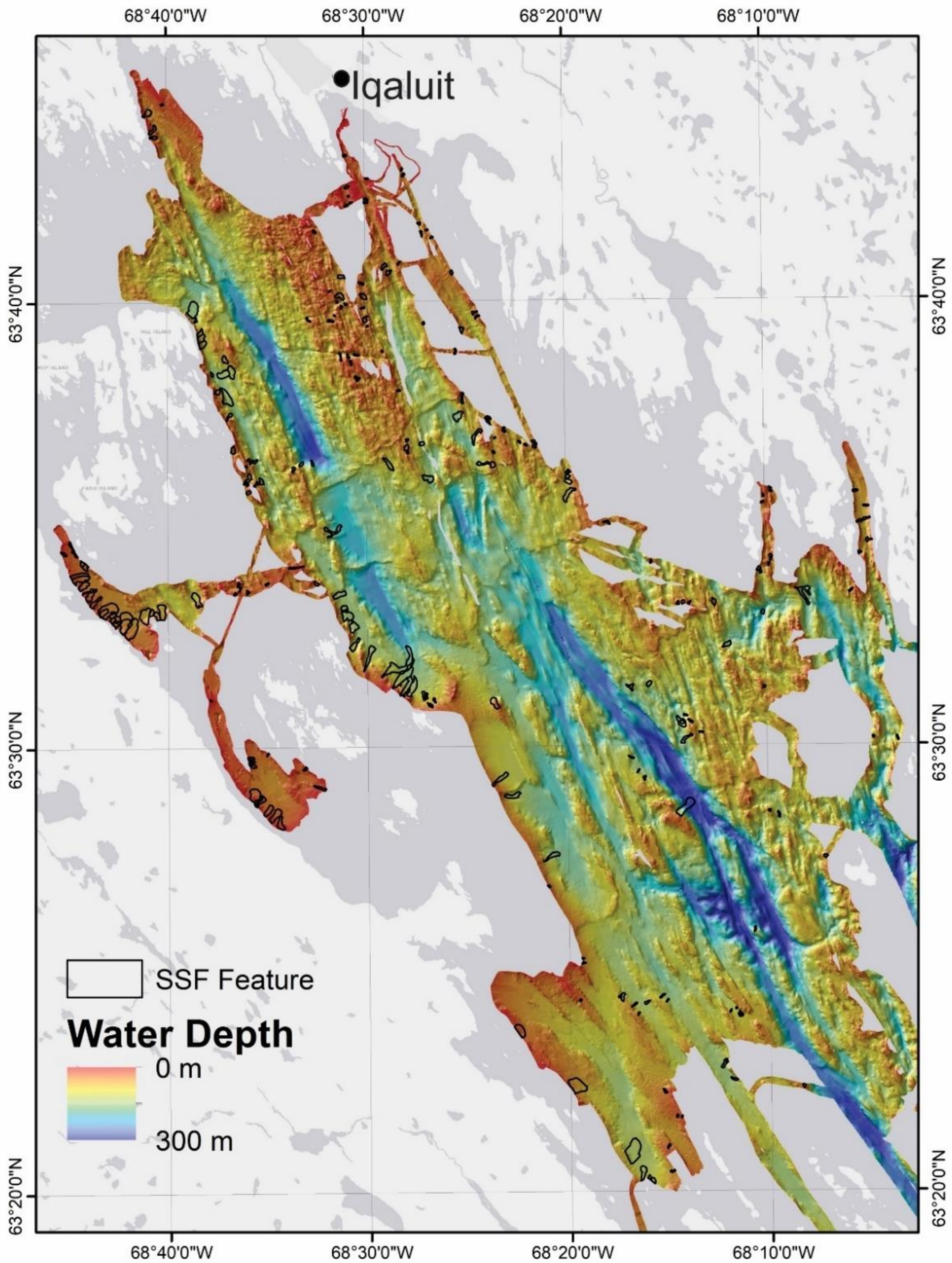

Figure 1.2 MBES bathymetric coverage (2.5 m resolution) in IFB with Iqaluit at top. Submarine slope failure (SSF) footprints are delineated with black outlines.

beginning a deglacial period of 2000 years that ended c. 7800 cal BP, when the ice front withdrew entirely from the bay (Squires 1984). This retreat is documented in the terrestrial record by large moraine complexes (Hall and Frobisher Bay moraines) on the flanking peninsulas (Miller 1980; Squires 1984). Following the retreat of continental ice from inner Frobisher Bay, a seasonal sea-ice regime was established, with alternating warmer and cooler intervals ever since (Jacobs et al. 1985).

Following deglaciation, the region also underwent a period of isostatic adjustment. At deglaciation, the marine limit (highest post-glacial relative sea level [RSL]) in the inner bay was ~120 m above current higher high-tide level (Jacobs et al. 1985). Immediately following deglaciation, with initially rapid isostatic uplift, RSL dropped rapidly (100 m/ka), exponentially decreasing over time (Jacobs et al. 1985). Inner Frobisher Bay experiences extreme tidal ranges (11.1 m at spring tides, 12.6 m maximum recorded tide; CHS 2022) in a regime thought to have been established c. 2750 cal BP because of these changes in sea level (Dowdeswell et al. 1985).

1.4 Methods

This dissertation uses multiple remote sensing and direct sampling methods to investigate the seafloor of IFB. The foundational dataset of this work is a multibeam echo-sounding (MBES) bathymetric dataset of the study area collected over a number of years using multiple vessels. MBES is a technique that bounces sound off the seafloor and measures return time to establish water depths. It uses a fan of beams originating from the sounder to map a swathe of seafloor as the vessel moves (Figure 1.3). MBES surveying was accomplished using instruments aboard RV *Nuliajuk*, a Government of Nunavut fisheries research vessel, and CCGS *Amundsen*, a Canadian Coast Guard research icebreaker. Full technical details of each vessel and their sounder configurations, as well as post-collection MBES data processing, are provided in each of the thesis manuscript chapters (see next section). This bathymetric dataset is used to describe the overall morphology of the seafloor of IFB, and to identify and measure the SSFs found there (see Appendix B for details on each SSF). It forms the core of, and enables all further lines of investigation in, this research.

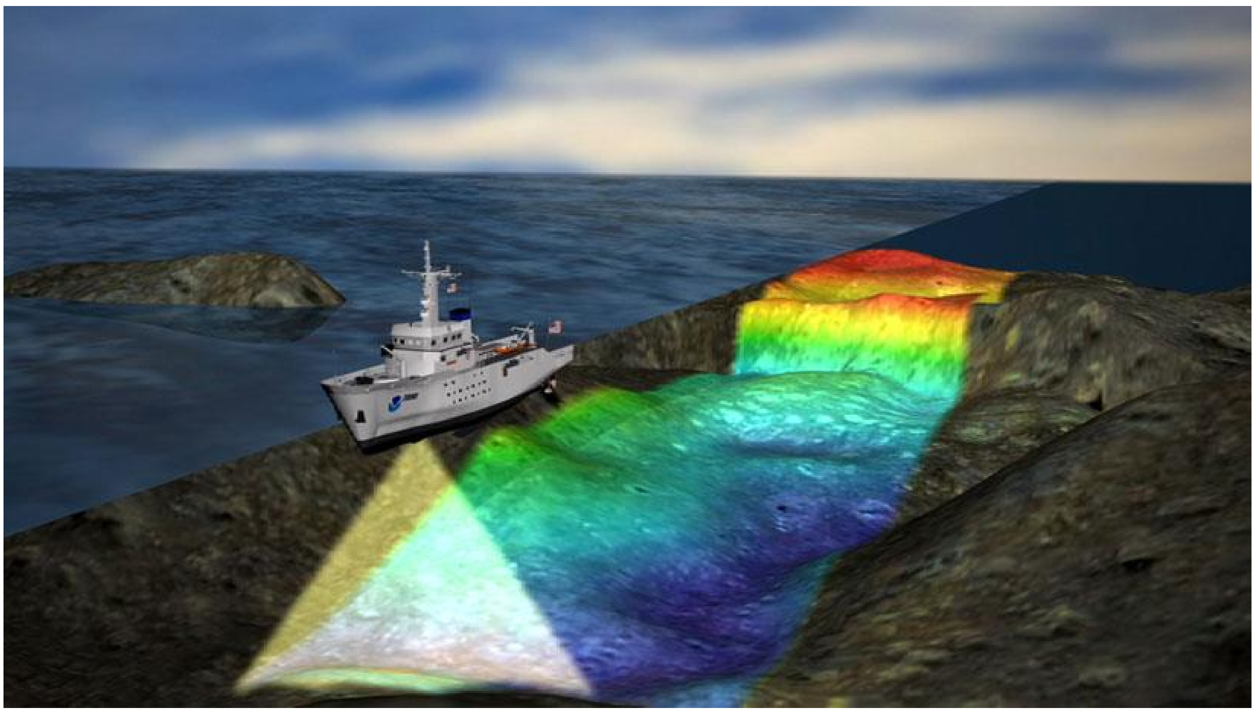

Figure 1.3 Graphic illustrating collection of multibeam echo-sounding data from a vessel (NOAA Ocean Exploration 2022)

Shallow sub-bottom acoustic records were collected concurrently with much of the MBES bathymetric record. Both RV *Nuliajuk* and CCGS *Amundsen* were equipped with 3.5 kHz sounders capable of sub-bottom penetration of up to ~20 m. The post-collection processing of data from the sub-bottom sounders is also described in the relevant manuscript chapters. The sub-bottom dataset is used to describe the undisturbed acoustic facies underlying the seafloor in IFB, examine different internal structures of failed sediments, and corroborate sediment distribution as observed in cores.

Direct sampling of the seafloor used three distinct coring systems. Due to vessel size and equipment resources, gravity coring occurred aboard RV *Nuliajuk*, while piston and box coring were more readily executed aboard CCGS *Amundsen*. Each of these coring techniques provides similar, but different, samples used to investigate the lithofacies underlying the seafloor. Full explanation of each of these systems is described in Chapters 2 and 4. All sampling locations are recorded online in the Natural Resources Canada (NRCan) Expedition Database (NRCan 2022).

Following collection, all sediment cores were received by the Geological Survey of Canada – Atlantic (GSC-A) core lab at the Bedford Institute of Oceanography. At that facility, cores underwent processing including collection of x-radiographs and photographs, the measurement of various physical properties, and subsampling for grain-size analysis and radiocarbon dating. A full description of the procedure used in this processing and subsampling is provided in Chapters 2 and 4 where the core data are presented and interpreted. All core descriptions, x-radiographs, photographs, physical property measurements, and subsamples are cataloged and archived at the GSC-A core lab. Grain-size data are accessible through the NRCan Expedition Database (op cit). Graphical representation of all sediment core data is available in Appendix A of this thesis.

Carbonate materials (typically bivalve shells) extracted from sediment cores were analyzed by accelerator mass spectrometry (AMS) to determine radiocarbon age. In cores with few datable materials, all suitable shells at various depths were dated. In those with an abundance of datable materials, samples near lithofacies boundaries farthest downcore were selected. In most cases, only a single specimen was dated, comprising either a single valve (or valve fragment) or an articulated bivalve pair. After removal from the cores, samples were cleaned, photographed, and identified by the late Alice Telka of Paleotec Services. In 2015-2017, the W.M. Keck-Carbon Cycle AMS Facility at the University of California (Irvine) analyzed all samples. In 2018, the André E. Lalonde AMS Laboratory at the University of Ottawa analyzed larger samples (>50 mg), while the Keck facility processed smaller samples. Ages were corrected for marine reservoir effect using the Marine20 calibration curve dataset ($\Delta R= 41 \pm 21$; Heaton et al. 2020), calibrated with Calib version 8.2 (Stuiver et al. 2021), and reported at the 1σ age range. Details on calibrated radiocarbon samples are provided in Chapter 2 Methods, Table 2.2, and Appendix C.

The impact of the "Portlandia Effect" (Vickers et al. 2010; England et al. 2013) may be widespread in the radiocarbon ages analyzed for this work (Deering et al. 2022). This causes ages for the shells of deposit feeding molluscs (particularly *Portlandia arctica*) in carbonate-rich substrate to exhibit older ages than suspension feeding molluscs in the same substrate. This limits the way in which affected shells can be used to constrain the age of stratigraphic features (England et al. 2013). Such potential impacts are described in Chapters 2 and 4 where chronology is a key dimension of the research.

1.5 Organization of Dissertation

This dissertation is arranged in chronological order, starting with the Cockburn Readvance and then moving on to more recent processes that shaped the seafloor. In addition to this introductory chapter, the dissertation comprises three original research manuscripts and a summary chapter. Each of these manuscripts focuses on different aspects of the seafloor geomorphology of IFB, one relating to deglacial features and the other two relating to SSFs. Each of these manuscripts can be read as stand-alone research papers, with two having undergone peer review and publication prior to submission of this dissertation for examination. Given their self-contained nature, there is necessarily some overlap between the background materials and methods descriptions in the manuscript chapters. My role in the production and publication of this research is outlined in the authorship statements following this chapter.

Chapter 2 establishes the deglacial basin stratigraphy for IFB. Using sediment cores and acoustic surveys, it examines the deglacial history of the basin in relation to the regional Cockburn Substage readvance during the early Holocene. This chapter has been published in a special issue of Canadian Journal of Earth Sciences with the theme of "Landscape and Seascape Responses to Canada's Changing Climate" under the title *Marine record of late-glacial readvance and last recession of Laurentide ice, inner Frobisher Bay, Baffin Island, Arctic Canada* (Deering et al. 2022). This publication venue was chosen as a way of showcasing the relevance of research into ancient deglacial processes to changes happening in the world today. While causes for climate changes may be different now than in the early Holocene, marine terminating ice fronts are undergoing similar retreat today. This chapter provides insight into how marine terminating ice fronts in bathymetrically complex embayments can react during ice sheet collapse. It is a contribution to our understanding of marine ice-front instability and retreat processes in the present era of rapid climate warming and widespread glacial recession.

Chapter 3 focuses solely on the acoustic bathymetric surveys of SSF features in IFB to describe their morphometry. Through the measurement of 12 and calculation of another seven physical parameters, 163 of the 246 mapped SSFs in the basin are described and categorized. Furthermore, this chapter compares the morphometry of this population of SSFs to other populations in the fjords of southern Alaska and the St. Lawrence Estuary. This chapter has been peer reviewed and published in a Geological Society of London Special Publication "Subaqueous Mass Movements and their Consequences: Assessing Geohazards, Environmental Implications and Economic Significance of Subaqueous Landslides” under the title *Morphological characterization of submarine slope failures in a semi-enclosed fjord, Frobisher Bay, eastern Canadian Arctic*. This publication venue was chosen because the volume linked to the “8th International Symposium on Submarine Mass Movements and their Consequences”, a conference focused on submarine slope failures. Conference participation allowed for review and assessment by colleagues in the discipline and publication in the companion volume provided access to an engaged audience of researchers and decision makers.

Chapter 4 builds off the undisturbed basin stratigraphy established in Chapter 2 to examine the chronology and stratigraphy of SSFs in IFB. Using multiple methods, including morphological analysis of acoustic data and stratigraphic analysis of sediment cores, the geographic distribution of SSFs is presented, different styles of SSF stratigraphy are described and a chronology of features is examined. Diagnostic morphological and stratigraphic indicators of SSFs are reported. Additionally, the implications of the above factors are examined in relation to possible triggering mechanisms for SSFs in IFB. This chapter will be submitted to Marine Geology for peer review and publication. This venue was chosen as it commonly publishes studies on SSFs and will provide wide distribution of study results and implications to an international audience.

Chapter 5 synthesizes the results of the three preceding chapters in relation to the research questions posed above and comments on the severity of SSFs as a geohazard in IFB with respect to planned and ongoing infrastructure development in the region. It provides information that may help engineers and geoscientists to recognize and map the occurrence of previous SSFs in the area and to identify preconditioning factors that heighten the risk of future SSFs in the region.

1.6 References

Canals M., Lastras G., Urgeles R., Casamor J.L., Mienert J., Cattaneo A., De Batist M., Haflidason H., Imbo Y., Laberg J.S., Locat J., Long D., Longva O., Masson D.G., Sultan N., Trincardi F., and Bryn P. (2004). Slope failure dynamics and impact from seafloor and shallow sub-seafloor geophysical data: case studies from the COSTA project. *Marine Geology*, 213, p. 9-72.

CHS (2022). *Canadian Tide and Current Tables 2022, Volume 4: Arctic and Hudson Bay*. Canadian Hydrographic Service, Fisheries and Oceans Canada, Ottawa

Clare M., Chaytor J., Dabson O., Gamboa D., Georgiopoulou A., Eady H., Hunt J., Jackson C., Katz O., Krastel S., Leon R., Micallef A., Moernaut J., Moriconi R., Moscardelli L., Mueller C., Normandeau A., Patacci M., Steventon M., Urlaub M., Volker D., Wood L., and Jobe Z. (2018). A consistent global approach for the morphometric characterization of subaqueous landslides; *in* Subaqueous Mass Movements, D.G. Lintern, D.C. Mosher, L.G. Moscardelli, P.T. Bobrowsky, C. Campbell, J.D. Chaytor, J.J. Clague, A. Georgiopoulou, P. Lajeunesse, A. Normandeau, D.J.W. Piper, M. Scherwath, C. Stacey and D. Turmiel (ed.); *Geological Society, London, Special Publications*, v. 477, URL <https://doi.org/10.1144/SP477.15>.

Cochard R., Ranamukhaarachchi S.L., Shivakoti G.P., Shipin O.V., Edwards P.J., and Seeland K.T. (2008). The 2004 tsunami in Aceh and southern Thailand: a review on coastal ecosystems, wave hazards and vulnerability. *Perspectives in Plant Ecology, Evolution and Systematics* 10: 3-40.

Deering R., Bell T., Forbes D.L., Campbell C. and Edinger E. (2018a). Morphological characterization of submarine slope failures in a semi-enclosed fjord, Frobisher Bay, eastern Canadian Arctic; *in* Subaqueous Mass Movements, D.G. Lintern, D.C. Mosher, L.G. Moscardelli, P.T. Bobrowsky, C. Campbell, J.D. Chaytor, J.J. Clague, A. Georgiopoulou, P. Lajeunesse, A. Normandeau, D.J.W. Piper, M. Scherwath, C. Stacey and D. Turmiel (ed.); *Geological Society, London, Special Publications*, v. 477, URL <https://doi.org/10.1144/ SP477.35>.

Deering R., Misiuk B., Bell T., Forbes D.L., Edinger E., Tremblay T., Telka A., Aitken A. and Campbell C. (2018b). Characterization of the seabed and postglacial sediments of inner Frobisher Bay, Baffin Island, Nunavut; *in* Summary of Activities 2018, Canada-Nunavut Geoscience Office, p. 139–152.

Deering R., Bell T., and Forbes D.L. (2022). Marine record of late-glacial readvance and last recession of Laurentide ice, inner Frobisher Bay, Baffin Island, Arctic Canada. *Canadian Journal of Earth Sciences*, doi: 10.1139/cjes-2021-0004

Dowdeswell J.A., Osterman L.E., and Andrews J.T. (1985). Quartz sand grain shape and other criteria used to distinguish glacial and non-glacial events in a marine core from Frobisher Bay, Baffin Island, N.W.T., Canada. *Sedimentology*, 32, p. 119-132.

England J., Dyke A.S., Coulthard R.D., McNeely R., and Aitken A. (2013). The exaggerated radiocarbon age of deposit-feeding molluscs in calcareous environments. *Boreas*, 42(2), p. 362-373.

ESRI (2021). Light Gray Canvas. [Basemap.] Available from https://basemaps.arcgis.com/arcgis/rest/services/World_Basemap_v2/VectorTileServer.

GEBCO Compilation Group. 2020. GEBCO 2020 Grid. doi:10.5285/a29c5465- b138-234d-e053-6c86abc040b9.

Gosse J.C., Tremblay T., Broom L.A., Campbell D.C., Wenzel G., Nedimoviæ M.R. and Forget Brisson L. (2020). Initial results from the ULINNIQ seismicity and tsunami hazard project, northeastern Baffin Island, Nunavut; in Summary of Activities 2019, Canada-Nunavut Geoscience Office, p. 101–124.

Haflidason H., Lien R., Sejrup H.P., Forsberg C.F., and Bryn P. (2005). The dating and morphometry of the Storegga Slide. *Marine and Petroleum Geology*, 22, p. 123-136.

Heaton T.J., Köhler P., Butzin M., Bard E., Reimer R.W., Austin W.E.N., Ramsey C.B., Grootes, P.M., Hughen K.A., Kromer B., Reimer P.J., Adkins J., Burke A., Cook M.S., Olsen J., and Skinner L.C. (2020). Marine20 – The marine radiocarbon age calibration curve (0-55,000 cal BP). *Radiocarbon*, 62(4), p. 779-820

Hodgson D.A. (2005). Quaternary geology of western Meta Incognita Peninsula and Iqaluit area, Baffin Island, Nunavut. Geological Survey of Canada, *Bulletin 582*, 72 p.

Hughes Clarke J.E., Muggah J., Renoud W., Bell T., Forbes D.L., Cowan B. and Kennedy J. (2015). Reconnaissance seabed mapping around Hall and Cumberland peninsulas, Nunavut: opening up southeastern Baffin Island to nearshore geological investigations. *in* Summary of Activities 2014, Canada-Nunavut Geoscience Office, 135-144 (http://cngo.ca/summary-of-activities2014)

Jacobs J.D., Mode W.N., Squires C.A. and Miller G.H. (1985). Holocene environmental change in the Frobisher Bay Area, Baffin Island, N.W.T.: deglaciation, emergence, and the sequence of vegetation and climate. *Géographie physique et Quaternaire,* v. 39, no. 2, p. 151–162.

Lastras G., Amblas D., Calafat A.M., Canals M., and Frigola J. (2013). Landslides cause tsunami waves: insights from Aysén Fjord, Chile. *Eos*, 94(34), p. 297-298.

Leynaud D., Mienert J., and Vanneste M. (2009). Submarine mass movements on glaciated and non-glaciated European continental margins: A review of triggering mechanisms and preconditions to failure. *Marine and Petroleum Geology*, 26(5), p. 618-632.

MacLean B., Williams G., and Zhang S. (2014). New insights into the stratigraphy and petroleum potential of the Baffin shelf's Cretaceous rocks. *Bulletin of Canadian Petroleum Geology*, v. 62, p. 289–310, URL https://doi.org/10.2113/gscpg bull.62.4.289.

Mate D.J., Campbell D.C., Barrie J.V., Hughes Clarke J.E., Muggah J., Bell T., and Forbes D.L. (2015). Integrated seabed mapping of Frobisher Bay, southern Baffin Island, Nunavut to support infrastructure development, exploration and natural-hazard assessment; *in* Summary of Activities 2014, Canada-Nunavut Geoscience Office, p. 145–152.

McGranahan G., Balk D., and Anderson B. (2007). The rising tide: assessing the risks of climate change and human settlements in low elevation coastal zones. *Environment and Urbanization*, *19*(1), 17-37.

Miller G. H. (1980). Late Foxe glaciation of southern Baffin Island, N.W.T., Canada. *Geological Society of America Bulletin*, 91(7), p. 399–405.

Miller G.H., Wolfe A.P., Briner J.P., Sauer P.E. and Nesje A. (2005). Holocene glaciation and climate evolution of Baffin Island, Arctic Canada. *Quaternary Science Reviews,* 24(14), p. 1703–1721, URL <https://doi.org/10.1016/j.quascirev.2004.06.021>.

Natural Resources Canada (2022). Expedition Database; website, Natural Resources Canada, Dartmouth, NS, URL ,

NOAA Ocean Exploration (2022). Multibeam Sonar; website, URL https://oceanexplorer.noaa.gov/technology/sonar/multibeam.html

Normandeau A., Campbell D.C., Bennett R., Macquarrie M., MacKillop K., Philibert G., Sedore P., Maselli V., and Jenner K.A. (2020). Holocene and active marine geohazards offshore eastern Baffin Island, Nunavut; in Summary of Activities 2019, Canada-Nunavut Geoscience Office, p. 93–100.

Nunatsiaq News (2021). *A future landslide-triggered tsunami in Greenland could be a lot bigger than experts first thought*. Website retrieved from: https://nunatsiaq.com/stories/article/a-future-landslide-triggered-tsunami-in-greenland-could-be-a-lot-bigger-than-experts-first-thought/. September 30, 2022.

Squires C.A. (1984). The late Foxe deglaciation of the Burton Bay area, southeastern Baffin Island, N.W.T.; MA thesis, University of Windsor, Windsor, Ontario, 115 p.

Steenkamp H. M. and St-Onge M. R. (2014). Overview of the 2013 regional bedrock mapping program on northern Hall Peninsula, Baffin Island, Nunavut; *in* Summary of Activities 2013, Canada-Nunavut Geoscience Office, p. 27–38.

St-Onge M.R., Jackson G.D. and Henderson I. (2006). Geology, Baffin Island (south of 70°N and east of 80°W), Nunavut; Geological Survey of Canada, Open File 4931, 3 sheets at 1:500 000 scale, 1 CD-ROM, URL <https://doi.org/ 10.4095/222520>.

Stuiver M., Reimer P.J., and Reimer R.W. 2021: CALIB Radiocarbon Calibration, version 8.2; computer software.

Syvitski J.P.M., Burrell D.C., and Skei J.M. (1987). Subaqueous slope failure. *In* Syvitski J.P.M. et al. (Eds.) *Fjords: Processes and Products*, p. 175-210. Springer-Verlag Publishing.

Telegeography (2017). *Submarine cable frequently asked questions*. Website retrieved from: http://www2.telegeography.com/submarine-cable-faqs-frequently-asked-questions. May 9, 2017.

Todd B.J., Shaw J., Campbell D.C., and Mate D.J. (2016). Preliminary interpretation of the marine geology of Frobisher Bay, Baffin Island, Nunavut. *In* Summary of Activities 2016, Canada-Nunavut Geoscience Office, p. 61-66.

Tremblay T., Day S., McNeil R., Smith K., Richardson M., and Shirley J. (2015). Overview of surficial geology mapping and geochemistry in the Sylvia Grinnell Lake area, Baffin Island, Nunavut; *in* Summary of Activities 2015, Canada-Nunavut Geoscience Office, p. 107– 120.

Van Daele M, Versteeg W, Pino M., Urrutia R., and De Batist M. (2013). Widespread deformation of basin-plain sediments in Aysén fjord (Chile) due to impact by earthquake-triggered, onshore-generated mass movements. *Marine Geology,* 337: 67-79.

Vanneste M, Sultan N, Garziglia S., Forsberg C.F., and L'Heuruex J.-S. (2014). Seafloor instabilities and sediment deformation processes: the need for integrated multi-disciplinary investigations. *Marine Geology.* 352: 183-214.

Vickers K.J., Ward B.C., Utting D.J., and Telka A.M. (2010). Deglacial reservoir age and implications, Foxe Peninsula, Baffin Island. *Journal of Quaternary Research*, 25(8), p. 1338-1346

Wacasey J.W., Atkinson G. and Glasspoole, L. (1980). Zoobenthos data from inshore stations of Upper Frobisher Bay 1969–1976; Canadian Data Report of Fisheries and Aquatic Sciences, no. 205, 42 p.

Yonggang J., Chaoqi Z., Liping L., and Dong W. (2016). Marine geohazards: review and future perspective. *Acta Geologica Sinica (English Edition),* 90(4): 1455-1470

Co-authorship Statement

This dissertation is presented in manuscript format. Chapters two and three have been published. They are presented in this dissertation as they were published, with some minor grammatical corrections. The author of this dissertation is the principal researcher for all manuscripts.

Chapter two was published in *Canadian Journal of Earth Sciences* (doi: 10.1139/cjes-2021-0004). The author of this dissertation was the primary contributor to study design, data collection, processing of field samples, data analysis, and manuscript authorship. Co-supervisors Drs. Trevor Bell and Don Forbes, and supervisory committee members Drs. Calvin Campbell and Evan Edinger initiated this project in partnership with ArcticNet, the Geological Survey of Canada, the Government of Nunavut, and the Canada-Nunavut Geoscience Office. All participated in data collection, data analysis, and editing of the manuscript.

Chapter three was published in a Geological Society of London Special Publication *Subaqueous Mass Movements and their Consequences: Assessing Geohazards, Environmental Implications and Economic Significance of Subaqueous Landslides*. The author of this dissertation was the primary contributor to study design, data collection, data analysis, and manuscript authorship. Co-supervisors Drs. Trevor Bell and Don Forbes, and supervisory committee members Drs. Calvin Campbell and Evan Edinger participated in study design, data collection, and editing of the manuscript.

Chapter 4 is yet to be published. The author of this dissertation was the primary contributor to study design, data collection, data analysis, and manuscript authorship. Co-supervisors Drs. Trevor Bell and Don Forbes, and supervisory committee members Drs. Calvin Campbell and Evan

Edinger participated in study design, sample analysis, data collection and analysis, and editing of the manuscript.

The author of this dissertation has contributed to other work related to these manuscripts that has been submitted for publication and has not been included here. The technical report, "Characterization of the seabed and postglacial sediments of inner Frobisher Bay, Baffin Island, Nunavut", was published in the 2018 Canada-Nunavut Geoscience Office Summary of Activities, along with co-authors Drs. Benjamin Misiuk, Trevor Bell, Donald Forbes, Evan Edinger, Alec Aitken, and Calvin Campbell, and Tommy Tremblay and the late Alice Telka. The author of this dissertation was the primary contributor to the writing of this manuscript.

2. Marine record of late-glacial readvance and last recession of Laurentide ice, inner Frobisher Bay, Baffin Island

2.1 Introduction

Short-term decelerations or pauses of otherwise retreating glacial margins are commonly recognized in past and present-day ice sheets (Batchelor et al. 2018; Kingslake et al. 2018). Typically attributed to cooling temperatures, these fluctuations may also be connected to factors such as changes in internal ice sheet configuration (Jamieson et al. 2012), variable bathymetry or topography (Warren and Hulton 1990; Batchelor et al. 2018), changes in relative sea levels, or in precipitation (Gaglioti et al. 2019). In today's warming climate, with widespread rapid outlet glacier retreat, it is more important than ever to understand how these factors contribute to ice-front instability. A study of fluctuating former ice-fronts under an earlier warming climate may provide insight.

Near the peak of Holocene temperatures following the Younger Dryas, the remnants of the Laurentide Ice Sheet (LIS) on Baffin Island were undergoing widespread readvance along the eastern margin (Andrews and Ives 1978; Miller et al. 2005; Briner et al. 2009). The Cockburn Substage readvance (c. 9.5-8.5 ka cal BP) has been recognized in the region from a series of discontinuous end moraines stretching more than 1000 km from northwest to southeast Baffin Island (Ives and Andrews 1963; Fig. 2.1A). Typically, these moraines are found at the heads of fiords and marine embayments, both above and below present sea level (Margreth et al. 2017; Brouard and Lajeunesse 2019), and crossing uplands of intervening peninsulas.

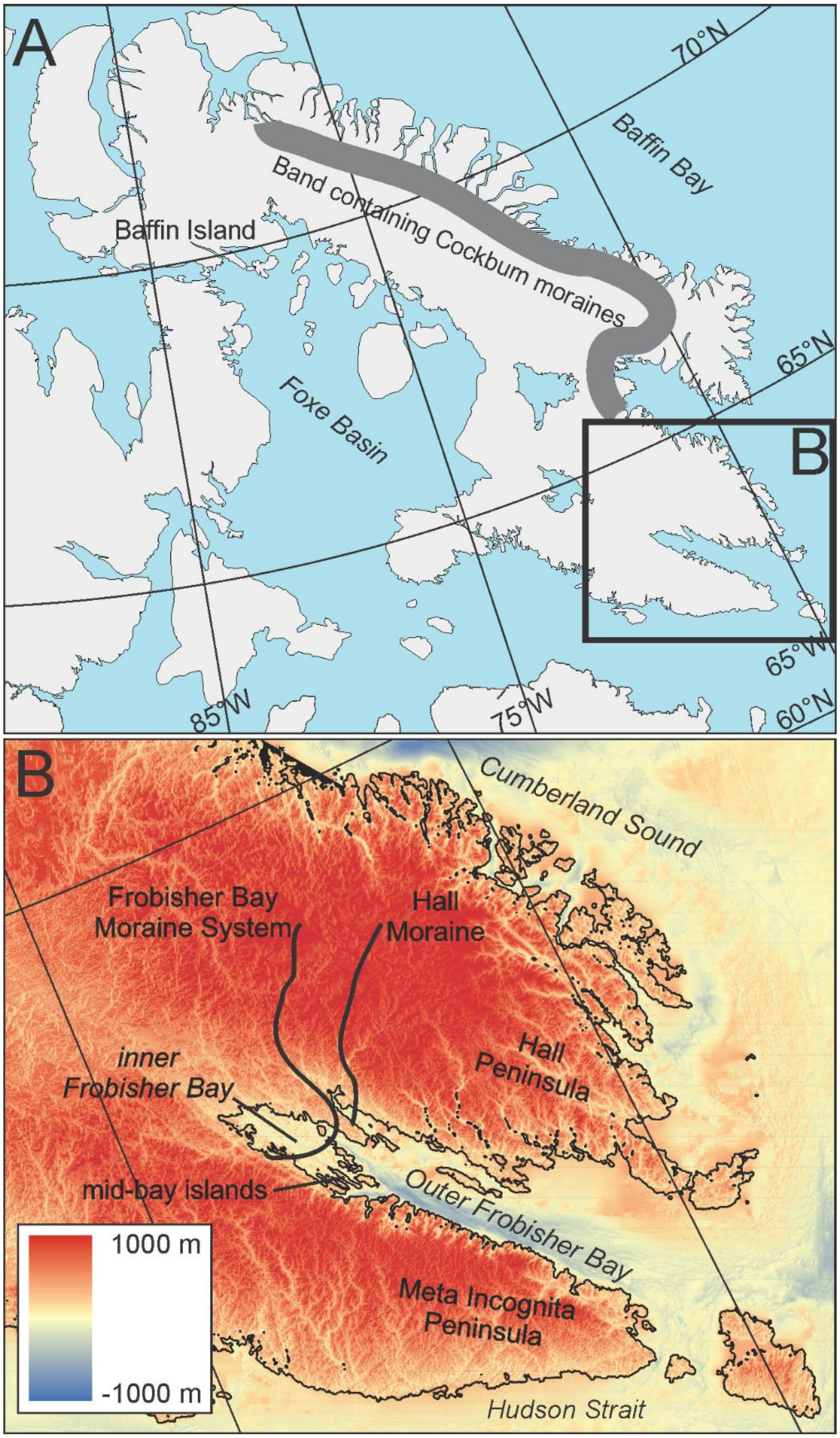

Figure 2.1 (A) Baffin Island showing regional distribution of Cockburn Substage moraines along the northeast coast (data from Andrews and Ives 1978; base map ESRI 2021). (B) Southeastern Baffin Island showing place names and moraine systems mentioned in the text. Background is GEBCO bathymetric and topographic data (GEBCO Compilation Group 2020).

Along the shores of inner Frobisher Bay, a series of end moraines marking a late-glacial readvance has been recognized for 55 years and named the Frobisher Bay Moraine system (Blake 1966; Fig. 2.1A, B). This moraine complex comprises multiple distinct ridges over a 20-km-wide swath, with the outermost one assigned an early Cockburn age (c. 9.5 ka cal BP; Blake 1966; Jacobs et al. 1985; Stravers et al. 1992; Hodgson 2005). The configuration of moraines beneath the bay, however, was unknown until 2015, following preliminary investigations using multibeam acoustic bathymetric surveys (Hughes Clarke et al. 2015; Mate et al. 2015; Tremblay et al. 2015).

This paper provides the first comprehensive mapping and analysis of the submarine component of the Frobisher Bay Moraine system, using a combination of acoustic bathymetric and sub-bottom surveying and seafloor sampling. Its primary purpose is to examine the geomorphology and sedimentary record of the presumed Cockburn Substage readvance and subsequent retreat on the seafloor of inner Frobisher Bay, focusing on the style of deglaciation. It maps, describes, and interprets the associated landforms and sediments, using radiocarbon ages of molluscan fossils from sediment cores to establish the chronology and changing style of post-Cockburn ice recession. Further, it establishes a chronostratigraphy of changing sedimentary characteristics and deposition rates in the basin from deglaciation to modern times.

2.1.1 Background

During the last glacial maximum (LGM), continental ice originating from the Foxe and Amadjuak domes of the LIS to the northwest of IFB covered much of southeast Baffin Island, extending locally onto the continental shelf (Hodgson 2005; Miller et al. 2005; Tremblay et al. 2015; Dalton et al. 2020). In Frobisher Bay, continental ice reached the mouth of the bay, with a grounded ice stream extending to at least the mid-bay islands (Fig. 2.1B; Margold et al. 2015a, b). The deep, fault-bounded, southwest trough of the outer bay may have been occupied by a floating ice shelf, which re-grounded on the sill near the mouth of the bay (Osterman 1982). To the north, Cumberland Sound was occupied by an ice stream originating from the confluence of Foxe-Amadjuak ice and a local ice cap on Hall Peninsula (Fig. 2.1B; Jennings 1993; Margold et al. 2015a, b). To the south, the well-documented Hudson Strait ice stream was formed at the confluence of Foxe and Labrador ice (Stravers et al. 1992; Andrews and Maclean 2003; Hodgson 2005; Margold et al. 2015a, b). Locally, small ice caps (Grinnell and Terra Nivea) occupied the highlands of outer Meta Incognita Peninsula (Fig. 2.1B).

Using glacial and raised marine geomorphic features, a deglacial history has been established for Frobisher Bay (Blake 1966; Miller 1980; Squires 1984; Jacobs et al. 1985; Stravers et al. 1992; Hodgson 2005). Foxe-Amadjuak ice had retreated at least partially from outer Frobisher Bay by c. 10 ka ^{14}C BP (c. 11.5 ka cal BP)[1] when ice from the Labrador Dome advanced north across Hudson Strait and into the outer bay as far as Gold Cove on the Hall Peninsula (Stravers et al. 1992; Kaufman et al. 1993). This late Younger Dryas advance is recorded both in the marine stratigraphic record and the terrestrial glacial geomorphology flanking the bay (Stravers et al. 1992). By c. 9.5-9.0 ka ^{14}C BP (c. 10.1-9.5 ka cal BP), Labrador ice had withdrawn and Foxe-Amadjuak ice had receded into inner Frobisher Bay an unknown distance (Stravers et al. 1992). Later, during the Cockburn Substage (c. 9.5-8.5 ka cal BP), both Foxe-Amadjuak and Labrador ice re-advanced into Frobisher Bay, but to a lesser extent (Stravers et al. 1992). By c. 7.0 ka ^{14}C BP (c. 7.8 ka cal BP), continental glacial ice had receded entirely from Frobisher Bay, leaving only local ice caps on adjacent uplands (Squires 1984). Following deglaciation, the seasonal sea-ice regime was established in inner Frobisher Bay (Hodgson 2005).

[1] ^{14}C ages presented in the text are previously published uncalibrated radiocarbon dates. Cal BP equivalent ages in parentheses have been calibrated as described in Methods below.

The two episodes of major continental ice readvance are marked in Frobisher Bay by two large moraine complexes. The Gold Cove Advance coincides with formation of the Hall Moraine, extending from near the mid-bay islands northeast towards Cumberland Sound (Fig. 2.1B; Blake 1966; Dyke 1979; Miller 1985). The Cockburn Substage readvance resulted in formation of the Frobisher Bay Moraine system that flanks the inner bay (Figs. 2.1B, 2.2; Jacobs et al. 1985; Hodgson 2005; Tremblay et al. 2015). Minimum age estimates for moraine abandonment are based on radiocarbon-dated raised marine features formed after glacial retreat (Table 2.1, Fig. 2.3); they range between 9.5 and 8.0 ka cal BP (Hodgson 2005). These estimates are consistent with the ages of other Cockburn Substage moraines found along the shores of Cumberland Peninsula and northeastern Baffin Island (Margreth et al. 2017).

Since deglaciation began, Frobisher Bay has been undergoing isostatic rebound, resulting in falling relative sea levels (except in the outermost parts of the bay; Miller et al. 1980). For the inner bay, there is a marked difference in recorded marine limit based on distance from the head of the bay. At the mid-bay islands, raised marine features have been mapped up to 119 m above present sea level (asl; Jacobs et al. 1985; Hodgson 2005). Some 20 km closer to the head of the bay, inside the outermost ridge of the Frobisher Bay Moraine, marine limit is at ~42 m asl, and drops to ~30 m asl nearer the head of the bay (Hodgson 2005).

Previous marine studies in Frobisher Bay have focused primarily on the deeper waters of the outer bay (e.g., Osterman 1982; Osterman and Andrews 1983; Stravers et al. 1992). Prior marine research in inner Frobisher Bay was limited mostly to shore-zone and nearshore geomorphology and ecological research (e.g., McCann et al. 1981; Atkinson and Wacasey 1987; Dale et al. 2002; Hatcher 2013).

Table 2.1 Previously reported radiocarbon dates from raised marine features around the shores of inner Frobisher Bay. Site #, Lat, and Long match locations shown in Figure 2.3. Elevations are in metres above sea level. Lab Id is original processing number of the sample. Method indicates whether sample was analyzed using atomic mass spectrometry (AMS) or conventional counting (C) methods. ^{14}C Age (±) is originally reported, uncalibrated age of sample. 1-sigma Cal Age Range is the calibrated age range of the sample, rounded to the nearest ten. Genus and species are listed where known. Sample Type indicates whether a single shell or multiple shells were combined for dating. Enclosing Material indicates where sample was collected. Deglacial Context and Age indicates shell position relative to the former ice-front. Portlandia Effect indicates where samples are known to be impacted (Y), known to be unimpacted (N), and where the impact is unknown (U). First Reference is the first record reporting the date (1, Manley 1995; 2, Blake 1966; 3, Lind 1983; 4, Andrews and Short 1983).

Site No.	Lat	Long	Elevation (m a.s.l.)	Lab ID	Method	^{14}C age (±)	1-σ cal age range	Species	Sample type	Enclosing material	Deglacial context and age	Portlandia Effect	First reference
T1	63.362	−68.372	18	AA-15130	AMS	8325 (75)	8750–8480	*Portlandia arctica*	Single valve	Exposure, diamicton	Glaciomarine, minimum	Y	1
T2	63.392	−68.417	87	GSC-462	C	8630 (240)	9350–8710	Molluscs	Bulk	Surface, silt	Glaciomarine, ice proximal	U	2
T3	63.415	−68.437	4	AA-16403	AMS	9100 (80)	9710–9460	*Portlandia arctica*	Single valve	Exposure, mud	Glaciomarine, minimum	Y	1
T4	63.417	−68.450	14	Beta-1871	C	7540 (115)	7920–7650	Molluscs	Bulk	Surface, silt + sand	Glaciomarine, minimum	U	3
T5	63.435	−68.500	15	Beta-1872	C	7995 (130)	8390–8080	Molluscs	Bulk	Surface, sand	Glaciomarine, minimum	U	3
T6	63.437	−68.423	28	AA-17861	AMS	9355 (75)	10110–9810	*Macoma calcarea*	Single valve	Exposure, mud	Glaciomarine, ice proximal	N	1
T7	63.610	−68.173	1	GSC-5903	C	7480 (120)	7850–7580	Molluscs	Bulk	Exposure, laminated sandy mud	Ice contact, delta	U	1
T8	63.642	−68.108	16	AA-15123	AMS	8350 (70)	8780–8510	*Macoma calcarea*	Single valve	Exposure, diamicton below sand	Ice contact, delta	N	1
T9	63.650	−68.100	39	GX-8159	C	8850 (190?)	9050–9040	Molluscs	Bulk	Bottomset, silty sand	Pro-glacial, delta	U	4
T10	63.693	−68.258	5	QC-905	C	8200 (150)	8680–8280	Molluscs	Bulk	Riverbank, sandy silt	Glaciomarine, minimum	U	4
T11	63.700	−68.233	34	QC-902	C	7910 (320)	8520–7800	Molluscs	Bulk	Unknown	Glaciomarine, minimum	U	4
T12	63.712	−68.297	13	QC-901	C	7740 (135)	8150–7830	Molluscs	Bulk	Riverbank, laminated sand and silt	Glaciomarine, minimum	U	4
T13	63.717	−68.250	11	GSC-2771	C	7780 (220)	8270–7790	Molluscs	Bulk	Bottomset	Post-glacial, delta	U	4
T14	63.742	−68.600	16	GX-8160	C	7480 (175?)	7920–7550	Molluscs	Bulk	Exposure, silty sand	Glaciomarine, minimum	U	4
T15	63.750	−68.533	3	GSC-553	C	6840 (160)	7290–6910	Molluscs	Bulk	Sandy silt	Post-glacial, delta	U	2

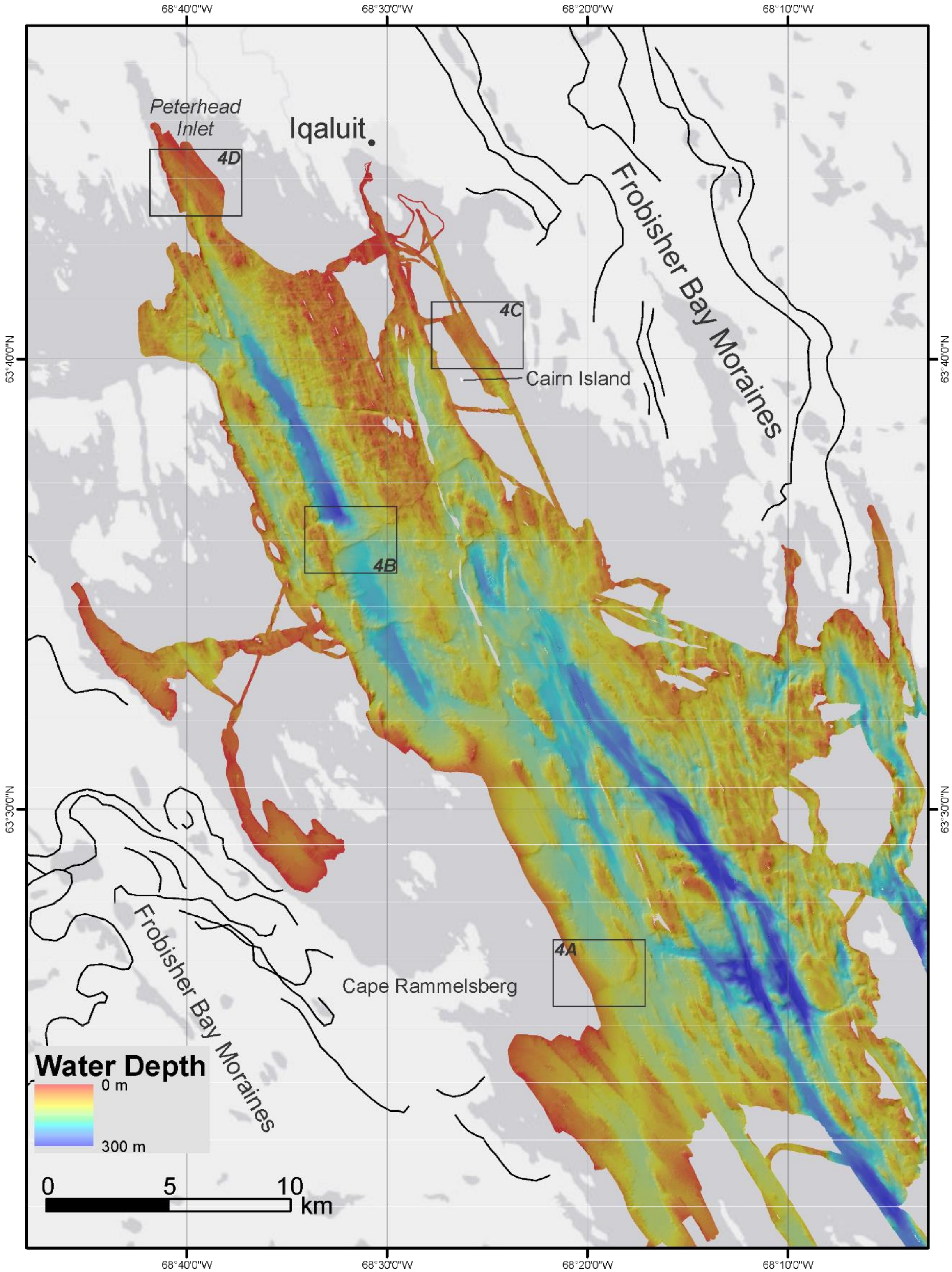

Figure 2.2 Multibeam bathymetric coverage in inner Frobisher Bay, showing complex bathymetry, streamlined glacial landforms, and place names mentioned in the text. Terrestrial Frobisher Bay Moraines are mapped as black lines (data from Hodgson 2005; base map ESRI 2021). Black boxes indicate areas shown in more detail in Figure 2.4.

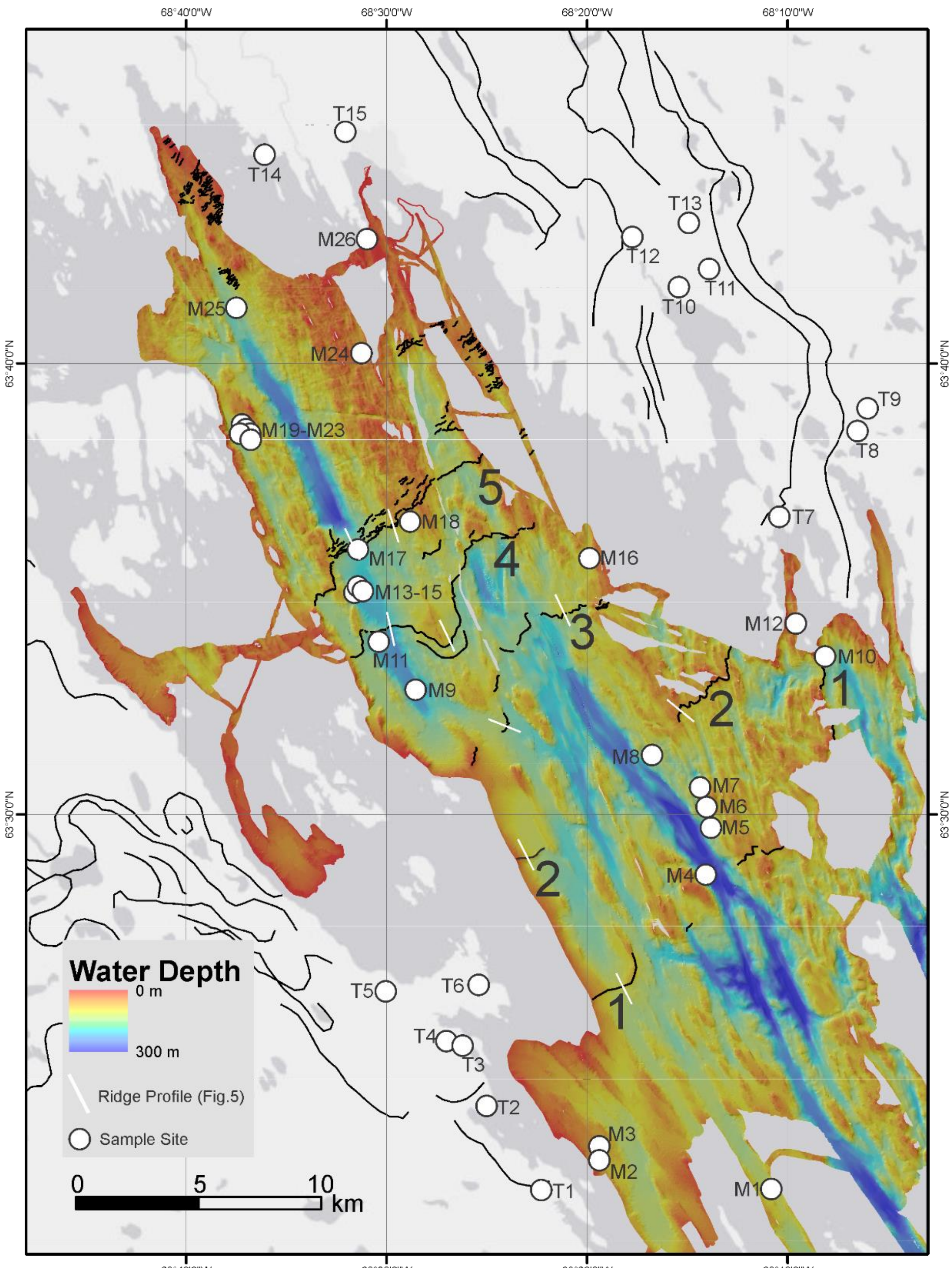

Figure 2.3 Sample site location and numbers for inner Frobisher Bay. Background is multibeam bathymetric coverage. White circles indicate locations where radiocarbon dated shells have been collected. Sites labels indicate whether they are from raised marine features (T) or from seafloor sediment cores (M). White lines indicate locations and orientations of ridge profiles in Figure 2.5 (not to scale). Map shows seafloor moraine ridges as black lines, labeled by numbers referred to in text. Site M25 indicates location of sub-bottom image in Figure 2.6B. Base map ESRI 2021.

2.1.2 Study Area

Frobisher Bay is a partially enclosed embayment located at the southeastern end of Baffin Island (Fig. 2.1). With its major axis extending ~265 km and aligned roughly northwest-southeast, Frobisher Bay is widest (66 km) at its mouth and tapers toward its head. The bay can be divided into three distinct physiographic regions: outer bay, mid-bay islands, and inner bay (Fig. 2.1B). The outer bay opens to the North Atlantic and is a half graben with water depths exceeding 800 m along the fault-bounded, near-vertical, southwest coast. The mid-bay islands with intervening channels (typically <20 m deep) extend across the bay approximately 55 km from its head, creating a natural barrier to circulation between the outer and inner bays.

Inner Frobisher Bay is a mostly enclosed basin approximately 55 km long by 25 km wide, with a bathymetry characterized by troughs, ridges, and relatively flat bathymetric highs. Numerous islands and peninsulas subdivide the bay into smaller, typically shallow, sub-basins. Two elongated troughs parallel to the axis have the deepest water (up to 350 m deep), while most of the seafloor is relatively shallow (<50 m deep) and smooth to hummocky. Like outer Frobisher Bay, the inner bay is bounded along its southwest side by a fault aligned northwest-southeast.

Inner Frobisher Bay is a semidiurnal macrotidal environment (11.1 m at spring tides, 12.6 m maximum recorded; Canadian Hydrographic Service 2001) with seasonal ice cover (Hatcher 2013). Surrounding the inner bay is a series of tidal flats and shallows, where sea ice can rest at low tide and entrain sediment (63,750-68,000 t km^{-2}; Dale et al. 2002). While much of this sediment is recirculated within the tidal flats, some coarse material makes it to deeper waters as ice-rafted debris (IRD; Dale et al. 2002). Waves and current export finer sediment from the flats (Hatcher et al. 2021).

Meta Incognita and Hall peninsulas flank Frobisher Bay to the southwest and northeast, respectively (Fig. 2.1B). These are primarily composed of Paleoproterozoic metamorphic and igneous rocks from the Trans-Hudson Orogen, with some minor outcrops of Paleoproterozoic marble and carbonate rocks occurring near the head of the bay (St-Onge et al. 2006; Steenkamp and St-Onge 2014). The signature of Ordovician carbonate exposures ~50 km northwest of the bay is commonly found in glacially derived sediments in inner Frobisher Bay, and is diagnostic of the former southeastward flow of Foxe-Amadjuak ice in the basin (Tremblay et al. 2015). The presence of carbonate in these sediments has implications for radiocarbon dates from sampled molluscan species, which may be influenced by the "Portlandia Effect" (England et al. 2013), potentially indicating ages hundreds to thousands of years older than they are. This must be taken into account when interpreting deglacial chronology in inner Frobisher Bay.

2.2 Methods

Surveys and sampling were undertaken as part of a larger multidisciplinary seafloor hazard mapping project in inner Frobisher Bay (Deering et al. 2018). Much of the field effort was focused on the numerous seafloor slope instabilities; however, some effort was made to target undisturbed seafloor sites near moraine features as understanding the deglacial history and stratigraphy was important for characterizing lithofacies and establishing the timing of failure events. Thus, much of the data presented in this paper was collected opportunistically, in many cases from samples collected primarily for the geohazard project.

2.2.1 Multibeam bathymetry and acoustic sub-bottom profiling

Bathymetric mapping using multibeam-echosounders (MBES) was accomplished using two vessels over 11 years. CCGS *Amundsen* acquired data using Kongsberg sounders (EM 300, 2006–

2008; EM 302, 2009–2010, 2014–2017) operating at a nominal frequency of 30 kHz. RV *Nuliajuk* (Government of Nunavut) mapped inner Frobisher Bay in a targeted effort, employing Kongsberg sounders EM 3002 (300 kHz, 2012–2013) and EM 2040C (variable 200–400 kHz, 2014–2016; Hughes Clarke et al. 2015). Along-track, sub-bottom, acoustic profiling was accomplished using Knudsen 320R (CCGS *Amundsen*) and CHIRP 3200 two-channel (RV *Nuliajuk*) 3.5 kHz echosounders operating concurrently with MBES.

MBES bathymetric data were processed using Qimera software (v. 1.7; Quality Positioning Services, Zeist, Netherlands). A bathymetric raster surface of 10 m resolution was generated. Depth values were normalized to chart datum (approximate mean lower low water) and tides determined using the Arctic9 tidal model (Collins et al. 2011). Sub-bottom acoustic data were analyzed using the Natural Resources Canada software, SegyJP2 (Courtney 2009).

2.2.2 Sediment coring

Sediment cores were collected using the same two vessels. Piston cores were collected from CCGS *Amundsen* each year from 2014 to 2017, using a corer rigged to collect cores up to 9 m in length and 9 cm in diameter. Gravity cores were collected from RV *Nuliajuk* in 2016 and 2017 using a gravity corer configured to collect 9-cm-diameter cores up to 2.6 m in length. *RV Nuliajuk* was able to access shallower areas that were inaccessible to *CCGS Amundsen* and was available for greater lengths of time.

All piston and gravity cores were cut into 1.5 m long sections, sealed, and transported refrigerated and upright to the Geological Survey of Canada (GSC-Atlantic) core laboratory at the Bedford Institute of Oceanography (BIO), where analysis followed a standardized procedure, detailed in Campbell et al. (2017) and summarized in Deering et al. (2018). This analysis included photography and x-radiography of split cores as well as measurements of physical properties (magnetic susceptibility, bulk density, shear strength, and colour). Acid-reactivity was measured at discrete depths downcore using a 10% HCl solution on a scale of 0 to 4 to determine relative carbonate concentration (Campbell et al. 2017). The reaction to acid was classified as 0 (no reaction) indicating carbonate absence, 1 (1 or 2 bubbles), 2 (multiple bubbles, not continuous), 3 (continuous bubbles) and 4 (frothing, continuous bubbles), indicating increasing concentration of carbonate. Subsamples were collected from cores for grain-size analysis and radiocarbon dating. All cores and associated subsamples are archived by GSC-A at BIO.

2.2.3 Radiocarbon dating

Carbonate materials (typically bivalve shells) extracted from sediment cores were analyzed by accelerator mass spectrometry (AMS) to determine radiocarbon age. In cores with few datable materials, all suitable shells at various depths were dated. In those with an abundance of datable materials, samples near lithofacies boundaries farthest downcore were selected. In most cases, only a single specimen was dated, comprising either a single valve (or valve fragment) or an articulated bivalve pair. After removal from the cores, samples were cleaned, photographed, and identified by the late Alice Telka of Paleotec Services. In 2015–2017, all samples were analyzed at the W.M. Keck-Carbon Cycle AMS Facility at the University of California (Irvine). In 2018, larger samples (>50 mg) were analyzed at the André E. Lalonde AMS Laboratory at the University of Ottawa, while smaller samples were analyzed at the Keck facility. Ages were corrected for marine reservoir effect using the Marine20 calibration curve dataset ($\Delta R = 41 \pm 21$; Heaton et al. 2020), calibrated with Calib version 8.2 (Stuiver et al. 2021), and reported at the 1σ age range.

2.3 Results

This section begins by describing the moraines and other deglacial features mapped on the seafloor in inner Frobisher Bay using acoustic surveying. It then contextualizes these features by describing and interpreting undisturbed acoustic facies and lithofacies found in the basin (i.e., sites unaffected by the numerous submarine slope failures; Deering et al. 2018). Lastly, it examines the newly collected radiocarbon dates in relation to lithofacies distribution, glacial ice-front positions, and sedimentation rates.

2.3.1 Seabed deglacial features

Over the course of several field seasons (2012-2016) approximately 75% of inner Frobisher Bay was mapped using MBES, revealing seafloor features relating to past glaciation. Streamlined glacial erosional and depositional features are common throughout the inner bay, ranging up to several kilometres in length. These have surface expressions ranging from smooth and muted to rough and irregular (Fig. 2.2, 2.4A, 2.4B), with orientations parallel to the direction of former ice flow. While they have not been mapped systematically throughout the inner bay, Tremblay et al. (2015) previously mapped drumlins, crag-and-tail, and ice-sculpted (‘whaleback’) landforms. There is no indication of the age of these features, but their widespread presence and convergent pattern supports the view that ice streaming has occurred in inner Frobisher Bay (e.g., Margold et al. 2015b).

A suite of flow-transverse ridges is found within 40 km of the head of inner Frobisher Bay. These features vary in size, morphology, and spacing as a function of location within the bay. Five large till-cored ridges, transverse to the direction of former regional ice flow, are found between 20 and 40 km from the head of the bay (Figs. 2.2, 2.3), exhibiting increasing cross-bay continuity from

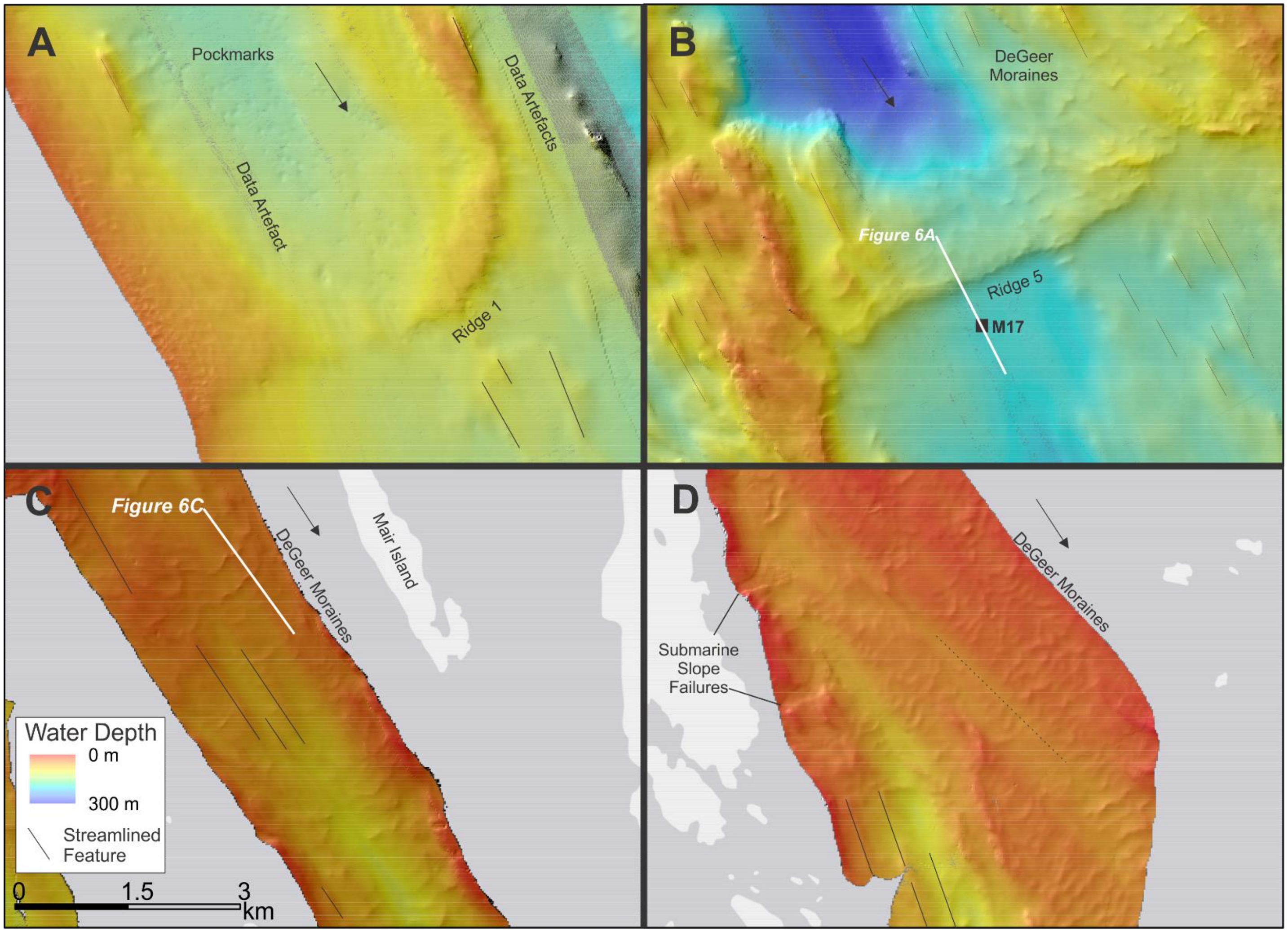

Figure 2.4 Shaded colour relief images from: (A) Ridge #1; (B) Ridge #5; (C) DeGeer moraine field near Cairn Island; and (D) DeGeer moraine field in Peterhead Inlet. Arrows indicate direction of ice flow. Thin black lines show streamlined glacial features. Dashed black line in D indicates possible late-phase streamlined glacial feature (cf. Tremblay et al. 2015). Other seafloor features are labelled. White lines indicate locations of sub-bottom images shown in Figures 2.6A and 2.6C. Base map ESRI 2021.

the most (ridge #1) to the least (ridge #5) seaward. While the latter is nearly continuous across the MBES coverage, in water depths ranging from 170 m to <10 m, the ridges farthest down-bay (ridges #1 and #2, Fig. 2.3) are composed of disjointed segments <5 km long. In the deep troughs along the southwest side of the bay the three younger ridges (3-5) appear to sit on top of a series of bedrock sills (Fig. 2.4A). Acoustic sub-bottom records across the intervening areas show no indication of buried ridges. The full extent of these features in shallow waters is unknown, as their mapped limits intersect the edge of MBES coverage. However, the ends of these ridges appear to coincide with ridge elements of the Frobisher Bay Moraine System on the northeast coast of the bay (Fig. 2.3; Hodgson 2005). On the southwest coast, the pattern of terrestrial ridges is more convoluted and does not pair as well with the seafloor ridges.

Morphologies are variable both within and between the five large ridges, with widths (parallel to ice flow) of 100 to 900 m (median 400 m), and relief above surrounding seabed ranging up to 30 m (median 20 m). Ridge #1 shows a primarily asymmetrical, wedge-like profile (Fig 2.5A), while ridges #2–5 vary in symmetry along their length (Figs 2.5A, B). Some of the ridges have extended flat tops (e.g., ridges #2 and 3, Fig. 2.5B). Up-ice (stoss) slopes are very gradual for all ridges, with down-ice (lee) slopes ranging up to 16°. Variations in symmetry and slope do not appear to relate to absolute water depth. However, wedge-like profiles are typically found in the deepest section(s) of individual ridges, coinciding with deep troughs that extend northwest to southeast in the inner bay.

The wedge-like ridge #1 and asymmetrical sections of the other four ridges are consistent in morphology with grounding-zone wedges (GZWs) deposited at former floating ice-fronts in other high latitude environments (Batchelor and Dowdeswell 2015), where vertical accommodation

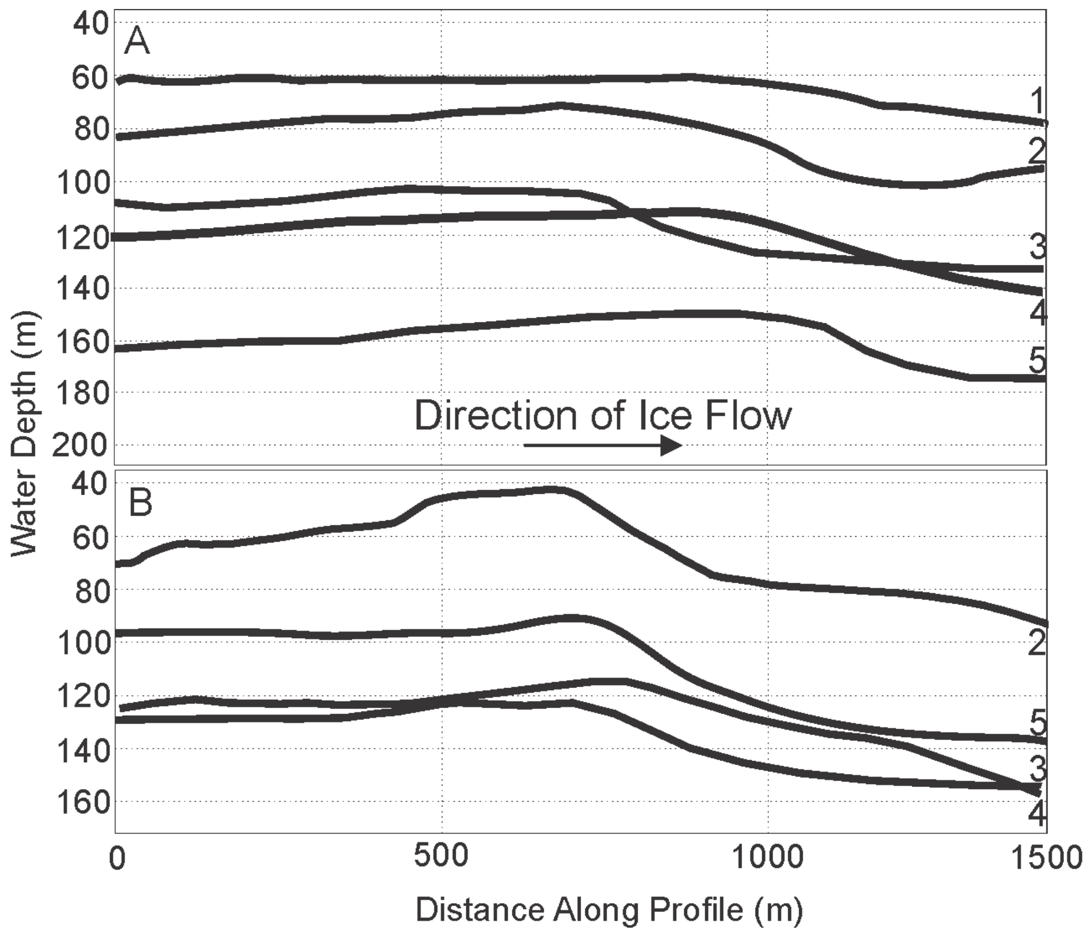

Figure 2.5 Bathymetric profiles across large flow-transverse ridges in inner Frobisher Bay, showing strongly asymmetrical wedges (A) and more symmetrical ridges (B). Locations and orientations of profiles are shown on Figure 2.3. ~5x Vertical exaggeration.

space is restricted by a floating ice tongue or shelf. In contrast, the more symmetrical elements of ridges #2-5 indicate that sectors of the ice-front had less restricted, vertical accommodation space at the grounding zone. Overall, the mixed morphology of the five ridges implies a variable configuration along the ice-front as it retreated in inner Frobisher Bay, possibly facilitated by the local bathymetry or local ice shelf instability.

The more continuous ridges (#3-5) exhibit clear overlap of streamlined features on the seabed (Fig. 2.4B). The relation between streamlined features and ridges #1-2 is less clear, with some burial but also lateral transitions from transverse to flow-parallel morphology (Figs. 2.2, 2.4A). Although the latter may well be much older, this juxtaposition without abrupt edges suggests the possibility of ice-streaming behaviour behind the grounding line as GZWs #1 and 2 were being deposited.

Two fields of small till-cored ridges are located in sheltered areas in the upper 20 km of inner Frobisher Bay (Figs. 2.2, 2.4C, 2.4D), with one on the landward side of Cairn Island (CI; 17 ridges), near the northeast coast, and one in Peterhead Inlet (PI; 43 ridges). A series of these ridges also occurs on the northwest flank of ridge #5 (Figs. 2.2, 2.4B). The smaller ridges are mostly straight and symmetrical, with crest lengths up to 1 km and typically <4 m relief above the surrounding seabed (Fig. 2.6C). Spacing between ridge crests is typically <125 m, but can reach up to 250 m. The ridges typically terminate within the MBES coverage (at present water depths up to 105 m; mean depth ~50 m), though some intersect the shallow edge of the MBES footprint (~10 m water depth). The full extent of the ridge fields is unknown, as this analysis is based only on those expressed on the seabed. Sub-bottom acoustic records show that some ridges continue beyond their mapped extent. The morphology of these ridges is consistent with De Geer moraines, typically found in groups, aligned parallel to past ice-fronts (De Geer 1889; Bouvier et al. 2015).

2.3.2 Acoustic facies

Sub-bottom acoustic data, collected concurrently with MBES data, are available for most of inner Frobisher Bay. Hundreds of kilometres of parallel survey lines, typically aligned northwest-southeast, are the basis on which the following four acoustic facies are described (Fig. 2.6).

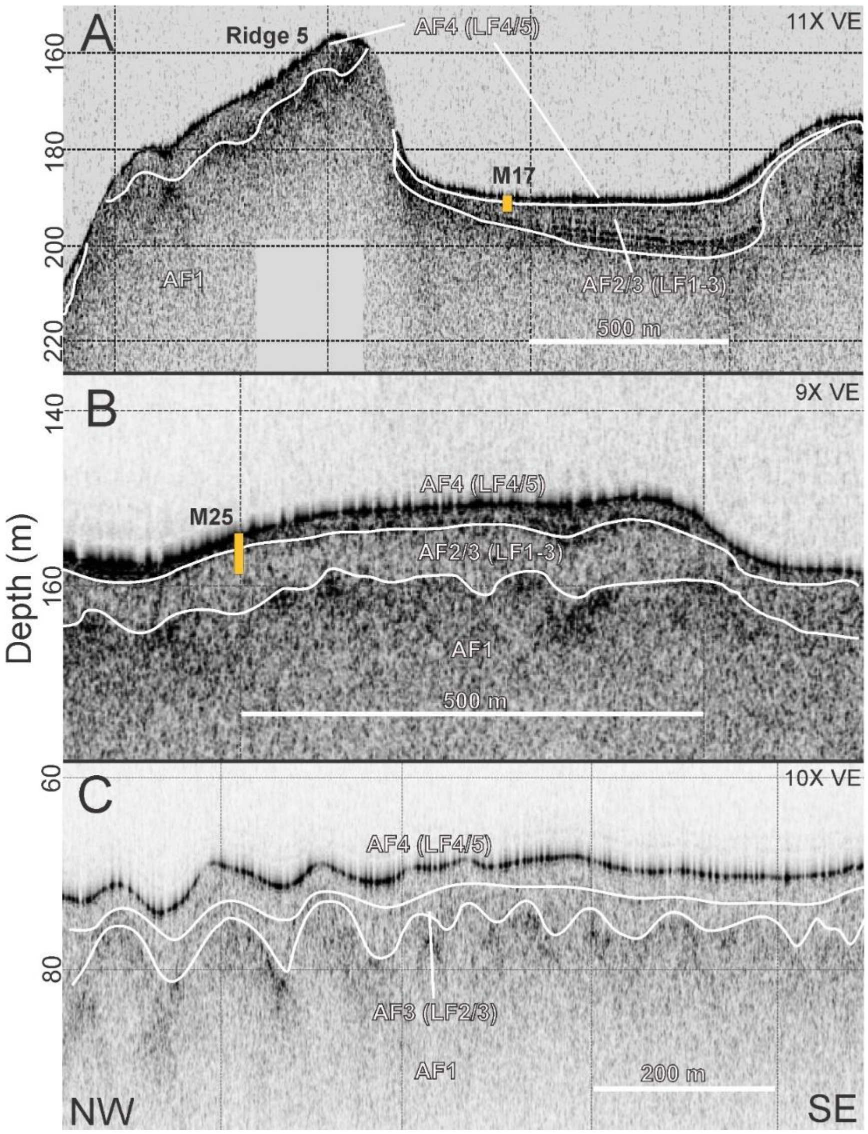

Figure 2.6 Interpreted sub-bottom images from: (A) across moraine ridge #5; (B) along a trough near the head of inner Frobisher Bay; and (C) across DeGeer moraines near Cairn Island. Depth in metres assumes two-way travel time of sound in water (1500 m/s). Acoustic facies and lithofacies as described in text are labeled with contacts shown as white lines. Bars denote locations and approximate penetration depths of cores M17 and M25 shown in Figure 2.8.

Acoustic Facies 1 (AF1) is ubiquitous throughout the basin, representing the acoustic basement. As such, the thickness of this unit is not well constrained. Typically, it is buried beneath other acoustic facies; however, it does appear to extend to the seabed on some prominent bedrock ridges.

Internally, this unit has a chaotic to massive structure, with some hummocky internal reflectors. The upper boundary of AF1 is typically rough, hummocky, non-conformable with internal reflectors, and poorly defined (Fig. 2.6B). In a deglacial environment, such as inner Frobisher Bay, this unit is interpreted as glacial till or bedrock.

Acoustic Facies 2 (AF2) is typically found above AF1 only in deep basins and local bathymetric lows. Unit thicknesses are variable, ranging from <5 to 20 m. This unit is typically ponded in basins, with strongly reflective, near-horizontal, acoustic stratification, which is non-conformable with underlying topography, and a diffuse lower contact (Fig. 2.6A). This facies can be interpreted as ice-proximal deposits, with high intensity reflections indicative of periodic deposition of coarse material in an otherwise fine matrix of sub-glacial meltwater suspension deposits.

Acoustic Facies 3 (AF3) is the most abundant and is found throughout the inner bay. Typically, it drapes underlying sediments, with a distinct, smooth, conformable lower contact (Fig. 2.6B). Internally, this unit is weakly stratified to massive. Unit thickness ranges from <1 m on bathymetric highs to >20 m in deep basins. This facies is interpreted as distal glaciomarine to post-glacial. The random occurrence of reflectors and acoustic stratification suggests a sedimentary regime characterized by episodic events (e.g., iceberg melt out or rollover, seasonal ice-rafted debris from tidal flats) depositing coarse materials, as opposed to the more continuous deposition proximal to an ice-front.

Acoustic Facies 4 (AF4) is common throughout the bay, forming the layer closest to the seafloor (Fig. 2.6A, B, C). The lower contact is mostly continuous, smooth, conformable, and highly reflective. The surface of this unit (the seabed) is typically smooth and highly reflective. Horizontal, strong reflectors can be found throughout the unit. Thickness is variable, but typically <5 m. This facies is interpreted as post-glacial to modern marine deposition.

2.3.3 Sediment Cores

Sixty-three cores were collected throughout the inner bay in water depths ranging from <20 to 200 m and included 12 piston (lengths 442-601 cm) and 51 gravity (5-188 cm long) cores. Seafloor sampling focused on submarine slope failures, resulting in the clustering of sampling sites around these features (n=39 cores). An effort was also made to collect cores (n=24) from undisturbed seafloor basins. Of the total cores collected, 26 with radiocarbon-dated materials are the focus of this study and described further below.

2.3.4 Lithofacies

Five distinct glaciomarine or marine lithofacies are identified, based on the physical properties and sedimentological descriptions of these cores (Fig. 2.7). Several of these lithofacies were previously described in Deering et al. (2018).

Lithofacies 1 (LF1) is the lowest unit found in a few piston cores collected near ridge 5 and close to the head of the bay. Total thickness of this unit is unknown but at least several metres, as it extends beyond core penetration depth where it was sampled. This unit is composed of fine to coarse grey-black sand with well-defined laminations of variable thickness (<10 cm), with relatively high carbonate content (3 on relative acid-reactivity scale). This sedimentology is associated with ice-proximal settling of fine suspended sediment from a carbonate-rich source periodically interrupted by coarse influx from increased melt, shifting proximity of meltwater outlets, or ice-marginal calving.

Lithofacies 2 (LF2) is typically the basal unit in both piston and gravity cores, extending beyond core penetration depth in most cases. Where the full unit is captured, it is 1-2 m thick. It is laminated with lighter and darker bands of carbonate-rich (2-3 on acid reactivity scale), black-grey

cm X-ray Photo	Lithofacies	Sedimentary Description	Depositional Environment	Bulk Density	Magnetic Susceptibility	Shear Strength	Clay:Silt:Sand
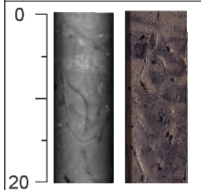	LF5 Bioturbated olive grey mud	Massive mud; scattered, randomly distributed sand; extensive burrows	Post-glacial (AF4; <1 ka cal BP)	1.3-2.1 g/cm^3	500-1500 SI	5-23 kPa	20:70:10
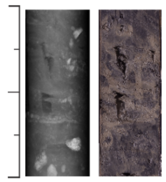	LF4 Pebbly, sandy olive grey mud	Coarsely stratified mud with extensive ice-rafted debris	Post-glacial (AF4; 1-7 ka cal BP)	1.3-2.1 g/cm^3	500-1500 SI	5-23 kPa	29:70:1
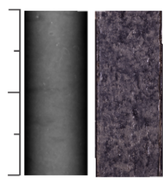	LF3 Grey-black massive carbonate-rich mud	Massive mud with scattered, randomly distributed sand	Ice-distal, Glaciomarine (AF3; >7 ka cal BP)	1.7 g/cm^3	500 SI	6-10 kPa	49:50:1 to 34:65:1
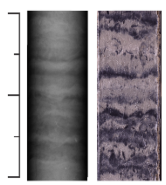	LF2 Grey and black laminated carbonate-rich mud	Laminated (2-3 cm) silt and clay	Ice-distal to ice-proximal, glaciomarine (AF3; >7 ka cal BP)	1.7-1.9 g/cm^3	500-800 SI	6-10 kPa	49:50:1
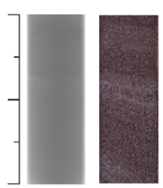	LF1 Grey laminated carbonate-rich sand and mud	Laminated (5-10 cm) sand w/silt and clay	Ice-proximal, glaciomarine (AF2; >7 ka cal BP)	2.2-2.4 g/cm^3	1900-2100 SI	8-12 kPa	1:9:90 to 5:25:60

Figure 2.7 Summary of characteristic lithofacies found in inner Frobisher Bay as described in the text. Split-core photographs and x-radiographs from piston cores shown in 20-cm-long sections at left. Also provided for each lithofacies are: brief sedimentary description; interpreted depositional environment; age ranges; and key physical properties.

mud. This is consistent with sedimentation dominated by settling of suspended silt and clay from a carbonate-rich glacial debris source.

Lithofacies 3 (LF3), which always appears above LF2 in packages <2 m thick with a conformable lower contact, is composed of apparently massive or faintly laminated, carbonate-rich (2-3 on acid reactivity scale), black-grey mud, with an increasing fraction of silt (50-65%) up-core and infrequently, scattered coarse sand and pebbles. This unit is consistent with sedimentation dominated by the settling of suspended, carbonate-rich silt and clay from extensive meltwater plumes, with some input from IRD.

Lithofacies 4 (LF4) is typically 2-3 m thick, and is composed of poorly stratified, minimally-bioturbated, carbonate-poor (1 on relative acid-reactivity scale), olive grey, predominantly silty mud, with intermittent horizontal bands (1-5/m, 5–10 cm thick) of coarse sand and pebbles (in a mud matrix) with conformable contacts. This unit is consistent with settling of suspended sediment interspersed with numerous IRD deposits. The contact between LF3 and LF4 is typically marked by a distinct change in sediment colour (from grey-black to olive grey) and increases in shear strength (from 6-10 to 5-23 kPa) and magnetic susceptibility (from ~500 to 500-1500 SI).

Lithofacies 5 (LF5) is found at the top of every core and is typically <50 cm thick. It is intensely bioturbated, massive, carbonate-poor (0 on acid reactivity scale), olive grey silty mud, with some coarse sand and gravel dispersed throughout. In both LF4 and LF5, there is a much greater proportion of IRD (possibly originating from seasonal sea ice on local tidal flats) than in underlying units.

2.3.5 Lithostratigraphy

The late Quaternary marine sediments of inner Frobisher Bay can be characterized by these five lithofacies that appear in the stratigraphy of two piston cores over 4.5 m in length (Fig. 2.8) located in front of ridge 5 (location M17 in Figs. 2.3, 2.4) and in a trough near the head of the bay (location M25 in Fig. 2.3). The lower 2.2 m (or half the length) of core M17 is LF1. Core M25 penetrated to LF1 at ~4.6 m below seabed. In both cores, this lithofacies contains a high proportion of sand, implying deposition adjacent to a grounding line or grounded ice-front. LF2 and LF3, together accounting for ~140 cm in M17 and ~300 cm in M25, are characteristic of glaciomarine sedimentation farther from the ice-front (Fig. 2.7). While some coarse materials would still be transported to these lithofacies through ice rafting, the relative proportion is lower compared to both underlying and overlying units. LF4 is ~60 cm thick in M17 and ~90 cm in M25, with a change in colour to olive-grey and a higher proportion of ice-rafted sand and pebble gravel (Figs. 2.7 and 2.8), and lower sedimentation rate, reflecting the loss of the glacial sediment source. The uppermost unit in both cores is LF5, from ~10 to ~60 cm thick (Fig. 2.8).

Comparison of lithofacies and acoustic facies for inner Frobisher Bay shows some correspondence between units, based on overlap between penetration and acoustic profiles (Fig. 2.6). AF2 corresponds to LF1, with distinct horizontal linear stratification in both. AF3 corresponds to LF2 and LF3, ranging from massive to stratified, with random reflectors appearing in both. The distinction between the two lithofacies is unclear within the corresponding acoustic facies. AF4 corresponds to LF4 and LF5, with the distinct horizontal reflector at the interface between AF3 and AF4 corresponding to the marked change in sedimentary properties between LF3 and LF4.

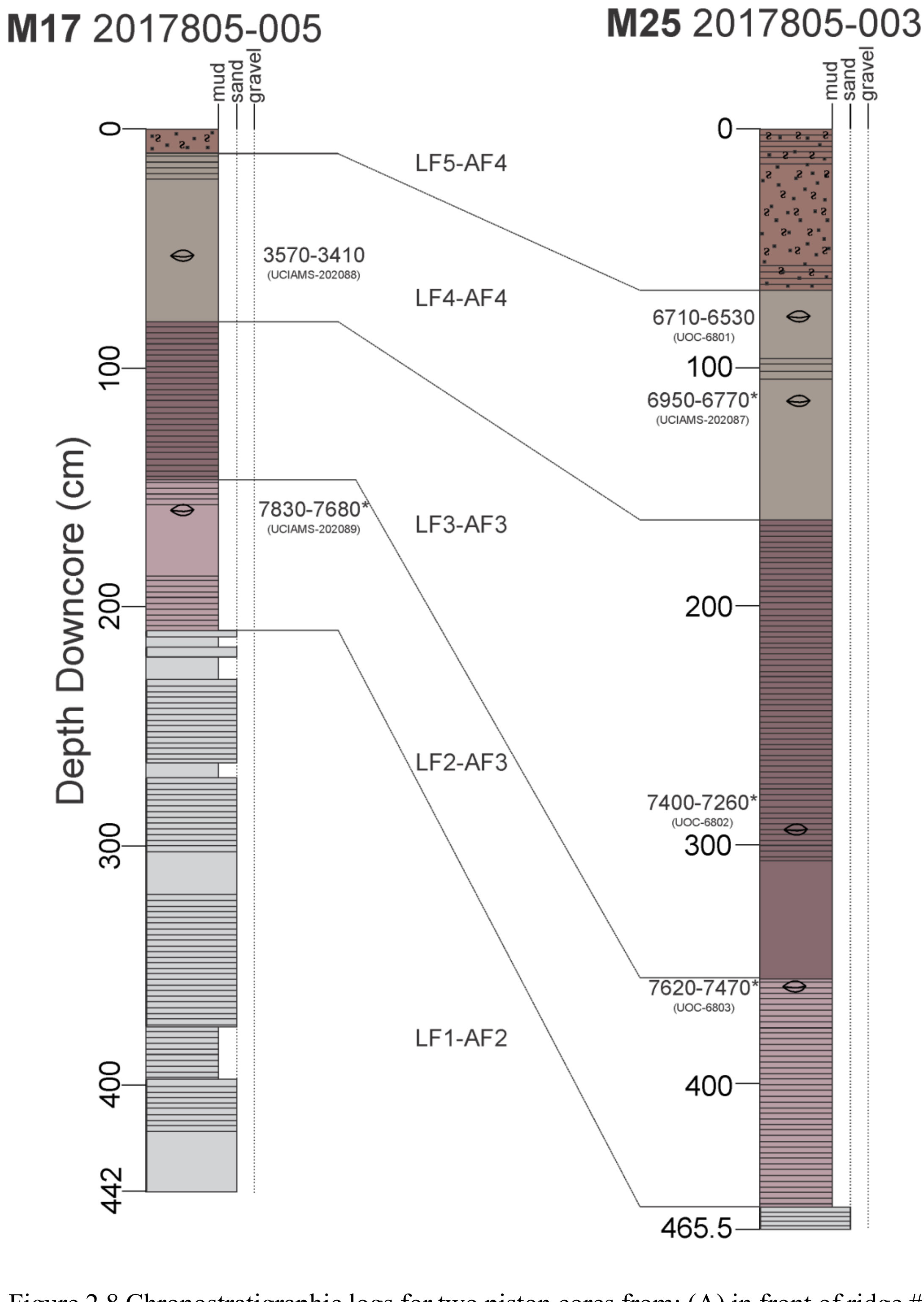

Figure 2.8 Chronostratigraphic logs for two piston cores from: (A) in front of ridge #5 (M17); and (B) a trough near the head of the inner bay (M25). Lithofacies indicated correspond to those illustrated in Figure 2.7 and described in the text. Radiocarbon dates are reported as the 1-sigma calibrated age range. Those potentially affected by the Portlandia Effect are marked with an asterisk. Depth downcore in cm shown at left.

2.3.6 Radiocarbon dates

Radiocarbon dates in inner Frobisher Bay may be influenced by the "Portlandia Effect" (England et al. 2013), wherein certain deposit-feeding molluscs (particularly *Portlandia arctica*) in calcareous substrate may exhibit older reservoir ages than suspension feeding molluscs living in the same substrate (such as *Hiatella arctica* and *Mya truncata*; Vickers et al. 2010). The extent of this effect in the bay is unknown; however, given the relatively high carbonate concentrations in glaciomarine facies (LF2 and LF3) and low concentrations in some post-glacial sediment (LF4), it is expected to be widespread. As such, all radiocarbon samples (both previously published and new to this study) have been classified based on whether or not they are likely to be impacted by old carbonate according to 1) the feeding behaviour of the analyzed species (e.g., deposit feeder vs. suspension feeder) and 2) the acid reactivity (i.e., the carbonate content) of the sediment from which they were collected (Table 2.2). Any species (or even where species unknown) found in carbonate free sediment (acid reactivity = 0) is assumed to be unaffected (designated N in Tables 2.1 and 2.2). In carbonate sediment (acid reactivity >0), deposit feeders are considered affected (Y), suspension feeders are considered unaffected (N), and where species is unknown the effect is unknown (U). Given that the "Portlandia Effect" causes shells to exhibit older radiocarbon dates than they should, this study uses them as a maximum age constraint only.

A literature review by Hodgson (2005) catalogues 15 radiocarbon dates derived from marine molluscs in raised marine sediments, collected from around the coast of inner Frobisher Bay (Fig. 2.3, Table 2.1; Hodgson 2005). Of these, only four were single or paired valves dated using AMS methods. Of those, only two (T6 and T8) are considered unaffected by the "Portlandia Effect". T6 is from a surface exposure in ice-proximal glaciomarine sediment on Cape Rammelsberg on the southwest coast. T8 is from an ice-contact delta in front of ridge 1 on the northeast coast. The other

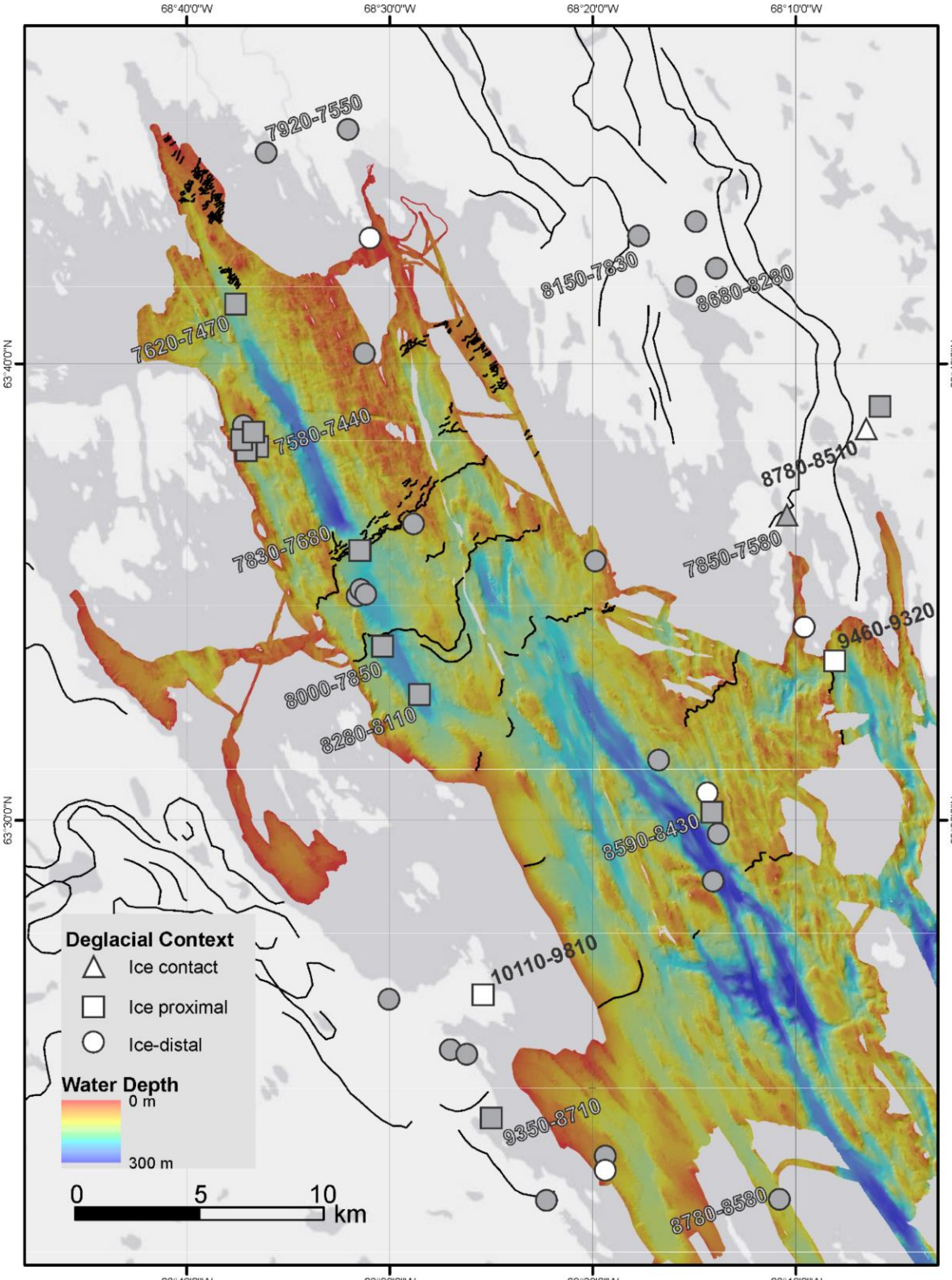

Figure 2.9 Key ice constraining radiocarbon dates in inner Frobisher Bay. Ranges shown are 1-sigma calibrated years before present, rounded to the nearest decade. Symbol colour indicates whether date is affected (grey) or unaffected (white) by the Portlandia Effect. Where this status is unknown it is shown as affected. Symbol shape indicates deglacial context of each sample as labeled in the legend. Background is multibeam bathymetric coverage. Base map ESRI 2021.

two valves dated using AMS methods (T1 and T3) are both *Portlandia arctica*, providing maximum ages on deglaciation. For the remaining 11 bulk-dated samples the "Portlandia Effect" is unknown.

In addition to these previously published dates, twenty-six new radiocarbon dates ranging in age from <1 to ~9.4 ka cal BP were obtained on marine molluscs collected from near the base of sediment cores (Fig. 2.9, Table 2.2). For all cores, the sample collected farthest downcore was also the oldest. Of these twenty-six dates, nine are considered to be unaffected by the Portlandia Effect. These constrain the marine deglacial chronology of inner Frobisher Bay by providing minimum ages on local ice retreat. The remaining 17 dates provide only maximum ages on ice retreat. For all piston cores, the lowest dateable material was ice-proximal, collected from either LF2 or LF3 at >400 cm downcore. In gravity cores, with their much shallower penetration, the lowest unit collected was in almost all cases post-glacial (LF4 or LF5, <7 ka cal BP; Fig. 2.7).

Table 2.2 New radiocarbon dates from sediment cores on samples first reported in this study. Site #, Lat, and Long match locations shown in Figure 2.3. Core Lab Id is the original processing number of the sediment core. Water depth is the depth in metres where the cores were collected. Seafloor context indicates whether the core was collected form a basin (B), slope (SL), or ridge (R). Lab Id is the original processing number of the radiocarbon sample. Depth downcore indicates the position of the radiocarbon samples in each core. LF is the lithofacies in which sample was found. Acid Reactivity indicates the reactivity (0-4; as described in the Methods section) of the sediment enclosing the sample. ^{14}C Age (±) is the uncalibrated age of sample. 1-sigma Cal Age Range is the calibrated age range of the sample, rounded to the nearest ten. Genus and species are listed where known. Portlandia Effect indicates where samples are known to be impacted (Y), unaffected (N), or unknown (U).

Site No.	Core lab ID	Lat	Long	Water depth (m)	Seafloor context	Lab ID	Depth downcore (cm)	LF	Acid reactivity	^{14}C age (±)	1-σ cal age range	Species	Portlandia Effect
M1	2017805-0006PC	63.362	−68.182	118	B	UOC-6804	55	4	1	3830 (26)	3640–3460	*Macoma calcarea*	N
						UOC-6805	120	3	2	7554 (28)	7870–7700	*Nuculana pernula*	Y
						UOC-6806	150	3	2	7631 (34)	7940–7790	*Yoldia hyperborea*	Y
						UCIAMS-202090	180	3	2	7770 (20)	8080–7930	*Yoldia hyperborea*	Y
						UCIAMS-202091	289	3	3	8150 (20)	8480–8330	*Ennucula tenius*	Y
						UCIAMS-202092	466	3	3	8380 (25)	8780–8580	*Ennucula tenius*	Y
M2	2017Nuliajuk-0015GC	63.373	−68.324	81	SL	UCIAMS-202080	26	5	0	900 (20)	410–260	Unknown fragment	N
M3	2017Nuliajuk-0016GC	63.378	−68.324	70	SL	UOC-6798	16	5	1	1104 (26)	560–430	*Clinocardium ciliatum*	N
						UCIAMS-202081	52	5	1	1425 (20)	830–690	Unknown fragment	U
						UOC-6799	88	4	1	1849 (26)	1280–1140	Snail fragment	U
						UCIAMS-202082	121	4	1	2215 (20)	1680–1520	Snail fragment	U
M4	2017Nuliajuk-0009GC	63.478	−68.236	237	B	UCIAMS-202078	21	5	0	1590 (15)	1020–860	Unknown fragment	N
						UCIAMS-202079	59	3	2	8075 (20)	8400–8260	Unknown fragment	U
M5	2016Nuliajuk-0030GC	63.495	−68.232	153	R	UCIAMS-202069	33	4	0	3010 (20)	2680–2500	Unknown fragment	N
						UCIAMS-187020	113	3	3	7660 (20)	7970–7820	*Yoldia hyperborea*	Y
M6	2016Nuliajuk-0029GC	63.503	−68.235	144	R	UCIAMS-187017	23	5	0	1065 (15)	530–410	*Hiatella arctica*	N
						UCIAMS-187018	66	2	3	7765 (20)	8080–7920	*Yoldia hyperborea*	Y
						UCIAMS-187019	119	2	3	8255 (20)	8590–8430	*Portlandia arctica*	Y
M7	2016Nuliajuk-0028GC	63.510	−68.241	160	R	UCIAMS-187016	44	4	0	3470 (15)	3210–3040	*Macoma calcarea*	N
M8	2016Nuliajuk-0027GC	63.522	−68.280	138	SL	UCIAMS-202068	59	3	3	7615 (20)	7930–7780	*Yoldia hyperborea*	Y
M9	2016804-0001PC	63.546	−68.475	210	B	UCIAMS-202070	43	5	0	990 (15)	470–330	Unknown fragment	N
						UOC-6797	132	4	1	2692 (26)	2280–2100	*Hiatella arctica*	N
						UCIAMS-187021	200	3	3	7125 (15)	7460–7320	*Portlandia arctica*	Y
						UCIAMS-187022	289	3	3	7235 (15)	7560–7420	*Portlandia arctica*	Y
						UCIAMS-187023	388	2	3	7935 (20)	8280–8110	*Nuculana pernula*	Y
M10	2016Nuliajuk-0026GC	63.558	−68.138	118	SL	UOC-6796	48	2	3	8699 (30)	9210–9020	*Yoldia hyperborea*	Y
						UCIAMS-187015	85	2	3	8920 (20)	9460–9320	*Macoma calcarea*	N
M11	2016804-0002PC	63.564	−68.506	204	B	UCIAMS-187024	166	3	3	6940 (20)	7300–7150	*Portlandia arctica*	Y
						UCIAMS-187025	294	2	3	7295 (25)	7610–7470	*Portlandia arctica*	Y
						UCIAMS-187026	473	2	3	7690 (20)	8000–7850	*Portlandia arctica*	Y
M12	2016Nuliajuk-0025GC	63.570	−68.162	46	B	UOC-6795	73	4	1	4301 (26)	4270–4080	*Mya truncata*	N
M13	2016804-0008PC	63.582	−68.520	190	B	UCIAMS-202074	110	4	3	1895 (15)	1310–1180	*Nuculana pernula*	Y
						UCIAMS-202075	192	4	1	4690 (20)	4790–4610	*Yoldia hyperborea*	Y
						UCIAMS-187032	230	4	1	5135 (15)	5330–5140	*Yoldia hyperborea*	Y
						UCIAMS-187033	364	4	2	5930 (15)	6190–6020	*gastropod*	N
						UCIAMS-187034	395	4	2	6165 (15)	6420–6280	*Portlandia arctica*	Y
						UCIAMS-187035	519	3	3	7085 (20)	7420–7280	*Portlandia arctica*	Y
M14	2016Nuliajuk-0021GC	63.582	−68.526	178	B	UCIAMS-187012	121	4	1	5020 (15)	5220–5010	*Macoma* sp.	N
						UCIAMS-187013	177	4	2	5560 (20)	5770–5600	*Yoldia* sp.	Y
M15	2016804-0007PC	63.583	−68.523	190	B	UCIAMS-202071	93	4	1	4890 (20)	5010–4830	*Nuculana* sp.	Y
						UCIAMS-187027	153	4	1	5420 (15)	5620–5470	*Portlandia arctica*	Y
						UCIAMS-187028	186	4	1	5485 (20)	5710–5550	*Yoldia hyperborea*	Y
						UCIAMS-187029	273	4	1	4080 (15)	3970–3800	Fish skull fragment	N
						UCIAMS-202072	303	4	1	4855 (20)	4970–4810	Unknown fragment	U
						UCIAMS-187030	331	4	2	5180 (15)	5410–5230	*Macoma calcarea*	N
						UCIAMS-202073	400	4	2	5365 (20)	5580–5430	*Yoldia hyperborea*	Y
						UCIAMS-187031	452	4	3	5920 (15)	6180–6010	*Yoldia hyperborea*	Y

Site No.	Core lab ID	Lat	Long	Water depth (m)	Seafloor context	Lab ID	Depth downcore (cm)	LF	Acid reactivity	^{14}C age (±)	1-σ cal age range	Species	Portlandia Effect
M16	2016Nuliajuk-0024GC	63.594	−68.332	98	B	UCIAMS-187014	63	5	1	1150 (15)	600–480	*Nuculana pernula*	Y
M17	2017805-0005PC	63.598	−68.524	180	B	UCIAMS-202088	53	4	0	3780 (20)	3570–3410	Unknown fragment	N
						UCIAMS-202089	160	2	1	7525 (20)	7830–7680	*Portlandia arctica*	Y
M18	2017Nuliajuk-0017GC	63.608	−68.480	103	R	UCIAMS-202083	37	4	0	3955 (15)	3810–3640	Unknown fragment	N
						UCIAMS-202084	66	4	1	6540 (15)	6850–6680	Unknown valve	U
						UOC-6800	128	3	2	7145 (28)	7480–7330	*Portlandia arctica*	Y
						UCIAMS-202085	155	3	2	7395 (20)	7700–7560	*Portlandia arctica*	Y
M19	2015805-0008PC	63.638	−68.611	125	SL	UCIAMS-169715	240	4	1	4030 (15)	3890–3720	Unknown	U
						UCIAMS-202065	283	4	1	4885 (15)	5000–4830	*Nuculana* sp.	Y
						UCIAMS-169716	326	4	1	5640 (15)	5880–5720	*Macoma* sp.	N
						UCIAMS-169717	388	4	1	6405 (20)	6700–6530	*Nuculana pernula*	Y
						UCIAMS 169718	436	3	2	6625 (20)	6950–6770	*Portlandia arctica*	Y
						UCIAMS-169719	501	3	2	6880 (20)	7250–7080	*Portlandia arctica*	Y
M20	2016804-0010PC	63.640	−68.612	115	SL	UCIAMS-187040	26	5	0	725 (15)	230–60	*Nuculana pernula*	N
						UCIAMS-202077	249	4	2	6300 (20)	6580–6410	*Nuculana pernula*	Y
						UCIAMS-187041	330	3	3	6730 (15)	7080–6900	*Portlandia arctica*	Y
						UCIAMS-187042	482	2	3	6925 (15)	7290–7140	*Portlandia arctica*	Y
M21	2014805-0004PC	63.640	−68.620	135	SL	UCIAMS-155830	292	4	0	5445 (25)	5660–5490	*Portlandia arctica*	N
						UCIAMS-155831	331	3	0	6565 (20)	6890–6710	*Portlandia arctica*	N
						UCIAMS-155832	400	3	1	6945 (25)	7300–7150	*Musculus* sp.	N
						UCIAMS-155833	511	2	1	7245 (25)	7560–7430	*Portlandia arctica*	Y
M22	2015805-0009PC	63.641	−68.615	115	SL	UCIAMS-169720	264	4	1	3160 (15)	2820–2690	Unknown	U
						UCIAMS-202066	281	4	1	3520 (20)	3280–3100	Unknown fragment	U
						UCIAMS-169721	361	4	1	5720 (15)	5950–5780	*Nuculana* sp.	Y
						UCIAMS-169722	402	4	1	6265 (20)	6550–6380	*Nuculana pernula*	Y
						UCIAMS-169723	489	3	2	6570 (20)	6890–6720	*Portlandia arctica*	Y
						UCIAMS-169724	526	3	2	6735 (20)	7090–6900	*Portlandia arctica*	Y
						UCIAMS-169725	571	2	3	6925 (20)	7290–7130	*Ennucula tenius*	Y
M23	2016804-0009PC	63.643	−68.619	101	SL	UCIAMS-202076	99	4	1	2665 (15)	2240–2050	Unknown fragment	U
						UCIAMS-187036	189	4	1	4355 (15)	4340–4150	*Nuculana pernula*	Y
						UCIAMS-187037	320	3	3	6945 (15)	7300–7150	*Portlandia arctica*	Y
						UCIAMS-187038	382	2	3	7070 (20)	7410–7270	*Portlandia arctica*	Y
						UCIAMS-187039	531	2	3	7265 (20)	7580–7440	*Portlandia arctica*	Y
M24	2016Nuliajuk-0003GC	63.669	−68.520	72	R	UCIAMS-202067	59	4	1	4785 (20)	4880–4700	*Nuculana Pernula*	Y
M25	2017805-0003PC	63.687	−68.625	146	B	UOC-6801	79	4	1	6407 (26)	6710–6530	*Macoma calcarea*	N
						UCIAMS-202087	114	4	1	6620 (20)	6950–6770	*Portlandia arctica*	Y
						UOC-6802	296	3	2	7051 (28)	7400–7260	*Portlandia arctica*	Y
						UOC- 6803	361	2	3	7305 (31)	7620–7470	*Portlandia arctica*	Y
M26	2017Nuliajuk-0021GC	63.711	−68.516	54	B	UCIAMS-202086	32	5	0	935 (20)	430–290	Unknown fragment	N

A further thirty-six radiocarbon dates from various depths within undisturbed sediment cores constrain the ages of lithofacies in each core (Table 2.2). Owing to the nature of a retreating ice-front, the chronostratigraphy (ages of the transitions between deglacial lithofacies LF1 to LF3) will be asynchronous throughout the basin, with glacial influence waning down-bay as the ice-front retreats up-bay. This can be seen in the transition between LF1 and LF2 (dated in two cores, Fig. 2.8), indicating that just in front of ridge #5 the transition occurred before a maximum age of 7830-7680 cal BP (M17, UCIAMS-202089, Table 2.2), while farther towards the head of the bay it occurred shortly before a maximum age of 7620-7470 cal BP (M25, UOC-6803, Table 2.2). The species in both cases was the pioneering, ice-proximal *Portlandia arctica* (Syvitski et al. 1989). The timing of the transition between LF2 and LF3 is unclear owing to few radiocarbon dated samples being collected around the contact. The transition between LF3 and LF4, which should be synchronous throughout inner Frobisher Bay, is dated to c. 7 ka cal BP, based on shells collected above and below the interface. The transition between LF4 and LF5 is dated to c. 1 ka cal BP. No stratigraphic inconsistencies between ages of deposit and suspension-feeding species were detected. Indeed, there were no stratigraphic inconsistencies for any species, including those potentially subject to the Portlandia Effect.

2.3.7 Sedimentation Rates

Sedimentation rate calculations are limited to pairs of shells within the same lithofacies where neither is affected by the Portlandia Effect (Table 2.2) or, for unaffected dates in post-glacial lithofacies, where it is assumed that 0 cm = 0 cal BP. While there is some variation between cores, sedimentation rates in inner Frobisher Bay can be linked to glaciomarine (LF3) and post-glacial (LF4+5) sediments. No unaffected dates were found in LF2 to calculate a sedimentation rate. LF3 has a single pair of suitable dates, providing a sedimentation rate of ~160 cm/ka. LF4 and LF5 have 10 suitable dates giving rates ranging from ~10 to 110 cm/ka (mean: 40 cm/ka). The higher end of this sedimentation range is somewhat lower than rates calculated for the last 100 years near the head of the bay using ^{210}Pb methods in deposits with very high porosity (~175 cm/ka; Tremblay et al. 2020). Based on when these lithofacies were being deposited in the bay, it appears that sedimentation rates were high prior to 7 ka cal BP, after which they dropped substantially.

2.4 Discussion

2.4.1 Pre-Cockburn Recession in Inner Frobisher Bay

Sometime after LIS ice receded to inner Frobisher Bay, the ice-front reached an unknown minimum extent after 11 ka cal BP and prior to c. 8.8 ka cal BP, the age of a raised ice-contact delta on the outermost subaerial ridge of the Frobisher Bay Moraine system (Fig. 2.3; Hodgson 2005, T8, AA-15123). While the outermost Frobisher moraine represents the minimum extent of this retreat, the ice is thought to have receded further because Cockburn-aged features have been shown in other parts of the island to mark substantial readvances (Andrews and Ives 1978). In any case, the Cockburn readvance has removed any evidence of earlier retreat up-ice from the outermost ridge.

2.4.2 Cockburn Readvance in Inner Frobisher Bay

The Cockburn moraines represent the last major readvance of the LIS on Baffin Island. In inner Frobisher Bay, this event formed the outermost of the Frobisher Bay Moraines (Ridge #1, Fig. 2.3). Onshore, this limit is well constrained on the northeast side of the bay, with continuous ridges running from the coast to Cockburn-aged moraines farther inland on the Hall Peninsula. In contrast, on the opposite southwest shore, the limit of the readvance is less clear. While a moraine is found at approximately the same distance from the head of the bay, a credible, in situ, shell sample radiocarbon-dated c. 10 ka cal BP at Cape Rammelsberg is located up-ice from the proposed extent of the later readvance (Fig. 2.3; T6, AA-17861). The advancing ice may have overrun this site without removing the enclosing sediment, particularly if the ice-front was partially floating and only locally grounded.

The outermost ridge on the seafloor is discontinuous, with several multi-kilometre-long segments, approximately correlating to the outermost onshore moraine ridges, and typically preserved in shallower areas. This suggests that at the time of the Cockburn readvance limit, at least some of the ice-front—the portion spanning deeper troughs and basins—was grounded farther up the bay. It should be noted that the marine limit just beyond the outermost Frobisher Bay Moraine is 119 m asl (Hodgson 2005). Although the age of this higher shoreline is poorly constrained (see below), it shows that water depths in the bay at the time of the Cockburn readvance may have been considerably greater than today (by 10s to 100 m), with implications for how seafloor landforms are interpreted.

The precise timing of the onset of the Cockburn readvance in inner Frobisher Bay is unclear. Ice-contact dates corresponding to the outermost moraine on the northeast coast indicate that ice was at this location c. 8.8 ka cal BP (Fig. 2.3; Hodgson 2005, T8, AA-15123), as discussed above. Given the morphology and size of the ridge, it seems plausible that the ice-front remained stable there over an extended period. Evidence for this longevity also comes from changes in marine limit across the moraine. On the down-ice side, as noted above, it is recorded as 119 m asl, whereas behind the moraine it decreases by ~70 m (Hodgson 2005). The higher (outer) limit is believed to pre-date the Cockburn readvance, which removed any evidence of a higher marine limit closer to the head of the bay. Published relative sea-level curves (Jacobs et al. 1985; Hodgson 2005) suggest an age of ca. 10 ka cal BP for the 119 m shoreline (thus a maximum age for the Cockburn readvance), but these curves are poorly constrained (Andrews and Miller 1985).

2.4.3 Post-Cockburn Recession

Sometime around the end of the Cockburn Substage, the ice-front in Frobisher Bay began its last major retreat. This is recorded on the seafloor in two distinct landform assemblages: the first (from ridges #1 to 5; ~20-40 km from the head of the bay) comprises the five large till-cored ridges separated by areas with flow-parallel streamlined features; the second comprises the smaller till-cored ridges draping streamlined features up-bay from ridge #5 (~0-20 km from the bay head).

The five large, prominent, widely spaced, ridges (or GZWs) that correlate spatially to the onshore Frobisher Bay Moraines characterize the first landform assemblage (Figs. 2.3, 2.9). Separating these ridges are swaths of seabed many kilometres wide with few discernible transverse deglacial features and some flow-parallel streamlined features. Acoustic sub-bottom records show that the interpreted till surface has some expression between these large ridges, but nothing of the same prominence above the seabed, and the smaller features are masked by post-glacial sediments. This pattern of retreat is also seen in the onshore Frobisher Bay Moraine system and is morphologically consistent with other large Cockburn Substage moraines on Baffin Island. While coastal portions of the onshore ridges would have formed on the then-seafloor under higher relative sea levels, most were formed entirely terrestrially.

The spatial pattern of these ridges does not appear to relate to changes in bathymetry. Despite a shift from a seafloor characterized by interbasin ridges (in the southeast) to one dominated by relatively flat and shallow seabed (farther up-bay), the spacing of the large ridges appears to decrease only slightly. The overall continuity and sinuosity of individual ridges does appear to be somewhat influenced by local bathymetry. A prominent lobe on ridge #4 (Fig. 2.3) occurs on an interbasin plateau, indicating that this area provided some stability at the grounding zone that deeper troughs did not.

Assemblage two, northwest of ridge #5, is characterized by De Geer moraine fields near the head of the bay. The abundance and smaller size of these features imply that the ice-front did not remain stable in one location long enough to form a large moraine. De Geer moraines are considered to be features of sub-aquatic ice-front retreat. They have not previously been recognized in association with retreat from the Cockburn readvance.

If the large ridges, particularly the older ridges (#1 to 3), represent GZWs associated with a floating ice margin (cf. Dowdeswell and Fugelli 2012; Batchelor and Dowdeswell 2015), the younger ridges and De Geer moraines may represent a change to a calving tidewater ice-front as relative sea level fell dramatically over the interval of retreat.

2.4.4 Final Retreat from Bay and Drainage Basin

As the ice-front retreated and relative sea levels dropped, the LIS margin changed from a marine to a terrestrial terminus in inner Frobisher Bay. Based on radiocarbon-dated shells collected at Peterhead Inlet (Fig. 2.2) near the head of the bay, the ice-front had retreated to a terrestrial position by 7.9-7.6 ka cal BP (Jacobs et al. 1985, T14, GX-8160). However, this date should be considered a maximum estimate given the nature of the sample (bulk) and the unknown impact of the Portlandia Effect.

At c. 7.0 ka cal BP there is a distinct change in sedimentary properties in the basin, marking the transition from LF3 to LF4. This sediment change, including a distinct colour shift from grey-black to olive grey, an increase in silt content, a greater range in bulk density and magnetic susceptibility, and most notably a sharp decrease in relative carbonate concentration, is indicative of a greater proportion of sediment input to the basin from local sources and a decreased supply of carbonate-rich glacigenic mud (Fig. 2.7; Hodgson 2005; Tremblay et al. 2015). Also notable are the decrease in sedimentation rates above this contact and an increase in IRD, possibly originating from sea ice interacting with local tidal flats. This change is likely related to the retreat of Foxe-Amadjuak ice from the Frobisher Bay drainage basin.

2.4.5 Marine Deglacial Chronology from Landform Assemblages

Landform assemblages similar to those in inner Frobisher Bay (described above) have been used previously to develop a model for marine ice-front retreat rates (Dowdeswell et al. 2008; Batchelor and Dowdeswell 2015; Dowdeswell et al. 2016). This model describes three distinct types of deglacial retreat: rapid (only flow-parallel features), rapid episodic (flow-parallel features overprinted by GZWs), and slow (series of small, flow-transverse ridges). Based on this model, the first (older) landform assemblage in inner Frobisher Bay is indicative of a series of four rapid, but episodic, ice-front retreats followed by periods of relative stability to create the five large ridges. The cause of the episodic retreat in the basin has not been established, but it was clearly influenced not only by the floating ice shelf, but also by the grounded ice margin on land. This implies a factor influencing the mass balance along the entire ice-front, such as climatic fluctuations, or possibly repeated surges. Farther north on eastern Baffin Island, a colder Baffin Bay prior to 8 ka (after which modern tundra vegetation became established) and freshwater discharge cooling events c. 9.3 and 8.2 ka have been proposed to account for readvances and stillstands in the waning phase or aftermath of the Cockburn Substage (Miller et al. 2005; Crump et al. 2020).

The second landform assemblage (~0-20 km from the head of the bay) is consistent with slow retreat in this model. Literature on De Geer moraines elsewhere hypothesizes that they can form on an annual seasonal cycle, with each ridge representing a year (De Geer 1889; Bouvier et al. 2015; Todd et al. 2007; Todd 2016). If that is the case, based on the spacing between ridges (~125-250 m), retreat from ridge 5 to the head of the bay (~20 km) may have taken ~80-160 years.

2.4.6 Marine Deglacial Chronology from Seafloor Sediment Cores

Establishing a definitive marine deglacial chronology for inner Frobisher Bay using established methods has been complicated by the widespread impact of the Portlandia Effect on most of the radiocarbon dates used in this study. Further, previously published dates used to establish the current deglacial chronology must be re-evaluated based both on the quality of the samples (mostly bulk shell samples with conventional radiocarbon dating) compared to modern standards (single shell valves using AMS dating) and the now known influence of the Portlandia Effect. The magnitude of this effect and its relative impact on different species is not well constrained for affected samples in this variable carbonate sedimentary environment. However, it should be noted that for all sediment cores introduced in this study the only date inversion (older date above younger) in a core comes from within the footprint of a submarine slope failure. Further, among older dates (c. 9.4–8.0 ka cal BP), there is agreement (within hundreds of years) between new marine and previously published terrestrial ages (c. 9.5–7.8 ka cal BP; Fig. 2.9) with similar age estimates on the large ridges.

Portions of the deglacial chronology can still be constrained using only those dates that are unaffected by the Portlandia Effect. The marine sediment core closest to the outermost ridge (#1) has a date in LF2 of 9.46-9.32 ka cal BP (Fig. 2.3; Table 2.2, M10, UCIAMS-187015), supporting the hypothesis established in previous publications that the readvance responsible for the Frobisher

Bay Moraine system is synchronous with the Cockburn Substage (c. 9.5-8.5 ka cal BP). Paired with a terrestrial date from an ice-contact delta on the same ridge at c. 8.78-8.51 ka cal BP (Fig. 2.3; Table 2.1, T8, AA-15123) it suggests that ice was stable along or near ridge #1 for 500-1000 years. Up-ice from Ridge #1 the deglacial chronology is not well established, with previous chronologies being based on radiocarbon dates now considered influence by the Portlandia Effect.

The calibrated dates within two piston cores near the head of the bay may help constrain the timing of deglaciation of inner Frobisher Bay. These two cores (Fig. 2.3) are located in front of ridge #5 (M17) and approximately 11 km northwest of ridge #5 (M25), midway to the head of the bay in Peterhead Inlet. In the core proximal to ridge #5, there is a distinct package of ice proximal LF1 at the bottom (Fig. 2.8). In the Peterhead Inlet core, there is a marked increase in sand near the base of the core, giving some indication of glacial proximity (Fig. 2.8). In both cases, these sandy units are indicative of glacial ice still being present within the inner bay. In both cores, LF1 is overlain with packages of LF2 (glaciomarine ice-proximal to ice-distal) with radiocarbon dated shells. In M17 that shell is dated to c. 7.83-7.68 ka cal BP (Table 2.2, UCIAMS-202089). In M25 that shell is dated to c. 7.62-7.47 ka cal BP (Table 2.2, UOC-6803). Even assuming these dates are affected by the Portlandia Effect and are presenting as older than they should, this indicates that the retreat from Ridge 1 to Ridge 5 took at least ~680 years. Further, ice had to have a marine terminus until at least c. 7.62 ka cal BP and the retreat from Ridge 1 to the head of the bay occurred over a span of at least 900 years. The previous estimate for the timing of ice retreat from Peterhead Inlet at the head of inner Frobisher Bay was a minimum age of c. 7.8 ka cal BP (Jacobs et al. 1985).

2.5 Conclusions

Inner Frobisher Bay represents but a small portion of the area covered by the LIS, but the latter's retreat from the Cockburn Substage readvance provides insight into how marine-terminating ice-fronts in bathymetrically complex embayments can react during ice sheet collapse. The seabed ridges of inner Frobisher Bay connect the onshore Frobisher Bay Moraine ridges on each side of the bay. Together with radiocarbon ages, these features indicate that the deglaciation of the inner bay involved an episodic retreat of glacial ice, initially with a partially floating front, followed by more regular retreat of a tidewater ice-front. The size of the large ridges and the volume of glaciomarine sediment indicate that the ice remained a potent agent of sediment transport during the first phase. The stillstands or minor readvances marked reversals of retreat and formation of large ridges. Questions remain as to what caused the pauses and why the shift in style of deglaciation occurred. Was it caused by factors at the local ice-front (possibly resulting from rapidly diminishing relative sea level and depth) or by internal changes in configuration and dynamics of the source ice?

While the age range of deglaciation in the inner bay (c. 9.5-7.8 ka cal BP) was initially constrained by onshore research, the reliability of those data has now been drawn into question. The widespread impact of the Portlandia Effect on radiocarbon dates in inner Frobisher Bay makes the deglacial chronology of the basin much less clear. This study reinforces the idea that the Cockburn readvance occurred in inner Frobisher prior to c. 8.5 ka cal BP and provides evidence that it occurred as early as c. 9.4 ka cal BP. Further, it suggests that the LIS had a marine terminus in Frobisher Bay until at least c. 7.6 ka cal BP. Further research is required to clarify the magnitude and uniformity of the impact of the Portlandia Effect on radiocarbon dates in inner Frobisher Bay.

The timing and stratigraphy of the post-Cockburn ice retreat from inner Frobisher Bay are similar to other marine-terminating ice-fronts on Baffin and elsewhere, but the bathymetric variability complicates the pattern of recession. This study provides the first comprehensive analysis of the seafloor deglacial morphology and substrate of the inner bay, clarifying the sequence of retreat and moraine formation in the late stages of Laurentide Ice wasting on southern Baffin Island. It also demonstrates the episodic nature of marine ice-front recession, forming five large ridges before the transition to more regular tidewater ice-front retreat. Furthermore, this study provides marine chronostratigraphic evidence (LF3-LF4 transition) for the retreat of the LIS out of the Frobisher Bay drainage basin to have occurred c. 7 ka cal BP. This study is a contribution to our understanding of marine ice-front instability and retreat processes in the present era of rapid climate warming and widespread glacial recession.

2.6 References

Andrews J.T. and Ives J.D. (1978). "Cockburn" nomenclature and the late Quaternary history of the eastern Canadian Arctic. *Arctic and Alpine Research*, 10(3), p. 617-633

Andrews J.T. and Short S.K. (1983). Radiocarbon Date List V: Baffin Island, N.W.T., Canada, and Radiocarbon Date List II: Labrador and Northern Quebec, Canada. University of Colorado, Institute of Arctic and Alpine Research, Occasional Paper 40, 71 p.

Andrews J.T. and Miller G.H. (1985). Holocene sea level variations within Frobisher Bay. In: J.T. Andrews (ed.), Quaternary environments, eastern Canadian Arctic, Baffin Bay, and western Greenland. Boston, Mass.: Allen & Unwin, pp. 585-607.

Andrews J.T. and Maclean B. (2003). Hudson Strait ice streams: a review of stratigraphy, chronology, and links with North Atlantic Heinrich events. *Boreas*, 32, p. 4-17

Atkinson E.G. and Wacasey J.W. (1987). Sedimentation in Arctic Canada: Particulate organic carbon flux to a shallow marine benthic community in Frobisher Bay. *Polar Biology*, v. 8, p. 3-7

Batchelor C.L. and Dowdeswell J.A. (2015). Ice-sheet grounding-zone wedges (GZWs) on high-latitude continental margins. *Marine Geology*, 363, p. 65-92

Batchelor C.L., Dowdeswell J.A., and Rignot E. (2018). Submarine landforms reveal varying styles of deglaciation in North-West Greenland fjords. *Marine Geology*, 402, p. 60-80.

Blake W., Jr. (1966). End moraines and deglaciation chronology in northern Canada with special reference to southern Baffin Island. Canada Geological Survey paper 66-26, 31 p.

Briner J.P., Davis P.T., and Miller G.H. (2009). Latest Pleistocene and Holocene glaciation of Baffin Island, Arctic Canada: key patterns and chronologies. *Quaternary Science Reviews*, 28(21-22), p. 2075-2087

Brouard E. and Lajeunesse P. (2019). Glacial to postglacial submarine landform assemblages in fiords of northeastern Baffin Island. *Geomorphology*, 330, p. 40-56

Bouvier V., Johnson M.D., and Påsse T. (2015). Distribution, genesis and annual-origin of De Geer moraines in Sweden: insights revealed by LiDAR. *GFF*, 137(4), p. 319-333, doi:10.1080/11035897.2015.1089933.

Campbell D.C., Jenner K.A., Higgins J. and Piper D.J.W. (2017). Analysis of piston cores and high-resolution sub-bottom profiler data, Baffin Bay slope, Nunavut. Geological Survey of Canada, Open File 8135, 179 p.

Collins A.K., Hannah C.G., and Greenberg D. (2011). Validation of a high resolution modelling system for tides in the Canadian Arctic Archipelago. *Canadian Technical Report of Hydrography and Ocean Sciences*, 273, 72 p.

Courtney R.B. (2009). SegyJP2 software, Natural Resources Canada, available at: ftp://ftp.nrcan.gc.ca/gsc/courtney/SegyJp2/SegyJp2.htm

Crump S.E., Young N.E., Miller G.H., Pendleton S.L., Tulenko J.P., Anderson R.S., and Briner J.P (2020). Glacier expansion on Baffin Island during early Holocene cold reversals. *Quaternary Science Reviews*, v. 241, 106419.

Dale J., Leech S., McCann S.B., and Samuelson G. (2002). Sedimentary characteristics, biological zonation and physical processes of the tidal flats of Iqaluit, Nunavut. In: Hewitt, K., Byrne, M., English, M. and Young, G. (eds.), Landscapes in Transition: Landform Assemblages and Transformations in Cold Regions. Dordrecht: Kluwer, pp. 205–234.

Dalton A.S., Margold M., Stokes C.R., Tarasov L., Dyke A.S. and 66 others. (2020) An updated radiocarbon-based ice margin chronology for the last deglaciation of the North American Ice Sheet Complex. *Quaternary Science Reviews*, v. 234, 106223.

De Geer G.F. (1889). Ändmoräner i trakten mellan Spånga och Sundbyberg. *Geologiska Föreningens i Stockholm Förhandlingar*, v. 11, p. 395 – 397.

Deering R., Misiuk B., Bell T., Forbes D.L., Edinger E., Tremblay T., Telka A., Aitken A. and Campbell C. (2018). Characterization of the seabed and postglacial sediments of inner Frobisher Bay, Baffin Island, Nunavut. *in* Summary of Activities 2018, Canada-Nunavut Geoscience Office, p. 139–152.

Dowdeswell J.A., Canals M., Jakobsson M., Todd B.J., Dowdeswell E.K., and Hogan K.A. (2016). The variety and distribution of submarine glacial landforms and implications for ice-sheet reconstruction. *Geological Society*, London, Memoirs, 46, p. 519-552

Dowdeswell J.A. and Fugelli E.M.G. (2012). The seismic architecture and geometry of grounding-zone wedges formed at the marine margins of past ice sheets. *Geological Society of America Bulletin*, 124(11-12), p. 1750-1761.

Dowdeswell J.A., Ottesen D., Evans J., Cofaigh C.Ó., and Anderson J.B. (2008). Submarine glacial landforms and rates of ice-stream collapse. *Geology*, 36(10), p. 819-822

Dyke A.S. (1979). Glacial and sea-level history of southwestern Cumberland Peninsula, Baffin Island, N.W.T., Canada. *Arctic and Alpine Research*, v. 11, p. 179-202

Dyke A.S., Moore A., and Robertson L. (2003). Deglaciation of North America. Geological Survey of Canada, Ottawa, Open File 1574.

England J., Dyke A.S., Coulthard R.D., McNeely R., and Aitken A. (2013). The exaggerated radiocarbon age of deposit-feeding molluscs in calcareous environments. *Boreas*, 42(2), p. 362-373

ESRI (2021). Light Gray Canvas [basemap]. Available at: https://basemaps.arcgis.com/arcgis/rest/services/World_Basemap_v2/VectorTileServer

Gaglioti B.V., Mann D.H., Wiles G.C., Jones B.M., Charlton J., Wiesenberg N., and Andreu-Hayles L. (2019). Timing and potential causes of 19th-century glacier advances in coastal Alaska based on tree-ring dating and historical accounts. *Frontiers in Earth Science*, 7, 15 p.

GEBCO Compilation Group (2020). GEBCO 2020 Grid. doi: 10.5285/a29c5465-b138-234d-e053-6c86abc040b9

Hatcher S.V. (2013). People at the tidal flats: coastal morphology and hazards in Iqaluit, Nunavut. Unpublished MSc. thesis, Department of Geography, Memorial University of Newfoundland, 232 p.

Hatcher S.V., Forbes D.L., and Manson G.K., 2021. Boulder-strewn flats in a high-latitude macrotidal embayment, Baffin Island: geomorphology, formation, and future stability. *Canadian Journal of Earth Sciences*, https://doi.org/10.1139/cjes-2021-0019.

Heaton T.J., Köhler P., Butzin M., Bard E., Reimer R.W., Austin W.E.N., Ramsey C.B., Grootes, P.M., Hughen K.A., Kromer B., Reimer P.J., Adkins J., Burke A., Cook M.S., Olsen J., and Skinner L.C. (2020). Marine20 – The marine radiocarbon age calibration curve (0-55,000 cal BP). *Radiocarbon*, 62(4), p. 779-820

Hodgson D.A. (2005). Quaternary geology of western Meta Incognita Peninsula and Iqaluit area, Baffin Island, Nunavut. *Geological Society of Canada Bulletin 582*, 72 p.

Hughes Clarke J.E., Muggah J., Renoud W., Bell T., Forbes D.L., Cowan B., and Kennedy J. (2015). Reconnaissance seabed mapping around Hall and Cumberland peninsulas, Nunavut: opening up southeastern Baffin Island to nearshore geological investigations. *in* Summary of Activities 2014, Canada-Nunavut Geoscience Office, p. 133-144

Ives J.D. and Andrews J.T. (1963). Studies in the physical geography of north-central Baffin Island, N.W.T.. *Geographical Bulletin*, 19, p. 5-48

Jacobs J.D., Mode W.N., Squires C.A. and Miller G.H. (1985). Holocene environmental change in the Frobisher Bay Area, Baffin Island, N.W.T.: deglaciation, emergence, and the sequence of vegetation and climate. *Géographie physique et Quaternaire*, v. 39, no. 2, p. 151–162.

Jamieson S.S.R, Vieli A., Livingstone S.J., Cofaigh C.Ó., Stokes C., Hillenbrand C, and Dowdeswell J.A. (2012). Ice-stream stability on a reverse bed slope. *Nature Geoscience*, 5, p. 799-802

Jennings A.E. (1993). The Quaternary history of Cumberland Sound, southeastern Baffin Island: the marine evidence. *Geographie physique et Quaternaire*, 47(1), p. 21-42.

Kaufman D.S., Miller G.H., Stravers J.A., and Andrews J.T. (1993). Abrupt early Holocene (9.9-9.6 ka) ice-stream advance at the mouth of Hudson Strait, Arctic Canada. *Geology*, v. 21(12), p. 1063-1066

Kingslake J., Scherer R.P., Albrecht T., Coenen J., Powell R.D., Reese R., Stansell N.D., Tulaczyk S., Wearing M.G., and Whitehouse P.L. (2018). Extensive retreat and re-advance of the West Antarctic Ice Sheet during the Holocene. *Nature*, 558, p. 430-434

Larsen E., Longva O. and Follestad B.A. (1991). Formation of De Geer moraines and implications for deglaciation dynamics. *Journal of Quaternary Science*, 6, p. 263-277.

Lind E.K. (1983). Holocene paleoecology and deglacial history of the Cape Rammelsberg area, southern Baffin Island, N.W.T., Canada. M.Sc. thesis, Department of Geology, University of Colorado, Boulder, Colorado, 219 p.

Manley W.F. (1995). Late-glacial record of ice-sheet interactions, Hudson Strait and southern Baffin Island, eastern Canadian Arctic. Ph.D. thesis, Department of Geological Sciences, University of Colorado, Boulder, Colorado, 252 p.

Margold M., Stokes C.R., and Clark C.D. (2015a). Ice streams in the Laurentide Ice Sheet: identification, characteristics and comparison to modern ice sheets. *Earth-Science Reviews*, 143, p. 117–146.

Margold M., Stokes C.R., Clark C.D., and Klemen J. (2015b). Ice streams in the Laurentide Ice Sheet: a new mapping inventory. *Journal of Maps*, 11(3), p. 380-395.

Margreth A., Gosse J.C., and Dyke A.S. (2017). Wisconsinan and early Holocene glacial dynamics of Cumberland Peninsula, Baffin Island, Arctic Canada. *Quaternary Science Reviews*, 168, p. 79-100

Mate D.J., Campbell D.C., Barrie J.V., Hughes Clarke J.E., Muggah J., Bell T., and Forbes D.L. (2015). Integrated seabed mapping of Frobisher Bay, southern Baffin Island, Nunavut to support infrastructure development, exploration, and natural-hazard assessment; *in* Summary of Activities 2014, Canada-Nunavut Geoscience Office, p. 145-152

McCann S.B., Dale J.E., and Hale P.B. (1981). Subarctic tidal flats in areas of large tidal range, southern Baffin Island, eastern Canada. *Geographie Physique et Quaternaire*, 35(2), p. 183-204

Miller G.H. (1980). Late Foxe glaciation of southern Baffin Island, N.W.T., Canada. *Geological Society of America Bulletin*, v. 91, no. 7, p. 399–405.

Miller G.H. (1985). Moraines and proglacial lake shorelines, Hall Peninsula, Baffin Island. In: J.T. Andrews (ed.), Quaternary environments, eastern Canadian Arctic, Baffin Bay, and western Greenland. Boston, Mass.: Allen & Unwin, pp. 546-557.

Miller G.H, Locke W.W. III, and Locke C.W. (1980). Physical characteristics of the southeastern Baffin Island coastal zone. In: *The Coastline of Canada* (McCann, S.B., ed.). Geological Survey of Canada, Paper 80-10, 251-265.

Miller G.H., Wolfe A.P., Briner J.P., Sauer P.E., and Nesje A. (2005). Holocene glaciation and climate evolution of Baffin Island, Arctic Canada. *Quaternary Science Reviews*, v.24(14-15), p. 1703-1721.

Osterman L.E. (1982). Late Quaternary history of southern Baffin Island, Canada: A study of foraminifera and sediments from Frobisher Bay. PhD Thesis, Department of Geological Sciences, University of Colorado.

Osterman L.E. and Andrews J.T. (1983). Changes in glacial-marine sedimentation in core HU77-159, Frobisher Bay, Baffin Island, N.W.T: A record of proximal, distal, and ice-rafting glacial-marine environments. *in* Glacial-Marine Sedimentation (B.F. Molnia ed.), Plenum Press, New York and London.

Squires C.A. (1984). The Late-Foxe deglaciation of the Burton Bay area, southeastern Baffin Island, N.W.T. Unpublished M.A. Thesis, Department of Geography, University of Windsor, 115 p.

Stravers J.A., Miller G.H. and Kaufman D.S. (1992). Late glacial ice margins and deglacial chronology for southeastern Baffin Island and Hudson Strait, eastern Canadian Arctic. *Canadian Journal of Earth Sciences*, v. 29, no. 5, p. 1000–1017, doi: 10.1139/e92-083

Steenkamp H. M. and St-Onge M. R. (2014). Overview of the 2013 regional bedrock mapping program on northern Hall Peninsula, Baffin Island, Nunavut. *in* Summary of Activities 2013, Canada-Nunavut Geoscience Office, p. 27–38.

St-Onge M.R., Jackson G.D. and Henderson I. (2006). Geology, Baffin Island (south of 70°N and east of 80°W), Nunavut. Geological Survey of Canada, Open File 4931, 3 sheets at1:500 000 scale

Stuiver M., Reimer P.J., and Reimer R.W. (2021). CALIB Radiocarbon Calibration, version 8.2. computer software.

Syvitski J.P.M., Farrow G.E., Atkinson R.G.A., Moore P.G. and Andrews J.T. (1989). Baffin Island fiord macrobenthos: bottom communities and environmental significance. *Arctic*, v. 42, p. 232-247.

Todd B.J. (2016). De Geer moraines on German Bank, southern Scotian Shelf of Atlantic Canada; *in* Atlas of Submarine Glacial Landforms: Modern, Quaternary, and Ancient (J.A Dowdeswell, M. Canals, M. Jakobsson, B.J. Todd, E.K. Dowdeswell and K.A. Hogan, eds.), Geological Society of London Memoirs, 46, p. 259-260.

Todd B.J., Valentine P.C., Longva O., and Shaw J. (2007). Glacial landforms on German Bank, Scotian Shelf: evidence for Late Wisconsinan ice-sheet dynamics and implications for the formation of De Geer moraines. *Boreas*, 36, p. 148-169

Tremblay T., Day S., McNeil R., Smith K., Richardson M., and Shirley J. (2015). Overview of surficial geology mapping and geochemistry in the Sylvia Grinnell Lake area, Baffin Island, Nunavut. *in* Summary of Activities 2015, Canada-Nunavut Geoscience Office, p. 107– 120.

Tremblay T., Hardy F., Forget Brisson L., and Lamothe M. (2018). The importance of sedimentological context in the IRSL single-grain chronology of glacial lakes and ice retreat on Boothia Peninsula and southern Baffin Island, NU. Presented at CANQUA-AMQUA Joint Meeting, Ottawa 2018.

Tremblay T., Kamula C.M., Ciastek S. and Kuzyk Z.A. (2020). Overview of the geochemical properties of the marine sediments of Koojesse Inlet, Frobisher Bay, Nunavut. *in* Summary of Activities 2019, Canada-Nunavut Geoscience Office, p. 125–144.

Vickers K.J., Ward B.C., Utting D.J., and Telka A.M. (2010). Deglacial reservoir age and implications, Foxe Peninsula, Baffin Island. *Journal of Quaternary Research*, 25(8), p. 1338-1346

Warren C.R. and Hulton N.R.J. (1990). Topographic and glaciological controls on Holocene ice-sheet margin dynamics, Central West Greenland. *Annals of Glaciology*, 14, p. 307-310

3. Morphological characterization of submarine slope failures in a semi-enclosed fjord, Frobisher Bay, eastern Canadian Arctic

Since 2006, opportunistic multibeam echosounder (MBES) surveys in coastal waters of eastern Baffin Island, Nunavut, have revealed an abundance of submarine slope failures (SSFs) at the head of Frobisher Bay (Fig. 3.1). Initial MBES surveys provided bathymetric information for safe navigation along the 265 km length of the bay (Hughes Clarke et al. 2015). Since 2012, a targeted marine geohazard mapping programme has been underway as part of a broader marine geoscience study in support of sustainable development (Mate et al. 2015). Specifically, the bay faces potential impacts from growing commercial fisheries, expanded terrestrial mining, increasing marine traffic, and infrastructure development for the rapidly growing city of Iqaluit and its planned new port. Of priority for the geohazard programme is to understand the preconditions and triggering mechanism(s) for SSFs, their frequency of occurrence, and their implications for coastal infrastructure integrity and local tsunami risk. This paper provides a morphometric analysis of SSFs in inner Frobisher Bay, and contrasts their overall dimensions and shape with other SSF datasets. It also generates hypotheses on potential triggers, transport processes and chronology to be tested by comprehensive sampling and dating programs.

The study of mass-transport complexes in the St Lawrence estuary in eastern Canada by Pinet et al. (2015) is one of the first comprehensive, statistical treatments of SSFs in a coastal shallow-marine setting. Regional syntheses of SSFs on continental margins (e.g., Leynaud et al. 2009; Twichell et al. 2009; Moscardelli and Wood 2016) or targeted analysis of individual features such as the Storegga Slide (Haflidason et al. 2005; Micallef et al. 2007) or events (e.g., 1964 Resurrection Bay earthquake: Haeussler et al. 2007), are more common. Access to MBES datasets and their near-complete, high-resolution, bathymetric coverage of the seabed is a key recent development and precursor for the statistical morphometric analysis of SSFs. This is especially true in the Arctic coastal zone, where seabed mapping has been limited by environmental factors (e.g., sea ice) and suitable mapping platforms (e.g., shallow draught, ice strengthened). For example, the Sedimentology of Arctic Fiords Experiment (SAFE: Syvitski and Schafer 1985, Syvitski et al. 1987) provided a wealth of new geoscientific information on modern processes of Arctic fjords but predated MBES surveying, and therefore was limited in its contributions to seabed geomorphology and, specifically, geomorphometry.

This paper presents the morphological description and geographical setting of 246 SSFs identified in MBES bathymetry from inner Frobisher Bay. A range of parameters are used to describe the dimensions and shape of individual features, and to draw comparisons between the SSF populations in Frobisher Bay and those in the St Lawrence River estuary (n = 96; Pinet et al. 2015) and Resurrection Bay, Alaska (n = 10; Haeussler et al. 2007). All three sites are formerly glaciated embayments, containing abundant glaciomarine deposits in seismically active regions.

3.1 Physiographical and geological setting

Frobisher Bay, a fjord located in SE Baffin Island, Nunavut, Canada is approximately 265 km long and is widest near its mouth (66 km), tapering to less than 20 km at its head. The bay can be divided into three sections based on bathymetry: the outer bay, the mid-bay, and the inner bay. By area, the outer bay is the largest, entailing almost 180 km of the total length. Geologically, it is a half-graben with depths reaching upwards of 800 m along its southern coast. The mid-bay divides Frobisher Bay with a series of low-lying islands and shallow channels, acting as a sill. The inner bay (Fig. 3.1) is the shallow (<250 m) semi-enclosed embayment NW of these islands.

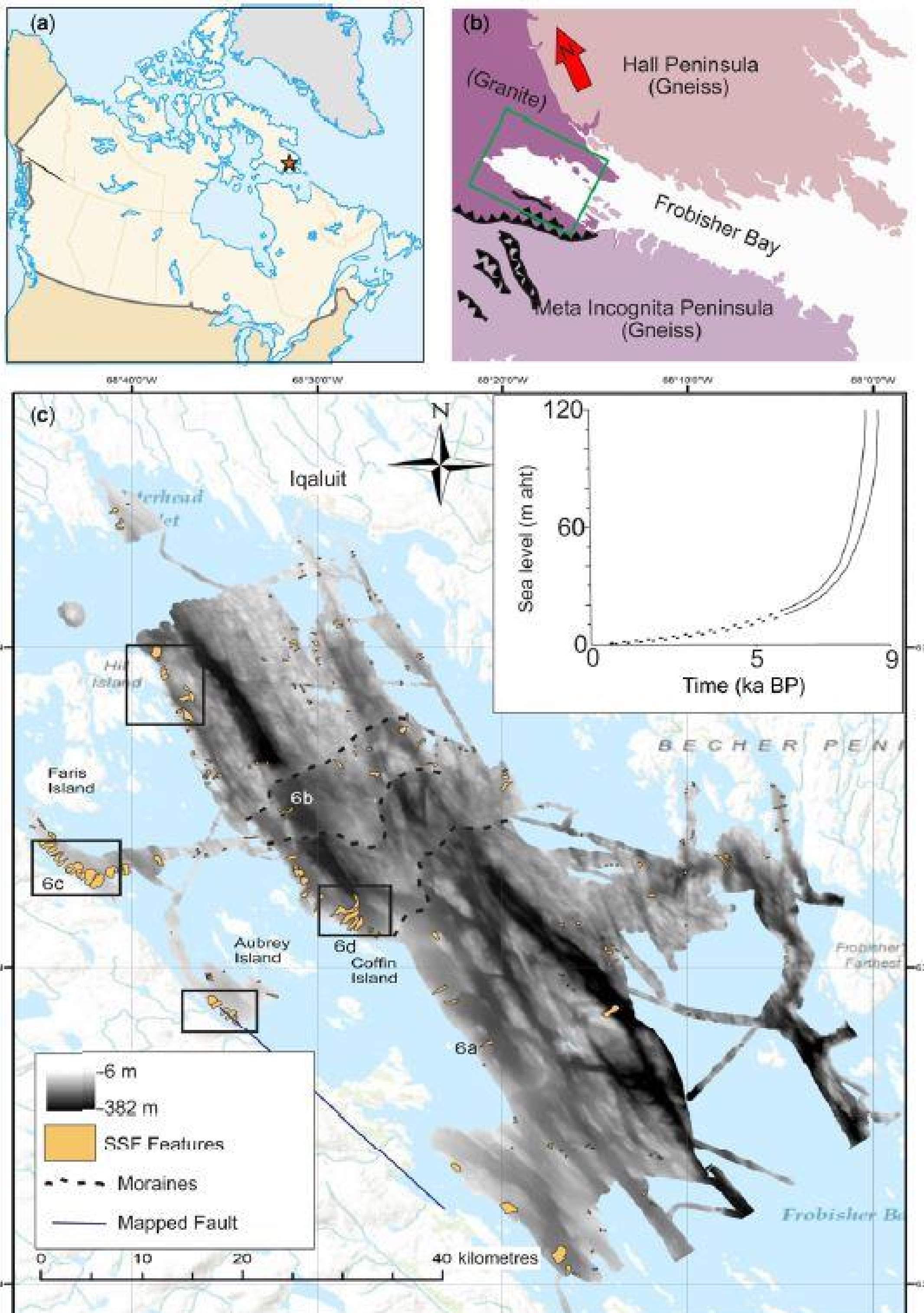

Figure 3.1 (a) Location of Frobisher Bay. (b) Geological map of SE Baffin Island (simplified from De Kemp et al. 2006). Black lines represent major faults, with arrows indicating the direction of

movement. The green box indicates area of (c). (c) MBES bathymetric coverage in inner Frobisher Bay. Depths are shown in metres. Submarine slope-failure (SSF) features are highlighted in orange. Boxes represent areas of high SSF feature density. Letters indicate the areas enlarged in Figure 3.6. Dashed lines represent mapped seabed moraines in inner Frobisher Bay. The solid blue line represents the fault that bounds the SW extent of the bay. (Inset) Emergence curve for the inner Frobisher Bay with the sea level shown as metres above high tide (simplified from Jacobs et al. 1985).

Inner Frobisher Bay is surrounded predominantly by Archean and Proterozoic gneisses of the Rae Domain (De Kemp et al. 2006; St-Onge et al. 2006). Inland, near Amadjuak Lake and NW from the head of the bay, lies an area of carbonate-rich Ordovician bedrock. This carbonate bedrock is thought to extend below the seabed of Frobisher Bay (MacLean et al. 2014). The Precambrian and Paleozoic bedrock is the source material for much of the glacially derived sediments that underlie the post-glacial marine sediments in the inner bay.

Inner Frobisher Bay was influenced primarily by continental glaciation during the last glacial maximum. Originating from the Foxe–Amadjuak Dome, centred over Foxe Basin to the NW, ice advanced to the SE (Stravers et al. 1992; Miller et al. 2005). This ice completely covered the basin until approximately 9.5 cal ka BP, resting on the bed of till that now underlies marine sediments on the floor of the inner bay. At this point, ice from the Foxe–Amadjuak Dome receded NW of the mid-bay islands, with its terminus now located in the inner bay. Over the next 2500 years, as the ice margin continued to recede up Frobisher Bay, glaciomarine sediments were deposited over till on the seabed. This long-lasted ice withdrawal from the inner bay produced a series of large recessional moraines both onshore and on the seabed. By c. 7 cal ka BP, the last of the Foxe–Amadjuak ice was gone from the inner bay (Squires 1984), leading to the establishment of the current sedimentary regime in the basin.

The former presence of ice sheets on SE Baffin Island continues to influence relative sea levels in the region. The marine limit for the inner bay is measured at approximately 120 m above the current higher high tide level (Jacobs et al. 1985). As the ice receded, the area underwent isostatic rebound, quickly lowering relative sea levels at first (100 m ka^{-1}) and slowly tapering off with time. This continuing change in relative sea level has had implications for tides in the region. The extreme tidal range seen today (11.1 m at springs, maximum recorded 12.6 m: CHS 2001) is thought to have been established at c. 2745 ± 145 14C years BP (Dowdeswell et al. 1985) as a result of changes in basin geometry.

Frobisher Bay is underlain by a typical postglacial embayment stratigraphy (Mate et al. 2015; Todd et al. 2016): bedrock or till are overlain by ice contact, glacioproximal, glaciodistal and postglacial marine sediments. MBES records from Frobisher Bay show that the distribution of these materials is highly variable, with exposed bedrock outcrops scattered throughout areas of thick glaciomarine sedimentation. Ice-rafted debris (IRD) is common due to the prevalence of sea ice and icebergs in the region.

3.2 Methods

Two research vessels running MBES units provided the primary source of data for this paper. Using a Kongsberg EM-302 30 kHz multibeam echosounder, CCGS Amundsen collected data in each of the years 2006–2010 and 2014–2017. RV Nuliajuk, equipped with a hull-mounted Kongsberg EM2040 200 and 400 kHz multibeam echosounder, comprehensively mapped inner Frobisher Bay in a number of campaigns from 2012 to 2016. An estimated 75% of inner Frobisher Bay has MBES bathymetric coverage, most below the 10 m isobath. The remaining 25% of the inner bay is in waters too shallow for either vessel. The unmapped areas of the inner bay include: the channels behind islands along the southern coast; inlets on the north coast; extensive tidal flats near Iqaluit; and Foul Inlet at the NW extremity of the bay. The hypsometric curve for inner Frobisher Bay shows that the majority of the bay has depths of less than 100 m, much of it being less than 50 m, and approximately 25% of the inner bay (including unmapped areas) has depths less than 10 m below the low tide line (Fig. 3.2).

Processing of MBES bathymetric data was completed using Teledyne Caris 2017 HIPS and SIPS 10.0 or later software. Bathymetric raster surfaces of 2 and 5 m resolution were generated using the CUBE algorithm in Teledyne Caris HIPS software. Depth values were normalized to chart datum (Mean Lower Low Water (MLLW) = 0).

Submarine slope failure footprints were outlined and assessed for completeness and utility in this study. They were measured for morphometric parameters using bathymetric raster surfaces in ArcMap 10.3 (ESRI's 2017 ArcGIS Desktop 10.3 software). The boundaries of the SSF features were delimited to include all visible areas of the footprint, from the top of the headwall to the edge of disturbance at the bottom of the feature. In cases where boundaries between disturbed and undisturbed areas were unclear, outlines were drawn to include the full possible extent.

Morphometric parameters were measured following the methods in Pinet et al. (2015), thereby allowing a direct comparison between regions. Twelve measured and seven calculated parameters were used to characterize the slope failures found in Frobisher Bay (Fig. 3.3; Table 3.1). Measured parameters were selected to provide a baseline description of these features in inner Frobisher Bay and a dataset upon which to perform further calculations. Seven parameters describe the size of these features:

- Area (A) (in km^2) of an SSF feature is defined as the two-dimensional extent of the footprint of the slope failure, including the headwall.
- Perimeter (P) (in km) is the length of the line required to fully outline the area of the SSF feature, following the conditions described above.

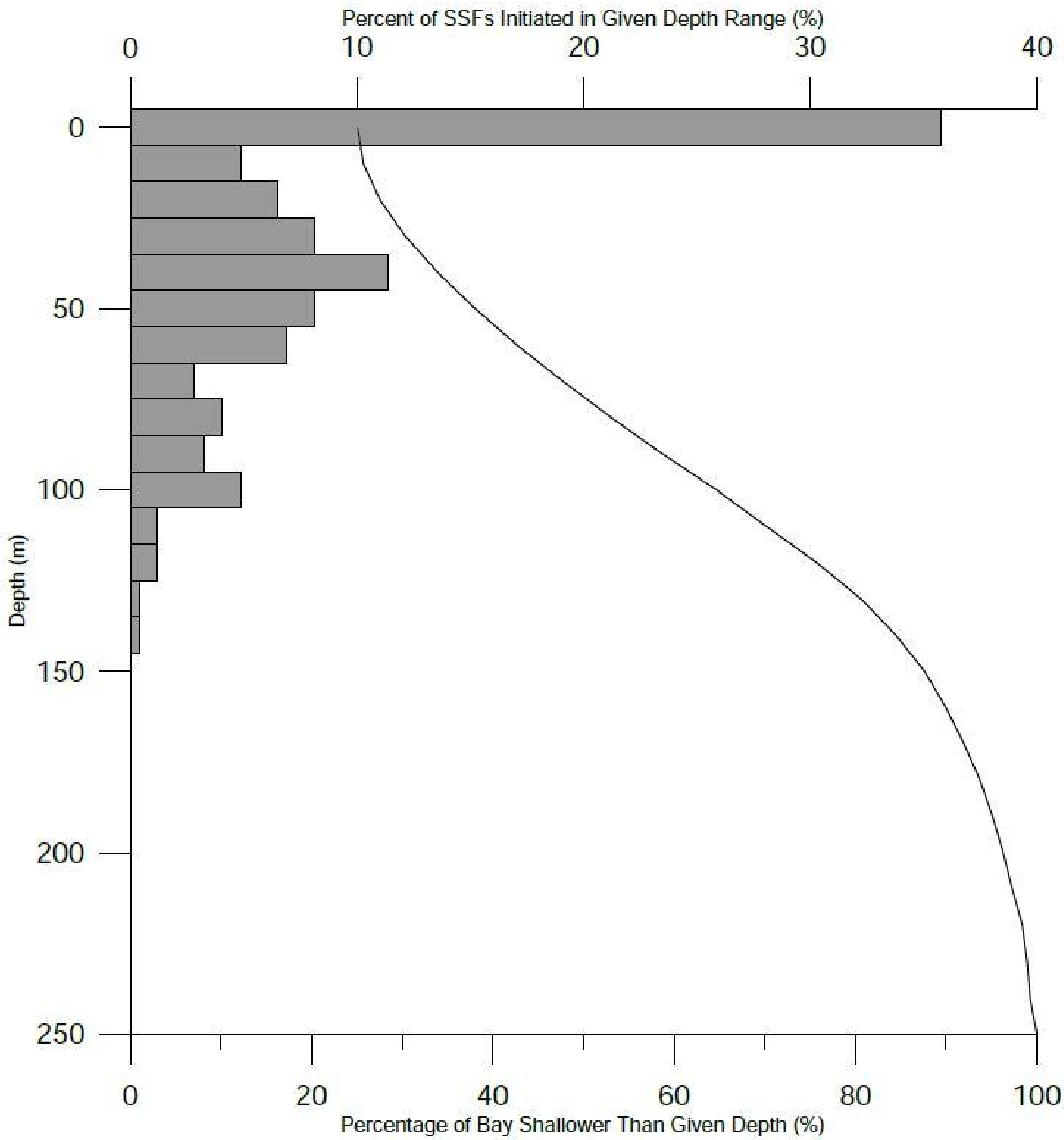

Figure 3.2 Hypsometric curve for inner Frobisher Bay, including an estimated 25% unsurveyed due to water depths of less than 10 m. Grey bars represent the distribution of initiation depths for submarine slope failure features in the inner bay.

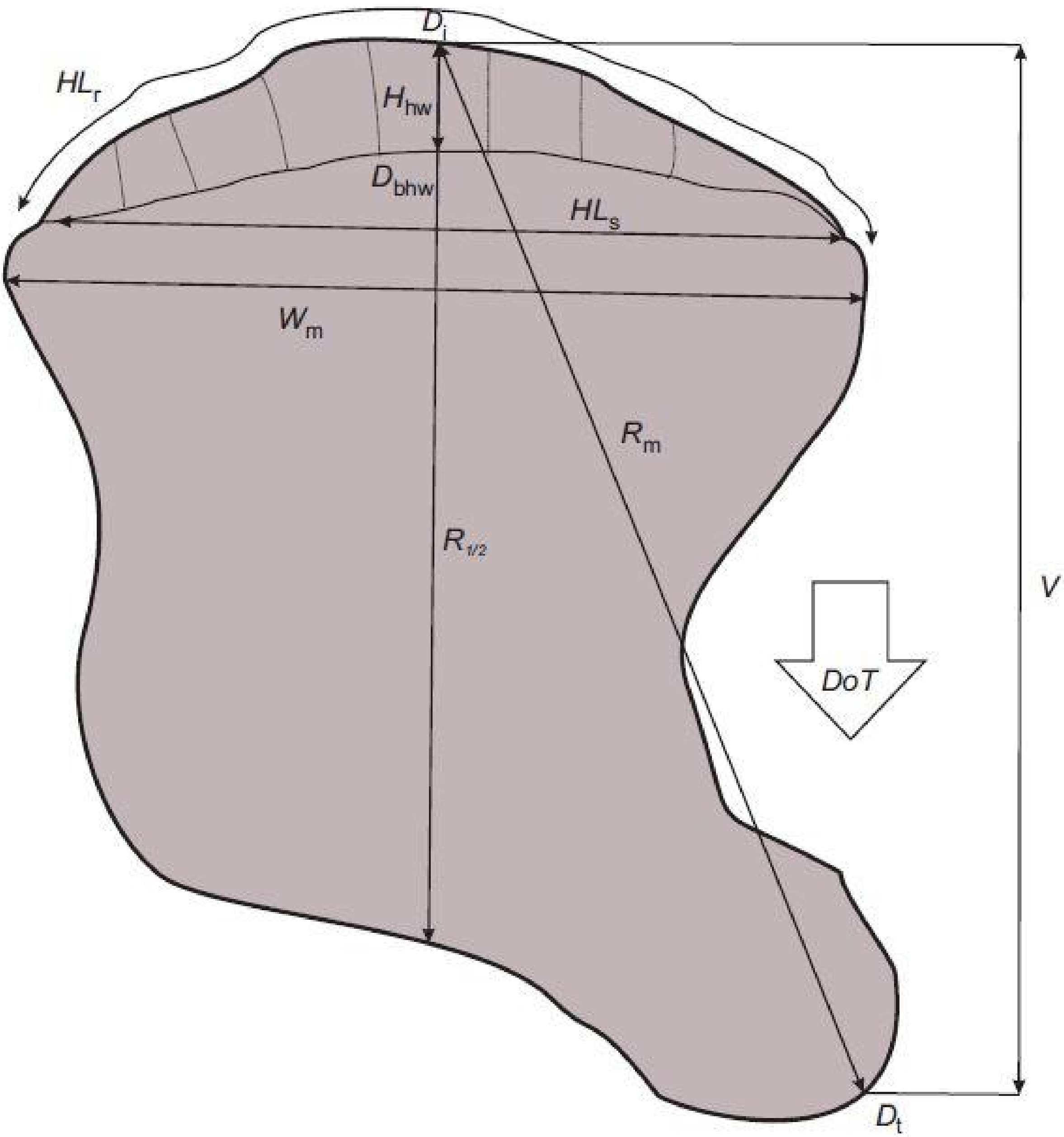

Figure 3.3 Illustration of morphometric parameters measured in this study. Descriptions of each parameter are found in Table 3.1.

- Maximum width (W_m) (in metres) is the length of the horizontal line required to connect the two edges of the SSF-feature footprint at its widest extent.

- Maximum run-out (R_m) (in metres) is the horizontal distance between the shallowest and deepest extents of the SSF-feature footprint.
- Run-out length at half-width ($R_{1/2}$) (in metres) is the length of the horizontal line running perpendicular to the line of maximum width from the top of the slope failure footprint to the edge it meets.
- Curvilinear length of the headwall (HL_r) (in metres) refers to the horizontal length of the headwall as measured following the convolutions between its endpoints.
- Straight-line headwall length (HL_s) (in metres) refers to the horizontal length of the line of shortest distance between these two endpoints. Where there was a coalesced headwall, the approach was to record the same values for multiple features.

Three parameters describe the depth over which these features are found:

- Initiation depth (D_i) and termination depth (D_t) of the feature, and depth at the base of the headwall (D_{bhw}). Depth measurements (in metres) measure the shallowest and deepest depths of the feature, as well as the depth of the base of the headwall, as interpreted from the MBES data.
- Maximum slope (α_{bathy}) within the SSF feature (in °) was measured using a slope raster generated from the MBES bathymetric dataset. It describes the greatest slope found within the feature at the time of data collection, typically found at the headwall.
- Direction of transport (DoT) is described with cardinal directions. Given the non-linear nature of many of the features found in inner Frobisher Bay, the direction of transport is measured as the direction of the line joining the points of shallowest and deepest water depth of the feature.

Table 3.1 Description of morphometric parameters outlined in Figure 3.2

Parameter		Description
Measured		
Area	A	Area of feature in square kilometres
Perimeter	P	Perimeter of feature in kilometres
Direction of transport	DoT	Cardinal direction of sediment transport
Maximum run-out	R_m	Maximum run-out length in metres
Maximum width	W_m	Maximum width of the feature in metres
Headwall length (curvilinear)	HL_r	Length of the headwall in metres, following the exact path of the headwall
Headwall length (straight line)	HL_s	Length of the headwall in metres, measured as a straight line between two end points
Run-out 1/2	$R_{1/2}$	Run-out in metres as measured by a straight line perpendicular to W_m at $1/2\ W_m$
Initiation depth	D_i	Water depth at the top of the slope failure feature in metres
Termination depth	D_t	Water depth at the bottom of the slope failure feature in metres
Depth at base of headwall	D_{bhw}	Water depth at the bottom of the headwall in metres
Maximum slope in feature (°)	α_{bathy}	Maximum slope in the feature, as measured from the bathymetry raster
Calculated		
Headwall curvature	CRV	HL_r/HL_s: measure of the convolution of the headwall (1 = straight)
Vertical extent	V	D_t-D_i: change in water depth along the run-out of the slope failure in metres
Headwall height	H_{hw}	$D_{bhw}-D_i$: height of the headwall in metres
Compactness	C	4π area/perimeter^2: measure of the similarity to a circle (1 = circular)
Regional slope (°)	α	Angle from D_i to D_t at $1/2\ W_m$ (calculated as in Pinet *et al.* 2015)
Regional slope (maximum) (°)	α_{max}	Angle from D_i to D_t (calculated as in Pinet *et al.* 2015)
Elongation	E	$R_m/R_{1/2}$

Seven calculated parameters describe the characteristics of SSFs not readily seen in the basic measured parameters. Two parameters act to further describe the headwall features: headwall curvature and headwall height.

- Headwall curvature (CRV) is a dimensionless parameter used to describe the degree of convolution of the headwall. It is the quotient of the curvilinear and straight-line headwall lengths. If the headwall is perfectly straight, the headwall curvature will equal 1. As sinuosity increases, this value increases.

- Headwall height (Hhw) is the difference between the depth at the top of the feature and the depth at the base of the headwall. This represents the maximum headwall height for the feature.
- Vertical extent (V) of the slope failure feature was calculated as the difference between the depth at the top of the slope failure feature and the depth at the bottom, as described above. This is not necessarily the depth at which sediment was transported in the submarine slope failure, it is simply indicative of the overall vertical extent of the feature.

Table 3.2 Summary statistics for morphometric parameters in three fjords

Parameter		Inner Frobisher Bay					St Lawrence estuary	Seward, Alaska
		Median (M_{IFB})	Minimum	Q_1	Q_3	Maximum	Median (M_{SLE})	Median (M_{SA})
A	Area (km^2)	0.09	0.01	0.04	0.34	2.15	3.34	1.47
V	Vertical extent (m)	29	1	16	42	199	50.2	*
W_m	Maximum width (m)	115	14	73	204	683	2900	*
$R_{1/2}$	Run-out at half-width (m)	203	46	136	383	1043	1500	*
R_m	Maximum run-out (m)	247	70	155	485	1692	1700	*
E	Elongation	1.7	0.3	1.2	2.4	7.7	0.55	*
C	Compactness	0.6	0.18	0.48	0.72	0.91	*	*
H_{hw}	Headwall height (m)	2	0.2	1.2	3	19.3	9	*
HL_r	Headwall length (m)	87	10	53	156	1026	4500	*
CRV	Headwall curvature	1.4	1	1.2	1.7	4.3	1.3	*
α	Regional slope (°)	7	0.4	4.2	10.1	40.6	2.3	*
α_{bathy}	Maximum measured slope	28.9	8.9	23.3	33.9	73.9	*	*
D_i	Initiation depth (m)	50.5	3.1	35.1	74.6	149.7	*	*

*, value not available.

Two parameters were calculated using the same method as Pinet et al. (2015) to characterize the regional slope of a feature:

- Regional slope (α) was calculated using the vertical extent and run-out length at half of the maximum width.

- Regional slope (maximum) (α_{max}) was calculated using the vertical extent and maximum run-out length. Both of these parameters act as an average slope for the slope failure feature, ignoring internal complexity and slope changes.

Finally, two calculated parameters compare the shape of the slope failure features to a perfect circle:

- Compactness (C), a dimensionless parameter with values of between 0 and 1, refers to the degree to which a shape resembles a circle, the most compact geometrical shape. For a perfect circle, 4π area/perimeter^2 will be equal to 1. As a shape deviates from a perfect circle, the perimeter increases disproportionately to the area and the compactness values tend towards 0 (Lee and Sallee 1970; Angel et al. 2010).
- Elongation (E), a dimensionless parameter, refers to the degree to which a feature resembles a feature of equal length and width (a perfect circle or square). It was calculated as the ratio between run-out length at half the maximum width and the maximum width of a feature. For features of greater width, values will range from 0 to 1. For those of greater length, values will be >1.

Descriptive statistics were used to both summarize the main elements of the SSF population in Frobisher Bay and contrast between different regions. Generally, the distribution parameters are log-normal, requiring a log transformation to approximate a normal distribution for statistical analysis.

3.3 Results

The inner Frobisher Bay database contains 163 fully surveyed and 83 partially surveyed SSFs. For the fully surveyed SSFs, descriptive statistics for morphometric parameters are shown in Table 3.2. Considering the full data set, SSFs are unevenly distributed throughout inner Frobisher Bay.

Four large clusters of SSFs are found along the SW coast, off Hill (n = 17) and Coffin (n = 16) islands, and in semi-enclosed embayments behind Faris (n = 26) and Aubrey (n = 12) islands (Fig. 3.1). In the embayment behind Faris Island, SSF footprints cover approximately one-third of the seabed, representing the highest density of these features in the bay (three per km^2). Clustering is also seen to a lesser extent in NE embayments (n = 12). Outside of these clusters, SSF features tend to be located along geological features such as faults or moraines where seabed slopes are steeper.

The direction of transport (DoT) was determined for all SSFs, including those partially mapped. Of the 246 features, over half (56%) were aligned perpendicular to the NW–SE orientation of the bay (Fig. 3.4).

The SSF features of inner Frobisher Bay display a wide range of shapes and sizes (Figs 3.5 and 3.6; Table 3.2). A typical morphology (median, range from first to third quartile [Q_1−Q_3]) involves a simple lobate form with a low headwall height (2.0 m, 1.2–3.0 m) spread over a 30 m depth range (29.4 m, 16.0–41.8 m), originating from a single headwall ('a' in Fig. 3.6a) in shallow water (50.5 m, 35.1–74.6 m: Figs 3.2 and 3.6a). These features may have levees ('b' in Fig. 3.6a) bounding either side of the run-out, and terminate in compressional ridges ('c' in Fig. 3.6a) or lobes ('d' in Fig. 3.6c). The Frobisher Bay features are somewhat compact (0.60, 0.48–0.72), tending to be confluent but typically elongate (1.7, 1.2–2.4), twice as long (203.0 m, 136.0–383.0 m) as they are wide (115.0 m, 73.0–204.0 m), and a few are very elongate (maximum 7.7). A small minority (6%) of features, commonly those with a non-confluent pattern, have very low compactness ($C < 0.3$: Fig. 3.6b), but otherwise have a typical morphology. In contrast, 20% are highly compact, taking on a circular form ($C > 0.75$: Fig. 3.6c). Many parameters show a high variance (Fig. 3.5). This includes SSF initiation depth, with most features (36%) in very shallow water (Fig. 3.2). The other

64% are initiated across a wide range of depths (5–145 m), with secondary modes at 40 and 115 m (Fig. 3.2).

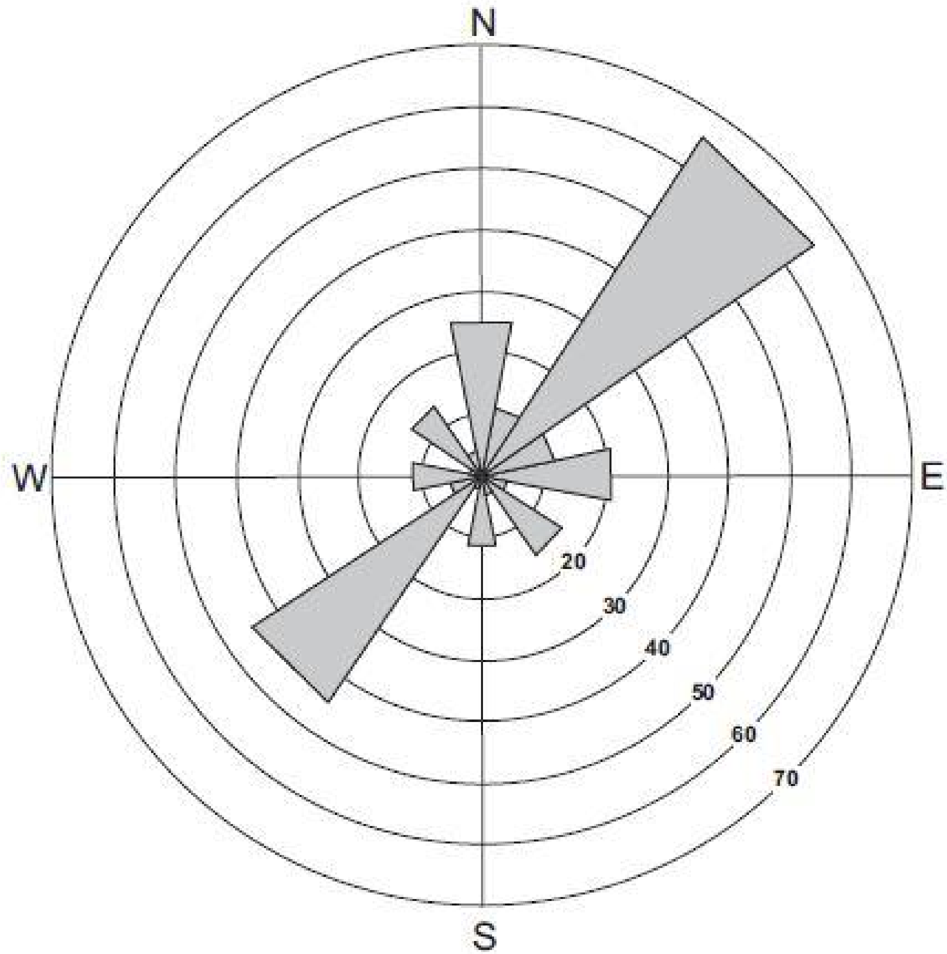

Figure 3.4 Directions of transport for submarine slope failures mapped in inner Frobisher Bay.

In areas of high feature density (Fig. 3.1), three complex forms are distinguished: nested, cascading and cross-cutting. Nested features contain multiple SSFs that share the same headwall but vary in downslope extent (‘e’ in Fig. 3.6c). Here the SSFs are differentiated based on surface roughness; the lower one appearing smoother with more subdued relief in contrast to the rougher upper one. A lobate ridge typically separates the two SSFs. Cascading features also display areas of contrasting roughness but the rougher surface is on the upper SSF, and the headwall for the lower SSF is developed in the toe area of the upper SSF ('f' in Fig. 3.6d). Cross-cutting features are those where SSFs partially overlap in their run-out zones to form a series of truncated toes ('g' in Fig. 3.6d). In some cases, there is contrasting surface roughness between the overlapping SSFs. The cross-cutting patterns also provide clues to the sequence of multiple SSF events.

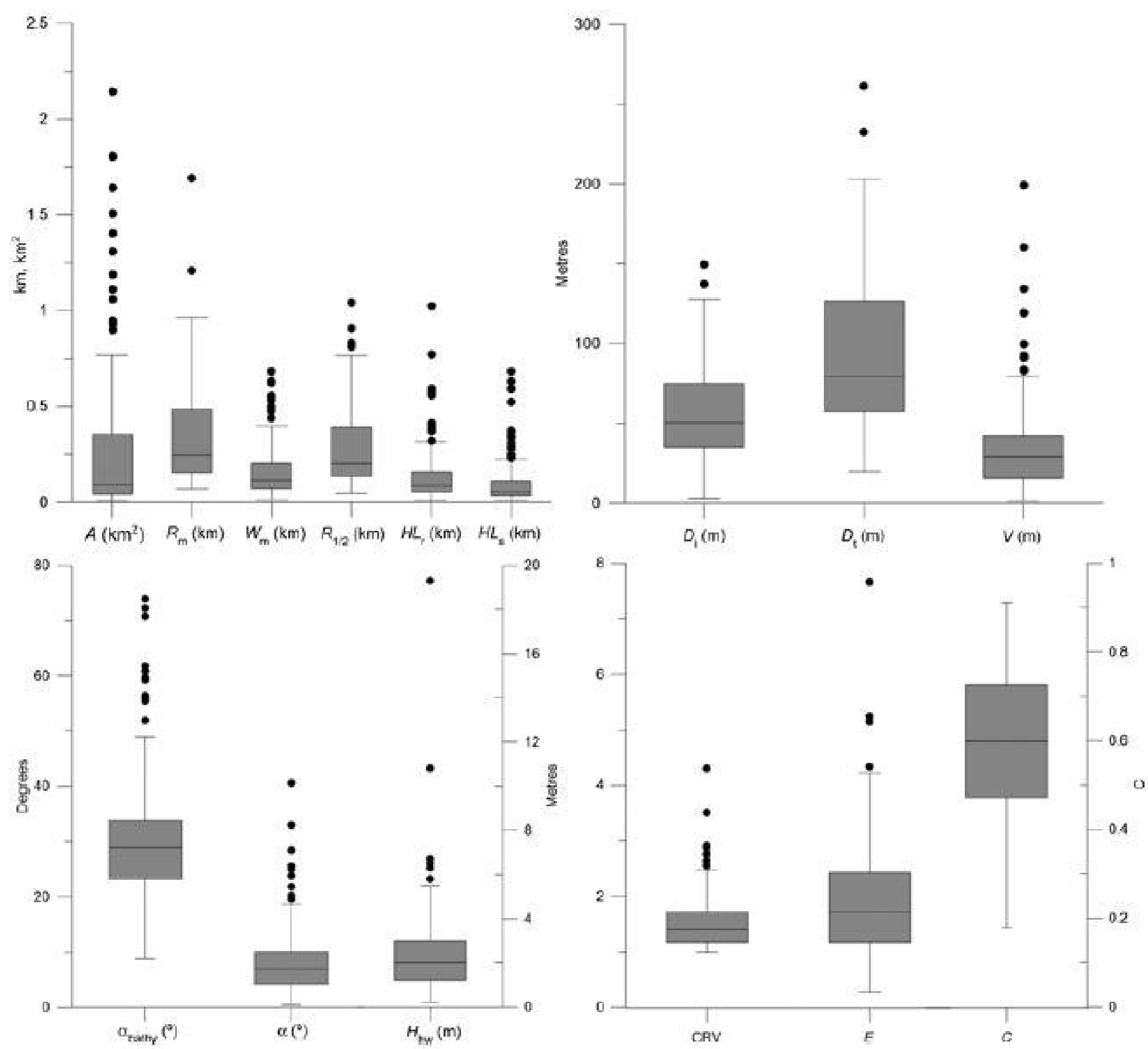

Figure 3.5 Distributions of morphometric parameters in inner Frobisher Bay. Boxes represent the interquartile range (IQR) and whiskers extend to $Q_1 - 1.5 \times IQR$ and $Q_3 + 1.5 \times IQR$. All parameters outside of that range are shown as points.

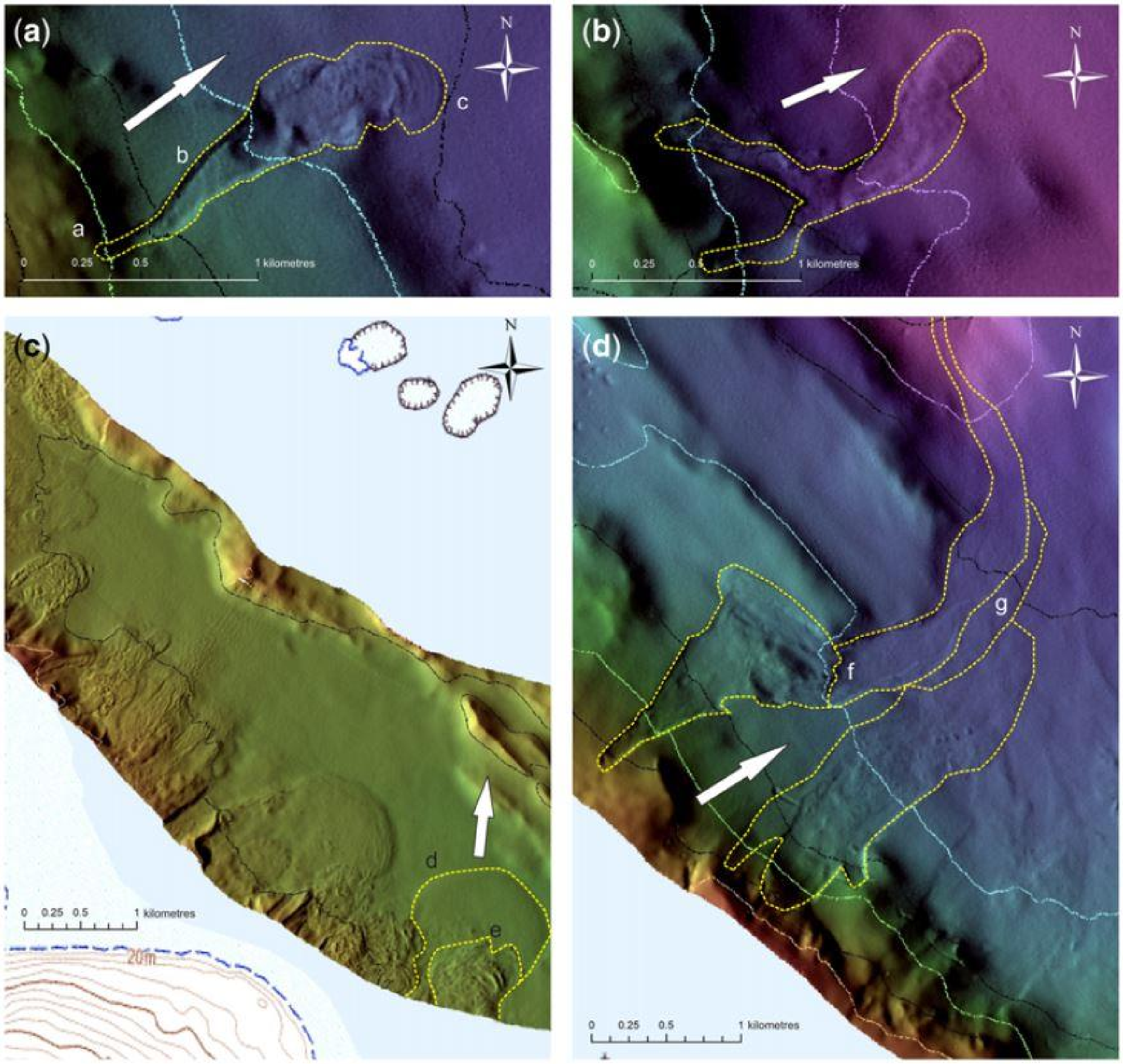

Figure 3.6 The variety of submarine slope failure (SSF) features in inner Frobisher Bay. Dashed yellow lines show the outline of SSF features. White arrows indicate the direction of transport. (a) A typical (Q_1−Q_3) feature, with a single headwall (a), levees (b) and compression ridges (c). (b) A non-confluent, non-compact SSF feature. (c) A high density of SSF features (three per km^2) behind Faris Island, showing a lobe (d) and nested SSF features (e). (d) An abundance of SSF features off Coffin Island, showing (f) cascading features and (g) cross-cutting features.

A comparison of median morphometric parameters between SSFs in inner Frobisher Bay, the St Lawrence estuary and Seward, Alaska (M_{IFB}, M_{SLE} and M_{SA}) reveals key differences (Table 3.2).

Generally, SSF features found in inner Frobisher Bay have smaller areas than those in the other fjords (0.09, 3.34 and 1.47 km^2). Other dimensional parameters (e.g., W_m, R_m) are related similarly, with values in inner Frobisher Bay being a fraction of those in the St Lawrence estuary (Table 3.2). Conversely, elongation (1.7 and 0.55) and regional slope values (7.0° and 2.3°) for inner Frobisher Bay are more than triple those of the St Lawrence estuary. The only parameter that is similar between the two regions is headwall curvature (1.4 and 1.3).

3.4 Discussion

3.4.1 Morphology of SSFs in inner Frobisher Bay

The geology of inner Frobisher Bay is a primary factor in the spatial distribution of SSF features. The clusters of SSF features along the southern coast of the inner bay are associated with steeper slopes found in the fault-affected nearshore (including islands) in the area (Fig. 3.1). Conversely, the northern coast has few islands and lacks the same prevalence of steep slopes. Furthermore, the orientation of geological features (e.g., shoreline, troughs and islands) controls the directionality of SSFs, with half (56%) being orientated perpendicular to these features, suggesting strong bathymetric slope control of run-out direction (Fig. 3.4).

The complexity of SSF features in inner Frobisher Bay suggests asynchronous formation. Nested features suggest that there were multiple periods of SSF formation in the past, unless secondary SSFs resulted from residual instability and retrogressive movement from a primary failure. The relative surface roughness of SSF features may suggest a range of ages. The implications of this are that not all features were formed from one triggering event (e.g., a large earthquake) but, instead, SSFs may form from active processes (e.g., cyclical tidal loading) in the inner bay, and they may themselves act to shape the seabed.

SSF features in inner Frobisher Bay are initiated mostly (69%) in shallow water (<30 m: Fig. 3.2), suggesting subaerial slope failures and changes in water depth as contributing factors to SSF occurrence. Seismic activity may trigger subaerial slope failures that continue onto the seabed adjacent to coastlines (Lastras et al. 2013).

Changes in pore pressure prompted by changes in water depth can act to destabilize sediments, making them more susceptible to other triggering mechanisms (Canals et al. 2004). Furthermore, rapid depth changes may trigger these events (Owen et al. 2007). In inner Frobisher Bay, the rapid decrease in water depth following deglaciation (100 m ka^{-1}) (Jacobs et al. 1985) and the great daily fluctuation in shallow depths caused by macrotidal conditions (11.1 m range) present other possible triggering mechanisms (Canals et al. 2004). With these triggering mechanisms acting at different times (c. 9 ka BP and c. 2745 ^{14}C years BP, respectively), establishing a chronology for these features is essential to evaluating their likely trigger(s). Remarkably, no SSF features are initiated below 150 m water depth (Table 3.2), possibly indicating a maximum depth of influence for these triggers. More than 50 sediment cores have been collected in inner Frobisher Bay (NRCan 2017), and analysis is in progress to establish a chronology and evaluate the viability of each of these triggering mechanisms in the region.

3.4.2 Comparison to other regions

Differences in median SSF areas between inner Frobisher Bay and other fjords can be accounted for by the types and volumes of failed sediment. Headwall heights for inner Frobisher Bay indicate that the SSFs are relatively thin, with median headwall heights less than one-tenth of those in the St Lawrence estuary and Resurrection Bay. This much larger volume of failed sediment in the St Lawrence estuary would contribute to an overall increase in the size of SSF features.

In Resurrection Bay, most SSFs occurred on delta fronts that provided both a rich source of sediment and oversteepened slopes that precondition sediments for failure (Haeussler et al. 2007). Conversely, inner Frobisher Bay lacks this degree of fluvial influence, with most SSFs occurring in post-glacial muds.

Further comparisons of morphometric parameters between inner Frobisher Bay and the St Lawrence estuary are inconclusive, providing no further insight into the factors governing SSFs in the region. For future morphometric comparison, a standard set of parameters calibrated to a variety of controlling environmental factors (e.g., sediment types) needs to be established.

3.5 Conclusion

Submarine slope failure features in inner Frobisher Bay are characterized by uneven spatial distribution, relatively small size, shallow initiation depth and high compactness values, although a variety of simple and complex morphologies exist. Taken together, these characteristics indicate a population of SSF features that were formed asynchronously. Active triggering mechanisms for SSFs in the region cannot be established from morphology alone, although shallow initiation depths hint at the possibility of rapid changes in water depth playing a key role in the basin.

The comparison of morphometric parameters between inner Frobisher Bay and the St Lawrence estuary SSF features show them to be different in all parameters except headwall curvature. To better interpret these results, a standard set of morphometric parameters for SSF features should be established and further investigation of controlling factors is needed.

3.6 References

Angel S., Parent J., and Civco D.L. (2010). Ten compactness properties of circles: measuring shape in geography. *The Canadian Geographer*, 54(4), p. 441-461.

Canals M., Lastras G., Urgeles R., Casamor J.L., Mienert J., Cattaneo A., De Batist M., Haflidason H., Imbo Y., Laberg J.S., Locat J., Long D., Longva O., Masson D.G., Sultan N., Trincardi F., and Bryn P. (2004). Slope failure dynamics and impact from seafloor and shallow sub-seafloor geophysical data: case studies from the COSTA project. *Marine* Geology, 213, p. 9-72.

CHS (2001). *Canadian Tide and Current Tables 2001, Volume 4: Arctic and Hudson Bay.* Canadian Hydrographic Service, Fisheries and Oceans Canada, Ottawa.

De Kemp E.A., Gilbert C., and James D.T. (2006). Canada-Nunavut Geoscience Office: geology of Nunavut. Map. Retrieved from http://cngo.ca/content/uploads/geology_of_nunavut.pdf

Dowdeswell J.A., Osterman L.E., and Andrews J.T. (1985). Quartz sand grain shape and other criteria used to distinguish glacial and non-glacial events in a marine core from Frobisher Bay, Baffin Island, N.W.T., Canada. *Sedimentology*, 32, 119–132.

Haeussler P.J., Lee H.J., Ryan H.F., Labay K., Kayen R.E., Hampton M.A., and Suleimani E. (2007). Submarine slope failures near Seward, Alaska, during the M9.2 1964 earthquake. In Lykousis V, Sakellariou D, and Locat J (Eds.) *Submarine Mass Movements and their Consequences*, p. 269-278. Springer Publishing.

Haflidason H., Lien R., Sejrup H.P., Forsberg C.F., and Bryn P. (2005). The dating and morphometry of the Storegga Slide. *Marine and Petroleum Geology*, 22, p. 123-136.

Hughes Clarke J.E., Muggah J., Renoud W., Bell T., Forbes D.L., Cowan B., and Kennedy J. (2015). Reconnaissance seabed mapping around the Hall and Cumberland Peninsulas, Nunavut: opening up the SE Baffin coastline to geological investigations. *In: Summary of Activities 2014*. Canada-Nunavut Geoscience Office, Iqaluit, Canada, 133–144.

Jacobs J.D., Mode W.N., Squires C.A., and Miller G.H. (1985). Holocene environmental change in the Frobisher Bay Area, Baffin Island, N.W.T.: deglaciation, emergence, and the sequence of vegetation and climate. *Géographie physique et Quaternaire,* 392, p. 151–162.

Lastras G., Amblas D., Calafat A.M., Canals M., and Frigola J. (2013). Landslides cause tsunami waves: insights from Aysén Fjord, Chile. *Eos*, 94(34), p. 297-298.

Leynaud D., Mienert J., and Vanneste M. (2009). Submarine mass movements on glaciated and non-glaciated European continental margins: A review of triggering mechanisms and preconditions to failure. *Marine and Petroleum Geology*, 26(5), p. 618-632.

Lee D.R. and Sallee G.T. (1970). A method of measuring shape. *Geographical Review*, 60(4), p. 555-563.

MacLean B., Williams G. & Zhang S. (2014). New insights into the stratigraphy and petroleum potential of the Baffin shelf's Cretaceous rocks. *Bulletin of Canadian Petroleum Geology,* 62, 289–310.

Mate D.J., Campbell D.C, Barrie J.V., Hughes Clarke J.E., Muggah J., Bell T., and Forbes D.L. (2015). Integrated seabed mapping of Frobisher Bay, southern Baffin Island, Nunavut to support infrastructure development, exploration and natural-hazard assessment; *in* Summary of Activities 2014, Canada-Nunavut Geoscience Office, p. 145–152.

Micallef A., Berndt C., Masson D.G., and Stow D.A.V. (2007). A technique for the morphological characterization of submarine landscapes as exemplified by debris flows of the Storegga Slide. *Journal of Geophysical Research: Earth Surface*, 112.

Miller G.H., Wolfe A.P., Briner J.P., Sauer P.E., and Nesje A. (2005). Holocene glaciation and climate evolution of Baffin Island, arctic Canada. *Quaternary Science Reviews*, 24, p. 1703-1721.

Moscardelli L. and Wood L. (2016). Morphometry of mass-transport deposits as a predictive tool. *Geological Society of America Bulletin*, 128, 47–80.

NRCan (2017). The Expedition database. Website. Retrieved from https://ed.marine-geo.canada.ca/index_e.php

Owen M., Day S., and Maslin M. (2007). Late Pleistocene submarine mass movements: occurrence and causes. *Quaternary Science Reviews*, 26, p. 958-978.

Pinet N., Brake V., Campbell C., and Duchesne M.J. (2015). Geomorphological characteristics and variability of Holocene mass-transport complexes, St. Lawrence Estuary, Canada. *Geomorphology*, 228, p. 286-302.

Squires C. A. (1984). *The late Foxe deglaciation of the Burton Bay area, southeastern Baffin Island, N.W.T.* Unpublished thesis.

St-Onge M.R., Jackson G.D., and Henderson I. (2006). *Baffin Island (South of 70°N and East of 80°W), Nunavut.* Scale 1 : 500 000. Geological Survey of Canada, Open File, 4931.

Stravers J.A., Miller G.H., and Kaufman D.S. (1992). Late glacial ice margins and deglacial chronology for southeastern Baffin Island and Hudson Strait, eastern Canadian arctic. *Canadian Journal of Earth Science*, vol. 29, p. 1000-1017.

Syvitski J.P.M., Burrell D.C., and Skei J.M. (1987). Subaqueous slope failure. *In* Syvitski J.P.M. et al. (Eds.) *Fjords: Processes and Products*, p. 175-210. Springer-Verlag Publishing.

Syvitski J.P.M. and Schafer C.T. (1985). Sedimentology of arctic fjords experiment (SAFE): Project introduction. *Arctic*, 38(4), p. 264-270.

Todd B.J., Shaw J., Campbell D.C., and Mate D.J. (2016). Preliminary interpretation of the marine geology of Frobisher Bay, Baffin Island, Nunavut. *In* Summary of Activities 2016, Canada-Nunavut Geoscience Office, p. 61-66.

Twichell D.C., Chaytor J.D., ten Brink U.S., and Buczkowski B. (2009). Morphology of late Quaternary submarine landslides along the U.S. Atlantic continental margin. *Marine Geology*, 264(1-2), p. 4-15.

4. Chronology and Stratigraphy of Submarine Slope Failures in Frobisher Bay, Baffin Island, Arctic Canada

4.1 Introduction

Submarine slope failures (SSFs) or turbidity currents they generate are known to sever communication cables and damage seafloor infrastructure (Mulder et al. 1997; Piper et al. 1999; Carter et al. 2009; Carter et al. 2014). They are also implicated in the genesis of tsunamis that can cause coastal property damage and loss of life (Lastras et al. 2013; Brothers et al. 2016; Løvholt et al. 2018; Turmel et al. 2018; Camargo et al. 2019). Submarine and subaerial slope failures in Norwegian fjords and other coastal settings are recognized as a significant hazard to coastal communities, leading to substantial investment in monitoring, prediction, and warning systems (L'Heureux et al. 2011; Glimsdal et al. 2016; Bellwald et al. 2019). SSF has been recognized as a potential hazard in the fjords of the Baffin region of the Canadian Arctic because of their similarity to the Norwegian coast and the history of earthquake activity in Baffin Bay (e.g., Forbes et al. 2018; Gosse et al. 2020; Nunatsiaq News 2021; Bennett et al. 2022; Sedore et al. 2022), but very little is known about the local potential for submarine seafloor instability and tsunami generation.

Over the past decade, opportunistic and targeted multibeam echosounding (MBES) has revealed 246 SSFs on the seafloor near the head of Frobisher Bay, Baffin Island, Nunavut (Figs. 4.1 and 4.2; Mate et al. 2015; Todd et al. 2016; Deering et al. 2018a, b). Inner Frobisher Bay (IFB) is home to Iqaluit, the capital of Nunavut, and is a region where planned and ongoing seafloor installations (proposed fibre optic cable, Miron 2019; port and urban waterfront infrastructure, Edgar 2018) may be impacted by marine geohazards. While other seafloor hazards (e.g., ice scour, fluid-release) are present in the bay, the relatively high abundance of SSFs warrants

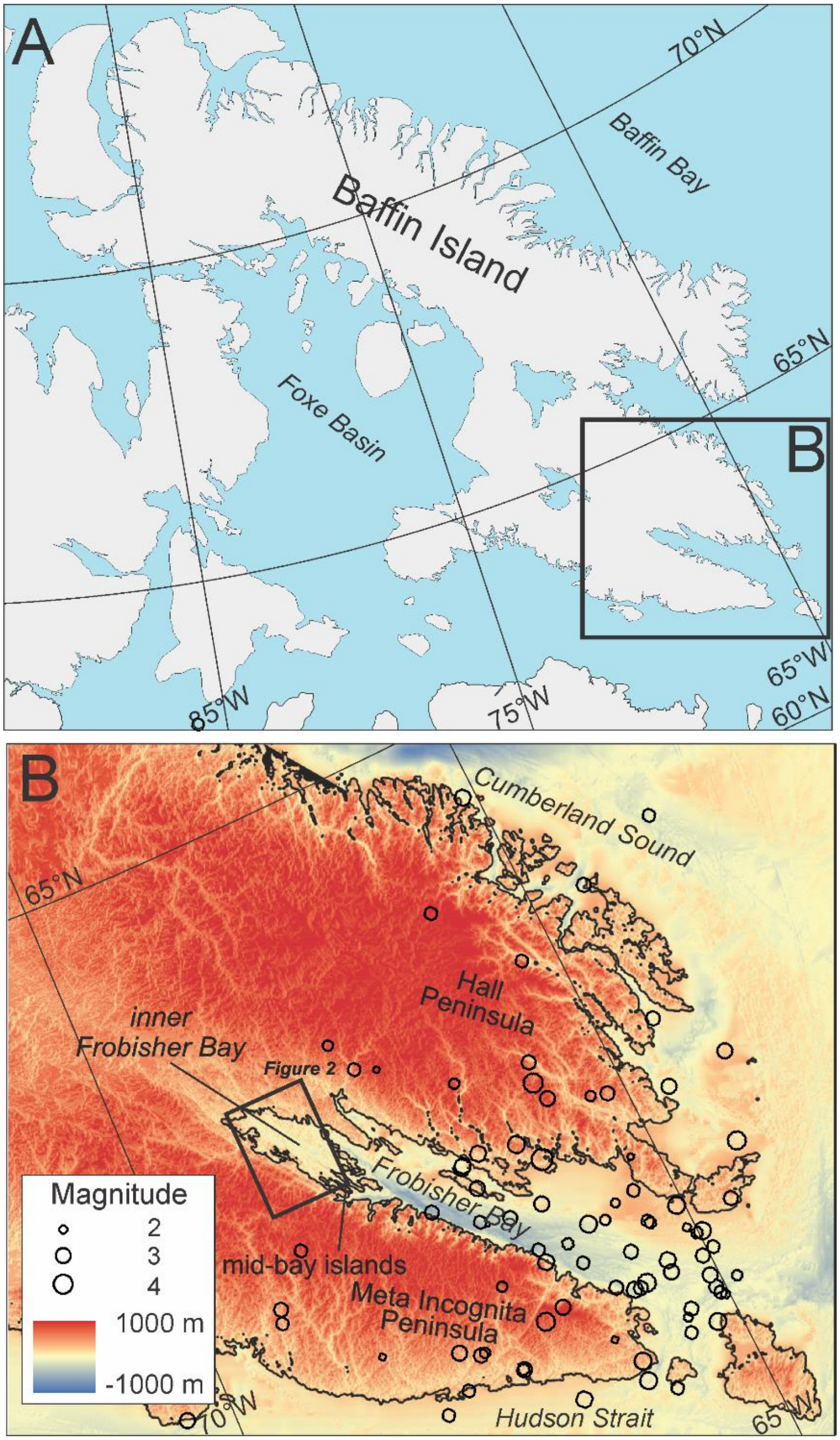

Figure 4.1 (A) Baffin Island showing regional place names and the location of Frobisher Bay (base map ESRI 2021). (B) Southeastern Baffin Island showing place names and outlining area shown in Figure 4.2. Circles denote earthquakes around southeastern Baffin Island since 1985 (Earthquakes Canada 2022). Background is GEBCO bathymetric and topographic data (GEBCO Compilation Group 2020).

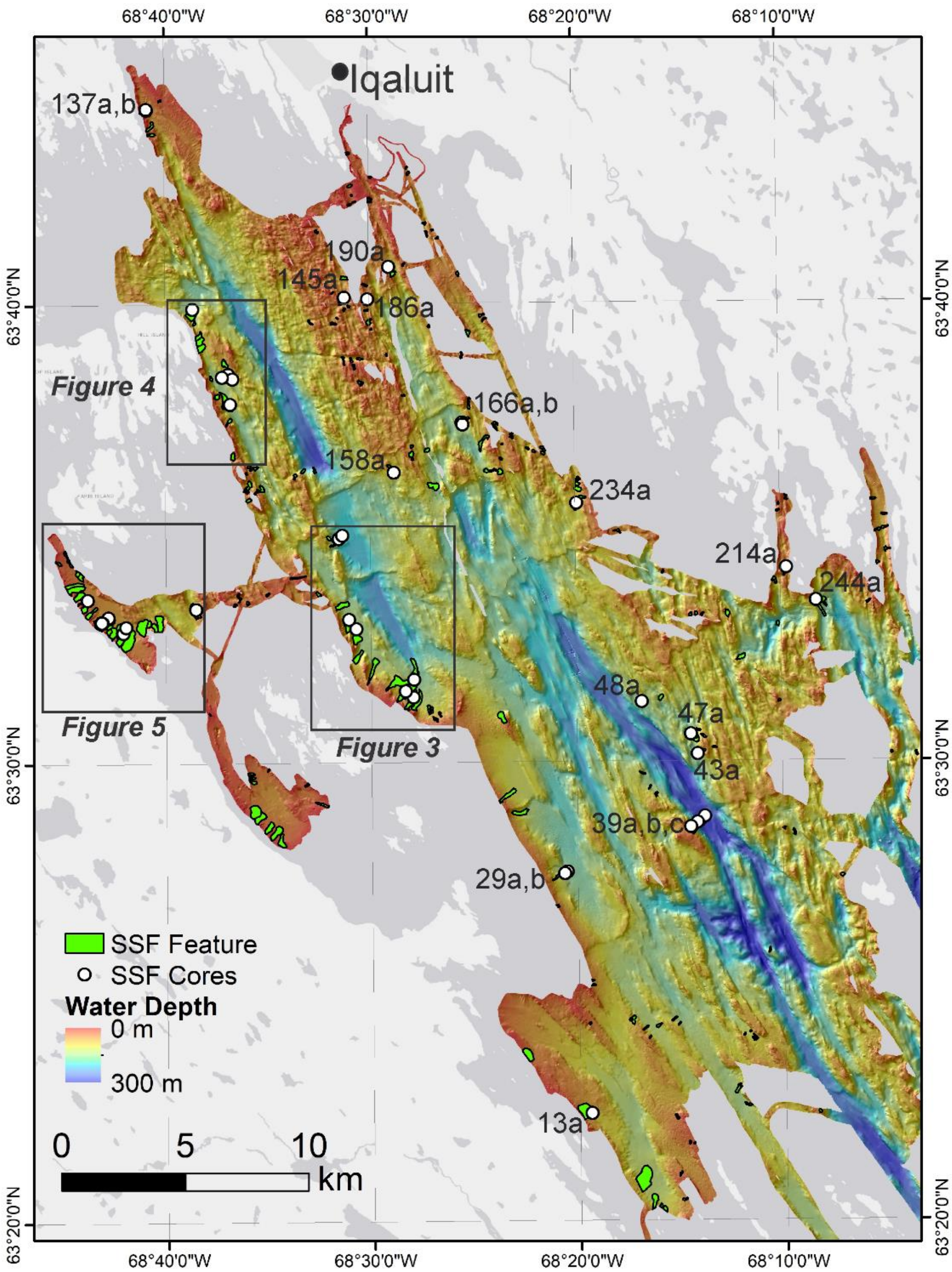

Figure 4.2 MBES bathymetric coverage (2.5 m resolution) in IFB with Iqaluit at top. Edge of grey area (water) is shoreline. Submarine slope failure (SSF) footprints are shown in green. Labelled boxes indicate areas enlarged in Figures 4.3, 4.4, and 4.5, to show areas of high SSF density. White circles with black outlines indicate locations of SSF cores.

a more robust understanding of their triggers and chronology to enable better-informed hazard assessment.

This paper presents a stratigraphic and chronological analysis of SSFs in IFB, providing insight into preconditioning factors and triggers that may account for their high abundance in the bay, as well as details on their frequency of occurrence. It describes a suite of diagnostic features useful for identifying SSFs from acoustic sub-bottom and bathymetric imagery and sediment cores. Coupled with the morphometric and geographic analyses reported in Deering et al. (2018a), this paper illustrates an integrated marine geoscience approach to the study of submarine slope failures in IFB.

The preconditioning factors, triggers, and stratigraphic indicators of large SSFs on continental margins (e.g., Storegga or Grand Banks; Piper and Aksu 1987, Haflidason et al. 2005, Twitchell et al. 2009) or fjords (e.g., Norway, Alaska; Haeussler et al. 2007, Syvitski et al. 1987) have been examined extensively in the literature; however, there is little information regarding smaller SSFs in shallow embayments such as IFB. Furthermore, the literature tends either to focus on individual features (e.g., Storegga) or to develop regional syntheses along entire continental margins (e.g., Leynaud et al. 2009), with some notable exceptions (e.g., Pinet et al. 2015, Brothers et al. 2016). While regional factors (e.g., glacial history of the basin, tectonic activity, etc.) may contribute to the distribution and formation of SSFs over a wide range of environments, their relative importance to the fundamental relationship that governs slope failure (i.e., shear stress vs. shear strength) depends on local factors (Canals et al. 2004). A relatively shallow, partially enclosed embayment is physiographically different from an open continental shelf or a fjord, and preconditioning factors and triggers may be different in the study area. Differences in SSF size should be considered when examining the post-failure stratigraphy and the features therein. Through widespread shallow sub-bottom acoustic (3.5 kHz) surveying and extensive sediment coring in IFB, the acoustic- and litho-stratigraphic signatures of both failed and unfailed sediment have been examined to provide evidence for the nature of failed sediments and the mechanisms and timing of SSFs.

There is no established method in the literature for dating a large population of SSFs, given that most studies focus on individual events (or relatively small groups). While some syntheses look at large populations of features (e.g., Owen et al. 2007 (n=26), Leynaud et al. 2009 (n=37), Urlaub et al. 2013 (n=68)), each individual SSF is typically dated separately, without considering the group as a whole. Individual methodologies tend to focus on the direct dating of features based on dateable materials from sediment cores. In IFB, this approach is impractical, given the 246 SSF features found there. Instead, methodologies using acoustic mapping (MBES and sub-bottom) or well-dated lithostratigraphy may be used to inform the chronology of the population. One objective of this paper is to assess the applicability of these methodologies for establishing ages for the population of SSFs in IFB.

4.2 Background

The SSFs in IFB are set in a basin with irregular bathymetry and a complex postglacial history (Deering et al. 2022). Understanding the physiography of this embayment, its deglacial chronology and stratigraphy, and how these factors affect the physics of slope stability is essential to understanding how and when the SSFs occurred.

4.2.1 Inner Frobisher Bay

IFB is a macrotidal, seasonally ice-covered, partially enclosed embayment that comprises the inner ~55 km of Frobisher Bay (~265 km in total length), separated from outer Frobisher Bay by a series of mid-bay islands and shallow channels. Water depths in IFB are relatively shallow (<350 m maximum depth, <100 m median depth) and the seafloor shows bathymetric complexity (Fig. 4.2; Deering et al. 2018b). Near the northeast and southwest coasts, dozens of small islands separated by narrow and commonly deep channels create small embayments off the main bay. The seafloor of the open basin is characterized by a series of troughs (150-250 m depth) and shallow ridges (<100 m depth) aligned roughly parallel to the main axis of the bay (Fig. 4.2). Near the head of the bay, in Foul Inlet and near Iqaluit, the seafloor largely comprises shallow plateaus. Seafloor morphology is derived largely from the underlying bedrock structure; however, glacial landforms occur at various scales and orientations (e.g., moraines, streamlined glacial features, and hummocky areas) throughout IFB (Todd et al. 2016; Deering et al. 2022).

Until c. 10 ka cal BP[2] the entirety of IFB was covered by grounded continental glacial ice originating from the Foxe-Amadjuak Dome (NW of the bay) of the LIS (Hodgson 2005; Tremblay et al. 2015; Deering et al. 2022). Around that time, the tidewater ice margin retreated northwest of the mid-bay islands, beginning the deglaciation of the inner bay that would last until c. 7.8 ka cal BP (Deering et al. 2022). During this period a series of readvances and stillstands, marked by seafloor moraines, occurred in the basin. At c. 7.0 ka cal BP, continental glacial ice retreated from the IFB drainage basin, marking the beginning of the post-glacial marine environment in the bay.

At its maximum, the marine limit (the highest postglacial relative sea level (RSL)) in the inner bay was ~120 m above current higher high tide (Hodgson 2005). As glacial ice receded, IFB underwent a period of rapid isostatic rebound and RSL fall (~100 m/ka), tapering off swiftly over time. The inner bay is influenced by a semidiurnal macrotidal regime (11.1 m tidal range at spring tide, 12.6

[2] All radiocarbon dates presented in the text have been calibrated as described in the Methods below.

m maximum recorded: CHS 2022) that was first established c. 2.4-2.0 ka cal BP due to changes in basin configuration resulting from RSL fall (Dowdeswell et al. 1985).

IFB is underlain by a typical deglacial stratigraphic sequence for a seasonally ice-covered Canadian Arctic embayment (Syvitski et al. 1987; Deering et al. 2022). Consisting of five lithofacies and four corresponding acoustic facies, the sequence is marked by decreasing glacial influence and increasing sea-ice influence over time. The lowermost lithofacies (LF1), overlying any ice-emplaced sediment such as till, is rapidly deposited, stratified silty-sand, typical of ice-proximal glaciomarine deposition. Above this, two lithofacies (LF2 and LF3) composed of rapidly deposited, sometimes laminated, carbonate-rich clayey-silt, are typical of ice-distal glaciomarine deposition. Nearest the seafloor the uppermost lithofacies (LF4 and LF5) are poorly organized clayey-silt units with an abundance of ice-rafted debris (IRD) and visible bioturbation, typical of post-glacial deposition. The progression between lithofacies is recognized primarily through shifts in physical properties (e.g., magnetic susceptibility and bulk density) and acoustic geometry (e.g., presence of internal reflectors) and marked changes in sedimentation rates (see below). A complete description of these facies can be found in Deering et al. (2022).

Shallow sub-bottom acoustic surveys indicate that there is an uneven distribution of basin sediments within IFB. Typically, sediment cover is thin on ridge tops (<1 m) relative to basins (>10 m) and post-glacial facies comprise the top 5 m or less of the stratigraphic column (Deering et al. 2018b, 2022).

Prior to c. 7.0 ka cal BP (i.e., while glacial ice was present in the basin), glaciomarine sedimentation rates of ~160 cm/ka were calculated from sparse radiocarbon dates, consistent with glaciomarine depositional rates reported in Baffin Island fjords (Andrews et al. 1985; Syvitski et al. 1987; Deering et al. 2018b; Carter 2021). Following c. 7.0 ka cal BP and the retreat of glacial ice from the IFB drainage basin, mean sedimentation rates declined considerably to ~40 cm/ka but ranged from ~10 to 110 cm/ka in various basin settings (Table 4.1; Deering et al. 2022).

4.2.2 Submarine slope failures

Slope instability occurs when the downslope-oriented shear stress in a system exceeds the shear strength of material composing a slope, as governed by the Mohr-Coulomb failure criterion (Equation 1; Hampton et al. 1996; Canals et al. 2004).

$$\tau = c + (\sigma - u) \tan(\phi) \qquad (1)$$

In Equation 1, τ is the shear strength (= shear stress at failure), *c* is the effective cohesion, σ is the total stress acting normal to the failure surface, *u* is the pore water pressure, and ϕ is the angle of internal friction. Internal and external factors can affect the shear strength of sediment on a given slope by changing the values of the variables within Equation 1. Generally, in the SSF literature, conditions that act to decrease the shear strength of a slope are referred to as preconditioning factors. Conditions or events which increase the shear stress acting upon a slope are referred to as triggering mechanisms. However, the distinction between these two categories appears somewhat fluid, as a sufficient decrease in shear strength may act to trigger an SSF and periodic fluctuations in shear stress may decrease overall shear strength in a system. For prehistoric SSFs (i.e., those without a recorded cause), preconditioning factors and triggering mechanisms are commonly unknown; the forces in equilibrium at any given time or place can be difficult to discern from a modern survey. Both preconditioning factors and triggering mechanisms of SSFs in various environments (e.g., continental margins and fjords) have been examined extensively in the literature and are summarized below.

Table 4.1 Cores and dates used in calculating sedimentation rates in IFB. All dates presented are considered robust. One pair of dates (Core Lab Id 2016804-0001PC) is used to calculate rates while all others are calculated assuming 0 cm = 0 cal BP. Core Lab Id is the original processing number of the sediment core. Water depth is the depth in metres where the cores were collected. Seafloor context indicates whether the core was collected from a basin (B), slope (SL), or ridge (R). Lab Id is the original processing number of the radiocarbon sample. Depth downcore indicates the position of the radiocarbon samples in each core. 14C Age (±) is the uncalibrated age of sample. 1-sigma Cal Age Range is the calibrated age range of the sample, rounded to the nearest ten. Midpoint of age range is the middle of the 1-sigma calibrated age range. Sedimentation rate is the rate calculated using the difference in depth and age from nearest sample (or seafloor).

Core Lab Id	Latitude	Longitude	Water Depth (m)	Seafloor Context	Sample Lab Id	Depth downcore (cm)	14C Age (±)	1-sigma Cal Age Range	Midpoint of age range (cal BP)	Sedimentation Rate (cm/ka)
2017805-0006PC	63.362	-68.182	118	B	UOC-6804	55	3830(26)	3640-3460	3550	15.49
2017Nuliajuk-0016GC	63.378	-68.324	70	SL	UOC-6798	16	1104(26)	560-430	495	32.32
2016Nuliajuk-0030GC	63.495	-68.232	153	R	UCIAMS-202069	33	3010(20)	2680-2500	2590	12.74
2016804-0001PC	63.546	-68.475	210	B	UCIAMS-202070	43	990(15)	470-330	400	107.50
2016804-0001PC	63.546	-68.475	210	B	UOC-6797	132	2692(26)	2280-2100	2190	25.70
2017805-0005PC	63.598	-68.524	180	B	UCIAMS-202088	53	3780(20)	3570-3410	3490	15.19
2017Nuliajuk-0017GC	63.608	-68.480	103	R	UCIAMS-202083	37	3955(15)	3810-3640	3725	9.93
2015805-0008PC	63.638	-68.611	125	SL	UCIAMS-169716	326	5640(15)	5880-5720	5800	56.21
2017805-0003PC	63.687	-68.625	146	B	UOC-6801	79	6407(26)	6710-6530	6620	11.93
2017Nuliajuk-0021GC	63.711	-68.516	54	B	UCIAMS-202086	32	935(20)	430-290	360	88.89

4.2.2.1 Preconditioning factors

SSF literature (e.g., Canals et al. 2004, Leynaud et al. 2009, Clare et al. 2016, Urlaub et al. 2018) describes earthquakes (reducing cohesion), tidal changes (varying stress acting normal to slope and pore water pressure), sedimentation (increasing load and affecting all variables), wave loading (stress acting normal to slope), weathering (cohesion, pore pressure), and the presence of gas (cohesion, pore pressure) as preconditioning factors of SSFs. Of these, sedimentation and presence of gas can be considered internal, while the others are external. Sedimentation processes, particularly in relation to high rates of deposition and variations in grain size, are described as key factors in previously glaciated regions (Canals et al. 2004; Clare et al. 2016; Urlaub et al. 2018). Glacial retreat from a basin results in rapid sedimentation and highly variable lithofacies over time, potentially causing oversteepened slopes and the build-up of excess pore pressure, which may render slopes more susceptible to failure when acted upon by an external triggering mechanism.

4.2.2.2 Triggering mechanisms

SSF literature (e.g., Canals et al. 2004, Leynaud et al. 2009, Clare et al. 2016, Urlaub et al. 2018, Bellwald et al. 2019) describes wave loading, earthquakes, tidal changes, diapirism, rapid sedimentation, and erosion as significant triggering mechanisms (stress inducers). In addition to these typically natural processes, human activities on or affecting the seafloor are also a possible trigger for SSFs. Triggering mechanisms will decrease the cohesion of slope sediments, upset the balance between total stress acting normal to the failure plane and pore pressure, or increase the angle of internal friction for the slope. As seen in Equation 1, the total stress acting normal to the failure plane is linearly related to the shear strength of a slope. The implication is that an increase in total stress will result in an increase in shear strength, unless it is counteracted by changes in other variables (e.g., increasing pore pressure).

4.2.3 SSFs in inner Frobisher Bay and Baffin Island fjords

In IFB, 246 SSFs have been identified from MBES records based on diagnostic features found in their surface morphology (Figs. 4.2-4.6; Deering et al. 2018a). Of these 246, two-thirds (163) have had their entire extent mapped, with the remaining one-third (83) only partially mapped (but still identifiable), typically due to their footprint originating in waters too shallow to survey. The SSFs are distributed throughout IFB with notable concentrations along the southwest coast and within smaller, semi-enclosed embayments (Figs. 4.3-4.5). They are commonly associated with bathymetric features (e.g., ridge flanks) with steeper slopes. A statistical analysis of morphometric measurements on these features (Deering et al. 2018a) show them to be typically small (median area = 0.09 km^2; maximum = 2.15 km^2), travelling short distances (median runout length = 247 m; maximum = 1692 m), involving a thin package of sediment (median headwall height = 2 m; maximum = 19.3 m), and initiating at sites currently in shallow water (median initiation depth = 50.5 m; all ≤ 150 m). Overall, these features are smaller than more widely documented SSFs on open continental margins and in partially enclosed channels or basins (e.g., St. Lawrence River, Quebec; Resurrection Bay, Alaska).

In recent years, SSFs have been recognized as a potential seafloor geohazard in Baffin Island fjords from Cumberland Sound to Eclipse Sound (Hughes Clarke et al. 2015; Broom et al. 2017; Normandeau et al. 2021; Bennett et al. 2022; Sedore et al. 2022). A study of 31 Baffin fjords identified SSFs in 77% of those examined (Bennett et al. 2022). These SSFs come in a variety of sizes ranging from larger features near Pond Inlet (up to 13.3 km^2; Broom et al. 2017) to smaller features in IFB (<2.15 km^2) and Pangnirtung Fjord (<2.1 km^2; Sedore et al. 2022). All would be considered small when compared against those on open continental margins. Ages have been established for some SSFs in Baffin fjords (e.g., Sedore et al. 2022) but a regional chronology of

SSFs remains a work in progress. Triggering mechanisms hypothesized for these events in Baffin fjords include seismicity (glacially induced or otherwise), fluvial input, sub-aerial debris flows, wave and tidal loading of shallow sediments, and iceberg grounding. In the case of iceberg grounding, a 2018 SSF event in Southwind Fjord has been linked to a specific iceberg impacting the seafloor (Normandeau et al. 2021).

4.3 Methods

This study was undertaken as part of a larger multidisciplinary seafloor hazard mapping project in IFB, the overall purpose of which was to achieve a more holistic understanding of the seafloor conditions to inform marine spatial planning (Mate et al. 2015; Todd et al. 2016; Deering et al. 2018b). Once the abundance of SSFs became known, some of the research effort was targeted toward their survey and sampling. As such, the data presented in this paper were collected using both targeted and opportunistic approaches.

4.3.1 Acoustic bathymetric profiling and sub-bottom surveying

Multibeam echosounding (MBES) and shallow sub-bottom profiler surveys were accomplished aboard two vessels from 2006 to 2017. Opportunistic survey data were acquired by *CCGS Amundsen* in each of the years 2006–2010 and 2014–2017 using Kongsberg EM 300 (2006–2008) and EM 302 (2009–2017) MBES systems operating at a nominal frequency of 30 kHz and a Knudsen 320R (3.5 kHz) sub-bottom profiler (Hughes Clarke et al. 2015; Mate et al. 2015). From 2012 to 2016 the Government of Nunavut's *RV Nuliajuk* comprehensively mapped IFB in a targeted effort, employing Kongsberg EM 3002 (300 kHz; 2012–2013) and EM 2040C (variable 200–400 kHz; 2014–2016) MBES sounders and a Knudsen CHIRP 3200 two-channel sub-bottom

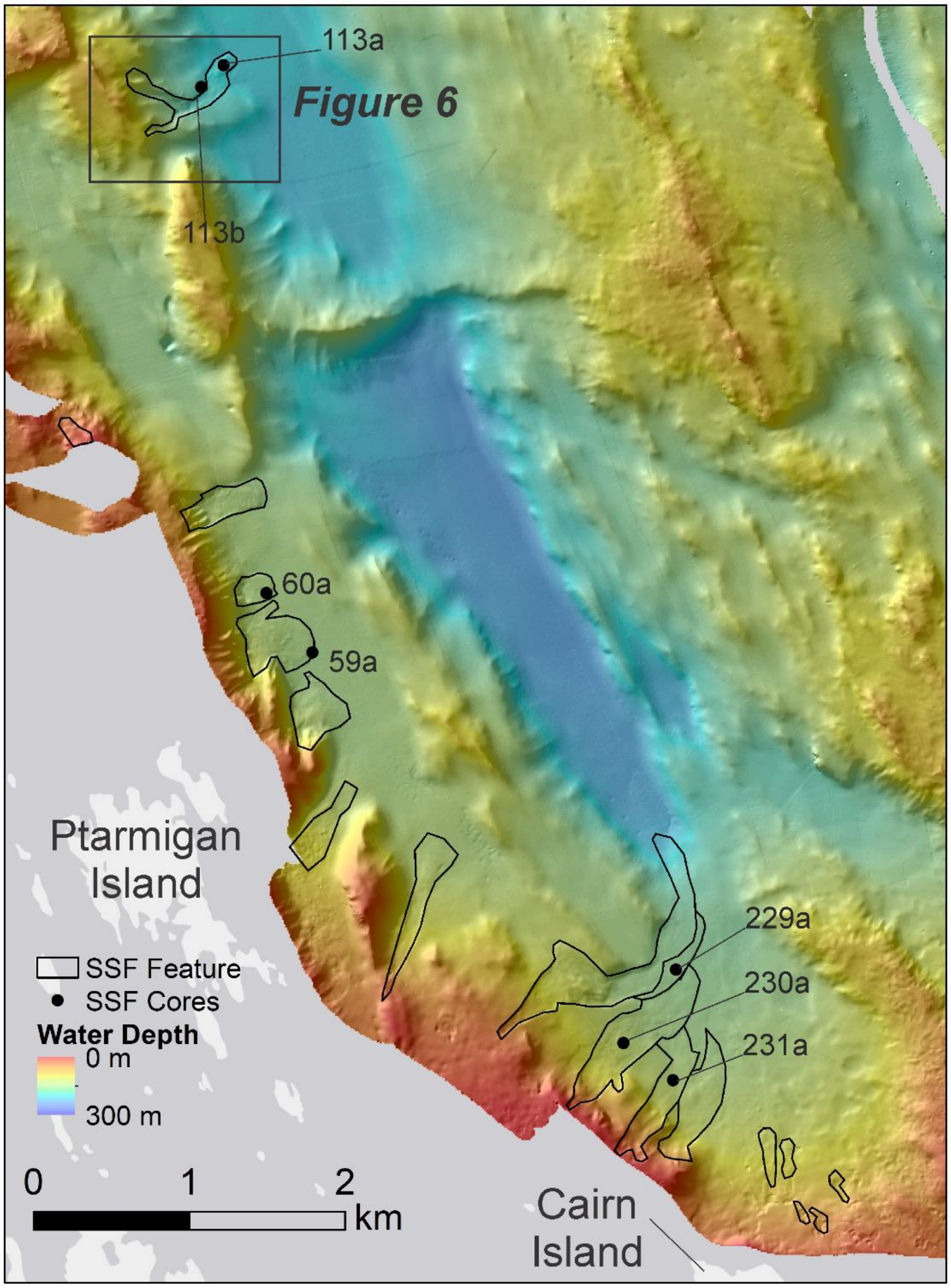

Figure 4.3 MBES bathymetric coverage (2.5 m resolution) of an area of high SSF density near Ptarmigan and Coffin islands on the southwest coast of IFB (Fig. 4.2), showing a range of SSF sizes. Boxed areas indicate SSF further examined in Figure 4.6. Sediment cores collected in SSF footprints are shown as black circles.

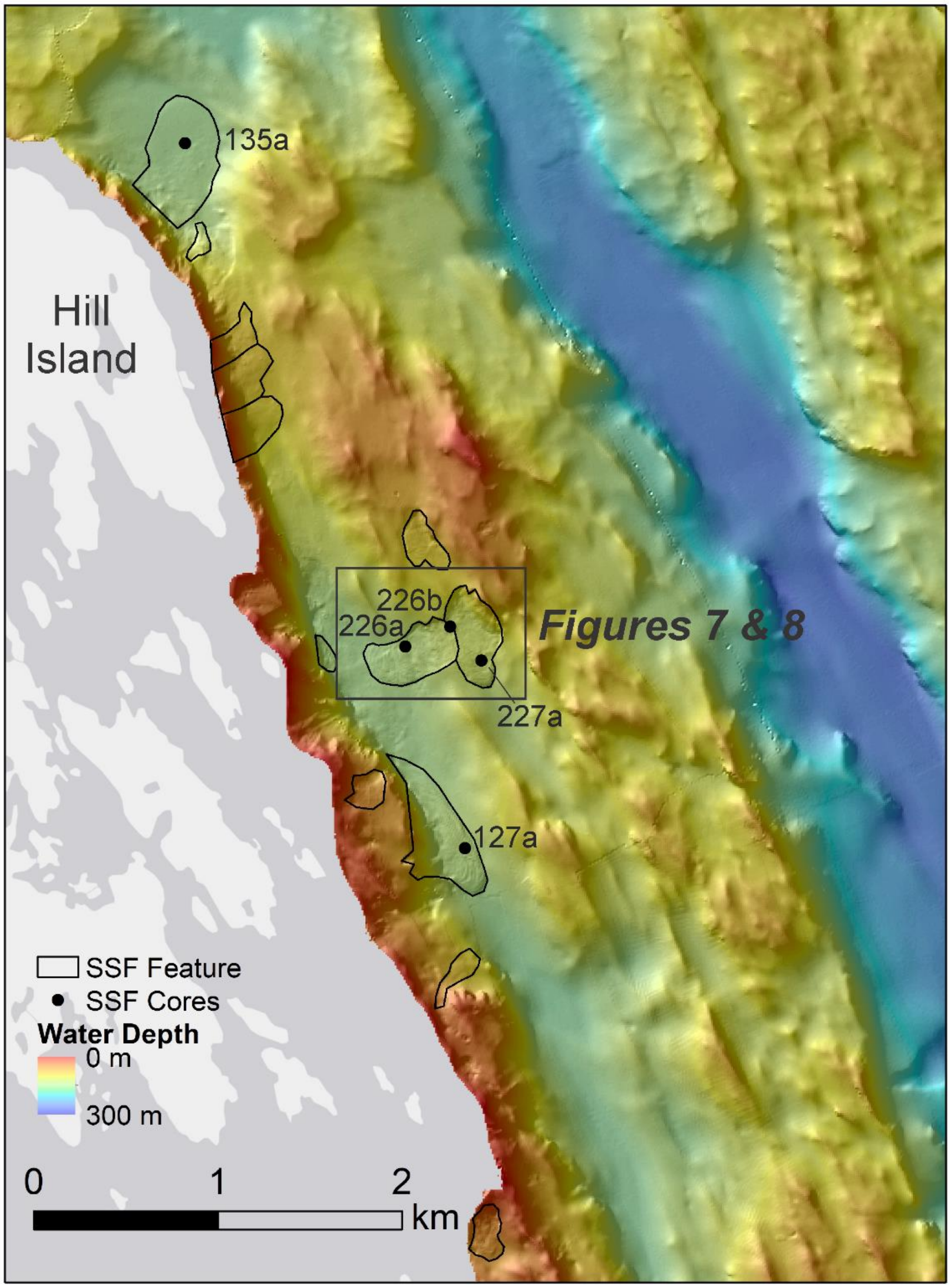

Figure 4.4 MBES bathymetric coverage (2.5 m resolution) of an area of SSFs near Hill Island (Fig. 4.2). Boxed area indicates SSF further examined in Figures 4.7 and 4.8. Sediment cores collected in SSF footprints are shown as black circles.

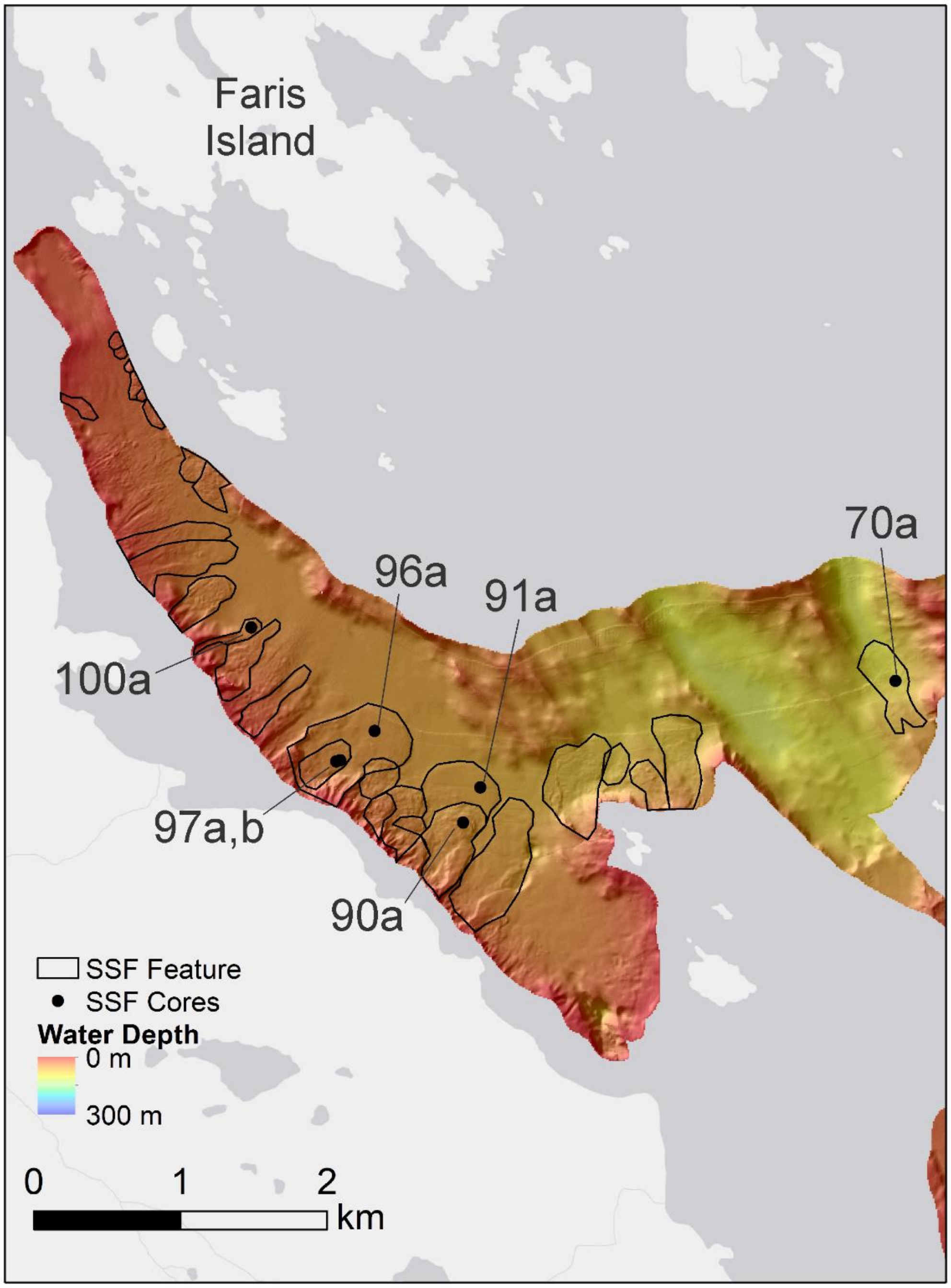

Figure 4.5 MBES bathymetric coverage (2.5 m resolution) of an area of high SSF density and overlap near Faris Island (Fig. 4.2), showing several nested SSF features. Sediment cores collected in SSF footprints are shown as black circles.

profiler. On both vessels acoustic sub-bottom profiles were collected concurrently with MBES data; however, equipment failure at times resulted in only MBES data being collected.

MBES bathymetric data were processed using Qimera software version 1.7 (Quality Positioning Services 2018). Bathymetric raster surfaces of varying resolutions (1 m, 2.5 m, 5 m, 10 m) were generated. Depth values were normalized to chart datum (mean lower low water [MLLW] = 0) and tides corrected using the Arctic9 tidal model (Collins et al. 2011). Sub-bottom acoustic data were analyzed using Natural Resources Canada's SegyJp2 Viewer (Courtney 2009).

Submarine slope failures were identified visually and mapped on the MBES bathymetric raster surfaces using ESRI ArcMap® software versions 10.3 and later (Deering et al. 2018a). Following this, areas of overlap between SSF footprints and acoustic sub-bottom profiles were identified, and a targeted analysis of these areas in the profiles was done in SegyJp2 Viewer, as described below.

4.3.2 Sediment coring

Sediment cores were collected using three coring systems on CCGS *Amundsen* and RV *Nuliajuk*. Piston cores were collected aboard the *Amundsen* every year from 2014 to 2017, using a 9-m-long piston corer equipped with a core-catcher and lined with transparent plastic core liner 10 cm in internal diameter. The piston corer was set off by a trigger weight corer with the same configuration as the gravity corer described below. At all piston coring sites a push core was also collected from a 160 L BX-650 MK-III box corer, using 40-cm-long sections of the same plastic core liner. Gravity cores were collected aboard *Nuliajuk* in 2016 and 2017 using a Geological Survey of Canada (GSC-Atlantic) gravity corer configured to collect cores up to 2.6 m long, equipped with a core-catcher and lined with the same plastic core liner described above. All cores longer than 1.5 m were cut into 1.5 m sections, which were then sealed and transported, refrigerated and upright, to the GSC-Atlantic core laboratory at the Bedford Institute of Oceanography (BIO), where a standardized procedure for analysis, detailed in Campbell et al. (2017), was undertaken. This procedure included split-core photography and measurements of magnetic susceptibility, bulk density, and shear strength along the length of the core. Additionally, X-radiographs of split cores were collected for all cores and subsamples were collected for grain-size analysis and radiocarbon dating. Data from these sources were compiled in downcore plots and used to characterize the sediments found in each core. All sediments and associated subsamples are archived at the GSC-Atlantic Collections Facility at the Bedford Institute of Oceanography.

4.3.3 Radiocarbon dating

All radiocarbon dates used in this paper have been reported previously as part of a larger dataset in IFB (Deering et al. 2022). This paper uses the subset of dates that constrain SSF chronology. Carbonate materials (typically individual or paired bivalves) extracted from sediment cores were analyzed by accelerator mass spectrometry (AMS) to determine radiocarbon age. Full details of radiocarbon sampling and processing can be found in Deering et al. (2022). Ages were calibrated and corrected for marine reservoir effect using Calib 8.2 (Stuiver et al. 2021), the Marine20 calibration curve and $\Delta R = 41 \pm 21$ (Heaton et al. 2020) and reported at the 1σ age range.

The impact of the "Portlandia Effect" (Vickers et al. 2010; England et al. 2013) may be widespread in the radiocarbon dates analyzed for this work (Deering et al. 2022). This causes ages for the shells of deposit feeding molluscs (particularly *Portlandia arctica*) in carbonate-rich substrate to exhibit older ages than suspension feeding molluscs in the same substrate. This limits the way in which affected shells, which provide only a maximum age, can be used to constrain the age of stratigraphic features (England et al. 2013). In the context of SSF chronologies, this means excluding them when calculating sedimentation rates, while noting the maximum age constraint they provide. For the purposes of this paper, dates unaffected by the "Portlandia Effect" are labelled 'robust', while those affected are referred to as 'biased'.

4.3.4 Sedimentation rates

Sedimentation rates in IFB are calculated using only robust dates (i.e., suspension feeders or deposit-feeding species in carbonate-poor substrate). Ideally, two radiocarbon dates from within a single lithofacies unit are used to calculate sedimentation rates. In the case of undisturbed post-glacial units where, in the absence of evidence to suggest otherwise (e.g., sediment compression), core tops may be assumed to represent the modern (0 cal BP) seabed, then a single robust radiocarbon-dated sample in the unit is used to establish a sedimentation rate.

Mean sedimentation rates were previously reported for lithofacies in IFB to contrast their depositional style during deglaciation and postglacial periods (Deering et al. 2022). In the context of this paper, the range of sedimentation rates calculated for IFB is used to establish an SSF chronology as described below. This approach has been used to account for variations in sedimentation rates throughout IFB that are spatially poorly defined. These sedimentation rates were calculated using shells from non-SSF cores. These cores were collected from a variety of seafloor environments (basin, ridges, and slopes) throughout IFB at a range of depths (Table 4.1).

Sedimentation rates calculated from eight individual and one pair of robust radiocarbon dates (Table 4.1) within undisturbed post-glacial units (LF4+LF5) range from ~10 to 110 cm/ka (mean = ~40 cm/ka; Deering et al. (2021)). Two of these rates calculated from shells in LF5 appear anomalously high to be applied basin-wide, potentially skewing the range and mean of sedimentation rates. These higher rates may be linked to localized sediment sources (e.g., a river mouth) or one-time anomalous inputs of sediment (e.g., ice-rafted debris). For the purposes of establishing SSF chronology these two higher rates are excluded, resulting in a more conservative range of 10-56 cm/ka (mean = ~23 cm/ka) and older resultant age estimates. While higher rates are evidently possible in IFB, they do not appear to be characteristic of the basin as a whole.

4.3.5 Developing an SSF chronology

Ages of SSF features were constrained using three approaches: 1) *extrapolated*; 2) *maximum constraint*; and 3) *relative*. The first two approaches utilize radiocarbon dates on organic material sampled from sediment cores from within SSF footprints. Ideally, such cores would contain two or more of the following sediment units, separated by identifiable contacts: undisturbed material underlying the failed SSF material (pre-SSF units); sediment that was transported during the failure (SSF units), and sediment deposited since the failure (post-SSF units). The presence and thicknesses of each of these sediment units depend on local factors, including where in the SSF footprint the core was collected (e.g., no or little SSF sediment should occur in the excavation zone), time since SSF occurrence (e.g., older failures should have thicker post-SSF units), and local sedimentation rates (e.g., higher rates will produce thicker post-SSF units). Given the approaches and uncertainties involved in dating SSF events, it is more prudent to describe the resultant chronologies in terms of constraints rather than absolute age determinations.

The *extrapolated* approach estimates the time necessary to deposit a given thickness of post-SSF sediment using the range of basin sedimentation rates to constrain the age of an SSF feature. The approach can be applied to cores where the lower contact of the post-SSF unit is well-defined and the upper contact is assumed to be the seabed. This approach assumes that sedimentation rates are constant within targeted units.

The *maximum constraint* approach uses radiocarbon dates in SSF or pre-SSF sediments to provide a maximum age on an SSF event. In this approach, biased dates can be used to provide a maximum age because they may appear older than they are; thus, they may constrain SSF ages less tightly than robust dates in a similar core stratigraphy. Proximity of dated samples to unit contacts is not a good indicator of the tightness of their age constraint given potential disturbance during transportation and loss of an unknown amount of sediment in excavation zones.

The *relative* approach uses MBES bathymetry or sub-bottom profiler data and the delineation of overlapping SSF footprints to determine a strictly sequential aging of SSFs, whereby one SSF footprint overriding another is considered to be younger. It provides information on the order in which overlapping features were formed.

4.4 Results

This section starts by summarizing the indicators of SSFs found in acoustic bathymetric and stratigraphic records. It then describes the stratigraphic context of failed sediments using sediment cores from the basin. Finally, it outlines the pertinent radiocarbon dates collected from within SSF footprints and illustrates how they are used to constrain SSF age. In IFB, 39 sediment cores (4 piston, 35 gravity) were collected from inside 31 SSF footprints (Table 4.2; Fig. 4.2). Of these 39 cores, 14 have radiocarbon age control (4 piston, 10 gravity; Table 4.3).

4.4.1 Morphological indicators of SSFs in MBES

Common diagnostic indicators for the 246 SSFs in MBES surveys in IFB include headwalls (n=113, 46%), excavation (i.e., negative surface expression; n=161, 65%), sidewalls (n=113, 46%), depositional lobes (n=246, 100%), and compression ridges (n=32, 13%; e.g., SSFs 226 and 227). These features are described in full in Deering et al. (2018a). SSF 113 illustrates the first four of these diagnostic features and is characteristic of many SSFs in IFB (Fig. 4.6). In that event a mass of sediment detached from a headwall and moved downslope, excavating a channel with steep sidewalls, before forming a depositional lobe as slope decreased (Fig. 4.6). After the initial (northern headwall) event, a second smaller SSF event occurred, creating a second headwall and erosional zone, but with deposition limited to the previously established depositional zone.

SSFs do not exhibit all diagnostic indicators for reasons including differences in style of failure, amount of sediment transported, and incomplete mapping (especially headwall mapping in shallow waters; Deering et al. 2018a). Therefore, the frequency of these features is not truly reflected in the counts for all mapped SSFs. In some cases, these indicators can also be seen in the sub-bottom acoustic data, but are typically more readily recognizable in MBES.

4.4.2 SSF indicators seen in sub-bottom acoustics

Three recurring acoustic stratigraphic features diagnostic of SSFs are identified in sub-bottom profiles (Fig. 4.8): a) *chaotic surfaces and internal reflectors*; b) *masking of acoustic stratigraphy*, and c) *truncation of acoustic reflectors*. Given the incomplete coverage of acoustic sub-bottom data, it is difficult to evaluate how typical these characteristics are of SSFs in the study area.

Chaotic surfaces and internal reflectors are visible in both the erosional and depositional zones of SSFs. Chaotic surfaces are characterized by rough, irregular seabed reflectors in an area of otherwise smooth seafloor (Fig. 4.8). Chaotic internal reflectors appear primarily in the depositional zone of SSFs, where the transportation and disturbance of sediment reorganized the typical acoustic stratigraphy seen in adjacent undisturbed sediments (See '*a*', Fig. 4.8).

Masking of acoustic stratigraphy is detectable in depositional SSF zones where transported sediment has been emplaced on top of largely undisturbed seafloor. In such cases, the transported

Table 4.2 Sediment cores collected from within SSF footprints in IFB. SSF ID is a unique identifier applied to each SSF feature. Core ID is an identifier applied to each sediment core collected within an SSF footprint. Cores are identified alphanumerically indicating number of cores in each footprint. Type indicates whether it is a gravity (G) or piston (P) core. Length is the total length of the core. # of dates indicates the total number of radiocarbon dates collected from each core (both robust and biased). Basal LF indicates the lithofacies found furthest down in the core. Post-SSF thickness indicates the amount of sediment overlying the upper SSF contact. Core Lab Id is the original processing number of the sediment core. Extrapolated minimum, maximum, and range indicates the range of time to deposit the post-SSF sediment thickness given the variable sedimentation rates in IFB.

SSF ID	Core ID	Type	Length (cm)	# of Dates	Basal LF	Post-SSF Thickness (cm)	Core Lab ID	Latitude	Longitude	Extrapolated Maximum (10 cm/ka)	Extrapolated Minimum (56 cm/ka)	Extrapolated range (ka)
13	13a	G	74	1	4	74	2017Nuliajuk-0015	63.373	-68.324	7.4	1.3	1.3-7.4
29	29a	G	10	0	2	10	2016Nuliajuk-0031	63.460	-68.344	1.0	0.2	0.2-1
	29b	G	30.5	0	4	30.5	2016Nuliajuk-0032	63.460	-68.342	3.1	0.5	0.5-3.1
39	39a	G	90	0	4	90	2017Nuliajuk-0008	63.476	-68.241	9.0	1.6	1.6-9.0
	39b	G	156.5	2	2	15	2017Nuliajuk-0009	63.478	-68.236	1.5	0.3	0.3-1.5
	39c	G	54	0	4	54	2017Nuliajuk-0011	63.480	-68.230	5.4	1.0	1.0-5.4
43	43a	G	122	3	2	4	2016Nuliajuk-0029	63.503	-68.235	0.4	0.1	0.1-0.4
47	47a	G	49	1	4	49	2016Nuliajuk-0028	63.510	-68.241	4.9	0.9	0.9-4.9
48	48a	G	66	1	2	9	2016Nuliajuk-0027	63.522	-68.280	0.9	0.2	0.2-0.9
59	59a	G	10	0	4	10	2016Nuliajuk-0017	63.549	-68.512	1.0	0.2	0.2-1.0
60	60a	G	33.5	0	4	33.5	2016Nuliajuk-0015	63.552	-68.518	3.4	0.6	0.6-3.4
70	70a	G	61.5	0	4	61.5	2016Nuliajuk-0008	63.556	-68.642	6.2	1.1	1.1-6.2
90	90a	G	54	0	4	54	2016Nuliajuk-0011	63.548	-68.701	5.4	1.0	1.0-5.4
91	91a	G	47	0	4	47	2016Nuliajuk-0010	63.550	-68.699	4.7	0.8	0.8-4.7
96	96a	G	39	0	4	39	2016Nuliajuk-0014	63.553	-68.714	3.9	0.7	0.7-3.9
97	97a	G	5	0	4	5	2016Nuliajuk-0012	63.551	-68.719	0.5	0.1	0.1-0.5
	97b	G	26	0	4	26	2016Nuliajuk-0013	63.552	-68.718	2.6	0.5	0.5-2.6
100	100a	G	88	0	4	88	2017Nuliajuk-0007	63.560	-68.730	8.8	1.6	1.6-8.8
113	113a	P	491	8	2	40	2016804-0007	63.583	-68.523	4.0	0.7	0.7-4.0
	113b	G	188	2	4	*	2016Nuliajuk-0021	63.582	-68.526	*	*	*
127	127a	G	74	0	4	74	2016Nuliajuk-0007	63.631	-68.614	7.4	1.3	1.3-7.4
135	135a	G	15	0	4	15	2016Nuliajuk-0006	63.665	-68.644	1.5	0.3	0.3-1.5
137	137a	G	5	0	4	5	2016Nuliajuk-0004	63.738	-68.681	0.5	0.1	0.1-0.5
	137b	G	18	0	4	18	2016Nuliajuk-0005	63.738	-68.681	1.8	0.3	0.3-1.8
145	145a	G	73	1	3	10	2016Nuliajuk-0003	63.669	-68.520	1.0	0.2	0.2-1
158	158a	G	15	0	4	15	2016Nuliajuk-0020	63.606	-68.481	1.5	0.3	0.3-1.5
166	166a	G	12	0	4	12	2016Nuliajuk-0018	63.623	-68.424	1.2	0.2	0.2-1.2
	166b	G	22	0	4	22	2016Nuliajuk-0019	63.624	-68.425	2.2	0.4	0.4-2.2
186	186a	G	34	0	2	10	2016Nuliajuk-0002	63.669	-68.501	1.0	0.2	0.2-1.0
190	190a	G	72.5	0	4	72.5	2016Nuliajuk-0001	63.680	-68.484	7.3	1.3	1.3-7.3
214	214a	G	75	1	4	75	2016Nuliajuk-0025	63.570	-68.162	7.5	1.3	1.3-7.5
226	226a	P	564	4	2	210	2014805-0004	63.640	-68.620	21.0	3.8	3.8-21.0
	226b	P	526	4	2	*	2016804-0010	63.641	-68.615	*	*	*
227	227a	P	581	7	2	100	2015805-0009	63.640	-68.612	10.0	1.8	1.8-10.0
229	229a	G	10	0	4	10	2017Nuliajuk-0001	63.530	-68.465	1.0	0.2	0.2-1.0
230	230a	G	50.5	0	3	42	2016Nuliajuk-0022	63.526	-68.472	4.2	0.8	0.8-4.2
231	231a	G	40	0	4	40	2016Nuliajuk-0023	63.524	-68.466	4.0	0.7	0.7-4.0
234	234a	G	72	1	4	43	2016Nuliajuk-0024	63.594	-68.332	4.3	0.8	0.8-4.3
244	244a	G	94	2	2	21	2016Nuliajuk-0026	63.558	-68.138	2.1	0.4	0.4-2.1

Table 4.3 Cores from within SSF footprints which contain radiocarbon dates. Core Id is an identifier applied to each sediment core collected within an SSF footprint. Cores are identified alphanumerically indicating number of cores in each footprint. Sample Lab Id is the original processing number of the radiocarbon sample. Depth downcore indicates the position of the radiocarbon samples in each core. LF indicates the lithofacies from which the sample was collected. Acid reactivity is a proxy for carbonate content of the sediment where the radiocarbon sample was collected (0-4, no reaction (no carbonate) to vigorous reaction (much carbonate)). 14C Age (±) is the uncalibrated age of sample. 1-sigma Cal Age Range is the calibrated age range of the sample, rounded to the nearest ten. Genus and species are listed where known. Portlandia Effect indicates where samples are known to be impacted (Y), unaffected (N), or unknown (U).

Core Id	Sample Lab Id	Depth downcore (cm)	LF	Acid Reactivity	^{14}C Age (±)	1-sigma Cal Age Range	Species	Portlandia Effect
13a	UCIAMS-202080	26	5	0	900(20)	410-260	Unknown fragment	N
39b	UCIAMS-202078	21	5	0	1590(15)	1020-860	Unknown fragment	N
	UCIAMS-202079	59	3	2	8075(20)	8400-8260	Unknown fragment	U
43a	UCIAMS-187017	23	5	0	1065(15)	530-410	*Hiatella arctica*	N
	UCIAMS-187018	66	2	3	7765(20)	8080-7920	*Yoldia hyperborea*	Y
	UCIAMS-187019	119	2	3	8255(20)	8590-8430	*Portlandia arctica*	Y
47a	UCIAMS-187016	44	4	0	3470(15)	3210-3040	*Macoma calcarea*	N
48a	UCIAMS-202068	59	3	3	7615(20)	7930-7780	*Yoldia Hyperborea*	Y
244a	UOC-6796	48	2	3	8699(30)	9210-9020	*Yoldia hyperborea*	Y
	UCIAMS-187015	85	2	3	8920(20)	9460-9320	*Macoma calcarea*	N
214a	UOC-6795	73	4	1	4301(26)	4270-4080	*Mya truncata*	N
113b	UCIAMS-187012	121	4	1	5020(15)	5220-5010	*Macoma sp.*	N
	UCIAMS-187013	177	4	2	5560(20)	5770-5600	*Yoldia sp.*	Y
113a	UCIAMS-202071	93	4	1	4890(20)	5010-4830	*Nuculana sp.*	Y
	UCIAMS-187027	153	4	1	5420(15)	5620-5470	*Portlandia arctica*	Y
	UCIAMS-187028	186	4	1	5485(20)	5710-5550	*Yoldia hyperborea*	Y
	UCIAMS-187029	273	4	1	4080(15)	3970-3800	Fish skull fragment	N
	UCIAMS-202072	303	4	1	4855(20)	4970-4810	Unknown fragment	U
	UCIAMS-187030	331	4	2	5180(15)	5410-5230	*Macoma calcarea*	N
	UCIAMS-202073	400	4	2	5365(20)	5580-5430	*Yoldia hyperborea*	Y
	UCIAMS-187031	452	4	3	5920(15)	6180-6010	*Yoldia hyperborea*	Y
234a	UCIAMS-187014	63	5	1	1150(15)	600-480	*Nuculana pernula*	Y
226b	UCIAMS-187040	26	5	0	725(15)	230-60	*Nuculana pernula*	N
	UCIAMS-202077	249	4	2	6300(20)	6580-6410	*Nuculana pernula*	Y
	UCIAMS-187041	330	3	3	6730(15)	7080-6900	*Portlandia arctica*	Y
	UCIAMS-187042	482	2	3	6925(15)	7290-7140	*Portlandia arctica*	Y
226a	UCIAMS-155830	292	4	0	5445(25)	5660-5490	*Portlandia arctica*	N
	UCIAMS-155831	331	3	0	6565(20)	6890-6710	*Portlandia arctica*	N
	UCIAMS-155832	400	3	1	6945(25)	7300-7150	*Musculus sp.*	N
	UCIAMS-155833	511	2	1	7245(25)	7560-7430	*Portlandia arctica*	Y
227a	UCIAMS-169720	264	4	1	3160(15)	2820-2690	Unknown	U
	UCIAMS-202066	281	4	1	3520(20)	3280-3100	Unknown fragment	U
	UCIAMS-169721	361	4	1	5720(15)	5950-5780	*Nuculana sp.*	Y
	UCIAMS-169722	402	4	1	6265(20)	6550-6380	*Nuculana pernula*	Y
	UCIAMS-169723	489	3	2	6570(20)	6890-6720	*Portlandia arctica*	Y
	UCIAMS-169724	526	3	2	6735(20)	7090-6900	*Portlandia arctica*	Y
	UCIAMS-169725	571	2	3	6925(20)	7290-7130	*Ennucula tenius*	Y
145a	UCIAMS-202067	59	4	1	4785(20)	4880-4700	*Nuculana Pernula*	Y

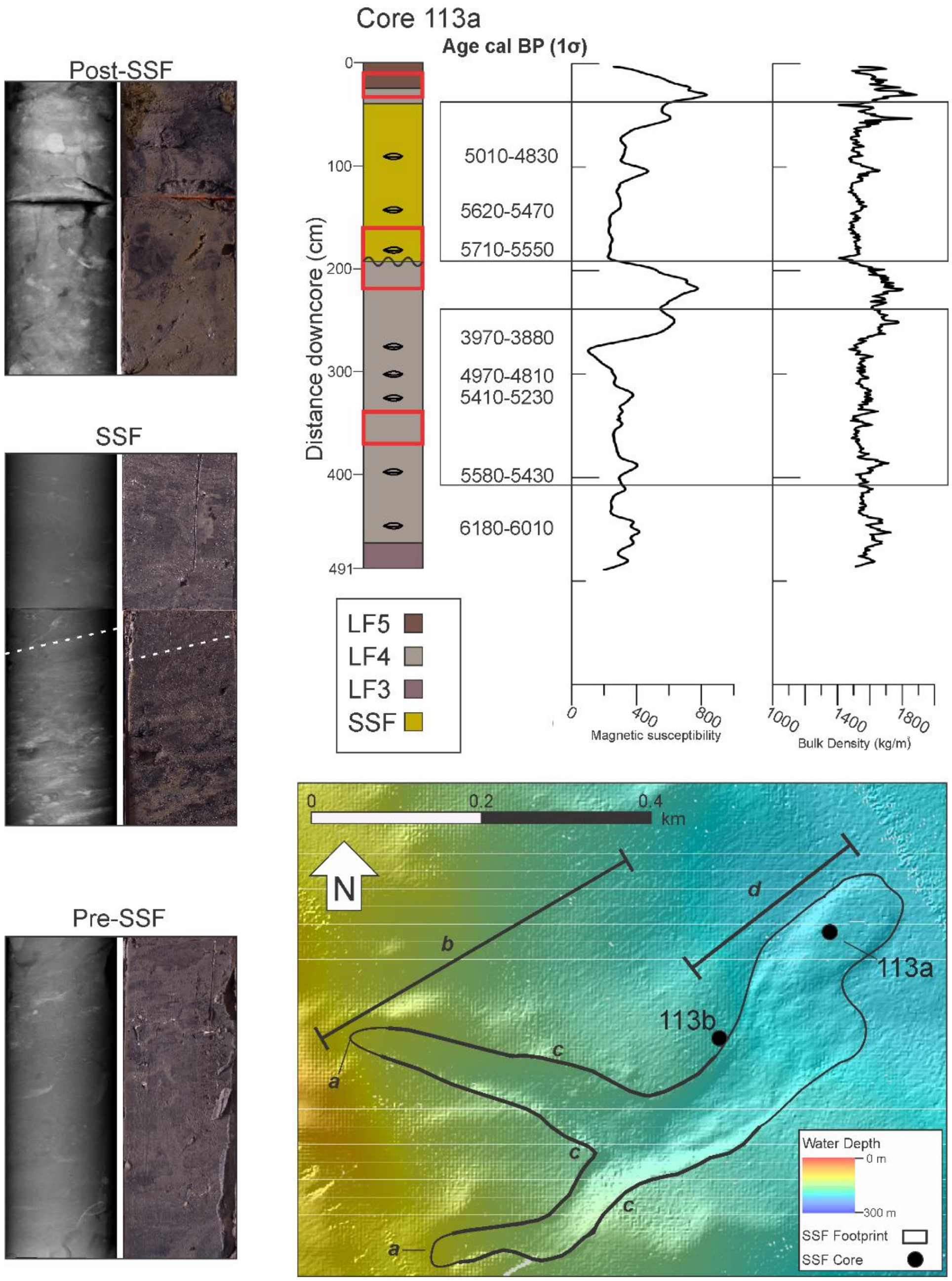

Figure 4.6 Composite diagram for SSF 113 and core 113a (Fig. 4.3). MBES bathymetric image (1 m resolution) at bottom right shows location and core numbers of SSF sediment cores collected from inside footprint. Lowercase letters show morphological indicators of SSFs including headwalls (a), the excavation zone (b), steep side walls (c; thicker outline), and the depositional zone (d). Sediment core diagram at top right includes lithofacies as described in text, calibrated 1-sigma radiocarbon date ranges of shells from within the core, magnetic susceptibility, and bulk density. Black boxes show areas where there is approximate repetition of radiocarbon date sequences. Wavy line indicates unconformity. Images at left show pre- and post-SSF sediment and the contact between them, with positions in the core indicated by red boxes on the lithofacies log.

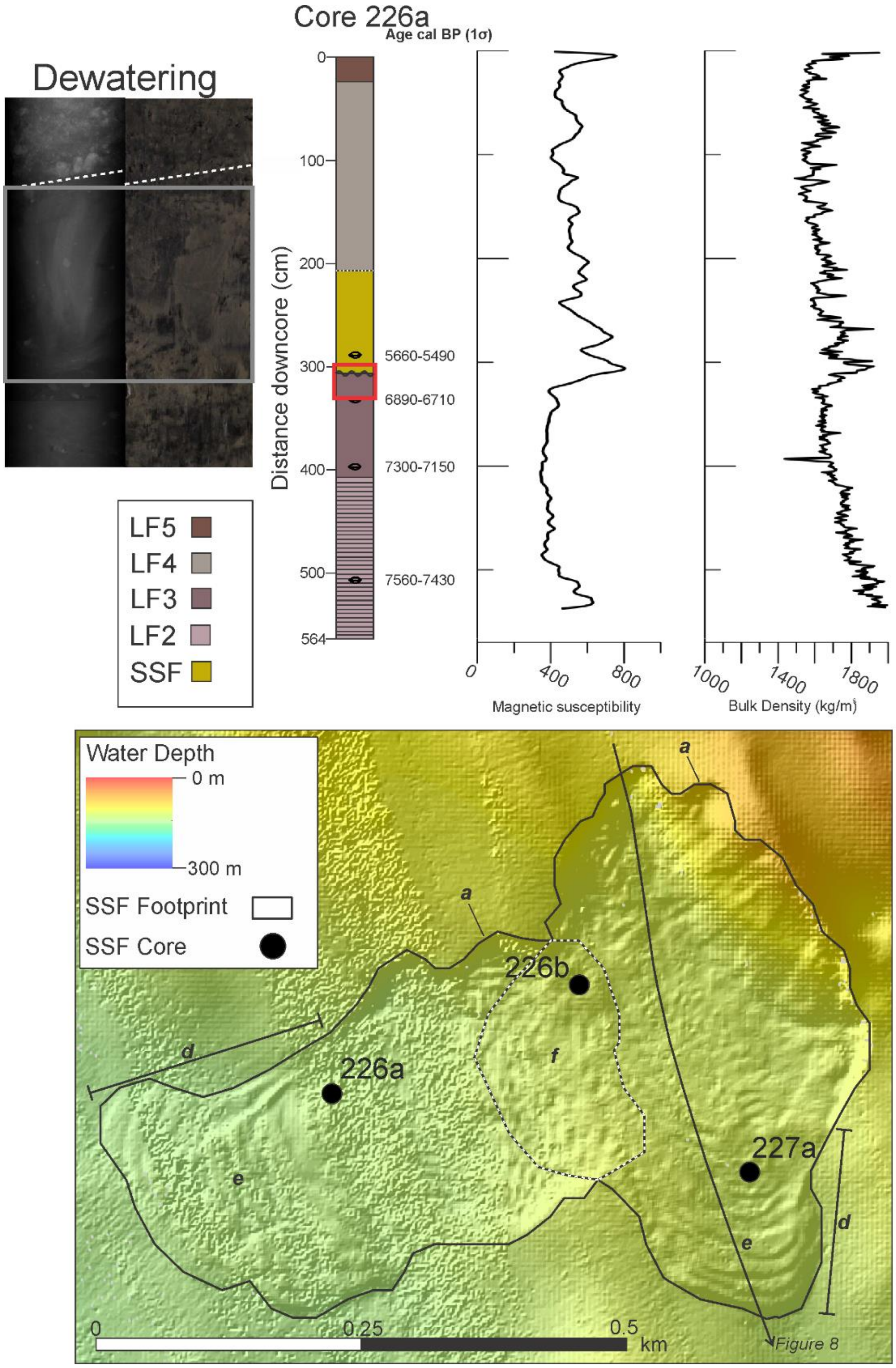

Figure 4.7 Composite diagram for SSFs 226 and 227 and core 226a located off Hill Island (Fig. 4.4). MBES bathymetric image (1 m resolution) at bottom right shows locations and core numbers of SSF sediment cores collected from inside footprints. Line indicates location of sub-bottom acoustic surveying shown in Figure 4.8. Dashed line indicates area of overlap between SSFs 226 and 227. Lowercase letters show morphological indicators of SSFs including headwalls (a), depositional zones (d), and compression ridges (e). Sediment core diagram at top right includes

lithofacies as described in text, calibrated 1-sigma radiocarbon date ranges of shells from within the core, magnetic susceptibility, and bulk density measurements. Note the abrupt change in magnetic susceptibility and bulk density around the erosional contact. Wavy line indicates unconformity. Image at left shows the contact between pre-SSF and SSF sediment with dewatering marks (location in core marked by red box on lithofacies log).

sediment intercepts and reflects acoustic energy, obscuring underlying undisturbed acoustic stratigraphy that can be seen outside of the SSF footprint (See '*b*', Fig. 4.8).

Truncation of acoustic reflectors is visible where sub-bottom survey lines intersect steep head and sidewalls of SSFs. This is characterized by the abrupt ending of a reflector seen in undisturbed acoustic stratigraphy at the scarp along the edge of an SSF.

4.4.3 SSF indicators observed in sediment cores

Evidence of SSFs in sediment cores is recognized by some or all of the following: a) *modifications of the stratigraphic sequence*; b) *modification of physical properties of sediments*; and c) *modification of chronological sequence*. Cores collected from different areas within a single SSF footprint may have different indicators, based on whether sediment was lost or gained at a particular location.

As background, all SSF cores collected from IFB have post-SSF sediments that are post-glacial (Deering et al. 2022). Correspondingly, acoustic sub-bottom records from SSF footprints show that post-SSF sediments are typically thin (≤2 m thick). Compared to underlying glaciomarine sediments, post-glacial lithofacies have lower clay content (20-29%) and more variable magnetic susceptibility (500-1500 SI), shear strength (5-23 kPa), and bulk density (1300-2100 kg/m^3). Post-glacial units have extensive deposits of IRD. In contrast, the ice-distal, glaciomarine lithofacies LF3 in IFB is characterized by its high proportion of clay (35-49%), low magnetic susceptibility

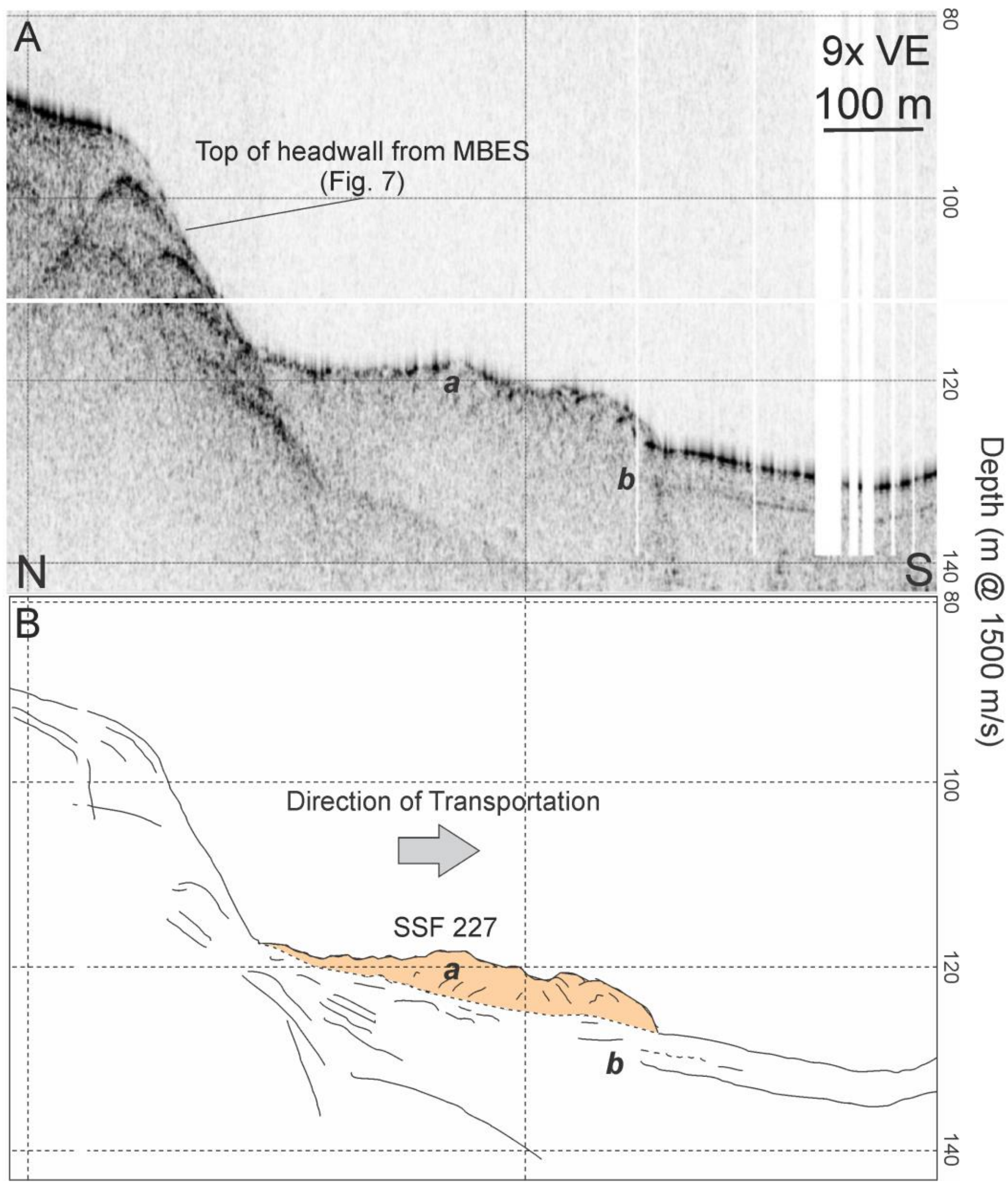

Figure 4.8 Acoustic sub-bottom imagery and interpretation for a Hill Island SSF (Figs. 4.4 and 4.7). Arrow indicates direction of sediment transportation. A) Sub-bottom imagery showing acoustic indicators of SSFs: chaotic internal reflectors (a) and truncation/masking of reflectors by deposited sediment (b). B) Schematic diagram of reflectors from sub-bottom image. Lines represent visible reflectors. Orange area shows transported sediment.

(500 SI), a narrow range of shear strength (6-10 kPa), and consistent bulk density (1700 kg/m^3). Deposition of post-glacial lithofacies has been constrained to <7 ka cal BP (Deering et al. 2022).

Modification of stratigraphic sequence by addition or loss of sediment alters the typical glaciomarine-deglacial sequence (LF1-LF5) seen in a core from an adjacent undisturbed location. This modification is ubiquitous in SSF cores from IFB. For example, in the case of three cores from erosional zones of SSFs (Cores 43a, 186a, 244a; SSF 43, 186, 244, respectively; Table 4.2), this modification manifests as an abrupt erosional contact between two lithofacies that typically are not found adjacent to each other in the stratigraphic sequence (e.g., LF5 overlaying LF3).

In cores that sample SSFs there is a wide spectrum of disturbance observed in the SSF material, from rare, relatively intact stratified sediment (see below, Core 113a, SSF 113, Fig. 4.6) to common, highly deformed, structureless units (e.g., Core 226a, Fig. 4.7). In areas where SSFs overlap, multiple disturbances (both depositional and erosional) may be detected in a single core (e.g., 226b; Fig. 4.7).

Modification of seafloor sediment physical properties can occur with the addition of transported sediment on top of otherwise undisturbed seafloor. The added sediment weight can cause the dewatering of sediment (i.e., the compaction of sediment caused by the squeezing out of interstitial water (Locat and Lee 2002)). This dewatering is recognized in x-radiographs of one SSF core (Core 226a, Fig. 4.7) based on both soft sediment deformation features and modification of physical properties (increased magnetic susceptibility and bulk density) below the erosional contact.

Modification of chronological sequence occurs in two ways: deviation from chronological order (i.e., sequence inversion/insertion); and changes in spacing (sequence lengthening or shortening).

Of the 14 radiocarbon-dated cores in IFB, only core 113a shows an inversion of dates (SSF 113, Fig. 4.6, described above). At a glance, this core appears to follow a similar stratigraphic sequence as a typical non-SSF core in IFB. It bottoms out (491 cm downcore) in glaciomarine ice-distal (LF3) sediment that transitions to post-glacial (LF4) at ~460 cm downcore and then to recent post-glacial (LF5) at ~30 cm downcore. However, a radiocarbon date inversion indicates the presence of SSF sediment deposition in this core and physical property data show the extent of the SSF unit. This core contains 8 radiocarbon dated samples, all in LF4 (Table 4.3). Of these 8, there are two sequences of three samples with similar spacing showing ages spanning 5.6-4.8 ka cal BP at 303-400 and 93-186 cm downcore. The upper sequence is interpreted to be a displaced coherent block of LF4 that was originally deposited upslope of the core site synchronously with the lower sequence, then transported by the SSF. At 273 cm downcore a radiocarbon date (3970-3800 cal BP, UCIAMS-187029; Table 4.3) in sequence with the underlying dates constrains this event further.

This interpretation of events is corroborated by changes in the magnetic susceptibility and bulk density measurements in the core. Starting from the bottom, this change is first apparent at ~270 cm downcore. Magnetic susceptibility (400 to 800 SI units) and bulk density (1600 to 1800 kg/m^3) both show increases, which persist up to ~200 cm downcore, where they resume their lower values. These prevail until ~60 cm downcore where physical properties show increased ranges to the top of the core. The two units of post-glacial (LF4) sediment that share an age range and lower physical property values, have differing physical properties than the intervening 70-cm-thick unit, also interpreted to be postglacial in origin (LF4). This is interpreted to mean that the upper ~1.4 m thick unit is SSF sediment.

The addition or loss of sediment from a stratigraphic sequence can be less readily recognizable as an SSF indicator in the chronology depending both on the spacing of radiocarbon dates collected within a core and local variability in sedimentation rates. This lengthening or shortening of stratigraphic sequence can be accompanied by a distinct contact between stratigraphic units, but this is not always the case. For example, in four cores (39b, 43a, 48a, 244a; Fig. 4.9, Table 4.3) collected from SSF erosional zones, anomalously old shells (> 7.5 ka cal BP; UCIAMS-202079, UOC-6796, UCIAMS-202068, UCIAMS-187018; Table 4.3) were collected from glaciomarine units (LF2 and LF3) close to (<30 cm core depth) the seafloor, indicating marked shortening of the expected stratigraphic sequence. In these cases, an erosional contact was marked by a clear change in colour and physical properties between the interpreted glaciomarine (LF3) and post-glacial (LF4) units. For most of the other 14 radiocarbon-dated cores from IFB, the change in dating sequence is typically more subtle with less constrained dating control, but all appear to involve sediment of the same facies being added to or removed from the sequence.

4.4.4 Established ages for SSFs in inner Frobisher Bay

Twelve cores from different SSF footprints had an SSF unit overlain by post-SSF sediments, varying in thickness from 4 to 210 cm (Table 4.2). The application of maximum age constraints (i.e., radiocarbon dates from within SSF or pre-SSF sediments) and sedimentation rates (10-56 cm/ka) to the post-SSF sediments indicated that seven SSFs had interpreted age ranges entirely since 1 ka cal BP (SSFs 29, 39, 43, 48, 145, 186 and 234; Table 4.4). The remaining five (SSFs 113, 186, 226, 227, 230, and 244) had minimum and maximum interpreted ages ranging from 0.4 to 3.8 ka cal BP and 2.1 to 5.7 ka cal BP, respectively (Table 4.4). These age ranges are based on a combination of maximum constraint and extrapolation approaches to provide a plausible age range. For example, in core 39b (Table 4.4) the extrapolated age range is 0.3-1.5 ka cal BP but the maximum constraint age is <1.0 ka cal BP, resulting in an interpreted age range of 0.3-1.0 ka cal BP. Conversely, in core 48a the maximum constraint age is <8.0 ka cal BP and the extrapolated age range is 0.2-0.9 ka cal BP, resulting in an interpreted age range of 0.2-0.9 ka cal BP.

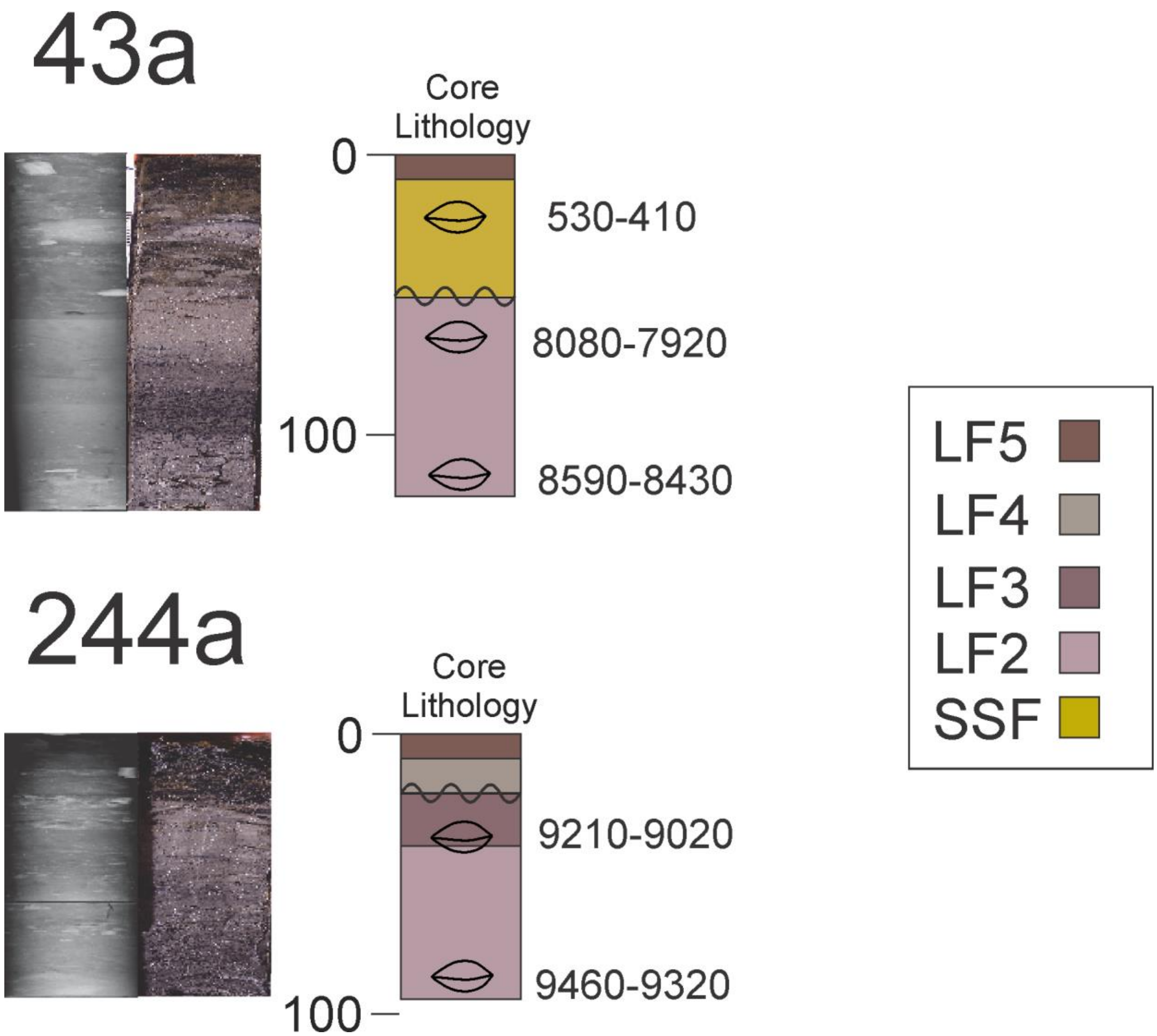

Figure 4.9 Photography, x-radiography, and lithofacies logs for cores 43a and 244a, collected from the erosional zones of two SSFs. Wavy lines indicate unconformity. Core diagram includes calibrated 1-sigma radiocarbon date ranges from shells within the core.

Table 4.4 Interpreted ages for twelve SSFs in IFB. SSF ID is a unique identifier applied to each SSF feature. Core ID is an identifier applied to each sediment core collected within an SSF footprint. Cores are identified alphanumerically indicating number of cores in each footprint. Post-SSF thickness indicates the amount of sediment overlying the upper SSF contact. Maximum constraint age for each SSF based on radiocarbon dates within the cores. Extrapolated minimum, maximum, and range indicates the range of time to deposit the post-SSF sediment thickness given the variable sedimentation rates in IFB. Interpreted age is the age of the SSF based on a combination of extrapolation and maximum constraint methods.

SSF ID	Core ID	Post-SSF Thickness (cm)	Maximum constraint age (ka cal BP)	Extrapolated age (ka cal BP; sed rate = 10 cm/ka)	Extrapolated age (ka cal BP; sed rate = 56 cm/ka)	Extrapolated age range (ka cal BP)	Interpreted age (ka)
29	29a	10	*	1.0	0.2	0.2-1.0	0.2-1.0
39	39b	15	<1.0	1.5	0.3	0.3-1.5	0.3-1.0
43	43a	4	<0.6	0.4	0.1	0.1-0.4	0.1-0.4
48	48a	9	<8.0	0.9	0.2	0.2-0.9	0.2-0.9
113	113a	40	<5.0	4.0	0.7	0.7-4.0	0.7-4.0
145	145a	10	<4.9	1.0	0.2	0.2-1.0	0.2-1.0
186	186a	10	*	1.0	0.2	0.2-1.0	0.2-1.0
226	226a	210	<5.7	21.0	3.8	3.8-21.0	3.8-5.7
227	227a	100	<2.9	10.0	2.3	1.8-10.0	1.8-2.9
230	230a	42	*	4.2	0.8	0.8-4.2	0.8-4.2
234	234a	43	<0.6	4.3	0.8	0.8-4.3	0.0-0.6
244	244a	21	<9.2	2.1	0.4	0.4-2.1	0.4-2.1

Twenty-five SSF cores contained only post-SSF sediments, therefore providing only minimum ages on the SSFs they were collected from. Post-SSF thicknesses in these cores ranged from 5 to 90 cm. Applying the range of sedimentation rates using the extrapolation method provides minimum ages for these features ranging from 0.1 to 9.0 ka cal BP. Age estimates from this group should be treated cautiously, as features could be much older than calculated[3].

Complex SSF footprints in IFB (those that include at least two individual SSFs; Fig. 4.5) appear to exclusively involve two features overlapping a single area. Some areas with a high density of

[3] A further two SSF cores proved unusable in establishing chronology (Cores 113b and 226b) as both cores potentially contain SSF material from two separate events, making the SSF/post-SSF contacts difficult to establish. Age ranges for their associated SSFs have been determined using other cores from their footprints.

SSF features may include features overlapped by two or more other features, but never stacked greater than two at a time.

One complex SSF footprint in IFB has absolute dating control on multiple features, the pair of SSFs 226 and 227. Morphological, stratigraphic, and chronological indicators from this pair

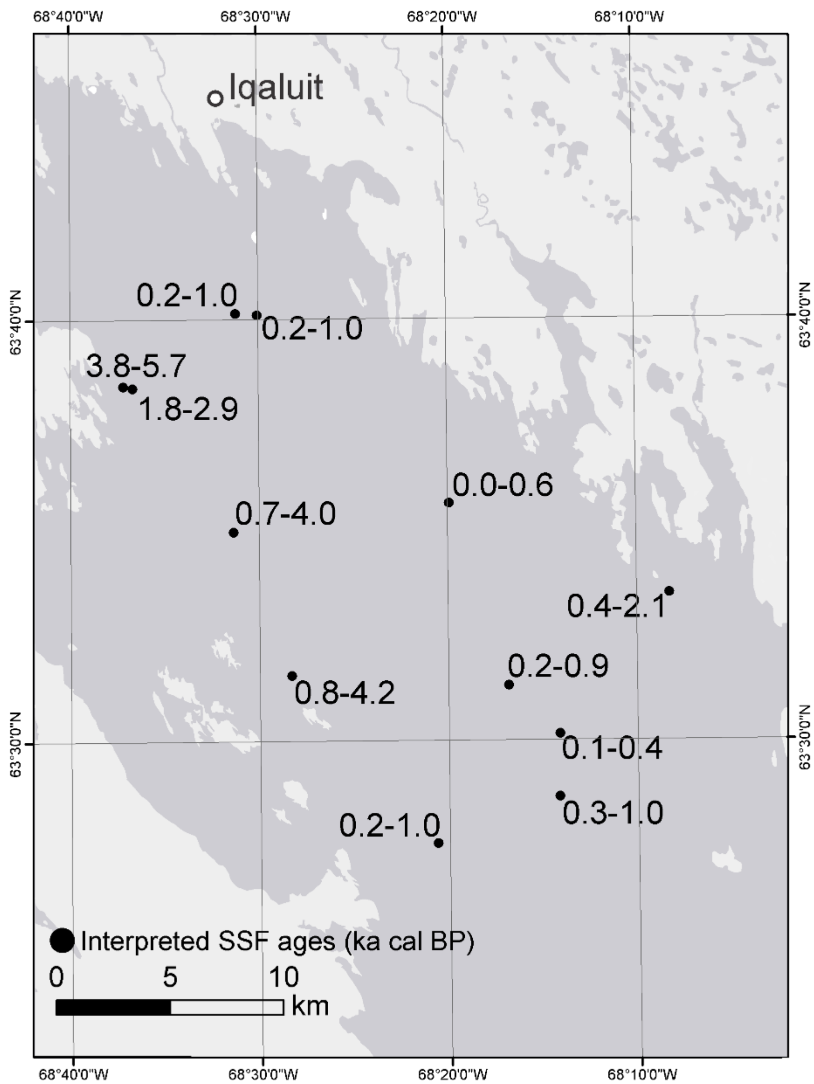

Figure 4.10 Map of IFB showing the interpreted ages of SSF (Table 4.4) at their respective locations.

provides support to the relative dating approach in IFB (Figs. 4.7 and 4.10). Based on morphology seen in MBES data it appears that SSF 226 occurred first, transporting sediment from the northeast to southwest, creating an excavation zone near its headwall. At some time after that SSF 227 occurred, transporting sediment primarily from the north to the south, but with some deposition into the excavation zone of 226 to the southwest (dashed polygon, Fig. 4.7). This overlap is supported by stratigraphic indicators in core 226b, which show signs of excavation (SSF 226) below a package of transported sediment (SSF 227). Further, the order of these events is corroborated by the interpreted age ranges of SSF 226 (3.8-5.7 ka cal BP) and SSF 227 (1.8-2.9 ka cal BP).

4.5 Discussion

Submarine slope failures are widespread in IFB. Based on MBES data, there are at least 246 of these features in the inner bay. To understand this population of SSFs it is crucial to evaluate the preconditioning factors that led to widespread instability in IFB, the triggering mechanisms that set them into motion, and their timing. The stratigraphic, acoustic, and chronological methods described and used in this paper provide insight into these key factors.

4.5.1 Preconditioning factors of SSFs in Inner Frobisher Bay

Preconditioning of submarine slope failures in IFB appears to be connected to two key factors: the presence of post-glacial sediments and complex seafloor morphology. As with SSFs in other settings, preconditioning factors in IFB are not necessarily limited to any one of the factors described. Realistically, it is some combination of the following that have preconditioned sediments for failure in the basin.

Sediment cores and acoustic surveys of SSFs in IFB show that these events typically have their failure planes within post-glacial lithofacies (LF4 and LF5) and involve glaciomarine sediments (LF3) only in the erosional zone. The overall lack of glaciomarine sediments within transported material indicates that if they are involved in failure, their relative proportion is far exceeded by post-glacial sediments. This suggests that either post-glacial sediments are more prone to failure or that other factors influencing SSFs (triggering mechanisms or preconditioning factors) were more active in the post-glacial period. One explanation for post-glacial sediments being more prone to failure could be related to the increased variability of bulk density (1300-2100 kg/m^3) and shear strength (5-23 kPa) in LF4 and LF5. Unlike glaciomarine lithofacies that have relatively consistent values for these properties, post-glacial sediments show a wide range even within single cores. These variable physical properties can set up combinations of "weaker" and "stronger" beds, which thereby become more susceptible to failure as sediments accumulate.

Another key factor in post-glacial sediments in IFB is their diverse textural composition, often alternating between mud, sandy mud and pebbly IRD within a single core with no apparent pattern (Deering et al. 2022). It is believed that ice-rafting is primarily from sea ice transporting sediment from local sources (e.g., tidal flats near Iqaluit; McCann and Dale 1986), given the relatively enclosed nature of IFB. Alternating stratification between thin units of disparate grain size could trap interstitial water in a coarser-grained (IRD) unit under a fine-grained (low-permeability) unit, causing pore pressure to increase as sediment accumulates, effectively creating a thin weak layer in a sequence. Further geotechnical testing of the sediment cores, such as tri-axial shear strength testing, could shed light on why post-glacial sediments appear more prone to failure than glaciomarine units.

The bathymetry of IFB appears to precondition SSFs through the presence of relatively steep slopes and an abundance of shallow water. As mentioned previously, the seafloor of the basin is characterized by a series of deep troughs and shallow ridges aligned roughly parallel to the main axis of the bay (NW-SE; Fig. 4.2), with shallow plateaus near the head of the bay. The seafloor morphology is derived primarily from the bedrock structure and glacial erosion (e.g., troughs), with glacial depositional landforms occurring at various scales and orientations playing a lesser role (e.g., moraines, streamlined glacial features, and hummocky areas; Deering et al. 2022).

SSFs are distributed throughout IFB, with concentrations along the southwestern coastline (Figs. 4.2-4.5). These concentrations of SSFs are not generally associated with localized conditions known for high incidence of slope failure (e.g., delta fronts or drift-mantled slopes; Deering et al. 2018a). However, more than half (56%) of the SSFs in the inner bay are oriented perpendicular to geological features associated with steeper slopes (e.g., troughs, islands, ridges, streamlined glacial features, and shorelines; Figs. 4.2-4.4). It is not unusual that steeper slopes precondition SSFs by affecting shear strength. This is well documented in the literature (Canals et al. 2004). The overall complexity of the seafloor in IFB increases the presence of these steeper slopes, providing more opportunities to establish areas of instability.

Approximately 69% of SSFs in IFB have their shallowest extent in < 30 m of water (35% in < 10 m), suggesting a connection between shallow water depths and their occurrence. The effect of the shallows may be a proxy for proximity to terrestrial sediment source (e.g., tidal flats and rivers), but in IFB the high tidal range may make shallow seafloor more susceptible to triggering mechanisms such as cyclic tidal drawdown, wave loading, and ice scouring (see below).

4.5.2 Chronology of SSFs

The ages interpreted for twelve SSFs in IFB range from < 0.5 to 5.7 ka cal BP. Seven of the dated SSFs are constrained to the last 1000 years (Fig. 4.10). Based on the oldest (3.8-5.7 ka cal BP) and youngest (0.1-0.4 ka cal BP) interpreted age ranges, SSFs have occurred in IFB since at least 5.7 ka cal BP and may be an active and ongoing seafloor geohazard. Further, while these twelve features appear to have formed asynchronously, the results of this study do not preclude synchronous formation of other SSFs in the population.

The chronology presented here is based on a complex and sometimes problematic set of radiocarbon dates. The widespread influence of the Portlandia Effect in IFB has complicated the establishment of sedimentation rates for the basin and loosened the chronology provided by the maximum constraint approach. While the sedimentation rates presented herein represent a probable range for the basin, several higher rates have been excluded as being attributed to localized factors. Had these higher rates been used in calculations, the lower (younger) bound of extrapolated age ranges would be nearly halved. This would broaden the range and open the possibility that the SSFs are even younger than what has been presented here. Rates determined locally to each SSF would provide a better extrapolated constraint. Given the interpreted young ages for many of the sampled SSFs in IFB, sedimentation rates could be determined by methods other than radiocarbon dating (e.g., ^{210}Pb, ^{137}Cs) to provide much better extrapolated age control.

Based on the overlapping morphology of some SSFs in IFB, it appears that some of these features were formed over multiple generations. As shown above, SSFs 226 and 227 overlap (Fig. 4.7). Their interpreted age ranges indicate that 227 formed at least 500 years after 226. These results may be used to help calibrate a “surface-roughness” approach to establishing relative ages of SSFs basin wide using sedimentation rates and amount of post-SSF infill. This approach has been explored in Pangnirtung Fiord (Sedore et al. 2022) but has fallen outside the scope of work in IFB. Future work in IFB may use this approach to better constrain a population-wide chronology for SSFs in the basin.

Given the way in which the chronology has been established in this paper, it would be highly speculative to extrapolate the proportions of ages of SSFs presented here to the entire population of 246 SSFs in IFB. The methods used here are better able to assign absolute ages to younger features. This is due to younger features typically having thinner post-SSF sediments, such that their SSF/post-SSF contact can be more readily captured using a short gravity corer and provide an absolute age estimate. This means that the proportions of interpreted ages presented here possibly skew younger than the actual proportions of the whole SSF population. Thus, while we know that some SSFs have ages less than 1 ka cal BP, we cannot say how many SSFs in IFB are that young. A more widespread application of relative dating approaches (e.g., based on surface roughness) may be used in future work to better understand the chronology of the entire SSF population in IFB.

4.5.3 Triggers of SSFs

IFB is potentially susceptible to the SSF triggering mechanisms found in other Arctic embayments. In IFB these potential widespread triggers include seismic activity, rapidly dropping RSL during and immediately following deglaciation, cyclical tidal loading, and seafloor impact of ice grounding. In localized areas, subaerial slope failures moving into the water and gas venting could be additional triggers. The viability of these triggering mechanisms can be evaluated based on the spatial and temporal distributions of SSFs in IFB.

As in all locations where it can occur, seismic activity has potential to trigger SSFs in IFB. While the prehistoric seismic record for Frobisher Bay is unknown, historic records for Baffin Island show earthquakes happening primarily further north or offshore. Outer Frobisher Bay shows some seismic activity since the historic record began in 1985 (Fig. 4.1B; Earthquakes Canada 2022). The established chronology for SSFs in IFB does not rule out minor seismic events triggering slope failures in the basin; however, the asynchronous ages rule out one large earthquake having caused all of the events simultaneously.

Rapid RSL fall during deglaciation appears unlikely to be a widespread trigger of SSFs in IFB. During early deglaciation (9-8 ka cal BP), RSL change was dominated by rapid elastic glacial-isostatic rebound (crustal uplift), which diminished exponentially, resulting in very rapid initial RSL fall and progressive deceleration. In IFB, RSL dropped from marine limit (~120 m asl) to ~42 m in less than 1000 years and continued falling to 30 m asl as ice withdrew from the bay (Deering et al. 2022). Both the chronology and stratigraphy of sampled SSFs in IFB suggest that these features formed largely in the post-glacial period (<7 ka cal BP), when ongoing RSL adjustments had slowed considerably. That said, slow post-glacial RSL fall may make shallow areas more prone to cyclic tidal loading and storm effects (described below).

Cyclic loading by tides appears to be a viable trigger for SSFs in IFB, given their spatial distribution. Approximately two-thirds of the SSFs in IFB have their shallowest extent in < 30 m and one-third in <10 m water depth, in the presence of a semidiurnal macrotidal range at large tide of 11.1 m (CHS 2022). The result is a significant (>33%) cyclical application and release of force normal to the seafloor (σ; Equation 1) on shallow sediments twice per day. Over time this may weaken slopes and cause them to collapse. With so many features extending into shallow water, this is a plausible trigger for many of the SSFs found in IFB and is consistent with the timing of the onset of the macrotidal regime (c. 2.4-2.0 ka cal BP; Dowdeswell et al. 1985).

Storm effects appear to be a viable trigger for SSFs in IFB, given their spatial distribution. With approximately two-thirds in <30 m and one-third in < 10 m water depth, large waves, storm surges, or water drawdown could trigger SSFs. The established chronology for SSFs in IFB does not rule out storms triggering slope failures in the basin; however, the asynchronous ages rule out one large event having caused all of the events simultaneously.

Iceberg grounding appears unlikely to be a widespread trigger of SSFs in IFB. Given the distance from the mouth of Frobisher Bay and the filtering effect of the mid-bay islands and inter-island channels, few icebergs make it into IFB. However, in very shallow waters this same effect has the possibility to be simulated by local sea ice. On shallow (<50 m) plateaus near the head of the bay there is much evidence of seafloor ice scour (i.e. force exerted by grounding ice), but no features linked directly with SSFs (Deering et al. 2018b).

Subaerial slope failures moving underwater may be a trigger of SSFs along the southwest coast of IFB (Fig. 4.5). In this area, the shallowest extent of SSFs is in a thin strip of shallow, unmapped water immediately adjacent to the coast. While this area does not have classically steep fjord walls, unconsolidated sediment slopes (possibly lateral moraines; Hodgson 2005) are found directly adjacent to the coast, which could have failed and moved into the water. In other locations in IFB, subaerial triggers appear unlikely, based on distance from shore or lack of subaerial slopes susceptible to failure.

Venting of trapped gasses may be a localized trigger of SSFs in IFB. This venting could reduce cohesion in the sediment, setting an SSF event into motion. Pockmark features, formed as the result of this venting, have been mapped along the southwest coast (Deering et al. 2018b). No mapped SSFs in IFB can be conclusively linked to gas venting, but the presence of some pockmarks leaves open the possibility that this process may be a more impactful trigger in shallow, unmapped areas.

4.6 Conclusion

The 246 mapped submarine slope failures on the seafloor of inner Frobisher Bay did not all form synchronously. This process has been active in inner Frobisher Bay since at least 5.7 ka cal BP. Dating of features indicates also that slope failure has occurred multiple times in inner Frobisher Bay within the last millennium. This chronology suggests that seafloor slope failure is an active and ongoing marine geohazard in inner Frobisher Bay.

Most submarine slope failures in inner Frobisher Bay occur within sediments accumulated after continental glacial ice retreated from the drainage basin. Lithofacies associated with this sediment package have variable bulk density and shear strength, which may contribute to instability not seen in glaciomarine sediments in the bay. Given the relatively thin post-glacial sediment package in inner Frobisher Bay (typically <5 m) and the general lack of glaciomarine material found in failed material, the amount of sediment available to fail in any particular place appears limited.

Rapid onset changes in water depths associated with particular time periods (i.e., post-glacial rebound) do not appear to be relevant triggering mechanisms for SSFs in inner Frobisher Bay. A more continuous trigger, such as ongoing cyclic tidal loading, seismic activity, storm effects, or a combination of localized triggers appears more likely to be the cause of SSFs in the basin.

4.7 References

Andrews J.T., Jull A.J.T., Donahue D.J., Short S.K., and Osterman L.E. (1985). Sedimentation rates in Baffin Island fiord cores from comparative radiocarbon dates. *Canadian Journal of Earth Sciences*, 22(12), p. 1827-1834

Bellwald B., Hjelstuen B.O., Sejrup H.P., Stokowy T., and Kuvås J. (2019). Holocene mass movements in west and mid-Norwegian fjords and lakes. *Marine Geology*, 407, p. 192-212.

Bennett R., Normandeau A., and Campbell D.C. (2022). Distribution of slope failures in eastern Baffin Island fiords, Nunavut; Geological Survey of Canada, Open File 8861. https://doi.org/10.4095/329603

Broom L.M., Campbell D.C., and Gosse J.C. (2017). Investigation of a Holocene marine sedimentary record from Pond Inlet, northern Baffin Island, Nunavut; *In* Summary of Activities 2017, Canada-Nunavut Geoscience Office, p. 93–104.

Brothers D.S., Haeussler P.J., Liberty L., Finlayson D., Geist E., Labay K., and Byerly M. (2016). A submarine landslide source for the devastating 1964 Chenega tsunami, southern Alaska. *Earth and Planetary Science Letters*, 438, p. 112-121.

Camargo J.M.R., Silva M.V.B, Ferreira Júnior A.V., and Araújo T.C.M. (2019). Marine geohazards: a bibliometric-based review. *Geosciences*, 9(2), 37 p.

Campbell D.C., Jenner K.A., Higgins J. and Piper D.J.W. (2017). Analysis of piston cores and high-resolution sub-bottom profiler data, Baffin Bay slope, Nunavut; Geological Survey of Canada, Open File 8135, 179 p.

Canals M., Lastras G., Urgeles R., Casamor J.L., Mienert J., Cattaneo A., De Batist M., Haflidason H., Imbo Y., Laberg J.S., Locat J., Long D., Longva O., Masson D.G., Sultan N., Trincardi F., and Bryn P. (2004). Slope failure dynamics and impact from seafloor and shallow sub-seafloor geophysical data: case studies from the COSTA project. *Marine* Geology, 213, p. 9-72.

Carter J. (2021). The majestic glory of fjords: geomorphometry and sedimentology of selected fjords on Cumberland Peninsula and the northeast coast of Baffin Island. Master's thesis, Memorial University of Newfoundland

Carter L., Burnett D., Drew S., Marle G., Hagadorn L., Bartlett-McNeil D., and Irvine N. (2009). *Submarine cables and the oceans – connecting the world*. UNEP-WCMC Biodiversity Series No. 31. ICPC/UNEP/UNEP-WCMC, 68 p.

Carter L., Gavey R., Talling P.J., and Liu J.T. (2014). Insights into submarine geohazards from breaks in subsea telecommunication cables. *Oceanography*, 27(2), p. 58-67.

CHS (2022). *Canadian Tide and Current Tables 2022, Volume 4: Arctic and Hudson Bay*. Canadian Hydrographic Service, Fisheries and Oceans Canada, Ottawa.

Clare M.A., Clarke J.H., Talling P.J., Cartigny M.J. and Pratomo D.G. (2016). Preconditioning and triggering of offshore slope failures and turbidity currents revealed by most detailed monitoring yet at a fjord-head delta. *Earth and Planetary Science Letters,* 450, 208–220, https://doi.org/10.1016/j.epsl.2016.06.021

Collins A.K., Hannah C.G. and Greenberg D. (2011). *Validation of a high resolution modelling system for tides in the Canadian Arctic Archipelago*; Canadian Technical Report of Hydrography and Ocean Sciences, v. 273, 72 p.

Courtney R.B., 2009. SegyJP2 software, Natural Resources Canada, available at: ftp://ftp.nrcan.gc.ca/gsc/courtney/SegyJp2/SegyJp2.htm

Deering R., Bell T., Forbes D.L., Campbell C., and Edinger, E. (2018a). Morphological characterization of submarine slope failures in a semi-enclosed fjord, Frobisher Bay, eastern Canadian Arctic; *In* D.G. Lintern, D.C. Mosher, L.G. Moscardelli, P.T. Bobrowsky, C. Campbell, J.D. Chaytor, J.J. Clague, A. Georgiopoulou, P. Lajeunesse, A. Normandeau, D.J.W. Piper, M. Scherwath, C. Stacey and D. Turmiel (Eds.) *Subaqueous Mass Movements*, Geological Society, London, Special Publications, 477, doi: 10.1144/SP477.35

Deering R., Misiuk B., Bell T., Forbes D.L., Edinger E., Tremblay T., Telka A., Aitken A., and Campbell C. (2018b). Characterization of the seabed and postglacial sediments of inner Frobisher Bay, Baffin Island, Nunavut. *In* Summary of Activities 2018, Canada-Nunavut Geoscience Office, p. 139-152.

Deering R., Bell T., Forbes D.L. (2022). Marine record of late-glacial readvance and last recession of Laurentide ice, inner Frobisher Bay, Baffin Island, Arctic Canada. *Canadian Journal of Earth Sciences*, doi: 10.1139/cjes-2021-0004

Dowdeswell J.A., Osterman L.E., and Andrews J.T. (1985). Quartz sand grain shape and other criteria used to distinguish glacial and non-glacial events in a marine core from Frobisher Bay, Baffin Island, N.W.T., Canada. *Sedimentology*, 32, p. 119-132.

Earthquakes Canada (2022). Earthquake Database. Retrieved from https://earthquakescanada.nrcan.gc.ca/stndon/NEDB-BNDS/bulletin-en.php

Edgar C. (2018, June 25). *Construction on Iqaluit's small-craft harbour, deep-sea port starts in July*. Retrieved from https://nunatsiaq.com/stories/article/65674construction_on_iqaluits_small-craft_harbour_deep-sea_port_starts_in_j/

England J., Dyke A.S., Coulthard R.D., McNeely R., and Aitken A. (2013). The exaggerated radiocarbon age of deposit-feeding molluscs in calcareous environments; *Boreas*, 42(2), p. 362-373

ESRI (2021). Light Gray Canvas. [Basemap.] Available from https://basemaps.arcgis.com/arcgis/rest/services/World_Basemap_v2/VectorTileServer.

Forbes D.L., Bell T., Manson G.K., Couture N.J., Cowan B., Deering R.L., Hatcher S.V, Misiuk B., and St-Hilaire-Gravel D. (2018). Chapter 8: Coastal Environments and Drivers. In Bell T. and

Brown T.M. (Eds) *From Science to Policy in the Eastern Canadian Arctic: An Integated Regional Impact Study (IRIS) of Climate Change and Modernization*, p. 211-249, ArcticNet, Quebec City.

GEBCO Compilation Group. 2020. GEBCO 2020 Grid. doi:10.5285/a29c5465- b138-234d-e053-6c86abc040b9.

Glimsdal S., L'Heureux J.-S., Harbitz C.B., and Løvholt F. (2016). The 29th January 2014 submarine landslide at Statland, Norway – landslide dynamics, tsunami generation, and run-up. *Landslides*, 13, p. 1435-1444.

Gosse J.C., Trembley T., Broom L.A., Campbell D.C., Wenzel G., Nedimović M.R., and Forget Brisson L. (2020) Initial results from the ULINNIQ seismicity and tsunami hazard project, northeastern Baffin Island, Nunavut. *In* Summary of Activities 2019, Canada-Nunavut Geoscience Office, p. 101-124.

Haeussler P.J., Lee H.J., Ryan H.F., Labay K., Kayen R.E., Hampton M.A., and Suleimani E. (2007). Submarine slope failures near Seward, Alaska, during the M9.2 1964 earthquake. In Lykousis V, Sakellariou D, and Locat J (Eds.) *Submarine Mass Movements and their Consequences*, p. 269-278. Springer Publishing.

Haflidason H., Lien R., Sejrup H.P., Forsberg C.F., and Bryn P. (2005). The dating and morphometry of the Storegga Slide. *Marine and Petroleum Geology*, 22, p. 123-136.

Hampton M.A., Lee H.J., and Locat J. (1996). Submarine Landslides. *Reviews in Geophysics*, 34(1), p. 33-59.

Heaton T.J., Köhler P., Butzin M., Bard E., Reimer R.W., Austin W.E.N., Ramsey C.B., Grootes, P.M., Hughen K.A., Kromer B., Reimer P.J., Adkins J., Burke A., Cook M.S., Olsen J., and Skinner L.C. (2020). Marine20 – The marine radiocarbon age calibration curve (0-55,000 cal BP); *Radiocarbon*, 62(4), p. 779-820

Hodgson, D.A. (2005). Quaternary geology of western Meta Incognita Peninsula and Iqaluit area, Baffin Island, Nunavut; *Geological Society of Canada Bulletin 582*, 72 p.

Hughes Clarke J.E., Muggah J., Renoud W., Bell T., Forbes D.L., Cowan B., and Kennedy J. (2015). Reconnaissance seabed mapping around Hall and Cumberland peninsulas, Nunavut: opening up southeastern Baffin Island to nearshore geological investigations. *In* Summary of Activities 2014, Canada-Nunavut Geoscience Office, p. 133-144

Lastras G., Amblas D., Calafat A.M., Canals M., and Frigola J. (2013). Landslides cause tsunami waves: insights from Aysén Fjord, Chile. *Eos*, 94(34), p. 297-298.

Leynaud D., Mienert J., and Vanneste M. (2009). Submarine mass movements on glaciated and non-glaciated European continental margins: A review of triggering mechanisms and preconditions to failure. *Marine and Petroleum Geology*, 26(5), p. 618-632.

L'Heureux J.-S., Glimsdal S., Longva O., Hansen L., and Harbitz C.B. (2011). The 1888 shoreline landslide and tsunami in Trondheimsfjorden, central Norway. *Marine Geophysical Research*, 32, p. 313-329.

Locat J. and Lee H. J. (2002). Submarine landslides: advances and challenges. *Canadian Geotechnical Journal*, 39, p. 193-212

Løvholt F., Schulten I., Mosher D., Harbitz C., and Krastel S. (2018). Modelling the 1929 Grand Banks slump and landslide tsunami. *From* Lintern D.G., Mosher D.C., Moscardelli L.G., Bobrowsky P.T., Campbell C., Chaytor J.D., Clague J.J., Georgiopoulou A., Lajeunesse P., Normandeau A., Piper D.J.W., Scherwath M., Stavey C., and Turmel D. (eds.) *Subaqueous Mass Movements*, Geological Society, London, Special Publications, 447, 17 p.

Mate D.J., Campbell D.C, Barrie J.V., Hughes Clarke J.E., Muggah J., Bell T., and Forbes D.L. (2015). Integrated seabed mapping of Frobisher Bay, southern Baffin Island, Nunavut to support infrastructure development, exploration and natural-hazard assessment; *in* Summary of Activities 2014, Canada-Nunavut Geoscience Office, p. 145–152.

McCann S.B. and Dale J.E. (1986). Sea ice breakup and tidal flat processes, Frobisher Bay, Baffin Island. *Physical Geography*, 7(2), p. 168-180.

Miron K. (2019, August 19). *Canada commits to connecting Iqaluit to fibre optic internet*. Retrieved from https://nunatsiaq.com/stories/article/canada-commits-to-connecting-iqaluit-to-fibre-optic-internet/

Mulder T., Savoye B., and Syvitski J.P.M. (1997). Numerical modelling of a mid-sized gravity flow: the 1979 Nice turbidity current (dynamics, processes, sediment budget and seafloor impact). *Sedimentology*, 44, p. 305-326.

Normandeu A., MacKillop K., Macquarrie M., Richards C., Bourgault D., Campbell D.C., Maselli V., Philibert G., and Hughes Clarke J. (2021). Submarine landslides triggered by iceberg collision with the seafloor. *Nature Geoscience*, 14, p. 599-605.

Nunatsiaq News (2021). *A future landslide-triggered tsunami in Greenland could be a lot bigger than experts first thought*. Website retrieved from: https://nunatsiaq.com/stories/article/a-future-landslide-triggered-tsunami-in-greenland-could-be-a-lot-bigger-than-experts-first-thought/. September 30, 2022.

Owen M., Day S., and Maslin M. (2007). Late Pleistocene submarine mass movements: occurrence and causes. *Quaternary Science Reviews*, 26, p. 958-978.

Pinet N., Brake V., Campbell C., and Duchesne M.J. (2015). Geomorphological characteristics and variability of Holocene mass-transport complexes, St. Lawrence Estuary, Canada. *Geomorphology*, 228, p. 286-302.

Piper D.J.W., Cochonat P., and Morrison M.L. (1999). The sequence of events around the epicentre of the 1929 Grand Banks earthquake: initiation of debris flows and turbidity current inferred from sidescan sonar. *Sedimentology*, 46(1), p. 79-97.

Piper D.J.W. and Aksu A.E. (1987). The source and origin of the 1929 Grand Banks turbidity current inferred from sediment budgets. *Geo-marine Letters*, 7(4), p. 177-182.

Quality Positioning Services (2018). Qimera 1.7; computer software, Quality Positioning Services, Zeist, Netherlands

Sedore P., Normandeau A. and Maselli V. (2022). Submarine landslides in Pangnirtung Fiord, eastern Baffin Island, Nunavut; *In* Summary of Activities 2021, Canada-Nunavut Geoscience Office, p. 31-46

Stuiver M., Reimer P.J., and Reimer R.W. (2021). CALIB Radiocarbon Calibration, version 8.2; computer software.

Syvitski J.P.M., Burrell D.C., and Skei J.M. (1987). Subaqueous slope failure. *In* Syvitski J.P.M. et al. (Eds.) *Fjords: Processes and Products*, p. 175-210. Springer-Verlag Publishing.

Todd B.J., Shaw J., Campbell D.C., and Mate D.J. (2016). Preliminary interpretation of the marine geology of Frobisher Bay, Baffin Island, Nunavut. *In* Summary of Activities 2016, Canada-Nunavut Geoscience Office, p. 61-66.

Tremblay T., Day S., McNeil R., Smith K., Richardson M., and Shirley J. (2015). Overview of surficial geology mapping and geochemistry in the Sylvia Grinnell Lake area, Baffin Island, Nunavut; *in* Summary of Activities 2015, Canada-Nunavut Geoscience Office, p. 107– 120.

Turmel D., Locat J., Leblanc J., and Cauchon-Voyer G. (2018). Tsunami modelling of the 7250 cal years BP Betsiamites submarine landslide. *From* Lintern D.G., Mosher D.C., Moscardelli L.G., Bobrowsky P.T., Campbell C., Chaytor J.D., Clague J.J., Georgiopoulou A., Lajeunesse P., Normandeau A., Piper D.J.W., Scherwath M., Stavey C., and Turmel D. (eds.) *Subaqueous Mass Movements*, Geological Society, London, Special Publications, 447, 9 p.

Twichell D.C., Chaytor J.D., ten Brink U.S., and Buczkowski B. (2009). Morphology of late Quaternary submarine landslides along the U.S. Atlantic continental margin. *Marine Geology*, 264(1-2), p. 4-15.

Urlaub M., Talling P.J., and Masson D.G. (2013). Timing and frequency of large submarine landslides: implications for understanding triggers and future geohazards. *Quaternary Science Reviews*, 72, p. 63-82.

Urlaub M., Geersen J., Krastel S., and Schwenk T. (2018). Diatom ooze: crucial for the generation of submarine mega-slides? *Geology*, 46, 331–334

Vickers K.J., Ward B.C., Utting D.J., and Telka A.M. (2010). Deglacial reservoir age and implications, Foxe Peninsula, Baffin Island; *Journal of Quaternary Research*, 25(8), p. 1338-1346

5. Synthesis

The seafloor of inner Frobisher Bay (IFB) is distinguished by its bathymetric complexity. While many of the fjords along the Baffin Island coast have relatively featureless troughs and basin floors between sills typical of deglacial embayments (e.g., Syvitski et al. 1987, 2022), IFB is unusually shallow and feature-rich in its morphology. This can be ascribed to three key factors: resistant bedrock and structural control, a deglacial history marked by readvances and changes in style of ice front, and an abundance of seafloor geomorphic processes (sources of marine geohazards that have reshaped deglacial post-glacial deposits). This dissertation has focused on the latter two factors in analyzing the soft sediments that comprise the bed of IFB and the processes that have reworked them during and following deglaciation.

This work addresses the following research questions:

Research Question 1: *How do the character and distribution of seafloor landforms and sediments augment our understanding of Laurentide ice retreat in IFB and in bathymetrically complex shallow basins?*

Research Question 2: *What was the deglacial chronology for IFB?*

Research Question 3: *Do the large moraines in IFB coincide with the timing of the Cockburn Substage readvance as seen elsewhere on Baffin Island?*

Research Question 4: *What is the basin setting and morphological character of SSFs in IFB and how do they compare with other populations in similar marine settings?*

Research Question 5: *Is there a suite of diagnostic features that help to identify relatively small SSFs in the bathymetric, sub-bottom acoustic and sedimentary records?*

Research Question 6: *What were the timing, triggering mechanism(s) and preconditioning factor(s) for SSFs in IFB?*

Chapter 2 (Deering et al. 2022) addresses research questions 1, 2, and 3. Chapter 3 (Deering et al. 2018a) addresses research question 4. Chapter 4 addresses research questions 5 and 6.

5.1 Late-glacial recession, stratigraphy, and chronology

To understand the disturbed sediments in IFB it is necessary first to know something about the undisturbed deposits. Prior to the beginning of this project, little was known about the seafloor in the basin. The larger program of which this dissertation is a part had acquired multibeam bathymetric data for some of the basin (demonstrating the presence of SSFs), but there had been little geomorphic and stratigraphic analysis (Mate et al. 2015; Todd et al. 2016; Deering et al. 2018b). Opportunistic sub-bottom acoustic surveying had provided glimpses of what underlay the seafloor, but there were no sediment cores to link acoustic facies to lithofacies. This dissertation provides the first comprehensive analysis of the lithofacies that make up the seabed of inner Frobisher using 63 new sediment cores. It provides insight into the deglacial history of the basin through stratigraphic and geomorphic analysis, combined with 86 new radiocarbon dates. Filling the pre-existing marine data gap and increasing the chronological resolution of the previously established deglacial history in the region (e.g. Osterman 1982; Lind 1983; Squires 1984; Dowdeswell et al. 1985; Jacobs et al. 1985; Stravers et al. 1992; Hodgson 2005; Miller et al. 2005; Tremblay et al. 2015), this work contributes to understanding of the Cockburn Substage readvance on Baffin Island.

Research Question 1*: How do the character and distribution of seafloor landforms and sediments augment our understanding of Laurentide ice retreat in IFB and in bathymetrically complex shallow basins?*

- The deglacial seafloor landform assemblage suggests that the final deglaciation of IFB occurred in two phases: episodic, rapid retreat (represented by five large ridges) followed by slow retreat (represented by multiple De Geer moraines).
- The deglacial stratigraphic sequence in IFB is similar to that observed in numerous other glaciated embayments in eastern Canada (e.g., Piper et al. 1983; Syvitski and Lee 1997; Syvitski et al. 2022).
- Above the bedrock/till layer (seen only in the acoustic stratigraphic records) is a glaciomarine package of rapidly deposited clay and silt, with waning glacial influence (seen in decreasing clay and carbonate content) up-core, followed by a post-glacial package of relatively slowly deposited silt with more ice-rafted debris.
- A distinct change in sediment character occurred c. 7 ka cal BP, when sedimentation switched from glaciomarine to post-glacial. This change is believed to coincide with the retreat of Laurentide ice from the IFB drainage basin.

Research Question 2: *What was the deglacial chronology for IFB?*

- The marine record indicates that final recession from a late-glacial limit corresponding to the outermost Frobisher Bay moraine was underway no later than 8.5 ka cal BP.
- The marine deglacial chronology suggests that the LIS had a marine terminating front in IFB until at least 7.6 ka cal BP.

- As RSL continued to fall, further recession resulted in the final disappearance of Laurentide ice from the drainage basin, as described above.

Research Question 3*: Do the large moraines in IFB coincide with the timing of the Cockburn Substage Readvance as seen elsewhere on Baffin Island?*

- The five large seafloor transverse ridges correlate spatially to portions of the Frobisher Bay Moraine Complex, which had been mapped previously on the north and south coasts of the inner bay (Hodgson, 2005).
- The marine and onshore deglacial chronology suggests that the outermost large seafloor ridge formed at some time between 9.4-8.5 ka cal BP, corresponding with published ages of the Cockburn Substage (9.5-8.5 ka cal BP; Briner et al. 2009).

5.2 Marine geohazards

This dissertation reports the presence of and describes the 246 SSFs found on the seafloor of inner Frobisher Bay, using established stratigraphic and innovative morphometric methods. The initial focus of this segment of the project was on the morphology of the many mass-transport features. Given the large number in a single basin, IFB offered a unique opportunity to study a large population where many of the preconditioning factors and potentially the triggering mechanisms contributing to their occurrence would be the same. The results, as described in Chapter 4, show that not all features, despite similarities in their environment, share a similar morphology and, in fact, there is a wide spectrum of size, shape, and other parameters.

Research Question 4*: What is the basin setting and morphological character of SSFs in IFB and how do they compare with other populations in similar marine settings?*

- At least 246 SSFs can be found on the seafloor of inner Frobisher Bay.
- Concentrations of SSFs have been found along the southwest and northeast coasts of IFB, with the remainder of features originating primarily on the flanks of inter-basin bathymetric highs.
- Twelve measured and seven calculated morphometric parameters were used to describe small-scale SSFs in IFB.
- All SSFs in IFB are relatively small (<2.15 km^2) and initiated in shallow depths (<150 m water depth; 35% <10 m).
- The population of SSFs in IFB has a median area (0.09 km^2) much smaller than SSF populations in the St Lawrence estuary (3.34 km^2; Pinet et al. 2015) and Resurrection Bay, Alaska (1.47 km^2; Haeussler et al. 2007).

Following morphological analysis, using the deglacial basin stratigraphy established earlier in the project, this study aimed to determine preconditioning factors for SSFs in inner Frobisher Bay. This included some environmental parameters, such as steep slopes, but was largely focused on which lithofacies tend to fail in the basin and what the resulting sediments look like. This analysis included 39 sediment cores from inside SSF footprints and acoustic sub-bottom surveys across most of the 246 identified features.

Research Question 5: *Is there a suite of diagnostic features that help to identify relatively small SSFs in the bathymetric, sub-bottom acoustic and sedimentary records?*

- Five morphological indicators of SSFs in IFB were described using MBES data. They are headwalls, excavation, sidewalls, depositional lobes, and compression ridges.

- Three indicators of SSFs in IFB were described from sub-bottom acoustic data. They are chaotic surface and internal reflectors, masking of acoustic stratigraphy, and truncation of acoustic reflectors.

- Three indicators of SSFs in IFB were described from sediment cores. They are modification of stratigraphic sequence, modification of physical properties of sediments, and modifications of chronological sequences.

The morphological and stratigraphic analyses of SSFs in IFB have provided valuable insight into both the chronology of features in the basin and the triggering mechanisms that caused them in such abundance. Key to understanding possible triggering mechanisms is the timing of formation. If all formed synchronously, then a major, basin-wide trigger would likely be responsible. Alternatively, if they were occurring sporadically since deglaciation, then a series of small triggers would more likely be responsible. Furthermore, if all features were formed before or after a certain date, a temporally controlled trigger would be implied, unless the change resulted from a change in preconditioning.

Research Question 6: *What were the timing, triggering mechanism(s) and preconditioning factor(s) for SSFs in IFB?*

- Preconditioning factors of SSFs in IFB are related to the presence of post-glacial sediment and the bathymetric relief of the seafloor.

- Post-glacial sediments in IFB show a diversity of physical properties and textures, possibly favouring the formation of weak layers which are more prone to failure.

- The seafloor morphology of IFB is characterized by the presence of steep slopes and large swathes of relatively shallow seafloor, both shown to contain many SSFs in IFB.

- Triggering mechanisms for SSFs in IFB do not appear related to a single event.
- Plausible widespread triggering mechanisms for SSFs in IFB include seismic activity, cyclic tidal loading, and storm effects. Subaerial slope failures initiating mass transport into the water, gas venting, and ice grounding may be localized triggers in different parts of IFB.
- Interpreted ages for twelve SSFs in IFB range from <0.5 to 5.7 ka. The ages of half of the dated SSFs are constrained to the last 1000 years. Based on the oldest (3.8-5.7 ka cal BP) and youngest (0.1-0.4 ka cal BP) interpreted age ranges, SSFs have occurred in IFB since at least 5.7 ka cal BP (Figure 5.1).
- Based on the overlapping morphology of some SSFs in IFB it appears that some of these features were formed over multiple generations.
- Absolute ages for the 246 SSFs in IFB cannot be extrapolated from the interpreted age ranges of the 12 features described above. A more widespread approach will be needed in future work to establish a chronology for the entire population of SSFs.

5.3 Significance

The glacial history of IFB, as elucidated by the series of seafloor moraines there, provides chronological resolution to the last major readvance (and subsequent recession) of the northeast LIS on southern Baffin Island. Cockburn Substage readvance moraines are found extensively along the northeast coast of Baffin Island (Andrews et al. 1978; Margreth et al. 2017; Crump et al. 2020). In IFB this readvance and subsequent retreat can be seen as a series of five large seafloor moraines, each with some chronological control, and many small De Geer moraines (Chapter 2).

This chronology provides insight into the final (post-LGM) retreat of the LIS in the region, particularly as it converted from a marine-terminated to fully terrestrial ice front in IFB.

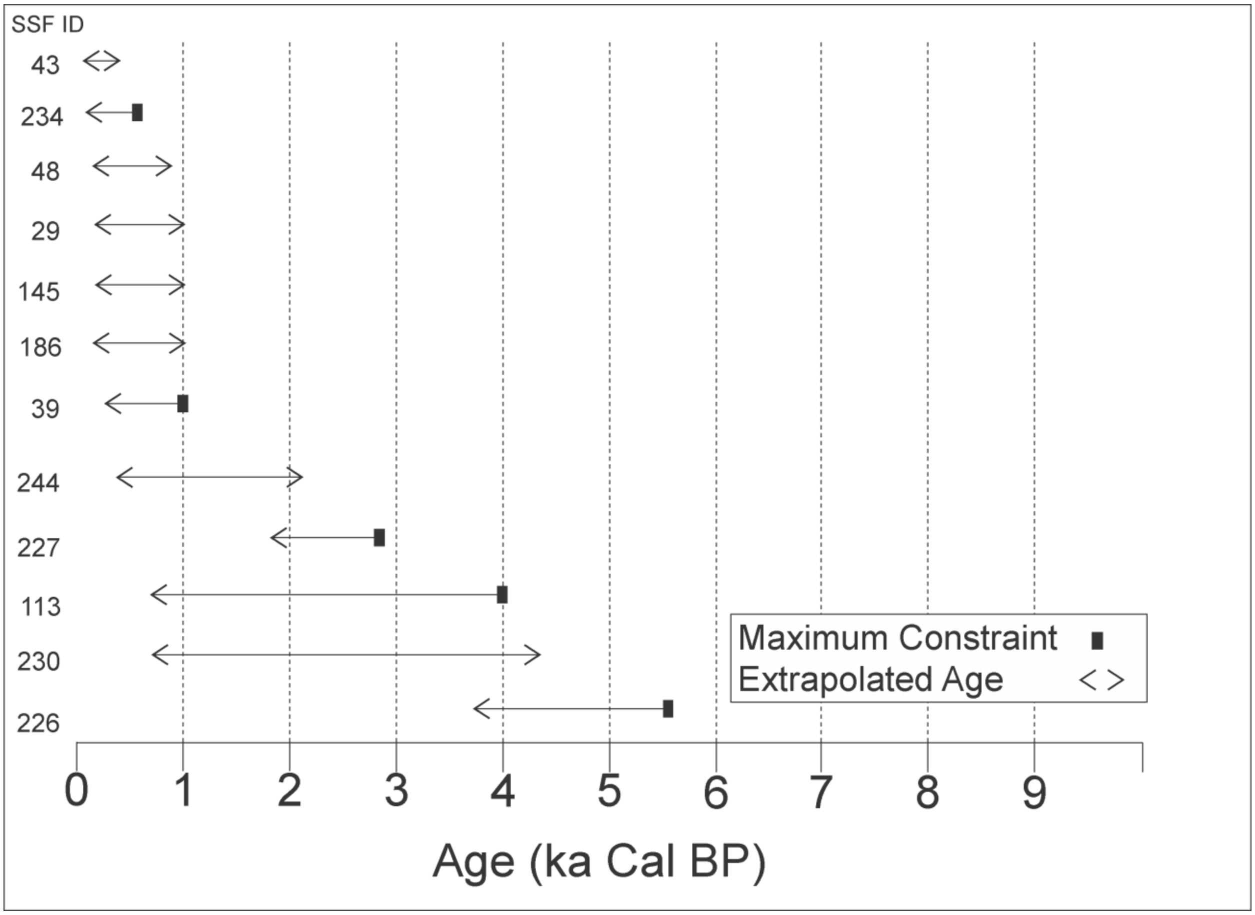

Figure 5.1 Interpreted age ranges of SSFs in IFB. Ages are based on maximum constraint using radiocarbon dates and extrapolation using sedimentation rates. A full explanation of chronological methods can be found in Chapter 4.

While the LIS is long gone, analogous ice sheets remain today in Greenland and Antarctica (e.g., Batchelor and Dowdeswell, 2015; Batchelor et al. 2018; Dowdeswell et al. 2008, 2012, 2016). These contemporary ice sheets have marine interfaces characterized by floating, pinned ice shelves and marine ice cliffs. Under our rapidly changing climate, they are undergoing retreat similar to that seen at the end of the last Ice Age. An understanding of the marine interface of the LIS in IFB and how it retreated in the early-mid Holocene may provide insight into how that same transition could play out in similar Greenland and Antarctic embayments in the future.

The examination of small-scale marine geohazards in the Canadian Arctic context could prove important for future sustainable development in the region (e.g., Gosse et al. 2020). IFB provided an unprecedented opportunity to identify a range of geohazards in an Arctic embayment. This promise of new insights is being gradually realized as additional fjords and embayments are mapped along the Baffin coast (e.g., Hughes Clarke et al. 2015; Broom et al. 2017; Normandeau et al. 2020; Cowan et al. 2021; Bennett et al. 2022). While IFB may prove to show an anomalously high density of SSFs, recent studies in other embayments have shown similar densities (e.g., Sedore et al. 2022). Should these features prove to be as common elsewhere, then this will be the first of many studies attempting to determine why such SSF density is seen in the region. Should IFB prove to be one of a few outliers regionally and globally, then this study will nevertheless be valuable, providing insight into the distinctive geological, geotechnical, and environmental enablers and drivers of SSFs in IFB. Enhanced understanding of the localities, frequency, and triggers of seafloor failures will contribute to better informed planning and infrastructure design and routing in the local context.

In terms of triggering mechanisms, a storm trigger implies an extra-tropical cyclone moving north from the Lab Sea, driving a surge and waves into Frobisher Bay. Some storms track this way and there is some literature suggesting an increase in frequency. However, the mid-bay islands limit wave fetch (Hatcher et al. 2021) and extreme water levels in the bay appear not to have been associated with strong wind events (Hatcher and Forbes 2015). Thus while storm-surge loading is a plausible mechanism, it is not clear how important a role it may have played in IFB. We know that in a macrotidal system, a storm surge has to coincide with a high spring tide to be damaging, but over the long term such a coincidence can occur. On the other hand, the change in applied stress (σ in Eq. 1) associated with macrotidal loading, particularly in shallow water (e.g. approximately doubling of depth at 10 m) would seem to be a highly plausible trigger, particularly at times of perigean tides (6-8 times per year) or highs of the 19-year lunar nodal cycle.

Small-scale SSFs have not had much focus in the literature until recently. Understandably, large-scale, destructive, far-reaching events have attracted the most attention. As high-resolution bathymetric coverage continues to spread into smaller and more remote basins, the number of these small-scale features recognized in the literature continues to grow (e.g., Bellwald et al. 2019; Brothers et al. 2016; Sedore et al. 2022). While, in principle, the mechanics behind large- and small-scale features should be the same, that must not be taken for granted. This study examines a large database of small-scale SSFs within a single basin that is unrivalled in number by any yet published in the literature. By investigating the stratigraphy, morphometry, and chronology of these features in IFB, this work attempts to better understand the drivers of these small-scale events.

Within the study of SSFs, the concept of morphometric classification is rapidly evolving. Over the past five years, the community has been working toward establishing a recognized set of standard morphometric parameters that can be applied to all SSFs (Clare et al. 2018). This study contributes to this discussion in two ways. First, it presents this author's suggestion of a set of useful standardized parameters. It is not an exhaustive list but does contribute new parameters to the discussion. Second, it shows the appropriateness of the measurement of particular parameters on very small-scale features. As mentioned above, much of the community's focus has been on large-scale SSFs, with no guarantee that the parameters measured for those would be relevant at this much smaller scale. Through its extensive database of features, this study examines that possible disconnect.

5.4 Implications and Future Work

Several practical recommendations arise from this work both for those developing seafloor infrastructure in the study area (and more generally, in northern Canada) and for those with a theoretical interest in the study of SSFs. Following these recommendations will result in more robust and sustainable results in both of these endeavours.

For those looking to develop seafloor and coastal infrastructure in Frobisher Bay, but also in the Canadian Arctic generally, greater attention needs to be paid to the local seafloor and its complexities. For example, at the local level, this study identifies that: 1) SSFs tend to be located along geological features, such as bedrock ridges, faults or prominent moraines where seabed slopes are steeper, and in shallow water (69% are initiated in water <30 m deep), though not always near the coastline (e.g., islands, shallows banks); 2) are typically small, elongate, thin seafloor features; and 3) typically occur in postglacial sediments (LF4 and LF5). Site selection in IFB based on these criteria would favour development in areas far from slopes with thick coverage of post-glacial sediments. Together with the diagnostic features that help to identify relatively small SSFs (see above), they can help guide geoscientists and engineers in their site assessment of seafloor hazards in IFB.

It cannot be assumed that the seafloor of an embayment such as IFB is relatively flat. Fjards and similar shallow embayments, even those with a history of glacial carving and rapid deglacial sedimentation, can still present a potentially challenging environment that should be surveyed prior to any sort of development. Desktop surveys of pre-existing bathymetric data (e.g., 1950s navigational charts), particularly in sparsely surveyed northern embayments, are not enough to grasp anything but very broad seafloor patterns in these areas. As multibeam acoustic bathymetric surveying coverage expands in these areas, old bathymetric data sources are being replaced and updated to better reflect present-day needs, but much work is yet to be done.

For those studying SSFs, the field of morphometrics may provide much insight into the processes that drive different events. However, for that possibility to become reality, much more morphometric work needs to be done on features, large and small, worldwide. A crucial first step is establishing a set of standard morphometric parameters and prescribing exactly how each of them is to be measured. Currently, the international SSF community is working toward this goal, making now the time to develop new and novel parameters and to standardize how "established" parameters are measured. The community is also working on constructing and organizing a database in which to compile and share morphometric data. All of this standardizing, measurement, and compilation of SSF data is a precursor to the ultimate goal of relating various morphometrics to different styles of SSF and the processes that cause them. While IFB provides a large database of features to study, even more (and from varying depositional environments) are needed for these bigger questions to be answered.

Further work is required to develop methods for establishing a chronology for a large population of SSFs. While this work touched on relative aging methods based on overlap of features, those are limited to localized populations. Alternatively, characterizing the surface roughness of SSF features could help determine relative timing of events. Possible avenues for establishing chronologies of SSF populations will likely rely on acoustic methods being calibrated with established radiocarbon age control. For example, calibrating the thickness of post-SSF sediments seen in sub-bottom acoustics using sedimentation rates to determine years of deposition since the

SSF. If radiocarbon dates are to be used in this way it is necessary to enhance our understanding of the impact of the Portlandia Effect in the basin. Questions remain as to how widespread this effect is, how uniformly it impacts different species and individuals, and how its magnitude might be affected by variable carbonate concentrations in the sediments.

5.5 Conclusions

The deglacial and post-glacial seafloor history of IFB has been eventful. Building upon underlying geologic structure, deglacial processes and sediments resulted in an active geomorphological regime that is still working today. During the Cockburn Substage, as the LIS retreated along most of its margins, the glacial ice front along the Baffin Island coast (including inner Frobisher Bay) experienced notable readvance. While some geomorphological evidence of this readvance is seen all along the Baffin coast, in IFB the event is writ large on both terrestrial and seafloor morphology. The Frobisher Bay Moraine Complex, a focus of terrestrial deglacial study in the region for many years, has now been shown to extend across the full width of the basin, connecting the northeast and southwest coasts.

An abundance of small-scale, localized marine geohazards, particularly SSFs, are imprinted upon the large-scale deglacial morphology that characterizes inner Frobisher Bay. These SSFs, shown to have been forming in the bay over several millennia following deglaciation, including within the last 1000 years, are the result of a combination of environmental factors including the deglacial and post-glacial stratigraphy of the inner bay and the presence of steep slopes created by the underlying geology. Questions remain as to what exactly triggered the 246 mapped SSF features in the basin, but evidence points to it being a sporadic or repetitive trigger instead of a single catastrophic formative event.

This dissertation provides the first comprehensive examination and analysis of the seafloor morphology, stratigraphy, and marine deglacial history of inner Frobisher Bay. It has advanced our knowledge of the deglacial history and stratigraphy of the basin and has provided insight into the many submarine slope failure features that mark its seafloor. This information should prove useful both for those seeking to develop infrastructure for the City of Iqaluit and to understand marine geohazards in the coastal marine environment, but should not represent the final study of this active and interesting Canadian Arctic embayment.

5.6 References

Andrews J.T. and Ives J.D. (1978). “Cockburn” nomenclature and the late Quaternary history of the eastern Canadian Arctic. *Arctic and Alpine Research*, 10(3), p. 617-633

Batchelor C.L. and Dowdeswell J.A. (2015). Ice-sheet grounding-zone wedges (GZWs) on high-latitude continental margins. *Marine Geology*, 363, p. 65-92

Batchelor C.L., Dowdeswell J.A., and Rignot E. (2018). Submarine landforms reveal varying styles of deglaciation in North-West Greenland fjords. *Marine Geology*, 402, p. 60-80.

Bellwald B., Hjelstuen B.O., Sejrup H.P., Stokowy T., and Kuvås J. (2019). Holocene mass movements in west and mid-Norwegian fjords and lakes. *Marine Geology*, 407, p. 192-212.

Bennett R., Normandeau A., and Campbell D.C. (2022). Distribution of slope failures in eastern Baffin Island fiords, Nunavut. Geological Survey of Canada, Open File 8861. https://doi.org/10.4095/329603

Briner J.P., Davis P.T., and Miller G.H. (2009). Latest Pleistocene and Holocene glaciation of Baffin Island, Arctic Canada: key patterns and chronologies. *Quaternary Science Reviews*, 28(21-22), p. 2075-2087

Broom L.M., Campbell D.C., and Gosse J.C. (2017). Investigation of a Holocene marine sedimentary record from Pond Inlet, northern Baffin Island, Nunavut. *In* Summary of Activities 2017, Canada-Nunavut Geoscience Office, p. 93–104.

Brothers D.S., Haeussler P.J., Liberty L., Finlayson D., Geist E., Labay K., and Byerly M. (2016). A submarine landslide source for the devastating 1964 Chenega tsunami, southern Alaska. *Earth and Planetary Science Letters*, 438, p. 112-121.

Clare M., Chaytor J., Dabson O., Gamboa D., Georgiopoulou A., Eady H., Hunt J., Jackson C., Katz O., Krastel S., Leon R., Micallef A., Moernaut J., Moriconi R., Moscardelli L., Mueller C., Normandeau A., Patacci M., Steventon M., Urlaub M., Volker D., Wood L., and Jobe Z. (2018).

A consistent global approach for the morphometric characterization of subaqueous landslides. *in* Subaqueous Mass Movements, D.G. Lintern, D.C. Mosher, L.G. Moscardelli, P.T. Bobrowsky, C. Campbell, J.D. Chaytor, J.J. Clague, A. Georgiopoulou, P. Lajeunesse, A. Normandeau, D.J.W. Piper, M. Scherwath, C. Stacey and D. Turmiel (ed.); Geological Society, London, Special Publications, v. 477, URL <https://doi.org/10.1144/SP477.15>.

Crump S.E., Young N.E., Miller G.H., Pendleton S.L., Tulenko J.P., Anderson R.S., and Briner J.P (2020). Glacier expansion on Baffin Island during early Holocene cold reversals. *Quaternary Science Reviews*, v. 241, 106419.

Deering R., Bell T., Forbes D.L., Campbell C., and Edinger, E. (2018a). Morphological characterization of submarine slope failures in a semi-enclosed fjord, Frobisher Bay, eastern Canadian Arctic. *In* D.G. Lintern, D.C. Mosher, L.G. Moscardelli, P.T. Bobrowsky, C. Campbell, J.D. Chaytor, J.J. Clague, A. Georgiopoulou, P. Lajeunesse, A. Normandeau, D.J.W. Piper, M. Scherwath, C. Stacey and D. Turmiel (Eds.) *Subaqueous Mass Movements*, Geological Society, London, Special Publications, 477, doi: 10.1144/SP477.35

Deering R., Misiuk B., Bell T., Forbes D.L., Edinger E., Tremblay T., Telka A., Aitken A., and Campbell C. (2018b). Characterization of the seabed and postglacial sediments of inner Frobisher Bay, Baffin Island, Nunavut. *In* Summary of Activities 2018, Canada-Nunavut Geoscience Office, p. 139-152.

Deering R., Bell T., Forbes D.L. (2022). Marine record of late-glacial readvance and last recession of Laurentide ice, inner Frobisher Bay, Baffin Island, Arctic Canada. *Canadian Journal of Earth Sciences*, doi: 10.1139/cjes-2021-0004

Dowdeswell J.A., Canals M., Jakobsson M., Todd B.J., Dowdeswell E.K., and Hogan K.A. (2016). The variety and distribution of submarine glacial landforms and implications for ice-sheet reconstruction. *Geological Society*, London, Memoirs, 46, p. 519-552

Dowdeswell J.A. and Fugelli E.M.G. (2012). The seismic architecture and geometry of grounding-zone wedges formed at the marine margins of past ice sheets. *Geological Society of America Bulletin*, 124(11-12), p. 1750-1761.

Dowdeswell J.A., Osterman L.E., and Andrews J.T. (1985). Quartz sand grain shape and other criteria used to distinguish glacial and non-glacial events in a marine core from Frobisher Bay, Baffin Island, N.W.T., Canada. *Sedimentology*, 32, p. 119-132.

Dowdeswell J.A., Ottesen D., Evans J., Cofaigh C.Ó., and Anderson J.B. (2008). Submarine glacial landforms and rates of ice-stream collapse. *Geology*, 36(10), p. 819-822

Gosse J.C., Trembley T., Broom L.A., Campbell D.C., Wenzel G., Nedimović M.R., and Forget Brisson L. (2020) Initial results from the ULINNIQ seismicity and tsunami hazard project, northeastern Baffin Island, Nunavut. *In* Summary of Activities 2019, Canada-Nunavut Geoscience Office, p. 101-124.

Haeussler P.J., Lee H.J., Ryan H.F., Labay K., Kayen R.E., Hampton M.A., and Suleimani E. (2007). Submarine slope failures near Seward, Alaska, during the M9.2 1964 earthquake. In

Lykousis V, Sakellariou D, and Locat J (Eds.) *Submarine Mass Movements and their Consequences*, p. 269-278. Springer Publishing.

Hatcher S.V., Forbes D.L., and Manson G.K. (2021). Boulder-strewn flats in a high-latitude macrotidal embayment, Baffin Island: geomorphology, formation, and future stability. *Canadian Journal of Earth Sciences*, https://doi.org/10.1139/cjes-2021-0019.

Hatcher S.V. and Forbes D.L. (2015). Exposure to coastal hazards in a rapidly expanding northern urban centre, Iqaluit, Nunavut. *Arctic*, v. 68, no. 4, p. 453-471.

Hodgson D.A. (2005). Quaternary geology of western Meta Incognita Peninsula and Iqaluit area, Baffin Island, Nunavut. *Geological Society of Canada Bulletin 582*, 72 p.

Hughes Clarke J.E., Muggah J., Renoud W., Bell T., Forbes D.L., Cowan B. and Kennedy J. (2015). Reconnaissance seabed mapping around Hall and Cumberland peninsulas, Nunavut: opening up southeastern Baffin Island to nearshore geological investigations. *Summary of Activities 2014*, Canada-Nunavut Geoscience Office, 135-144 (http://cngo.ca/summary-of-activities2014)

Jacobs J.D., Mode W.N., Squires C.A., and Miller G.H. (1985). Holocene environmental change in the Frobisher Bay area, Baffin Island, N.W.T.: deglaciation, emergence, and the sequence of vegetation and climate. *Géographie physique et Quaternaire*, v. 39, no. 2, p. 151–162.

Lind E.K. (1983). Holocene paleoecology and deglacial history of the Cape Rammelsberg area, southern Baffin Island, N.W.T., Canada. M.Sc. thesis, Department of Geology, University of Colorado, Boulder, Colorado, 219 p.

Margreth A., Gosse J.C., and Dyke A.S. (2017) Wisconsinan and early Holocene glacial dynamics of Cumberland Peninsula, Baffin Island, Arctic Canada. *Quaternary Science Reviews*, 168, p. 79-100

Mate D.J., Campbell D.C, Barrie J.V., Hughes Clarke J.E., Muggah J., Bell T., and Forbes D.L. (2015). Integrated seabed mapping of Frobisher Bay, southern Baffin Island, Nunavut to support infrastructure development, exploration and natural-hazard assessment. *in* Summary of Activities 2014, Canada-Nunavut Geoscience Office, p. 145–152.

Miller G.H., Wolfe A.P., Briner J.P., Sauer P.E., and Nesje A. (2005). Holocene glaciation and climate evolution of Baffin Island, Arctic Canada. *Quaternary Science Reviews*, v.24(14-15), p. 1703-1721.

Normandeu A., MacKillop K., Macquarrie M., Richards C., Bourgault D., Campbell D.C., Maselli V., Philibert G., and Hughes Clarke J. (2021). Submarine landslides triggered by iceberg collision with the seafloor. *Nature Geoscience*, 14, p. 599-605.

Osterman L.E. (1982). Late Quaternary history of southern Baffin Island, Canada: A study of foraminifera and sediments from Frobisher Bay. PhD Thesis, Department of Geological Sciences, University of Colorado.

Pinet N., Brake V., Campbell C., and Duchesne M.J. (2015). Geomorphological characteristics and variability of Holocene mass-transport complexes, St. Lawrence Estuary, Canada. *Geomorphology*, 228, p. 286-302

Piper D.J.W., Letson J.R.J., De Iure A.M., and Barrie C.Q. (1983). Sediment accumulation in low-sedimentation wave-dominated, glaciated inlets. *Sedimentary Geology*, 36, p. 195-215.

Sedore P., Normandeau A. and Maselli V. (2022). Submarine landslides in Pangnirtung Fiord, eastern Baffin Island, Nunavut. *In* Summary of Activities 2021, Canada-Nunavut Geoscience Office, p. 31-46

Squires C.A. (1984). The Late-Foxe deglaciation of the Burton Bay area, southeastern Baffin Island, N.W.T. Unpublished M.A. Thesis, Department of Geography, University of Windsor, 115 p.

Stravers J.A., Miller G.H., and Kaufman D.S. (1992). Late glacial ice margins and deglacial chronology for southeastern Baffin Island and Hudson Strait, eastern Canadian Arctic. *Canadian Journal of Earth Sciences*, v. 29, no. 5, p. 1000–1017, doi: 10.1139/e92-083

Syvitski J., Burrell D.C., and Skei J.M. (1987). Subaqueous slope failure. *In* Syvitski J.P.M. et al. (Eds.) *Fjords: Processes and Products*, p. 175-210. Springer-Verlag Publishing.

Syvitski J. and Lee H.J. (1997). Postglacial sequence stratigraphy of Lake Melville, Labrador. *Marine Geology*, 143(1-4), p. 55-79.

Syvitski J., Andrews J.T., Schafer C.T., and Stravers J.A. (2022). Sediment fill of Baffin Island fjords: Architecture and rates. *Quaternary Science Reviews*, 284, 107474.

Todd B.J., Shaw J., Campbell D.C., and Mate D.J. (2016). Preliminary interpretation of the marine geology of Frobisher Bay, Baffin Island, Nunavut. *In* Summary of Activities 2016, Canada-Nunavut Geoscience Office, p. 61-66.

Tremblay T., Day S., McNeil R., Smith K., Richardson M., and Shirley J. (2015). Overview of surficial geology mapping and geochemistry in the Sylvia Grinnell Lake area, Baffin Island, Nunavut. *in* Summary of Activities 2015, Canada-Nunavut Geoscience Office, p. 107– 120.

Appendix A. Sediment Cores

A.1 Core collection

Sediment cores for this research were collected aboard CCGS *Amundsen* (2014-2017) and RV *Nuliajuk* (2016-2017). Full details on collection are available in the Methods sections of Chapters 2 and 4. Full metadata for sediment cores collected for this project can be found on NRCan's Expedition Database (NRCan 2022). Key metadata are presented below (Table A.1).

Table A.1 Metadata for sediment cores collected in IFB for this project. Cruise is the number assigned by GSC-A for each trip. Station is a unique number assigned during each cruise or expedition to denote a sampling site. Year indicates the year in which the sample was collected. Type indicates the coring system used (Pi, Piston; G, Gravity; Pu, Push; TW, Trigger Weight). Latitude and Longitude are the position of the vessel at time of sampling. Water Depth is the depth in metres recorded acoustically at time of sampling. Length is the amount in centimetres of core collected at each station.

Cruise	Station	Year	Type	Latitude	Longitude	Water Depth (m)	Length (cm)
2014805	0004	2014	Pi	63.640465	-68.620120	135	564
2015805	0008	2015	Pi	63.637850	-68.611167	125	508
2015805	0008	2015	TW	63.637580	-68.611167	125	5
2015805	0009	2015	Pi	63.639767	-68.611750	115	581
2015805	0009	2015	TW	63.639767	-68.611750	115	~5
2015805	0010	2015	Pu	63.640167	-68.612183	121	22
2015805	0011	2015	Pu	63.644100	-68.610633	128	26
2016804	0001	2016	Pi	63.545900	-68.475400	210	513
2016804	0002	2016	Pi	63.563550	-68.505783	204	521
2016804	0003	2016	Pu	63.546000	-68.475166	208	21
2016804	0004	2016	Pu	63.564166	-68.501833	204	21
2016804	0005	2016	Pu	63.582000	-68.521000	187	25
2016804	0006	2016	Pu	63.583000	-68.522166	186	23
2016804	0007	2016	Pi	63.582900	-68.522866	190	491
2016804	0008	2016	Pi	63.582416	-68.519966	190	536
2016804	0009	2016	Pi	63.643150	-68.618583	101	536
2016804	0010	2016	Pi	63.641433	-68.615166	115	526
2016804	0011	2016	Pu	63.642716	-68.619300	104	29
2016804	0012	2016	Pu	63.641500	-68.615333	117	28.5
2016804	0013	2016	Pu	63.640600	-68.620883	135	22
2017805	0003	2017	Pi	63.687083	-68.624750	146	465.5
2017805	0005	2017	Pi	63.597950	-68.523683	180	442
2017805	0006	2017	Pi	63.362050	-68.182050	118	524
2016Nuliajuk	0001	2016	G	63.680291	-68.483726	66	72.5
2016Nuliajuk	0002	2016	G	63.668585	-68.501031	66	34
2016Nuliajuk	0003	2016	G	63.669201	-68.520091	72	73
2016Nuliajuk	0004	2016	G	63.737845	-68.681290	53	5
2016Nuliajuk	0005	2016	G	63.737560	-68.681103	51	18
2016Nuliajuk	0006	2016	G	63.665151	-68.644011	146	15
2016Nuliajuk	0007	2016	G	63.630586	-68.613690	131	74
2016Nuliajuk	0008	2016	G	63.556211	-68.642011	98	61.5
2016Nuliajuk	0009	2016	G	63.564180	-68.685011	80	61
2016Nuliajuk	0010	2016	G	63.549816	-68.699063	68	47
2016Nuliajuk	0011	2016	G	63.547668	-68.701448	60	54
2016Nuliajuk	0012	2016	G	63.551456	-68.718815	54	5
2016Nuliajuk	0013	2016	G	63.551528	-68.718276	54	26
2016Nuliajuk	0014	2016	G	63.553303	-68.713540	59	39
2016Nuliajuk	0015	2016	G	63.552368	-68.517828	135	33.5
2016Nuliajuk	0016	2016	G	63.548893	-68.512758	140	0
2016Nuliajuk	0017	2016	G	63.548913	-68.511906	140	10
2016Nuliajuk	0018	2016	G	63.622918	-68.424238	145	12

Table A.1 Cont.

Cruise	Station	Year	Type	Latitude	Longitude	Water Depth (m)	Length (cm)
2016Nuliajuk	0019	2016	G	63.623620	-68.424698	145	22
2016Nuliajuk	0020	2016	G	63.605621	-68.480570	105	15
2016Nuliajuk	0021	2016	G	63.581648	-68.525788	178	188
2016Nuliajuk	0022	2016	G	63.526191	-68.472028	122	50.5
2016Nuliajuk	0023	2016	G	63.524013	-68.465658	129	40
2016Nuliajuk	0024	2016	G	63.594133	-68.331988	98	72
2016Nuliajuk	0025	2016	G	63.570228	-68.161805	46	75
2016Nuliajuk	0026	2016	G	63.558175	-68.137678	118	94
2016Nuliajuk	0027	2016	G	63.521943	-68.280406	138	66
2016Nuliajuk	0028	2016	G	63.510045	-68.240681	160	49
2016Nuliajuk	0029	2016	G	63.502848	-68.235345	144	122
2016Nuliajuk	0030	2016	G	63.495233	-68.231798	153	179
2016Nuliajuk	0031	2016	G	63.459758	-68.343975	147	10
2016Nuliajuk	0032	2016	G	63.460435	-68.341966	148	30.5
2017Nuliajuk	0001	2017	G	63.530666	-68.465166	149	10
2017Nuliajuk	0002	2017	G	63.531666	-68.470700	140	23
2017Nuliajuk	0003	2017	G	63.552566	-68.705666	63	0
2017Nuliajuk	0004	2017	G	63.552600	-68.705600	67	5
2017Nuliajuk	0005	2017	G	63.553233	-68.705133	60	0
2017Nuliajuk	0006	2017	G	63.553500	-68.705166	60.4	31.5
2017Nuliajuk	0007	2017	G	63.559666	-68.730400	41	88
2017Nuliajuk	0008	2017	G	63.476333	-68.241450	143	90
2017Nuliajuk	0009	2017	G	63.478000	-68.236000	237	156.5
2017Nuliajuk	0010	2017	G	63.480283	-68.230066	260	0
2017Nuliajuk	0011	2017	G	63.480166	-68.230000	267	54
2017Nuliajuk	0012	2017	G	63.476000	-68.229666	268	84
2017Nuliajuk	0013	2017	G	63.349266	-68.276016	130	92
2017Nuliajuk	0014	2017	G	63.353333	-68.287833	124	51
2017Nuliajuk	0015	2017	G	63.372666	-68.323833	81	74
2017Nuliajuk	0016	2017	G	63.377833	-68.328833	69.4	139
2017Nuliajuk	0017	2017	G	63.607583	-68.480050	103	159
2017Nuliajuk	0018	2017	G	63.682333	-68.485000	68.8	116.5
2017Nuliajuk	0019	2017	G	63.721333	-68.514000	31.1	20
2017Nuliajuk	0020	2017	G	63.721250	-68.513500	34.6	53
2017Nuliajuk	0021	2017	G	63.710833	-68.501166	54	43
2017Nuliajuk	0022	2017	G	63.711800	-68.502416	46.5	102.5
2017Nuliajuk	0023	2017	G	63.732000	-68.515500	15.9	65

A.2 Sediment Core Diagrams

Sediment cores for this research were transported to the GSA-A Core Lab for analysis and archiving. A full description of core logging is presented in the Methods sections of Chapters 2 and 4.

The core diagrams presented below, following the order in Table A.1, were produced following the same format. This format includes (from left to right): x-radiograph split-core imagery, split-core photography, lithofacies diagram (following the legend in Fig. A.1), relative carbonate content, calibrated radiocarbon dates, grain size composition, magnetic susceptibility, bulk density, and shear strength. A summary of the physical properties measurements and their significance is presented in Table A.2. Sometimes a core diagram will be missing one or more of these components, based on how analysis proceeded. Not all cores presented in Table A.1 have an accompanying core diagram. For example, shorter cores (including trigger weight and push cores) were described visually while lacking most of the physical property measurements, and so were omitted from Appendix A.2.

In some diagrams, the core lab ID number is preceded with a number in the format *M##*. These numbers refer to entries in Table 2.2 of Chapter 2.

Table A.2 Summary of physical property measurements performed on sediment cores, the instruments used, and their significance. Simplified from Campbell et al. 2017.

Physical property	Instrument	Unit	Environmental significance
Relative $CaCO^3$ concentration	HCl, visual	Reaction intensity; none; 0-4	Provenance
Calibrated radiocarbon age	Accelerator mass spectrometer	Calibrated years before present (1950)	Date of deposition
Grain size	Laser particle analyzer	Percent	Provenance and depositional process
Magnetic susceptibility	Multisensor core logger	SI units	Provenance
Bulk density	Multisensor core logger	g/cm^3	Saturation and composition
Shear strength	Shear vane	kPa	Composition and structure

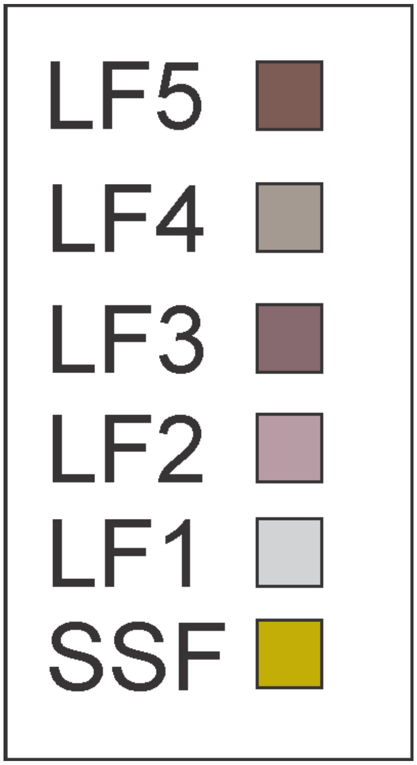

Figure A.1 Legend of lithofacies for sediment core diagrams in Appendix A. A full description of lithofacies is presented in Chapters 2 and 4.

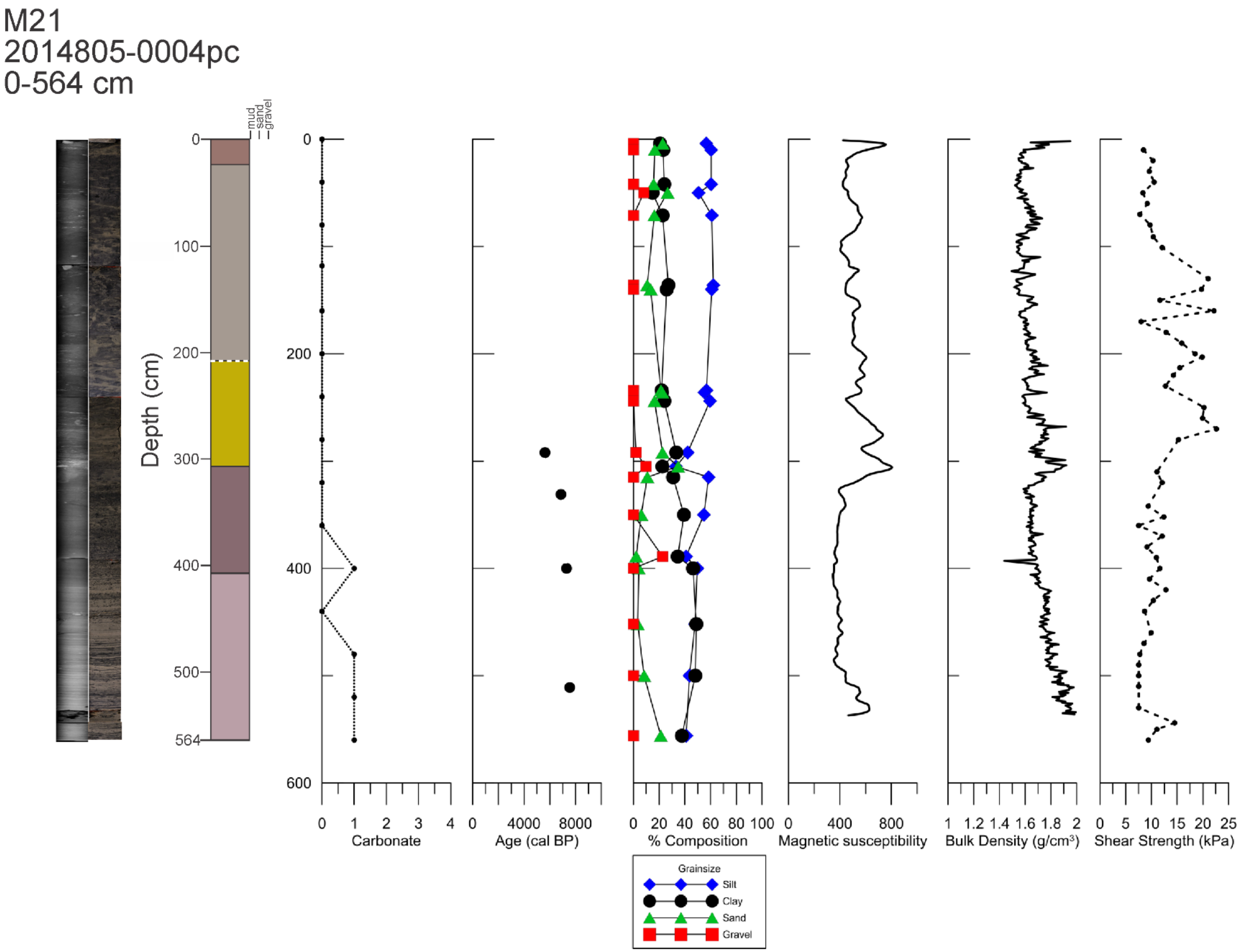

Figure A.2 Core diagram of 2014805-0004. Dashed line in log indicates uncertainty in location of contact. Also presented as core 226a in Table 4.2

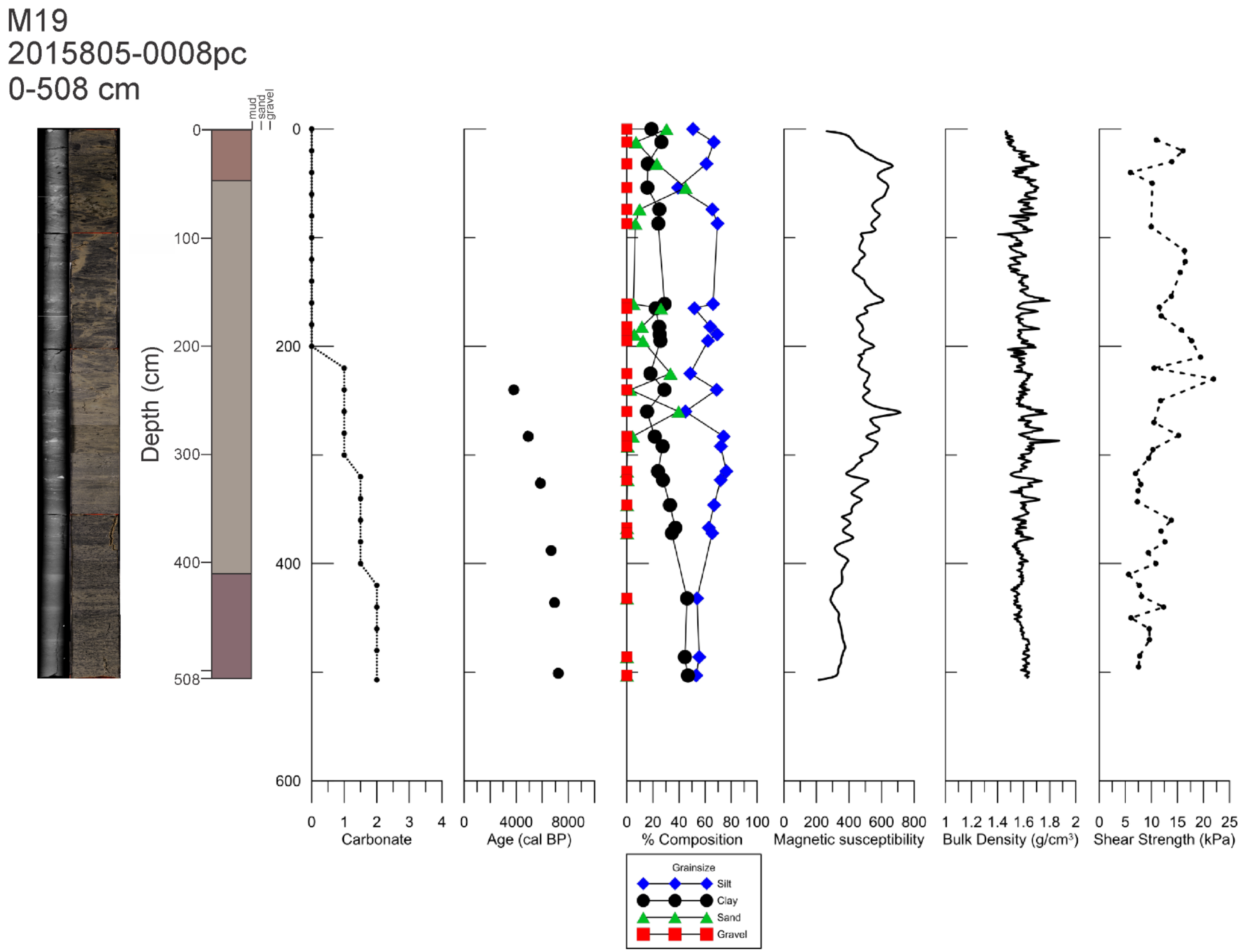

Figure A.3 Core diagram of 2015805-0008. Note: Carbonate concentration judged to half values during 2015 analysis.

M22
2015805-0009pc
0-581 cm

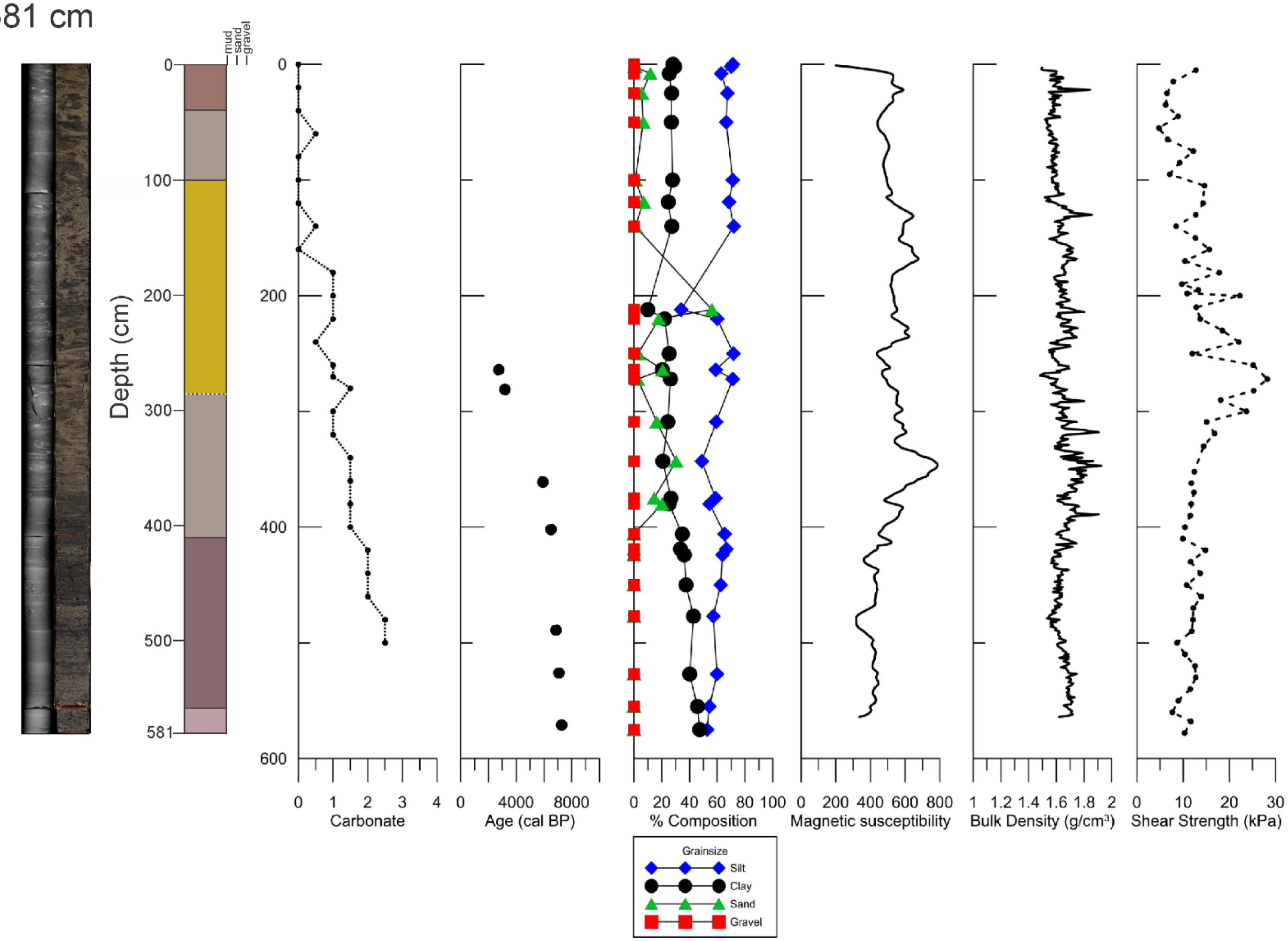

Figure A.4 Core diagram of 2015805-0009. Note: Carbonate concentration judged to half values during 2015 analysis. Also presented as core 227a in Table 4.2

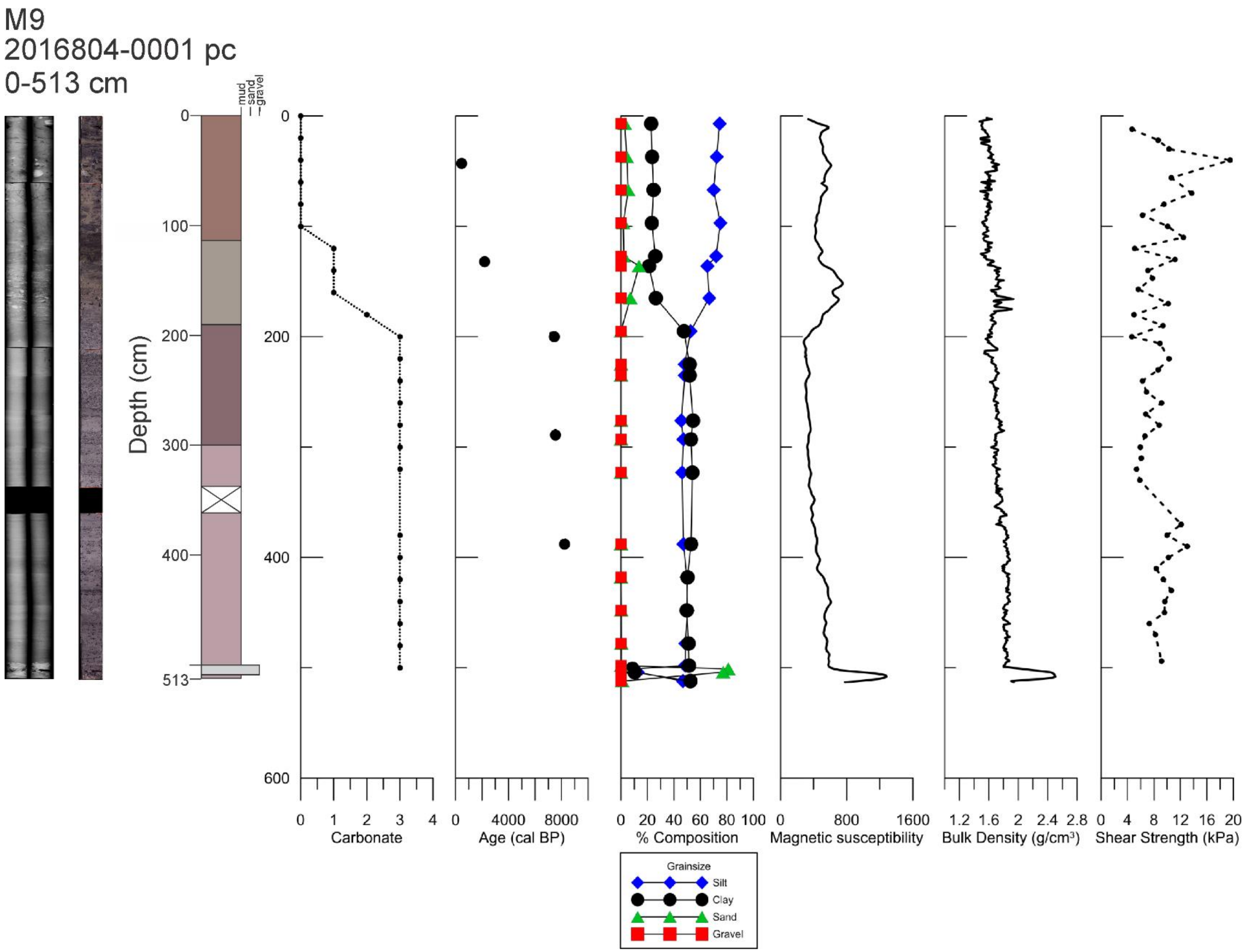

Figure A.5 Core diagram of 2016804-0001

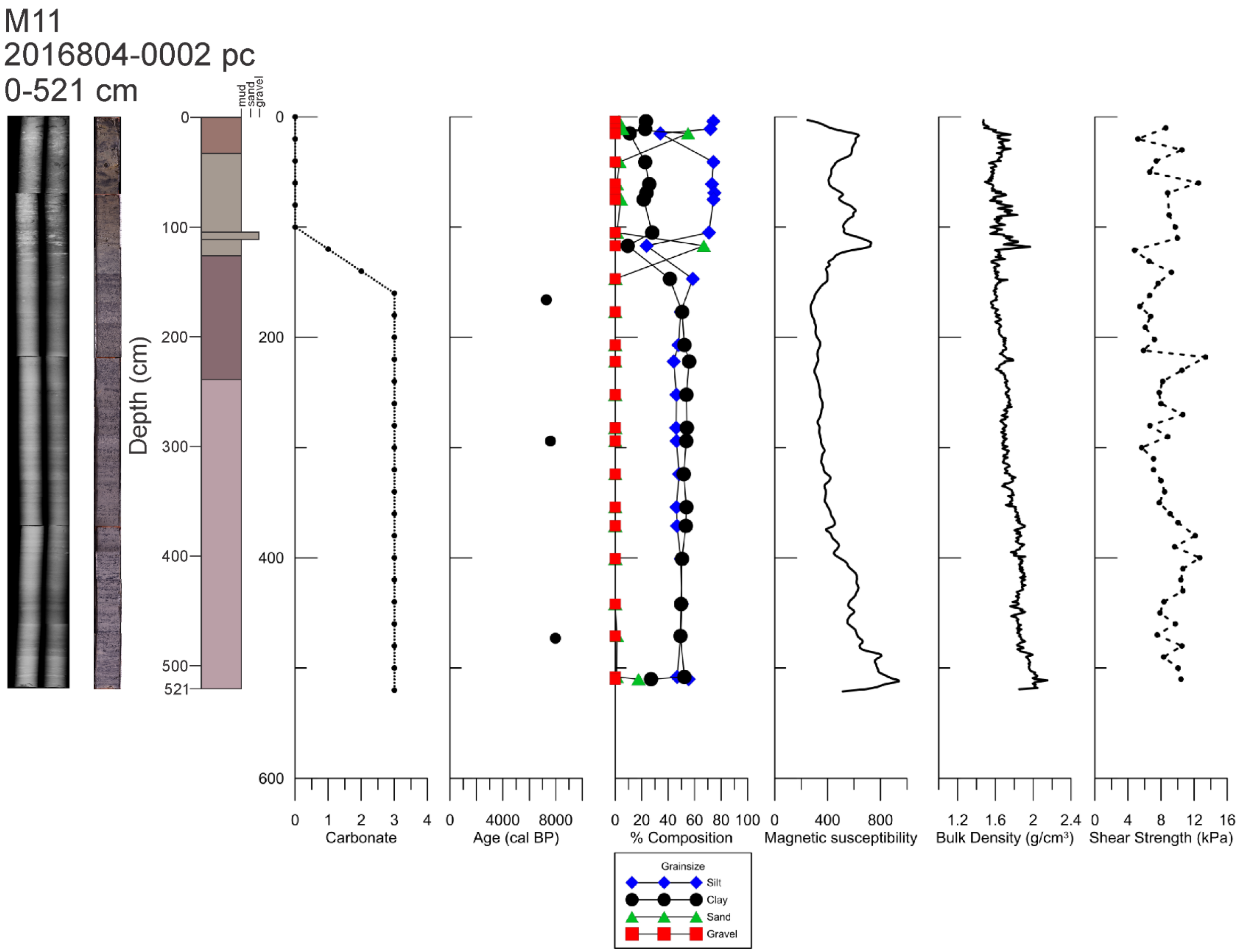

Figure A.6 Core diagram of 2016804-0002

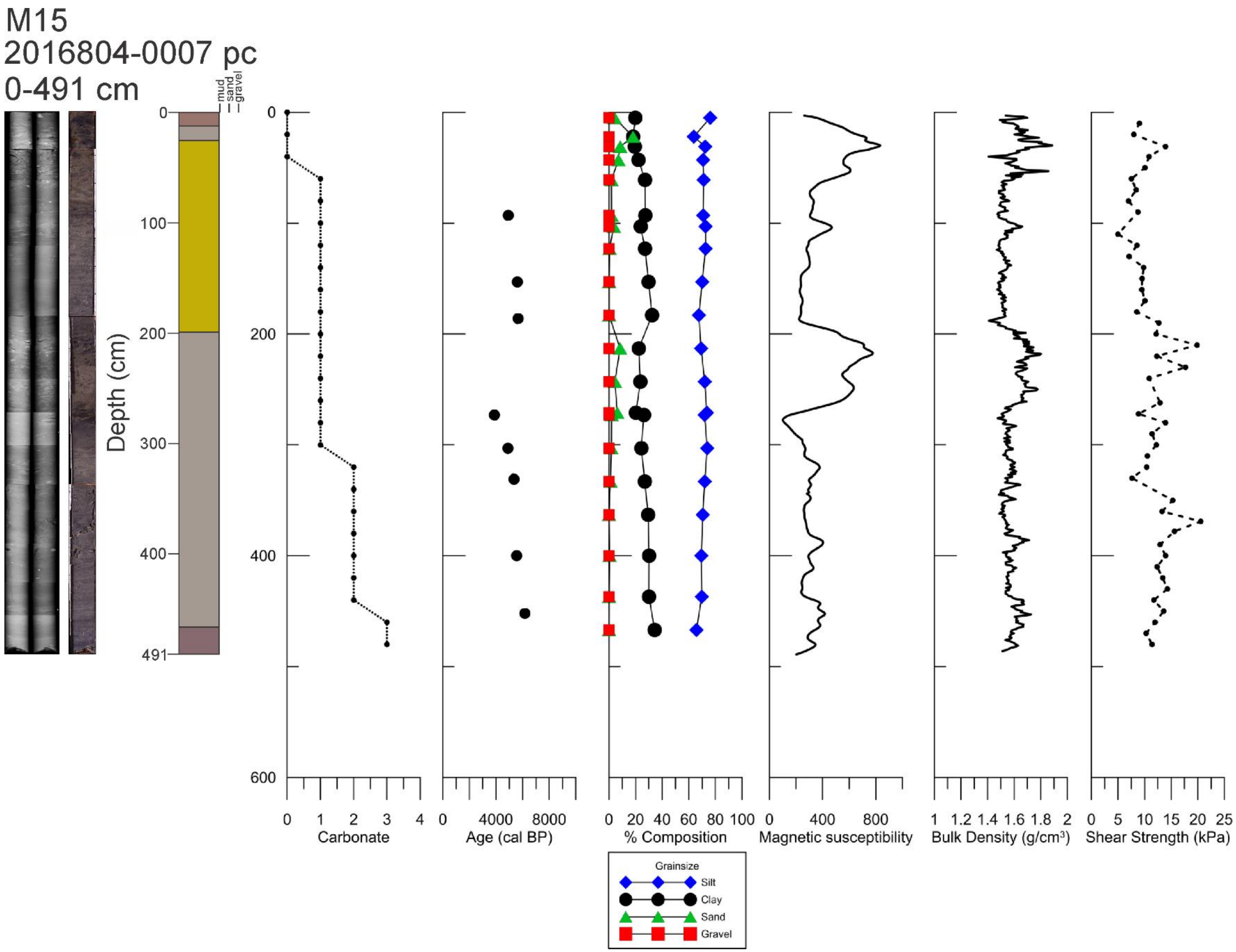

Figure A.7 Core diagram of 2016804-0007. Also presented as core 113a in Table 4.2

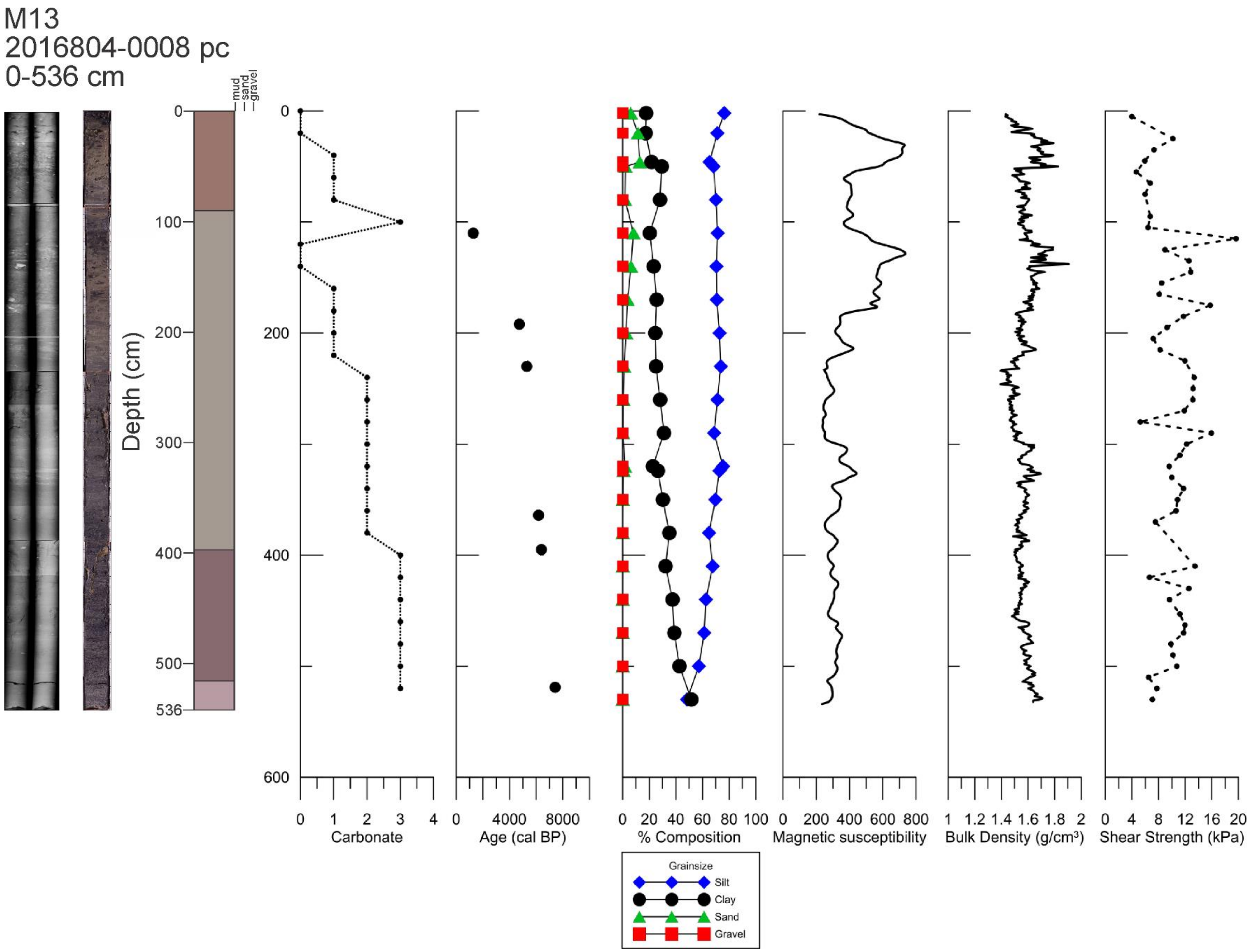

Figure A.8 Core diagram of 2016804-0008

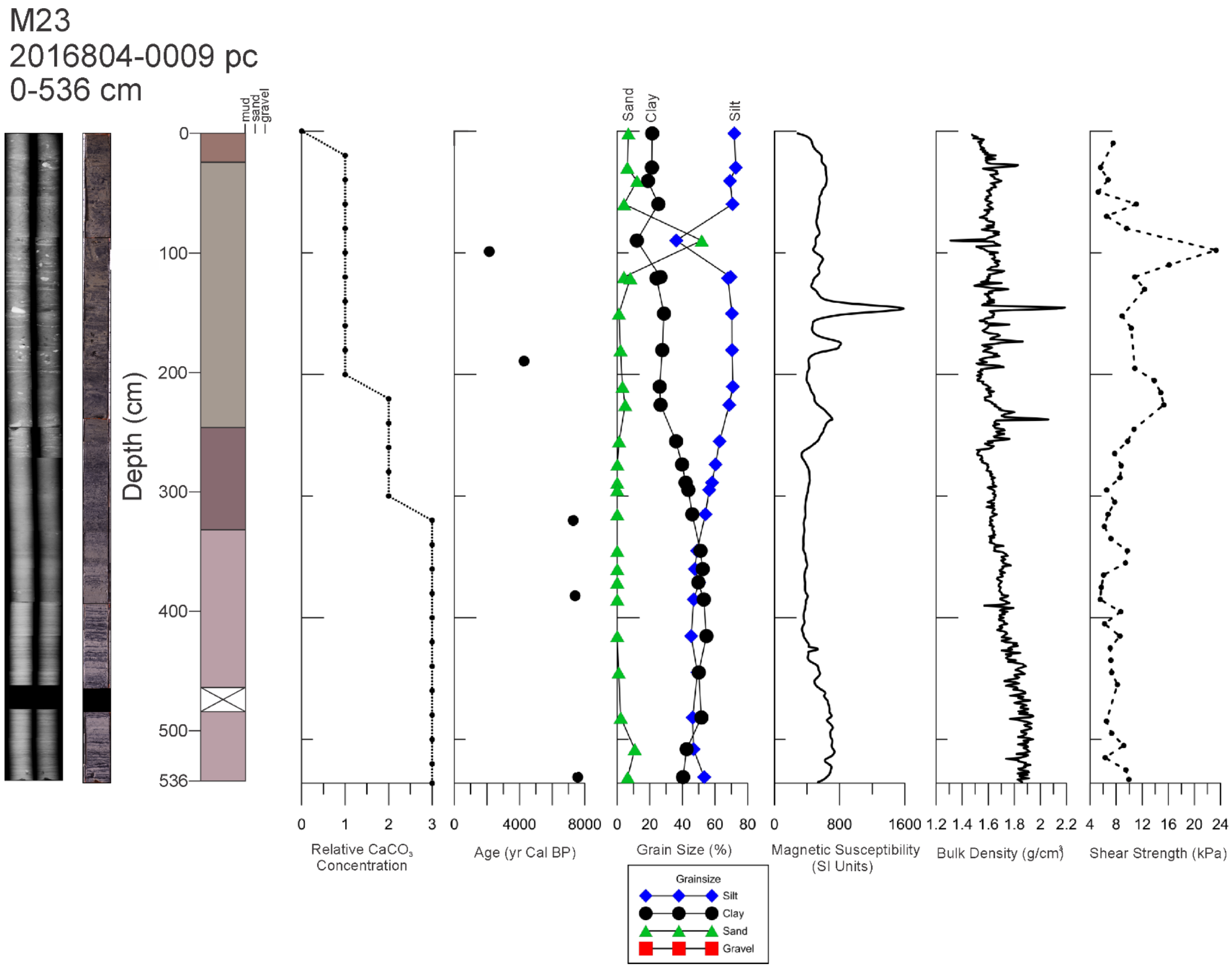

Figure A.9 Core diagram of 2016804-0009

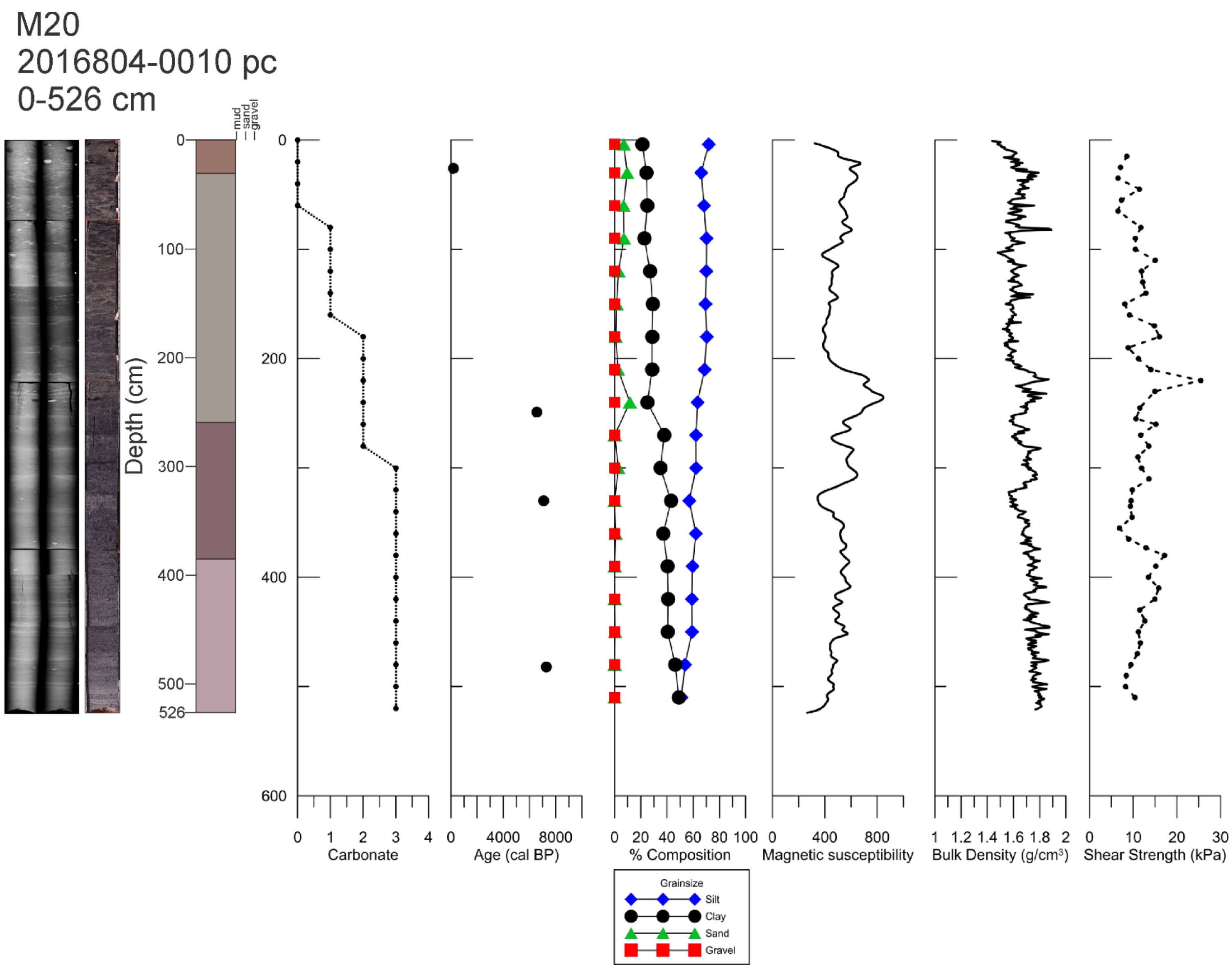

Figure A.10 Core diagram of 2016804-0010. Also presented as core 226b in Table 4.2

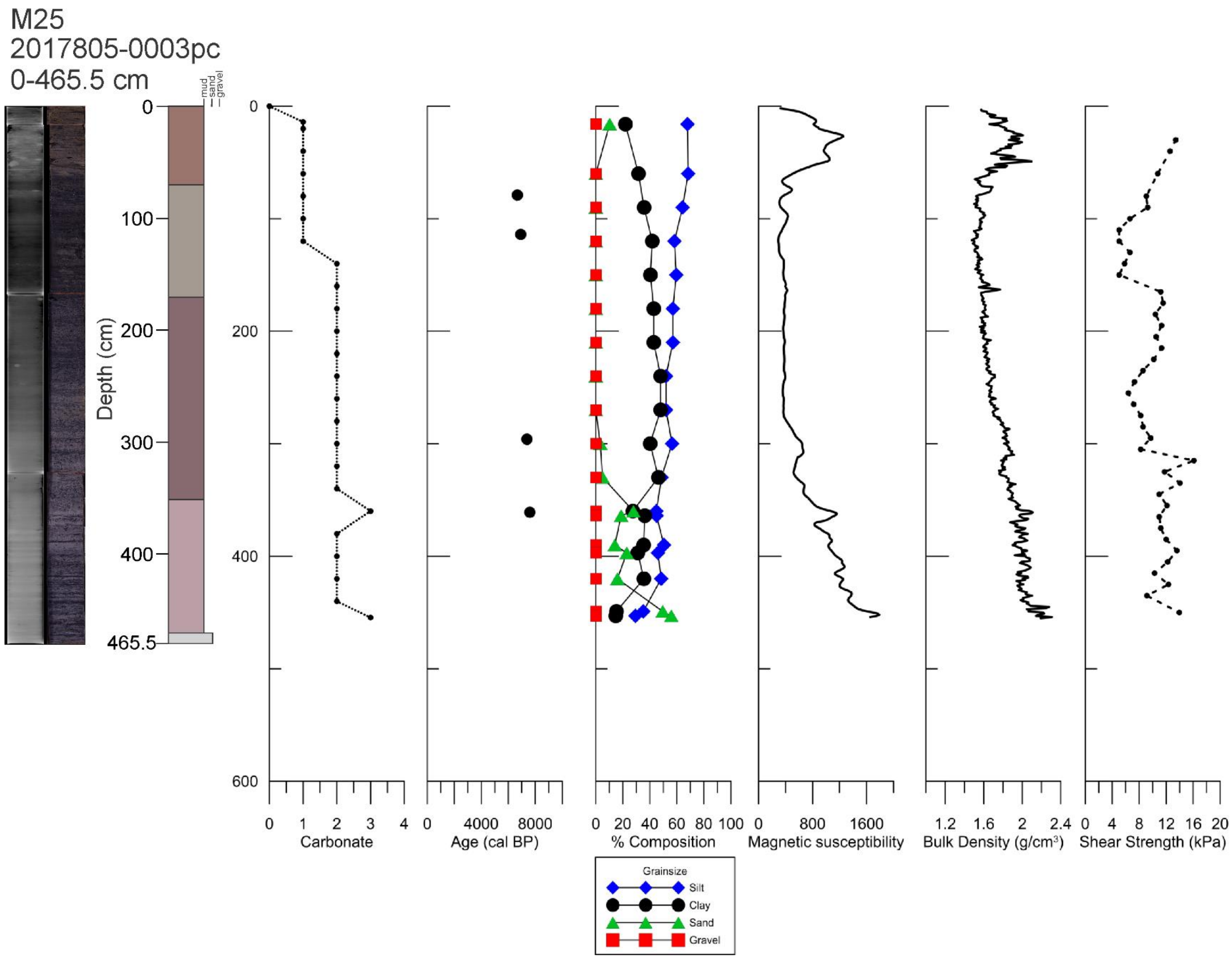

Figure A.11 Core diagram of 2017805-0003

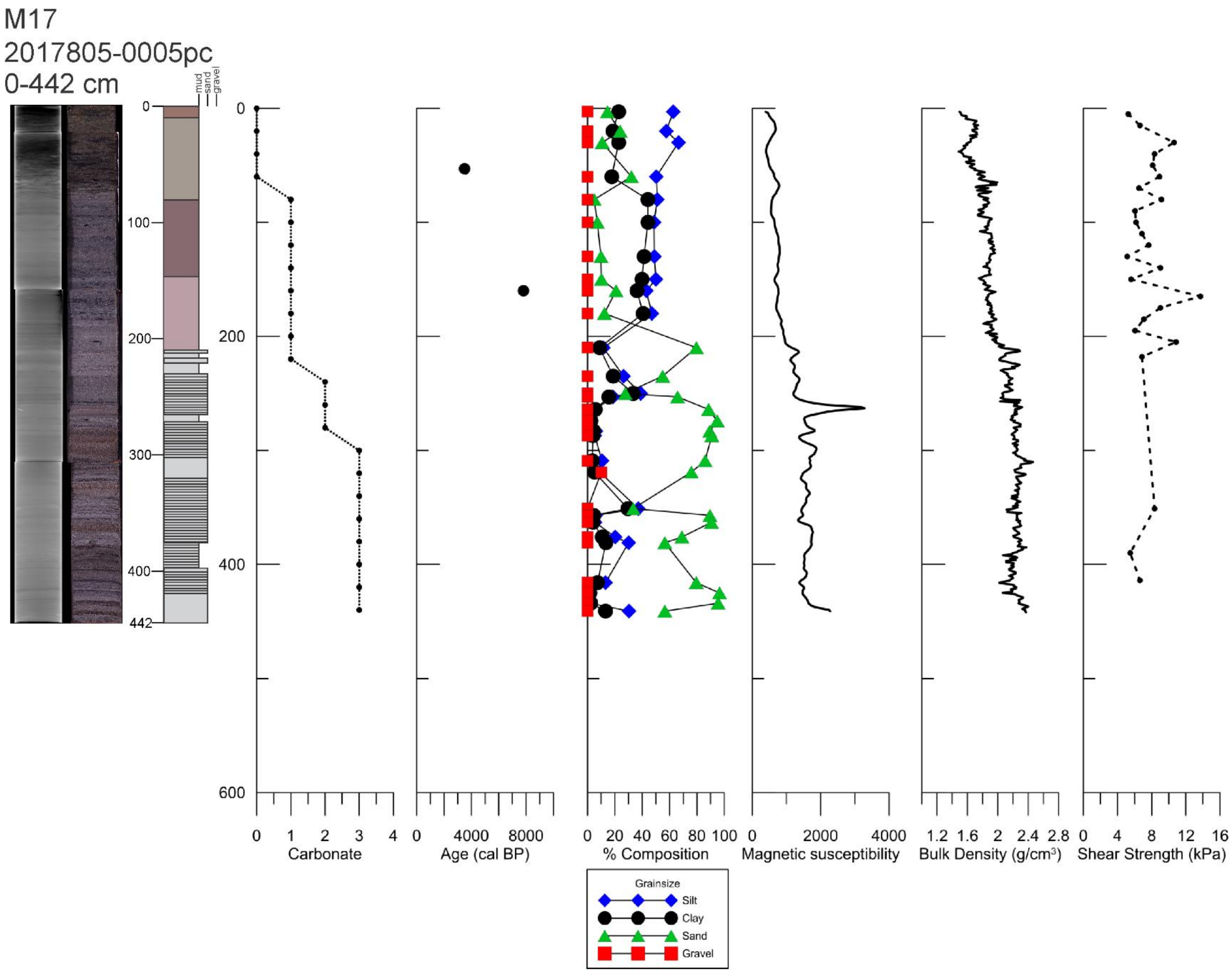

Figure A.12 Core diagram of 2017805-0005

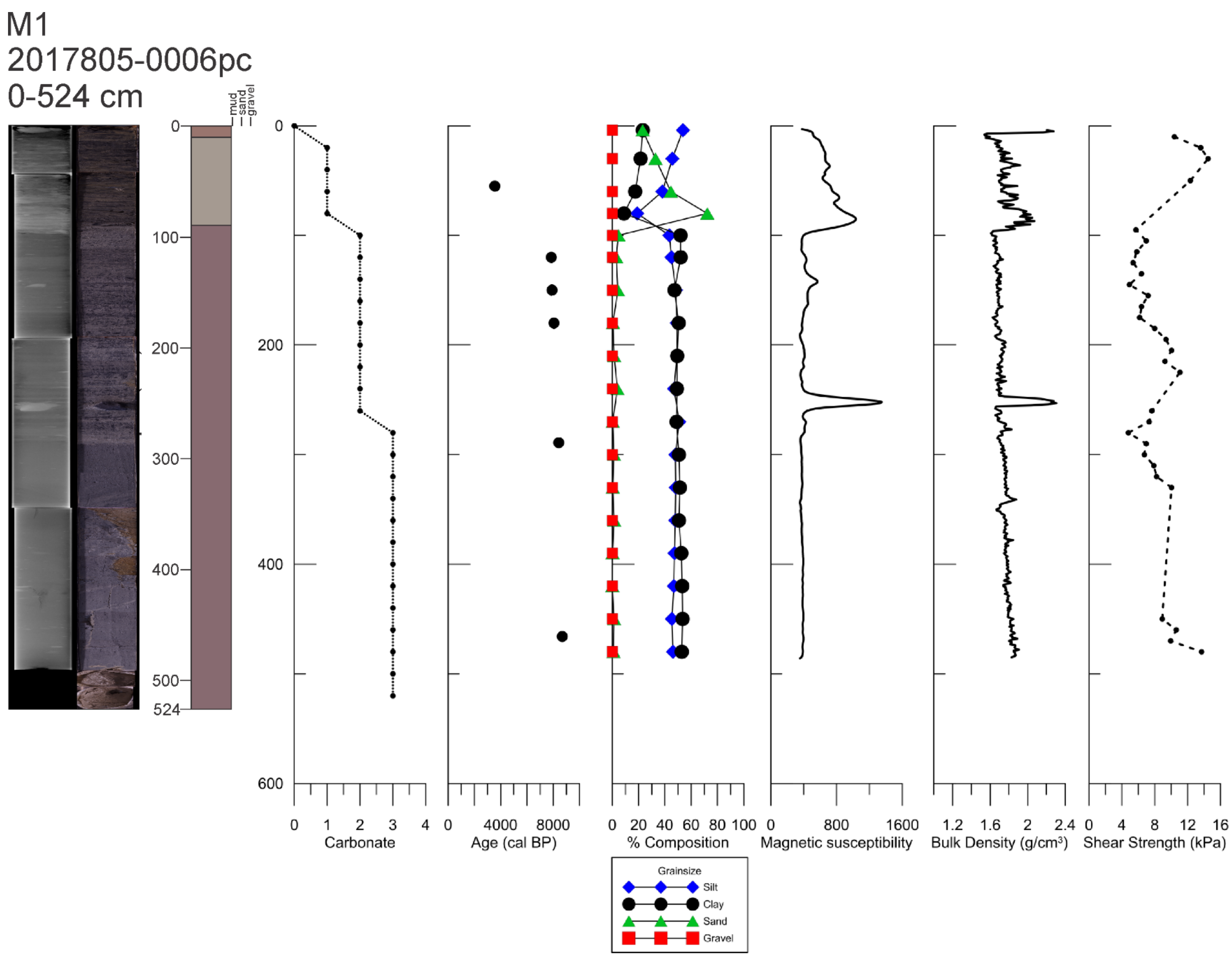

Figure A.13 Core diagram of 2017805-0006

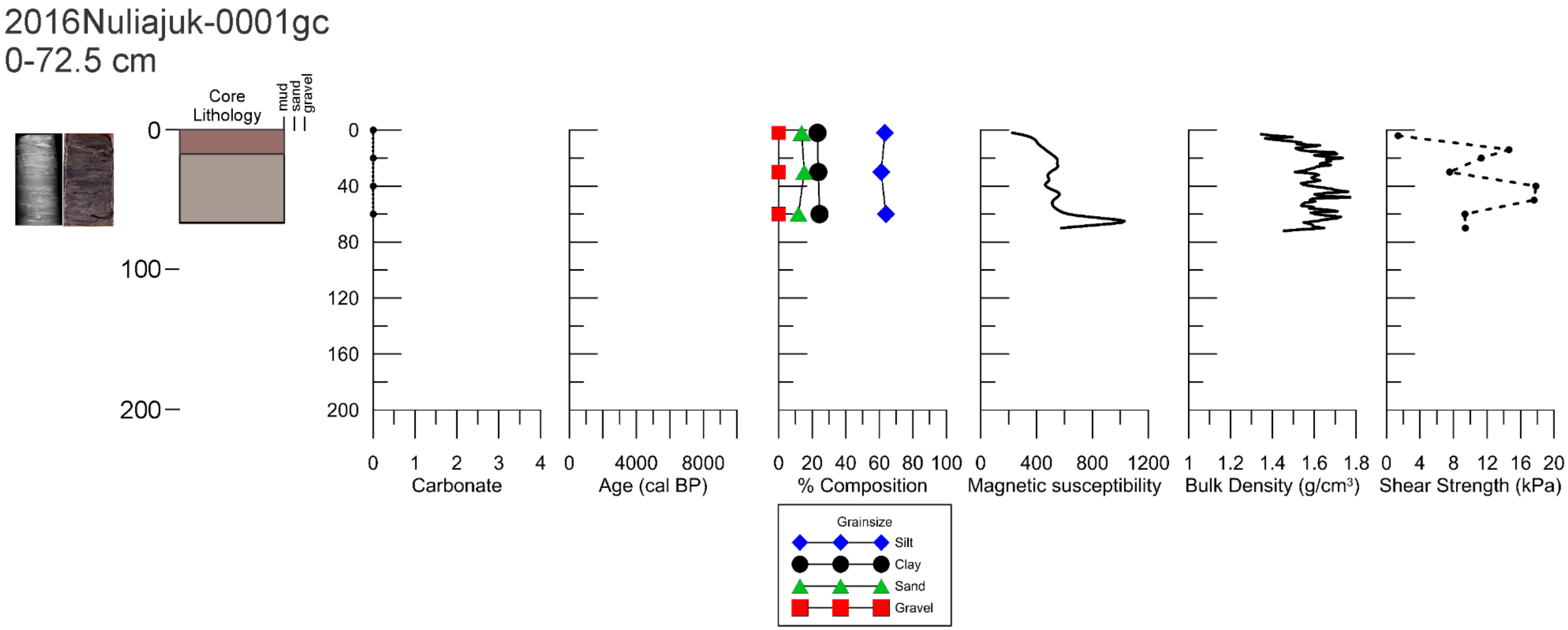

Figure A.14 Core diagram of 2016Nuliajuk-0001. Also presented as core 190a in Table 4.2

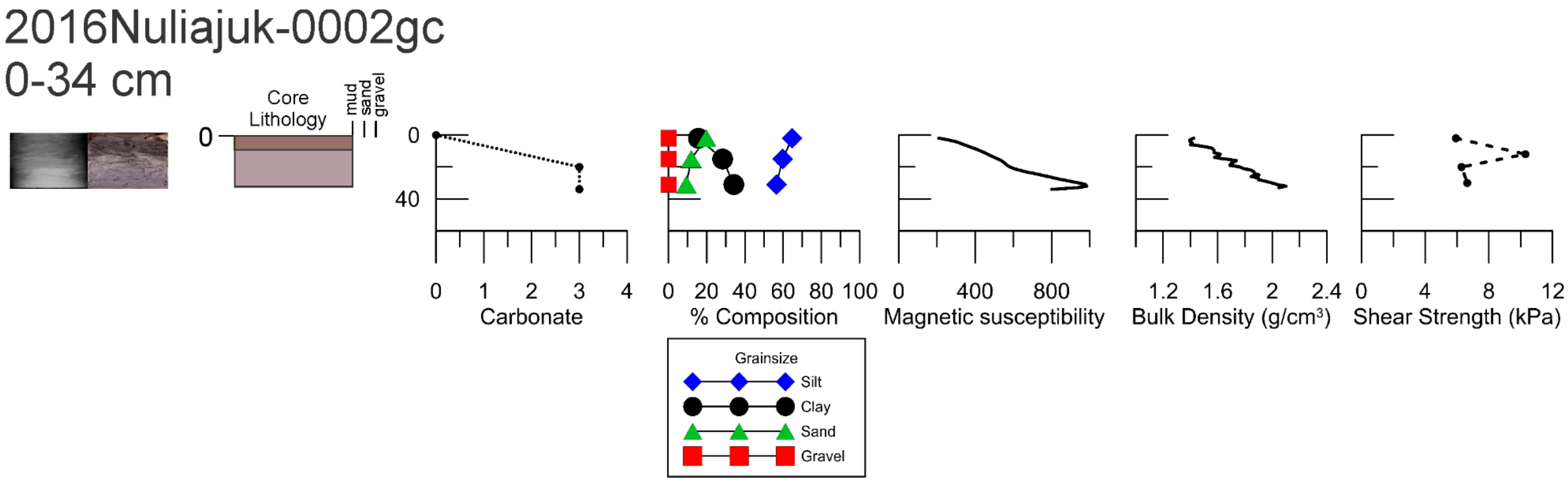

Figure A.15 Core diagram of 2016Nuliajuk-0002. Also presented as core 186a in Table 4.2

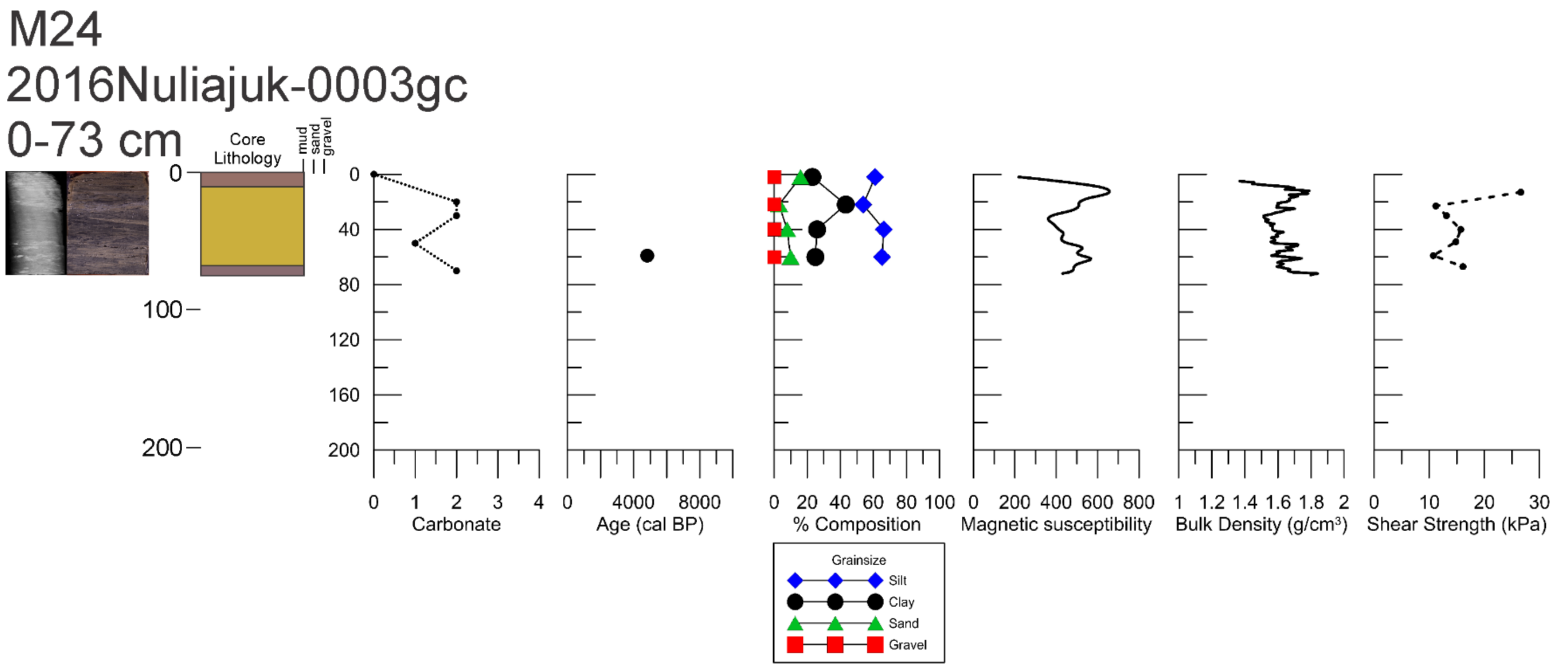

Figure A.16 Core diagram of 2016Nuliajuk-0003. Also presented as core 145a in Table 4.2

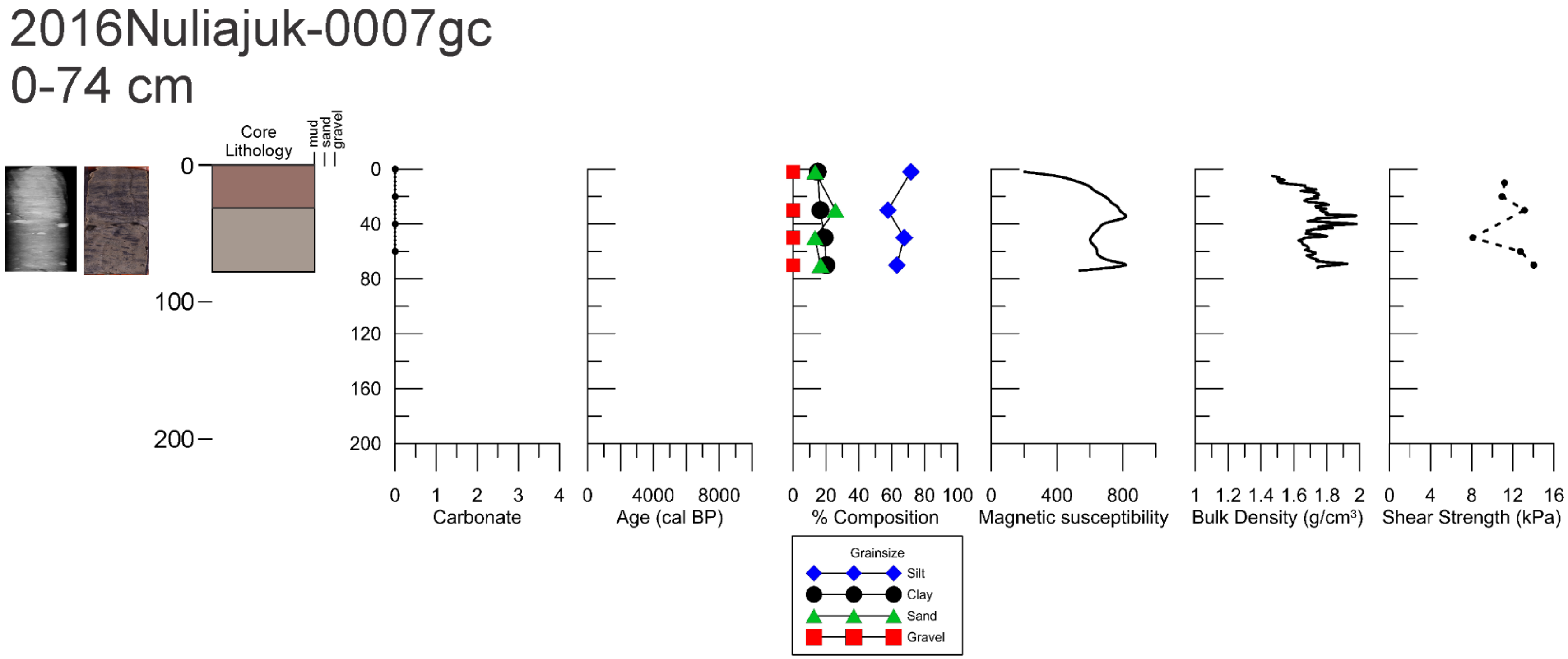

Figure A.17 Core diagram of 2016Nuliajuk-0007. Also presented as core 127a in Table 4.2

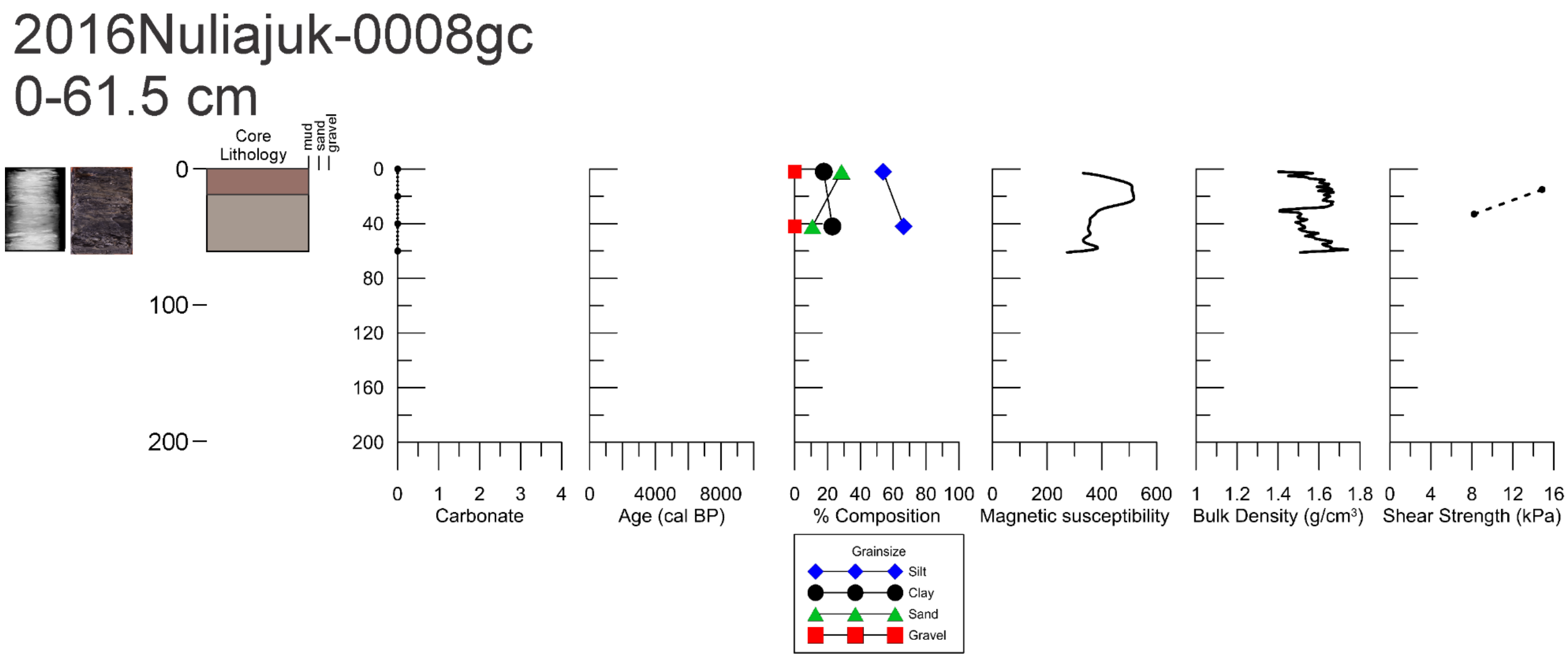

Figure A.18 Core diagram of 2016Nuliajuk-0008. Also presented as core 70a in Table 4.2

2016Nuliajuk-0009gc
0-61 cm

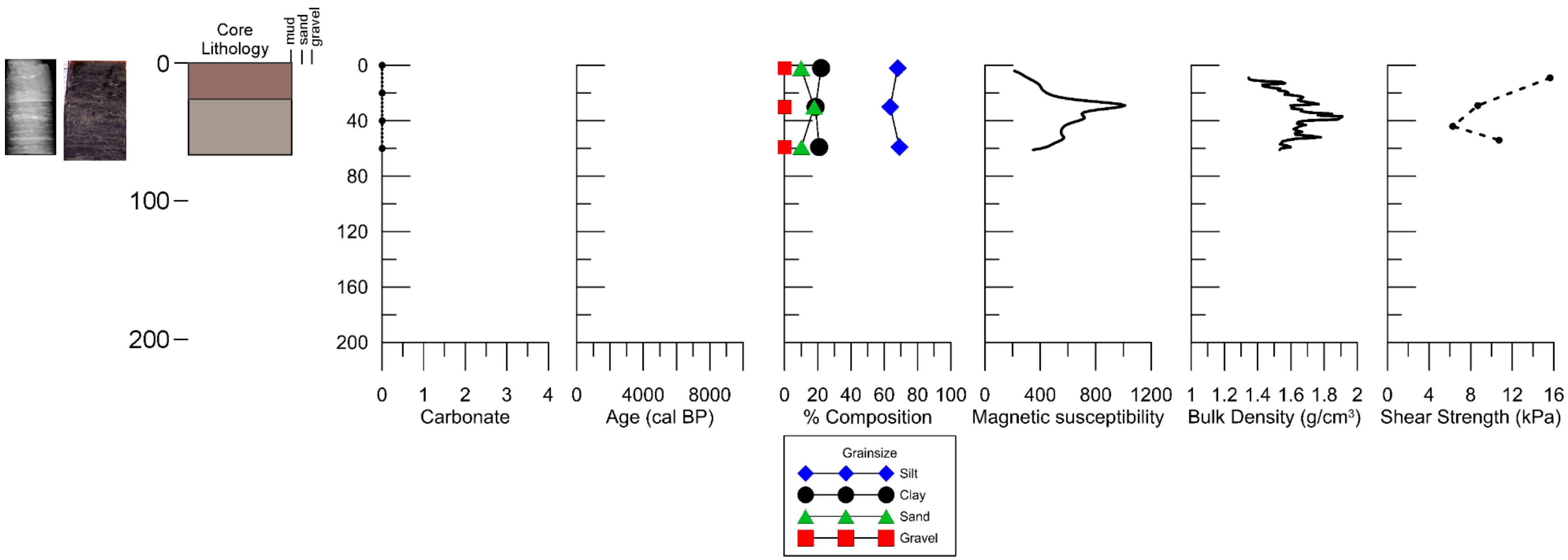

Figure A.19 Core diagram of 2016Nuliajuk-0009

2016Nuliajuk-0010gc
0-47 cm

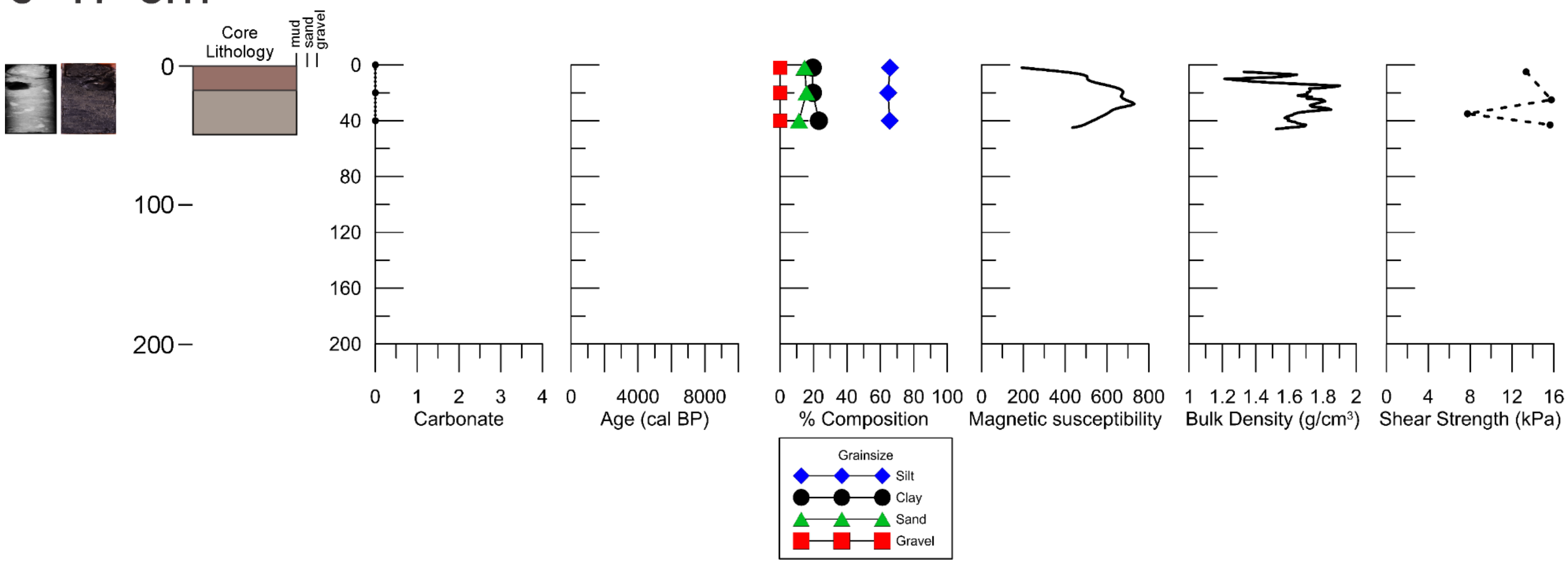

Figure A.20 Core diagram of 2016Nuliajuk-0010. Also presented as core 91a in Table 4.2

2016Nuliajuk-0011gc
0-54 cm

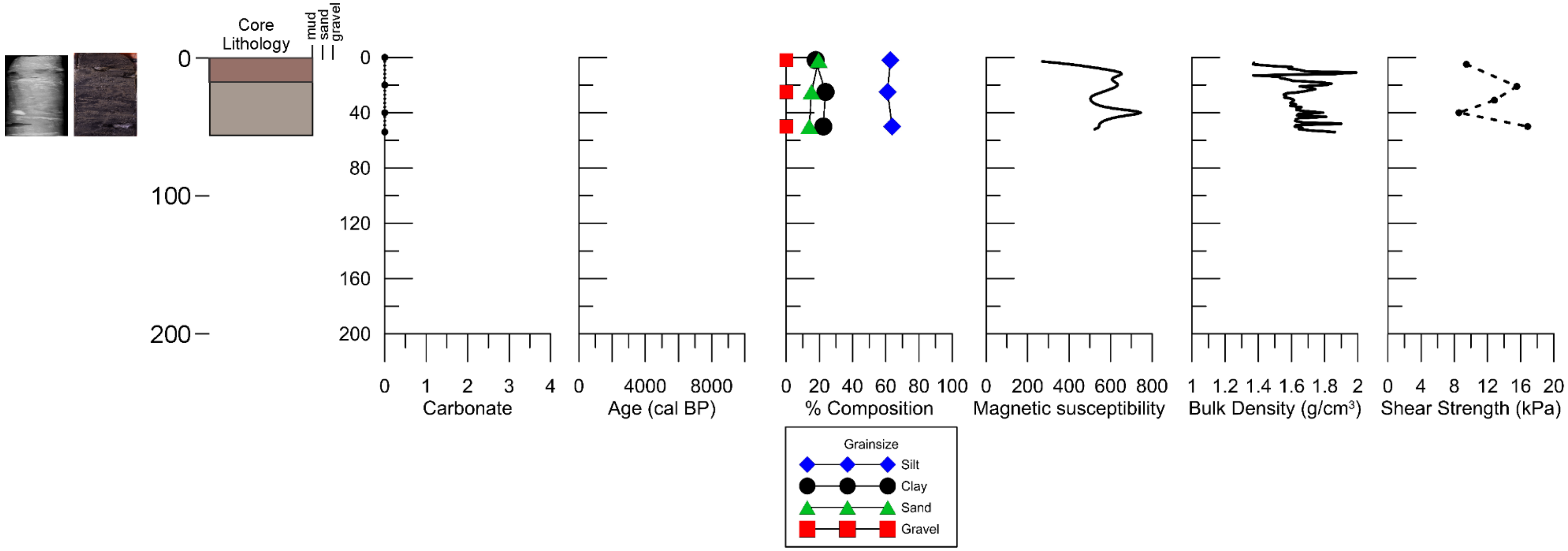

Figure A.21 Core diagram of 2016Nuliajuk-0011. Also presented as core 90a in Table 4.2

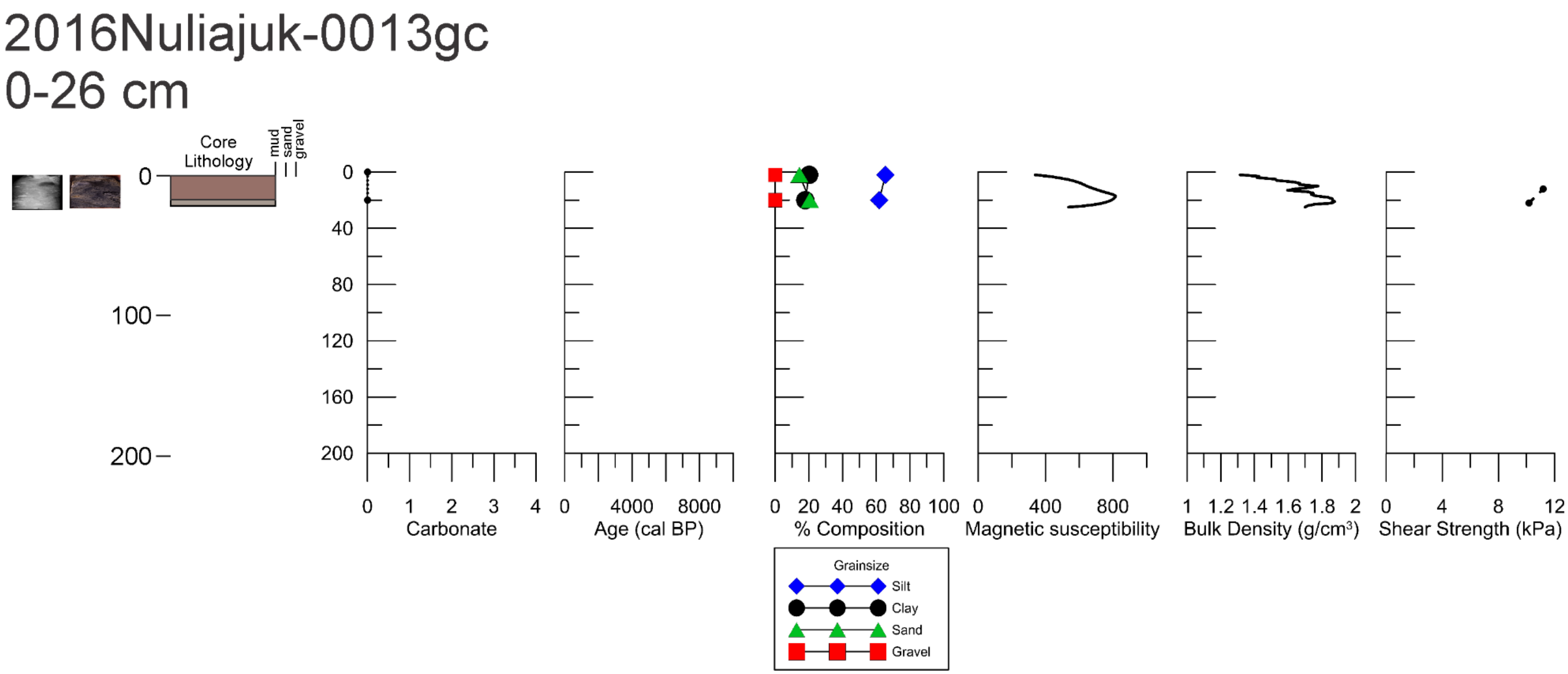

Figure A.22 Core diagram of 2016Nuliajuk-0013. Also presented as core 97b in Table 4.2

2016Nuliajuk-0014gc
0-39 cm

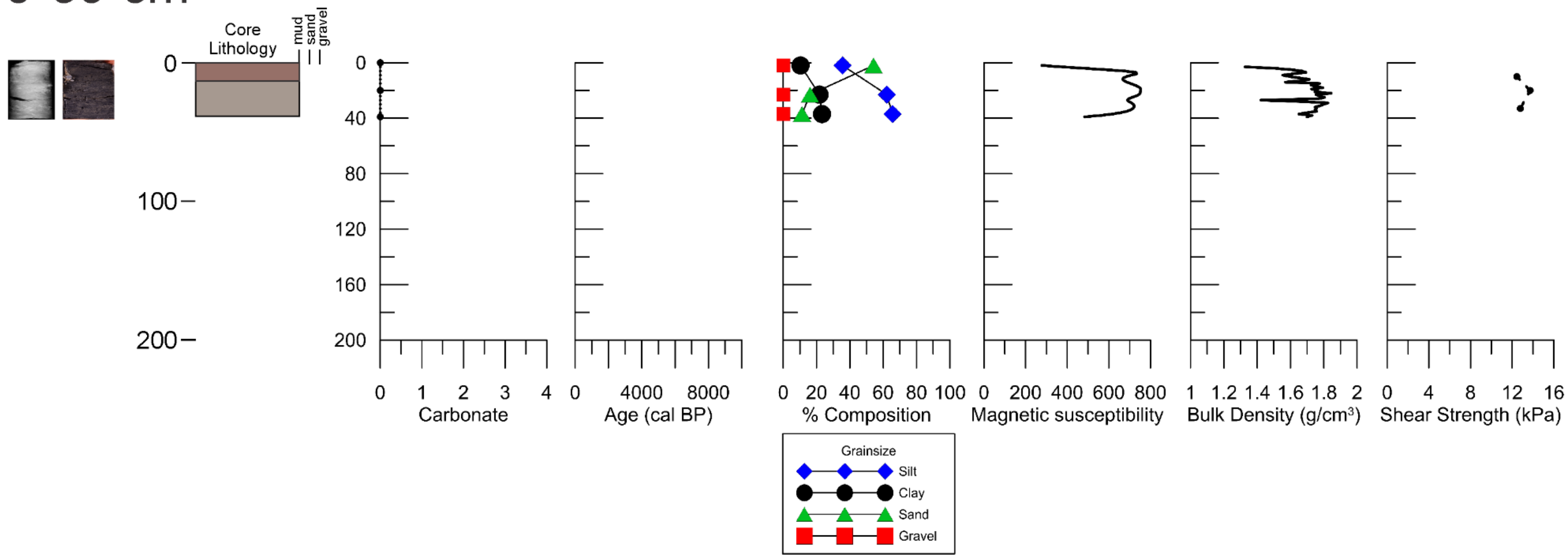

Figure A.23 Core diagram of 2016Nuliajuk-0014. Also presented as core 96a in Table 4.2

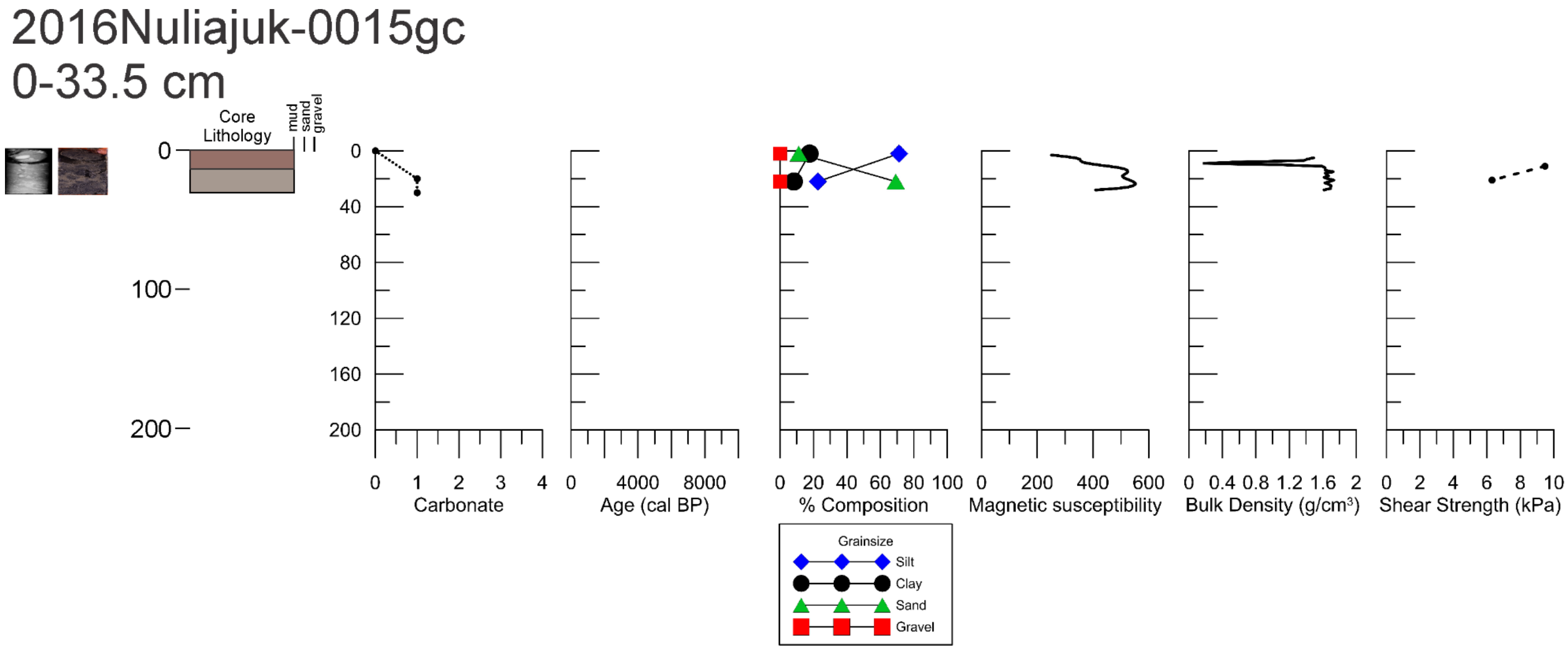

Figure A.24 Core diagram of 2016Nuliajuk-0015. Also presented as core 60a in Table 4.2

M14
2016Nuliajuk-0021gc
0-188 cm

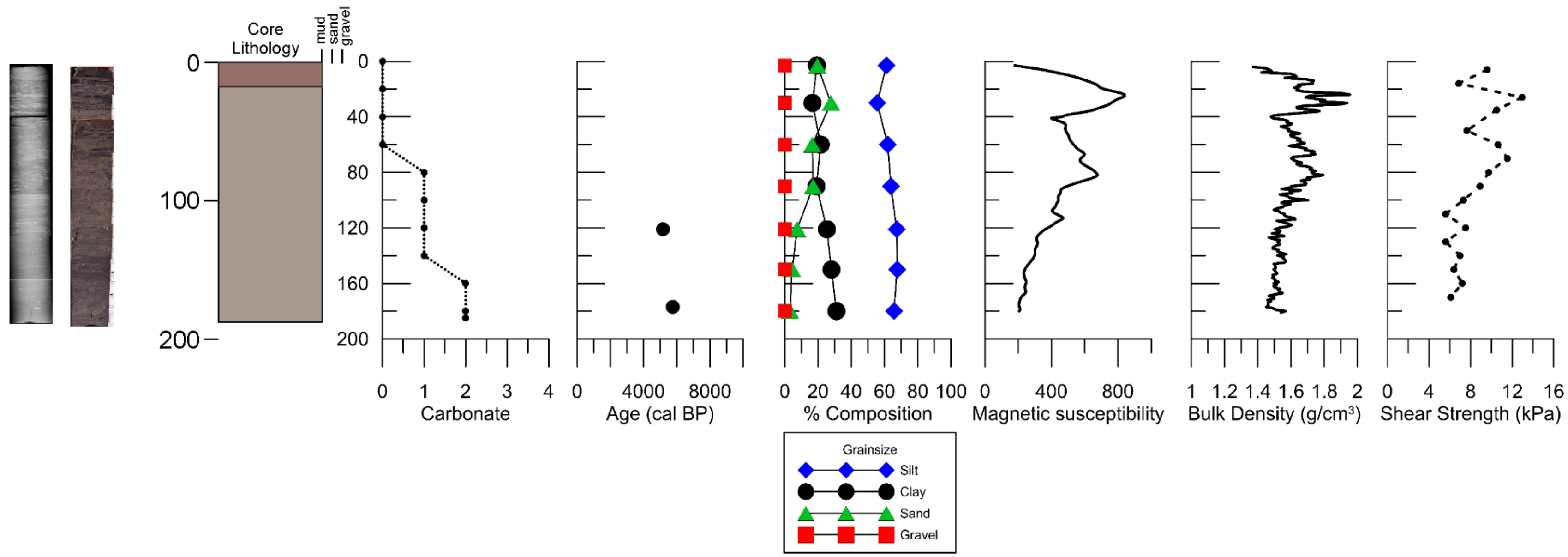

Figure A.25 Core diagram of 2016Nuliajuk-0021. Also presented as core 113b in Table 4.2

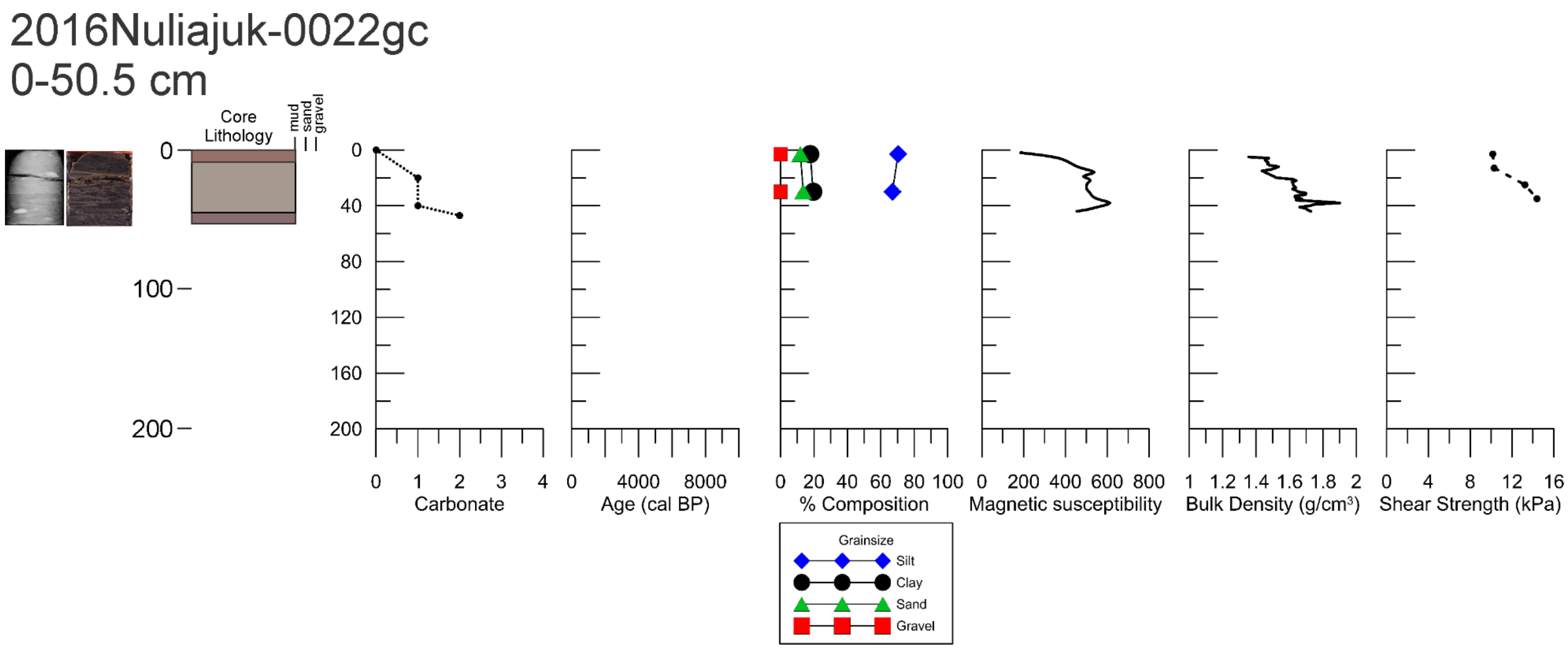

Figure A.26 Core diagram of 2016Nuliajuk-0022. Also presented as core 230a in Table 4.2

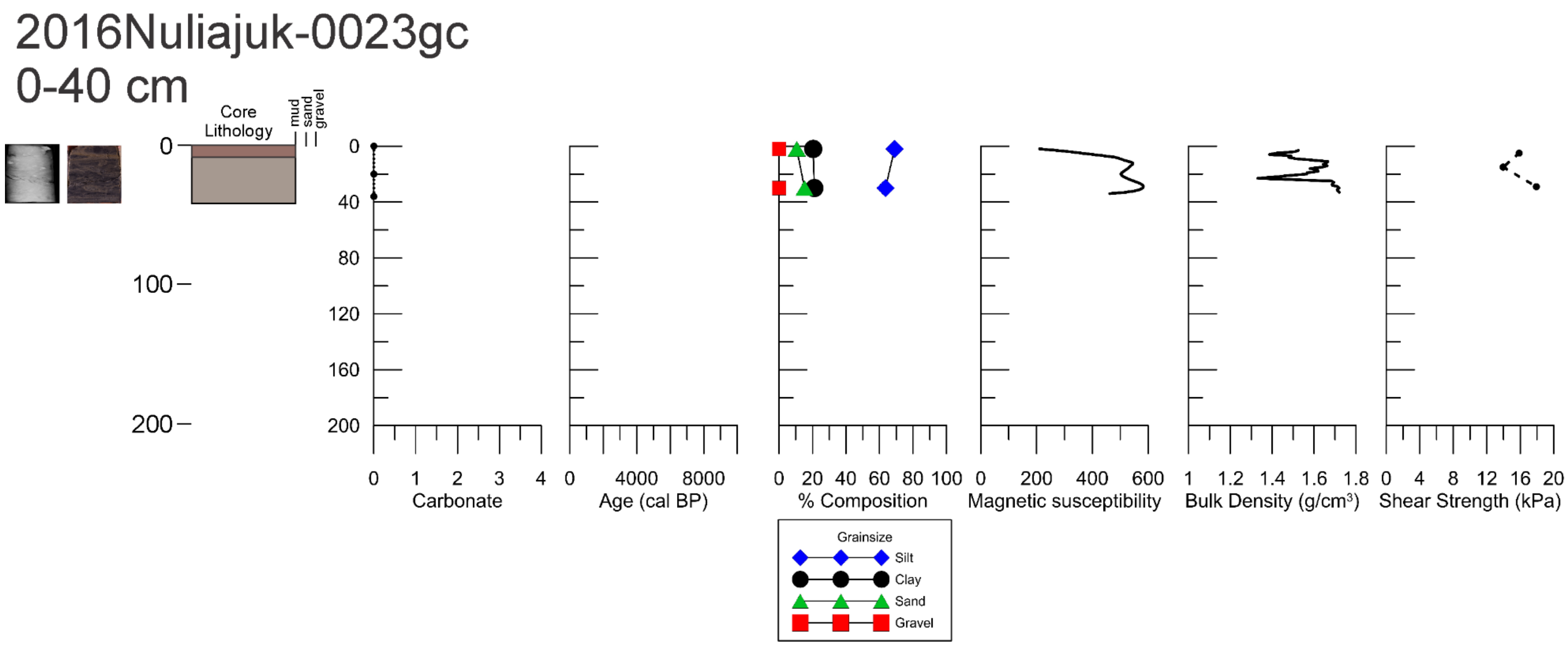

Figure A.27 Core diagram of 2016Nuliajuk-0023. Also presented as core 231a in Table 4.2

M16
2016Nuliajuk-0024gc
0-72 cm

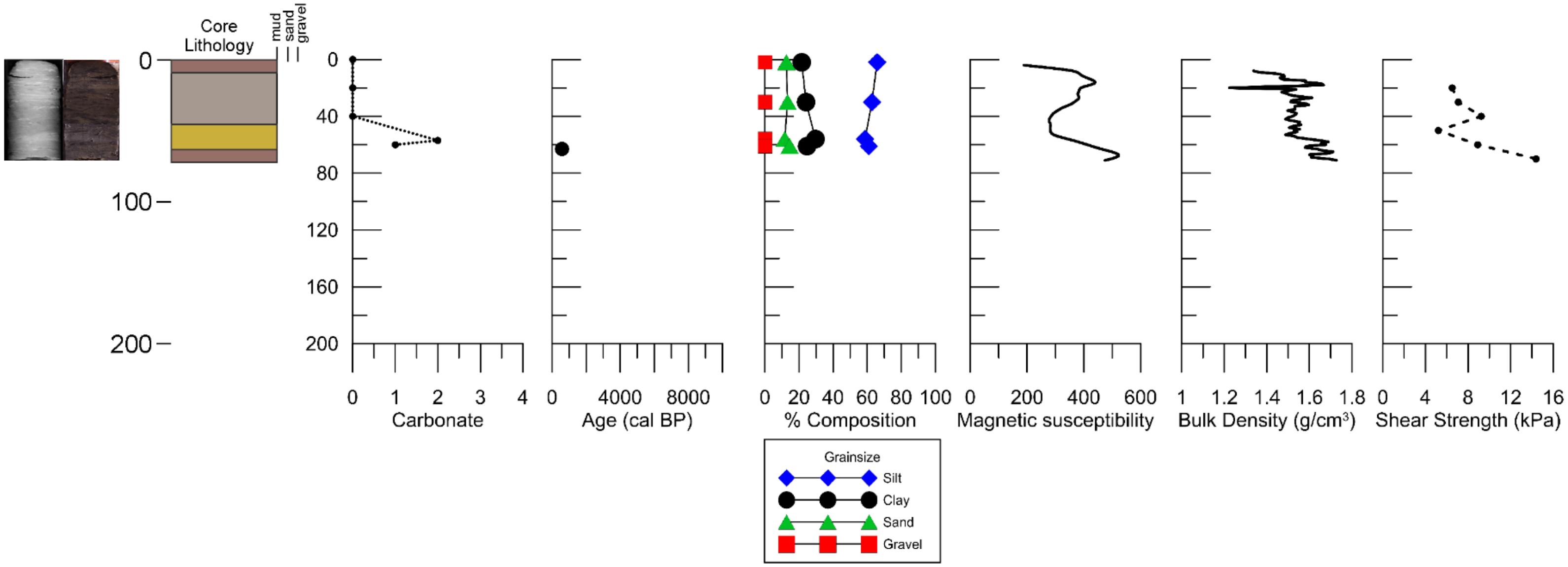

Figure A.28 Core diagram of 2016Nuliajuk-0024. Also presented as core 234a in Table 4.2

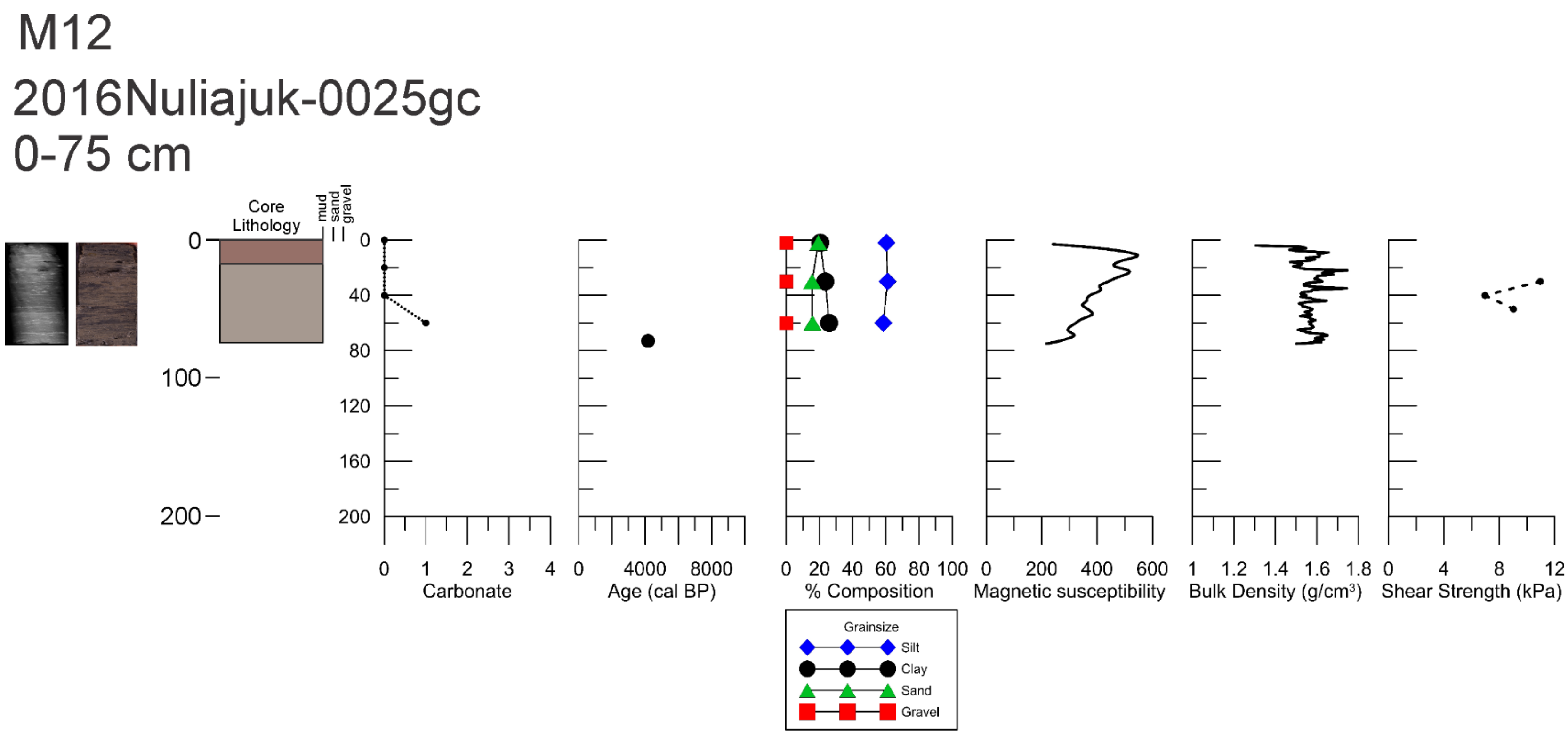

Figure A.29 Core diagram of 2016Nuliajuk-0025. Also presented as core 214a in Table 4.2

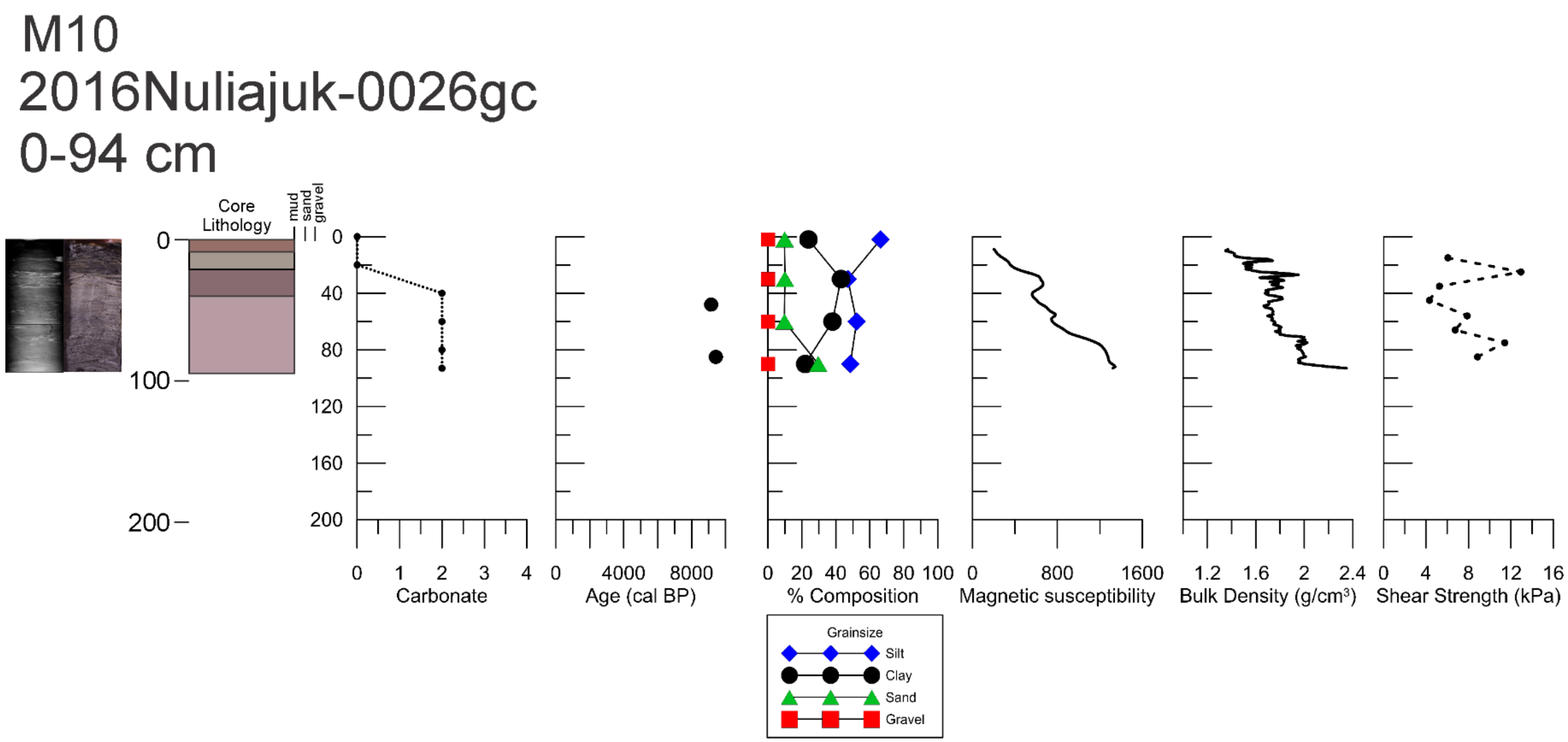

Figure A.30 Core diagram of 2016Nuliajuk-0026. Also presented as core 244a in Table 4.2

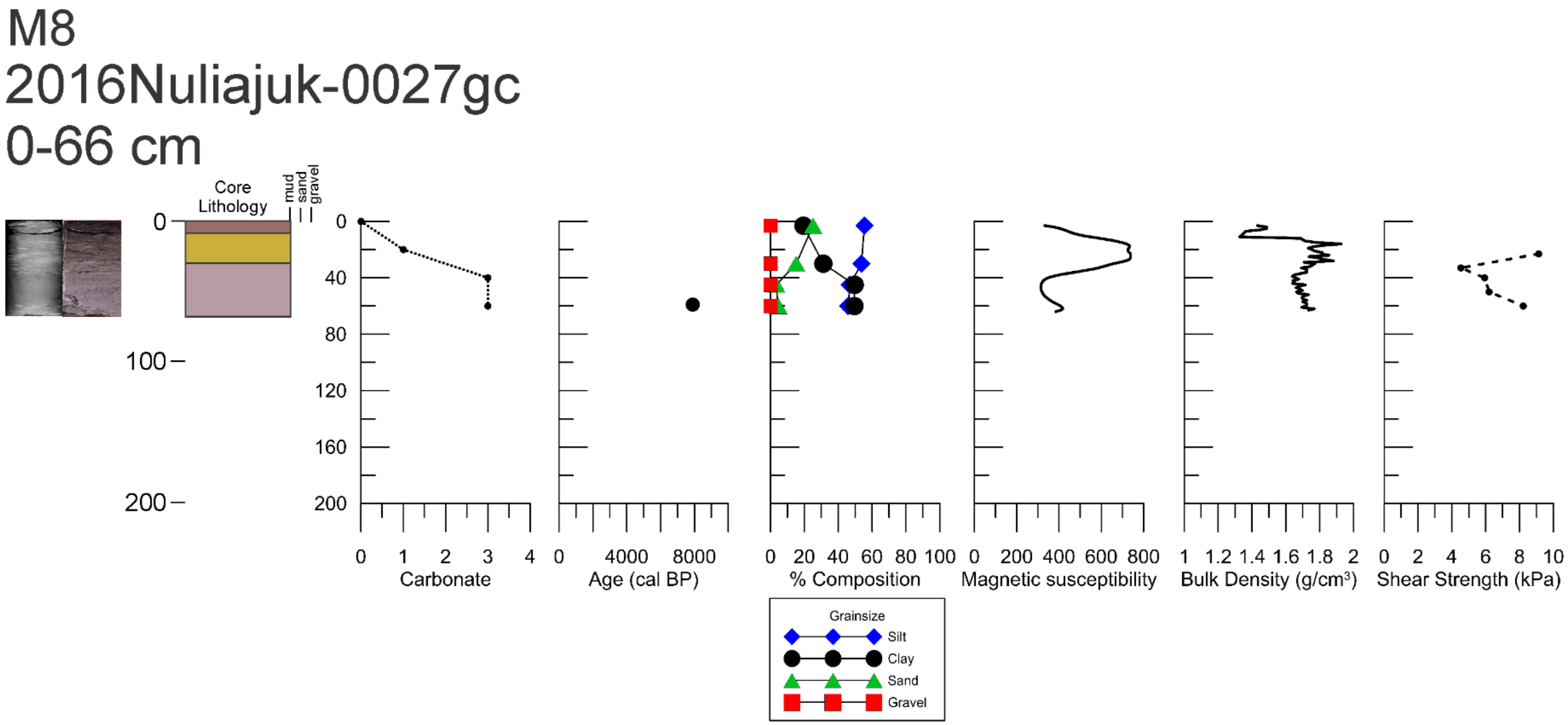

Figure A.31 Core diagram of 2016Nuliajuk-0027. Also presented as core 48a in Table 4.2

M7
2016Nuliajuk-0028gc
0-49 cm

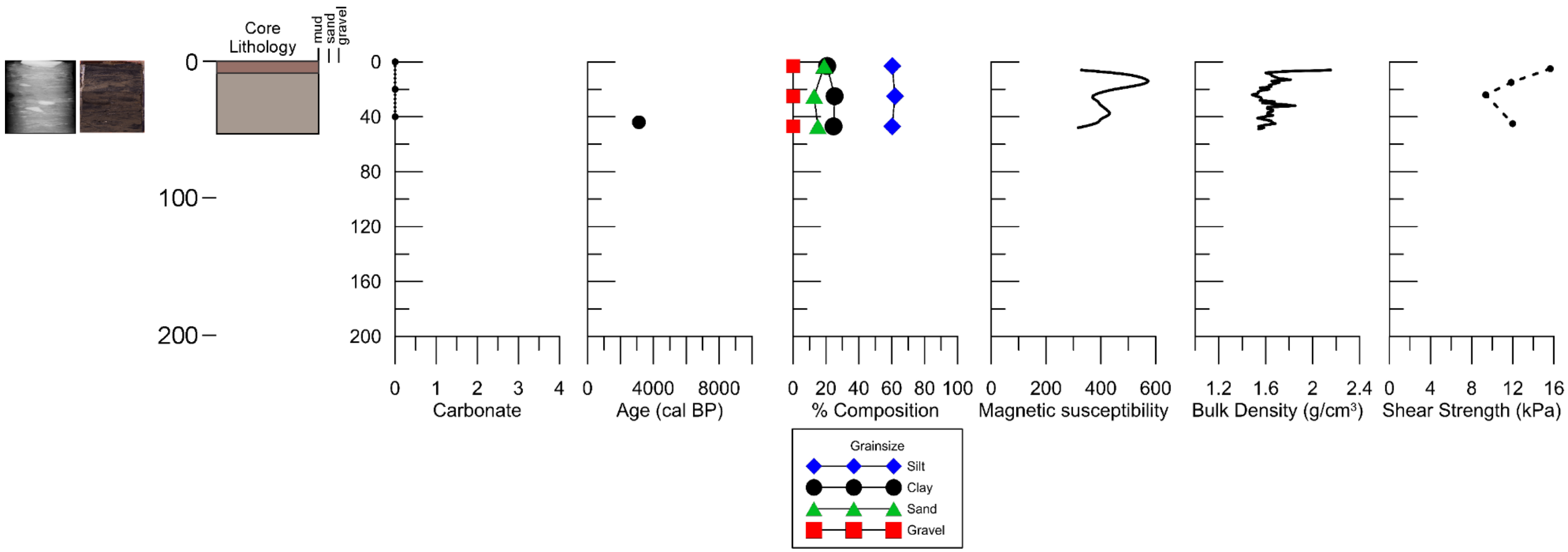

Figure A.32 Core diagram of 2016Nuliajuk-0028. Also presented as core 47a in Table 4.2

M6
2016Nuliajuk-0029gc
0-122 cm

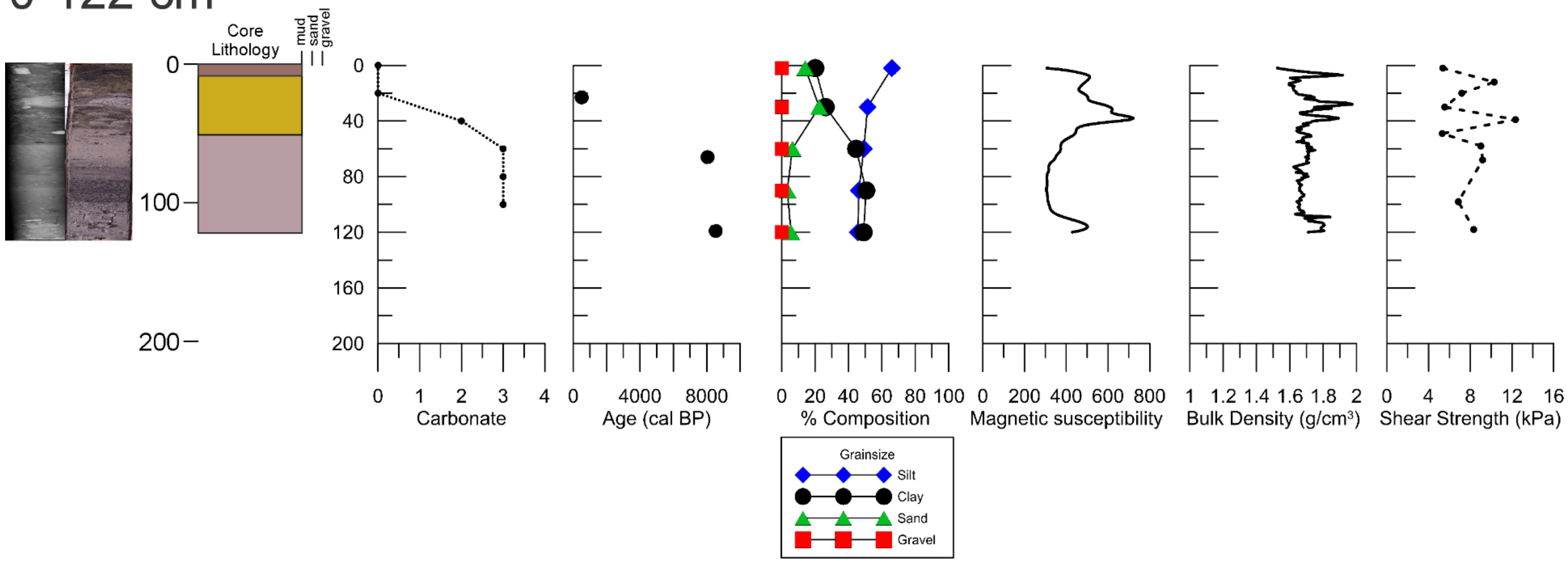

Figure A.33 Core diagram of 2016Nuliajuk-0029. Also presented as core 43a in Table 4.2

M5
2016Nuliajuk-0030gc
0-179 cm

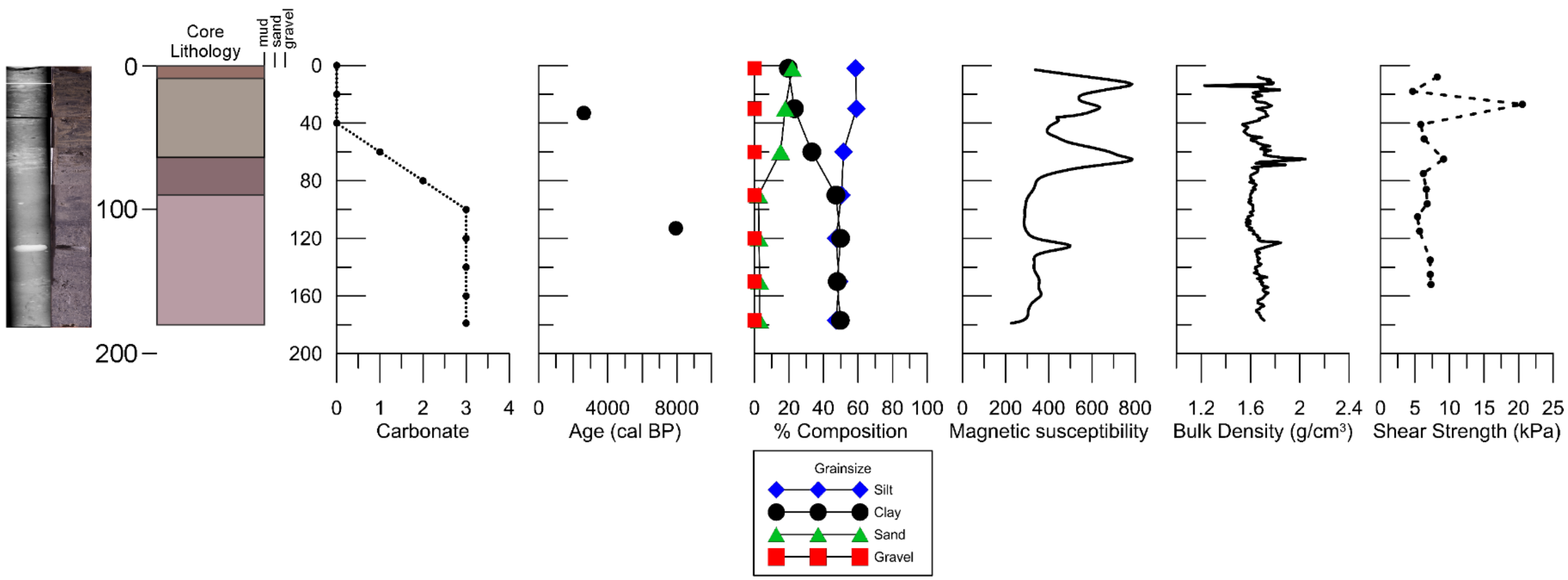

Figure A.34 Core diagram of 2016Nuliajuk-0030

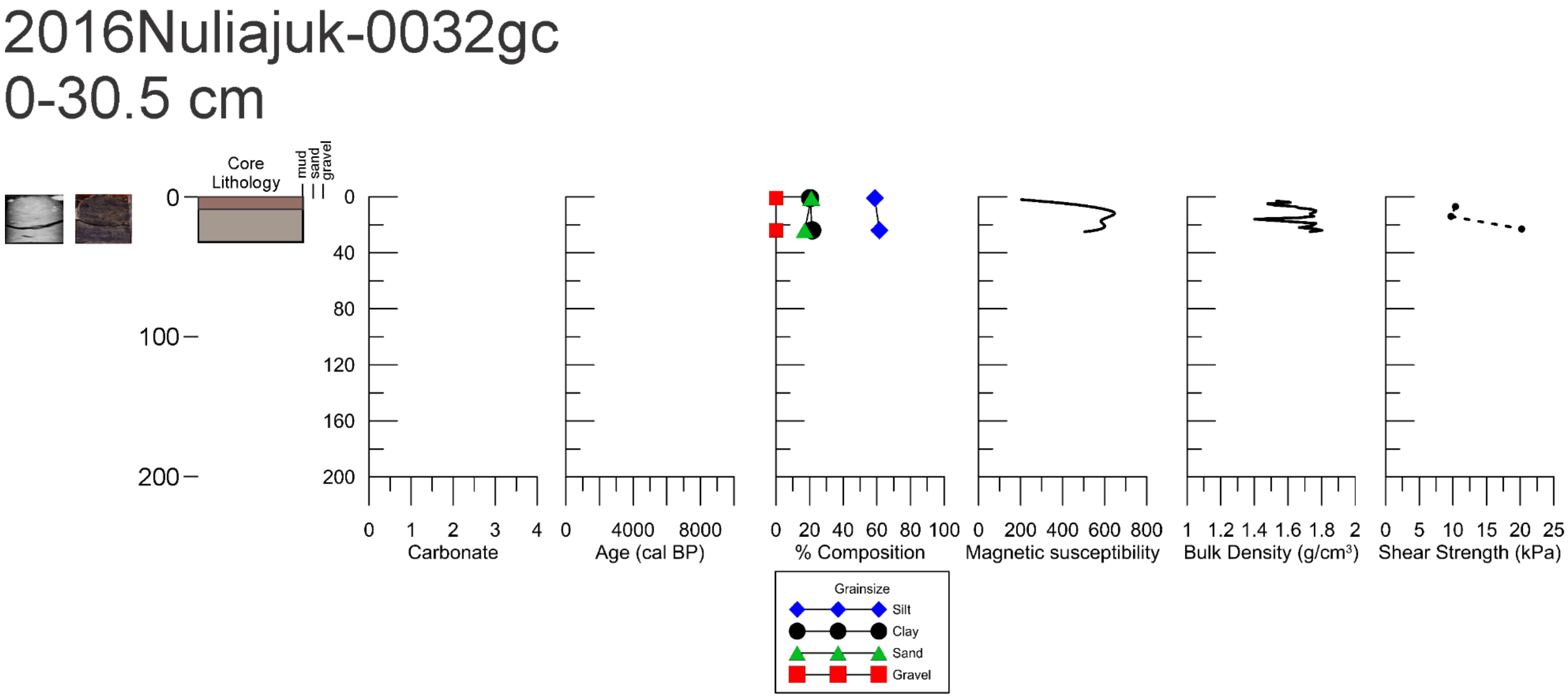

Figure A.35 Core diagram of 2016Nuliajuk-0032. Also presented as core 29b in Table 4.2

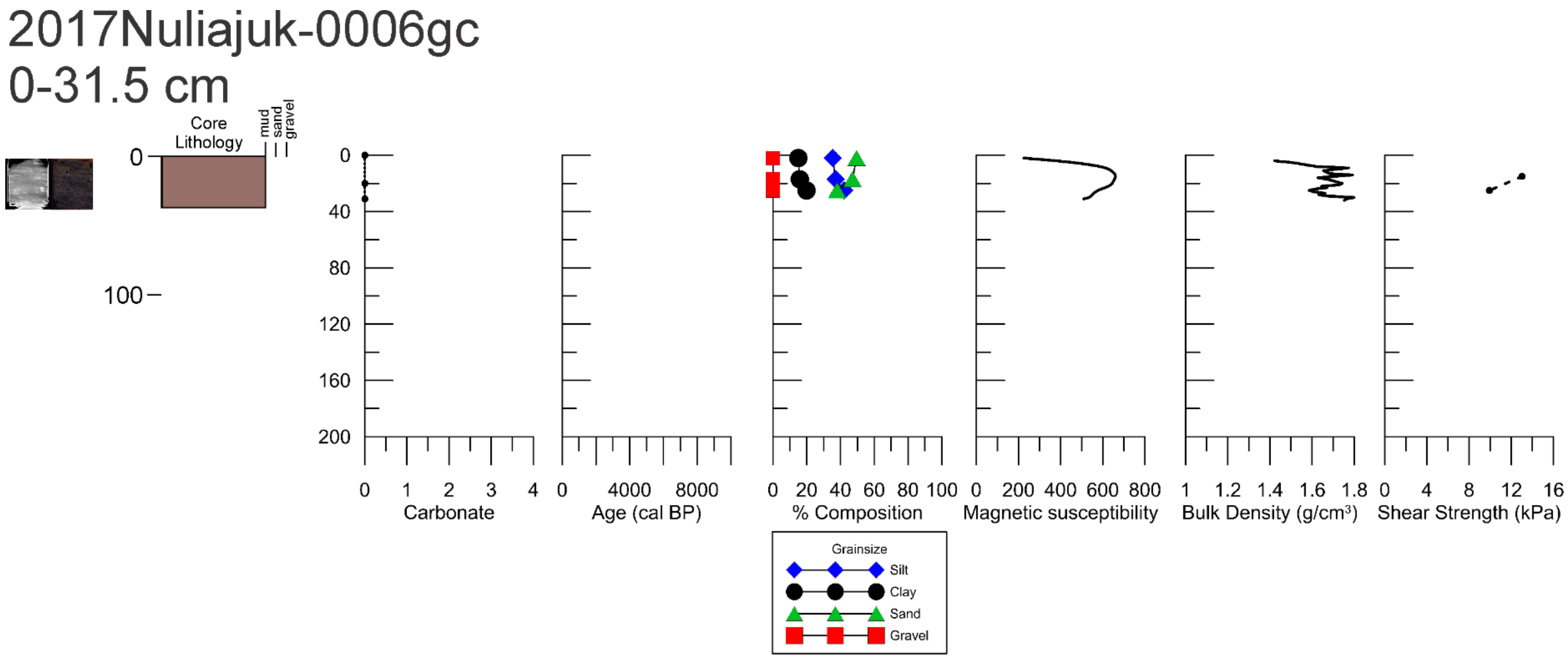

Figure A.36 Core diagram of 2017Nuliajuk-0006

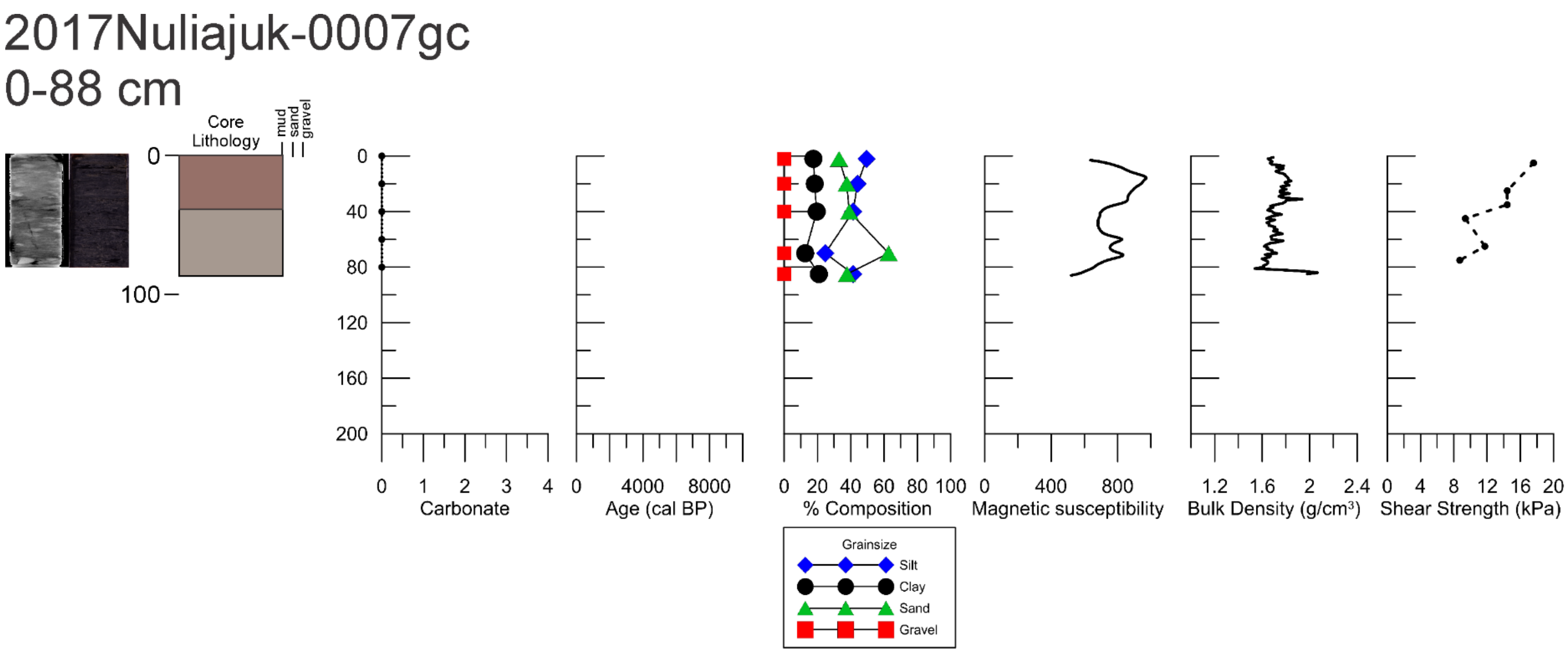

Figure A.37 Core diagram of 2017Nuliajuk-0007. Also presented as core 100a in Table 4.2

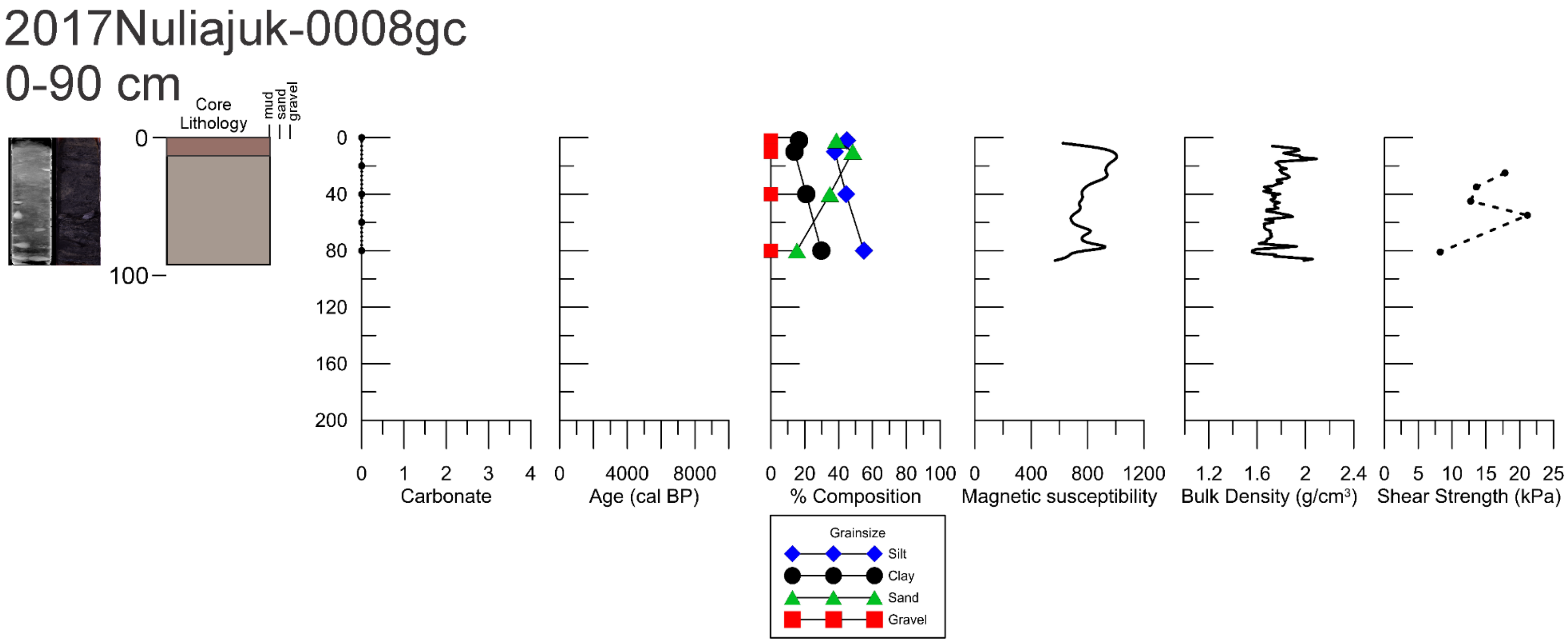

Figure A.38 Core diagram of 2017Nuliajuk-0008. Also presented as core 39a in Table 4.2

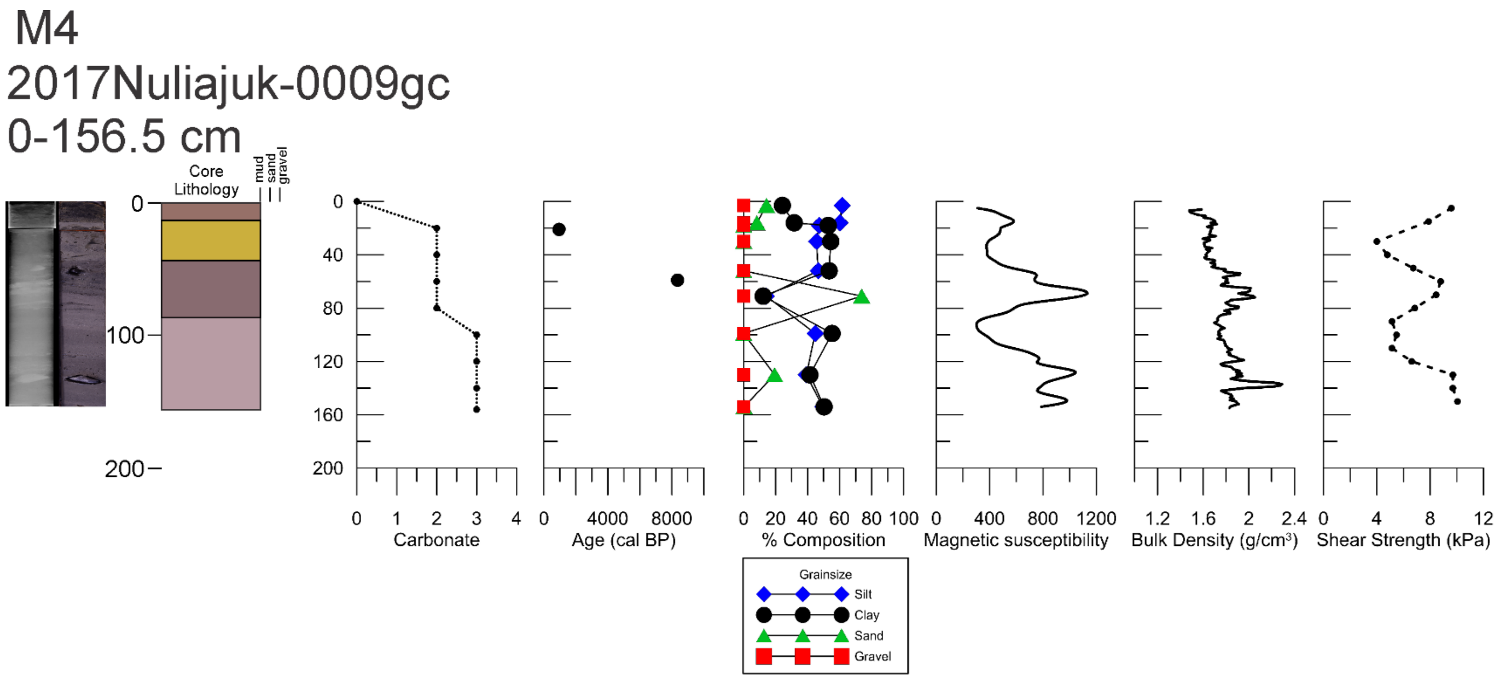

Figure A.39 Core diagram of 2017Nuliajuk-0009. Also presented as core 39b in Table 4.2

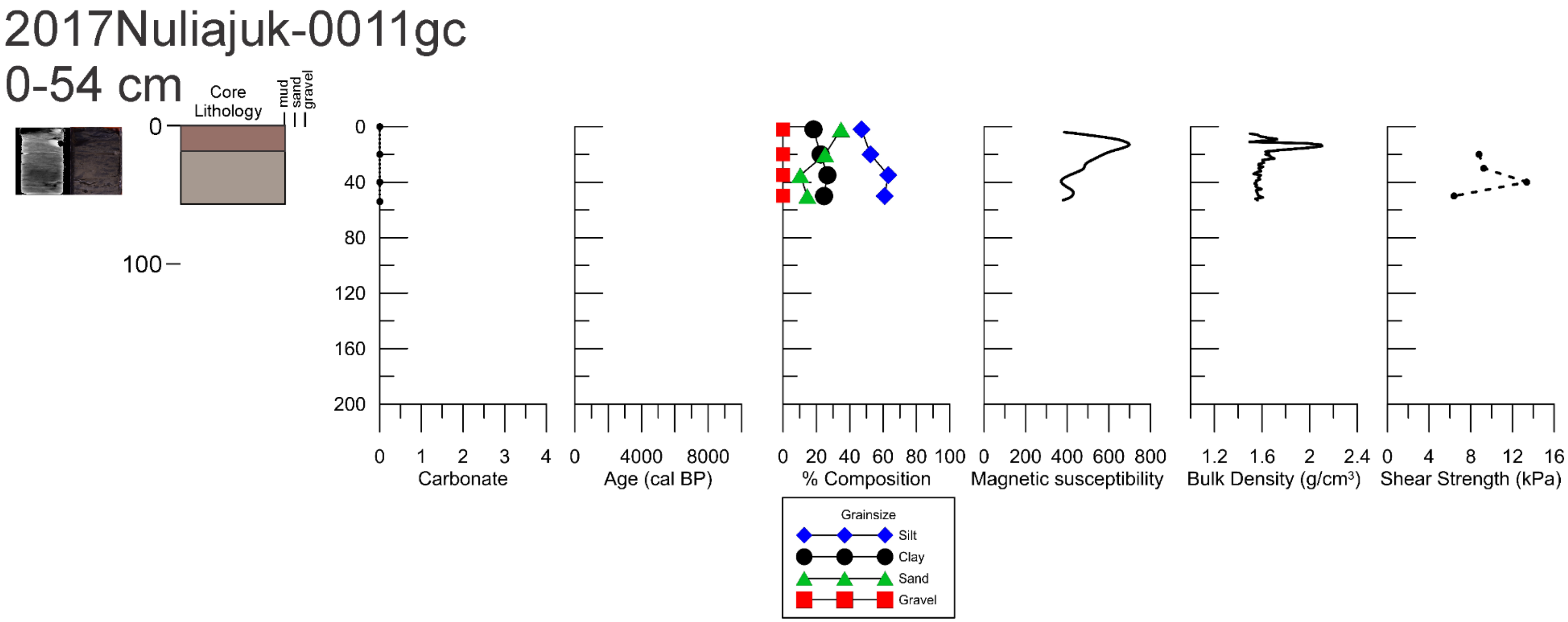

Figure A.40 Core diagram of 2017Nuliajuk-0011. Also presented as core 39c in Table 4.2

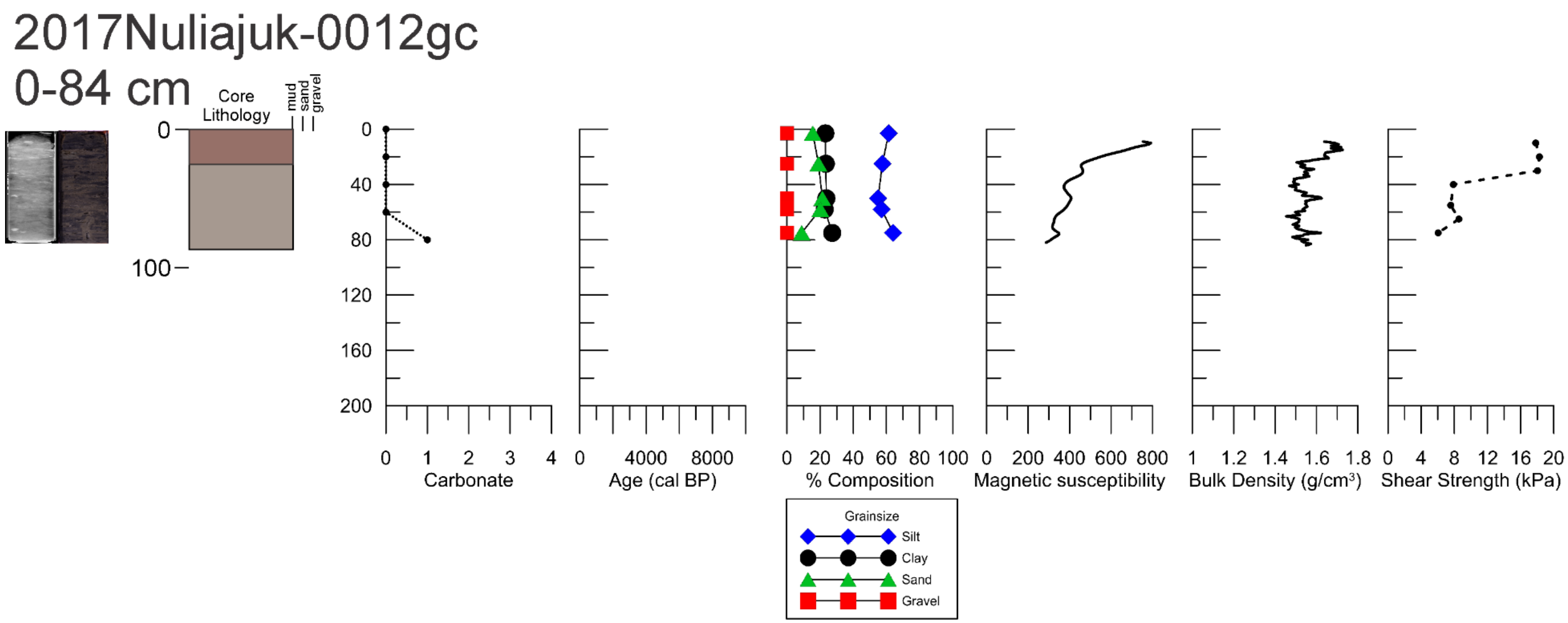

Figure A.41 Core diagram of 2017Nuliajuk-0012

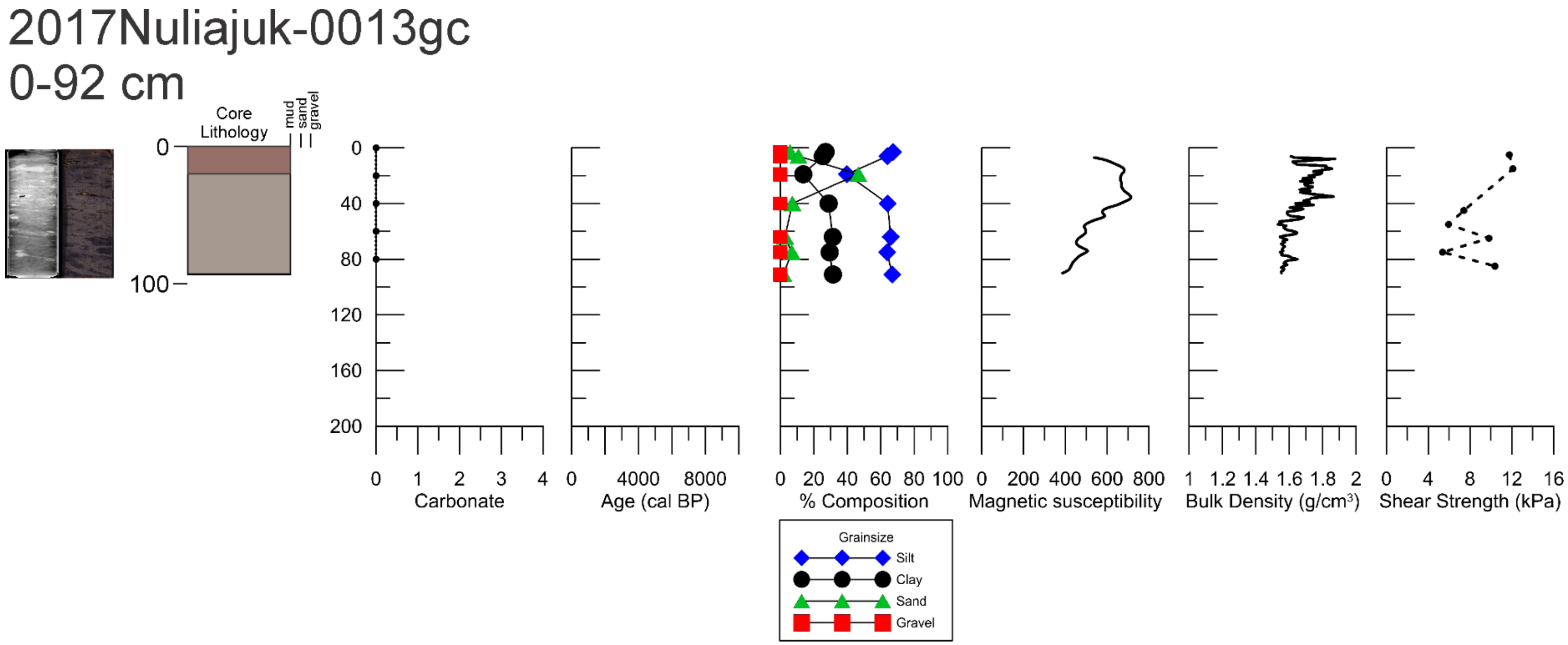

Figure A.42 Core diagram of 2017Nuliajuk-0013

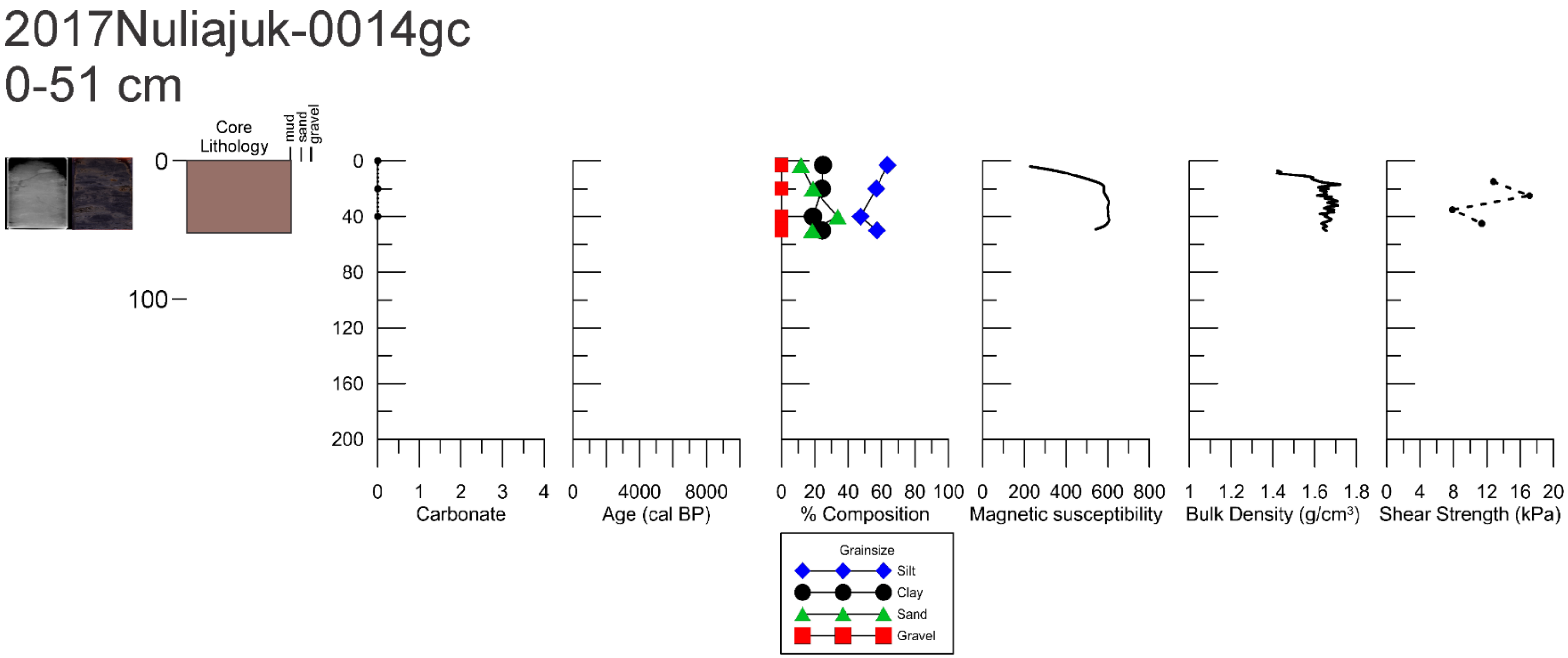

Figure A.43 Core diagram of 2017Nuliajuk-0014

M2
2017Nuliajuk-0015gc
0-74 cm

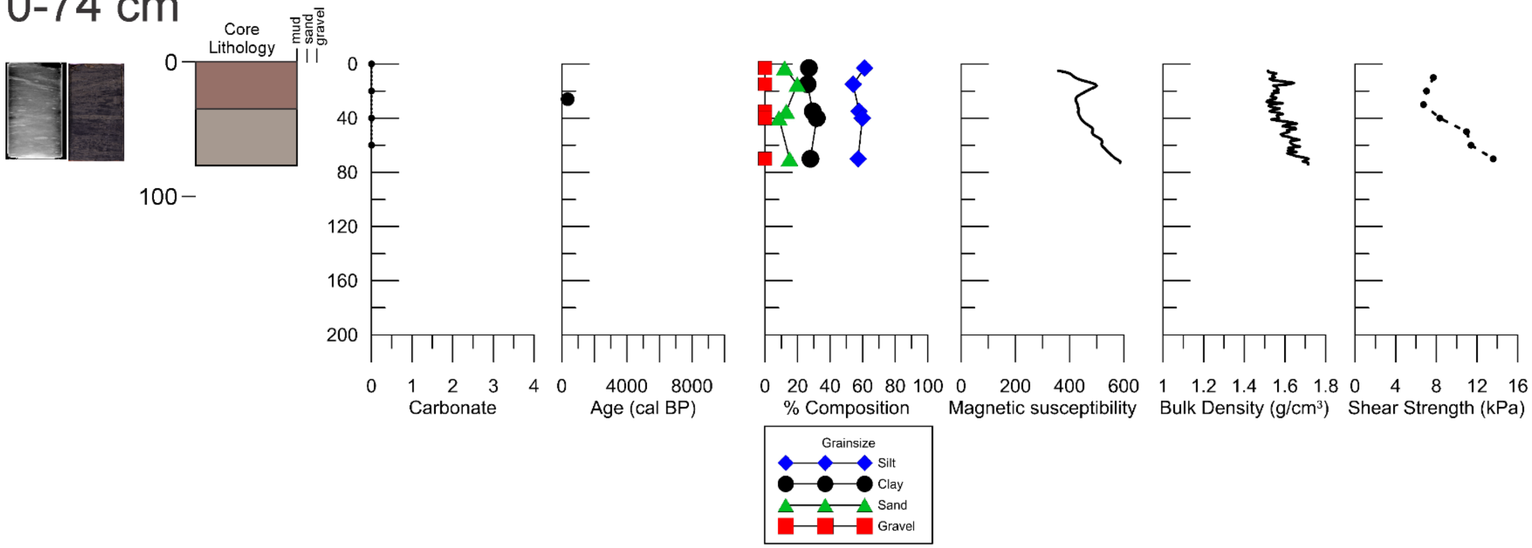

Figure A.44 Core diagram of 2017Nuliajuk-0015. Also presented as core 13a in Table 4.2

M3
2017Nuliajuk-0016gc
0-139 cm

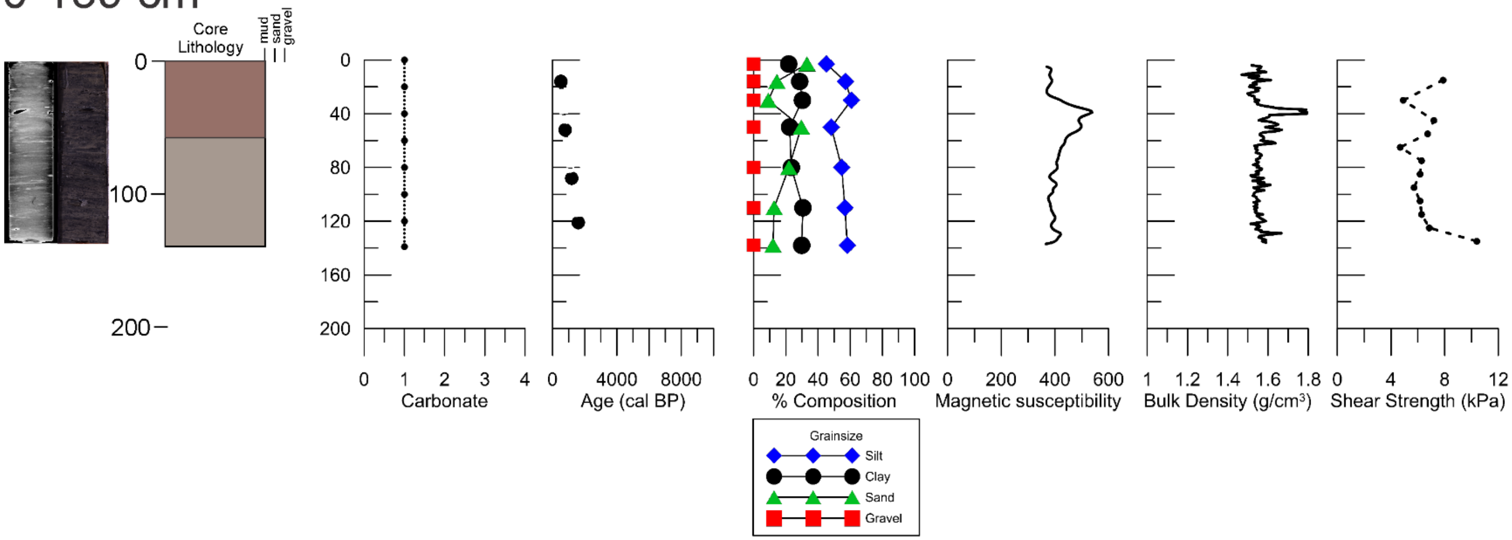

Figure A.45 Core diagram of 2017Nuliajuk-0016

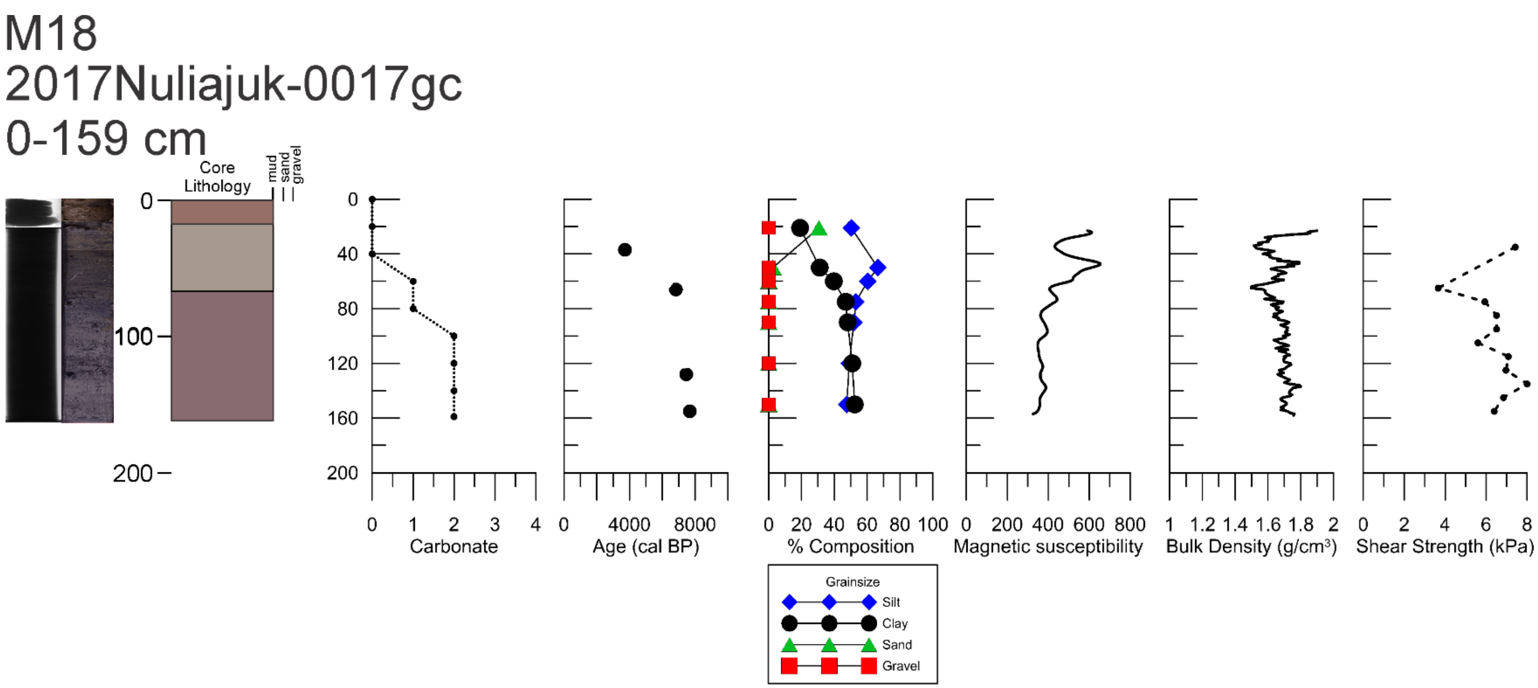

Figure A.46 Core diagram of 2017Nuliajuk-0017

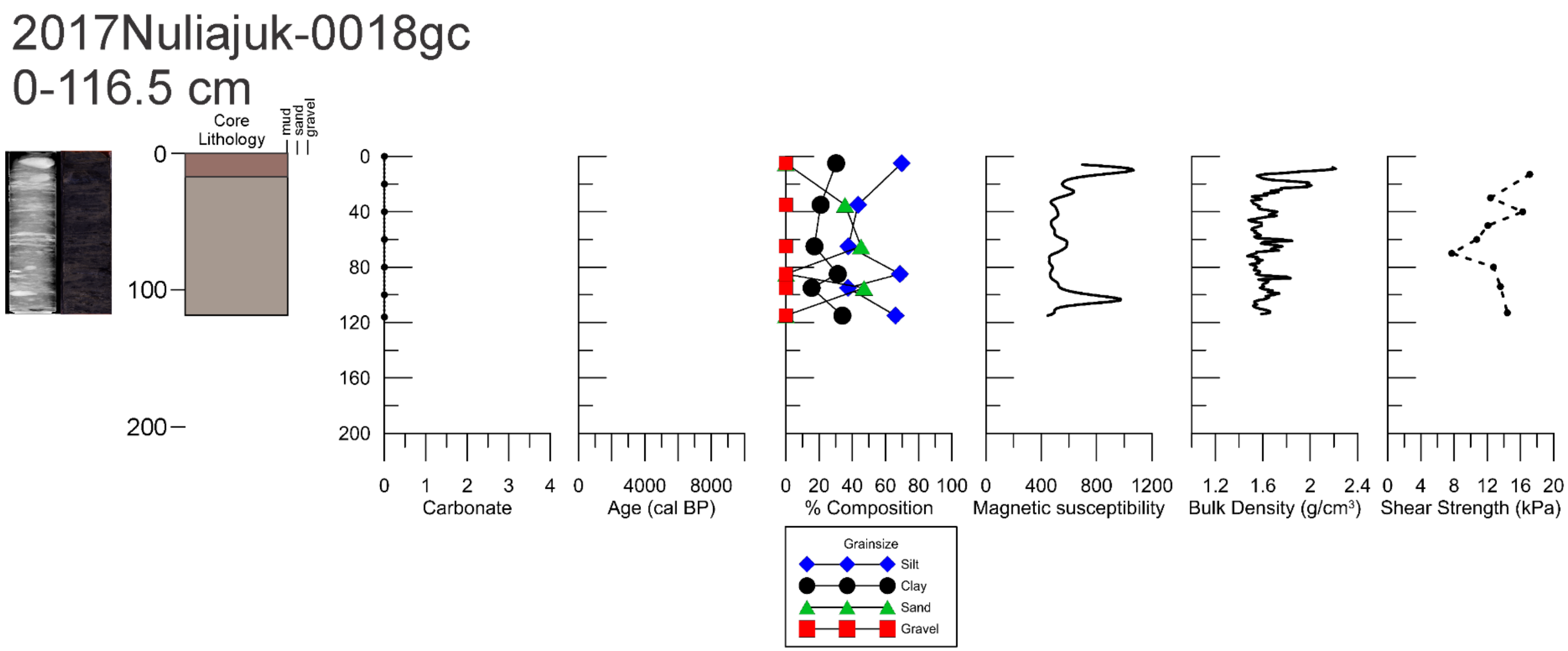

Figure A.47 Core diagram of 2017Nuliajuk-0018

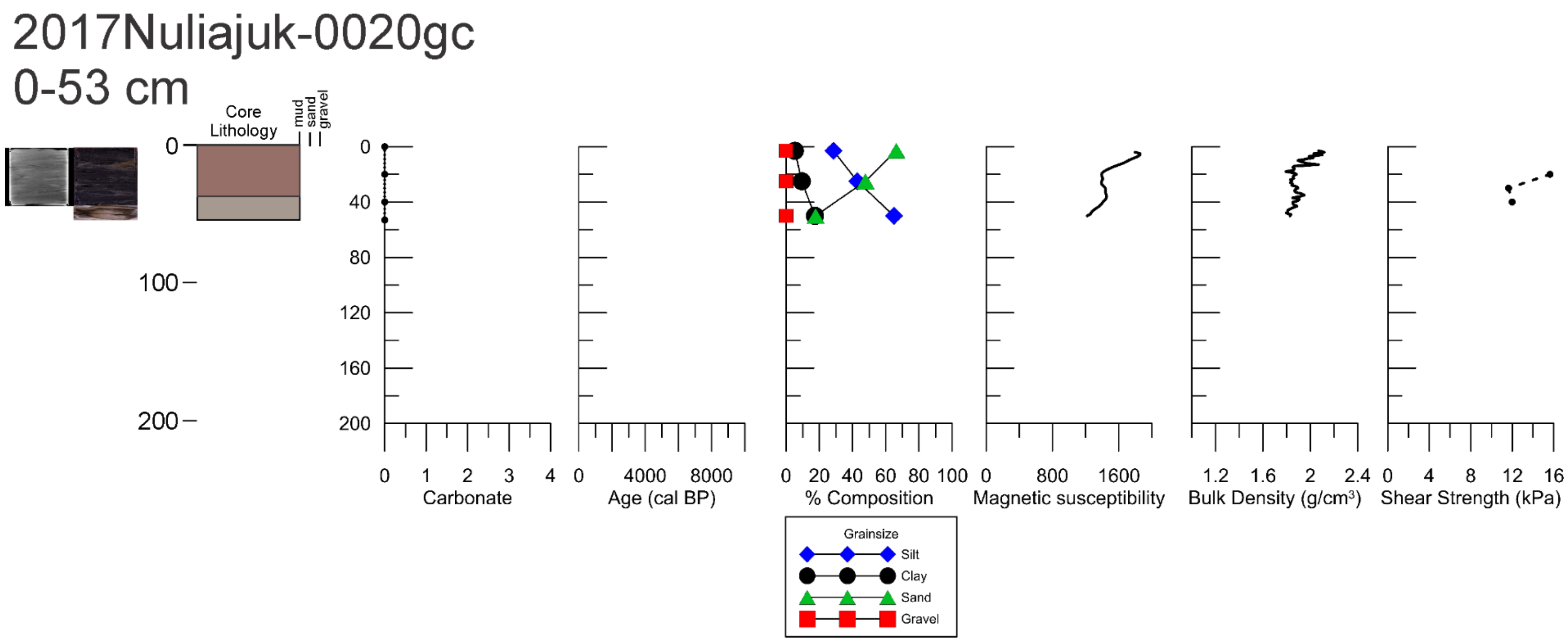

Figure A.48 Core diagram of 2017Nuliajuk-0020

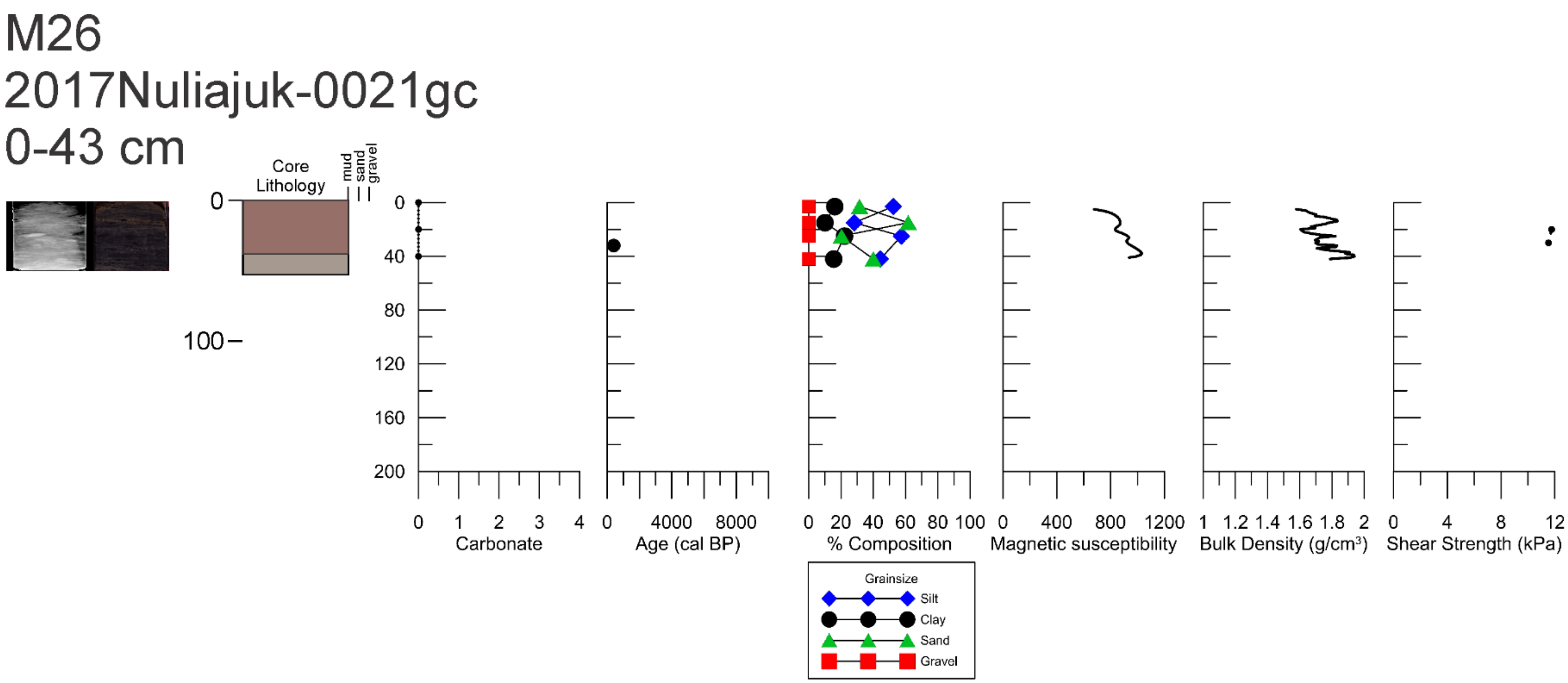

Figure A.49 Core diagram of 2017Nuliajuk-0021

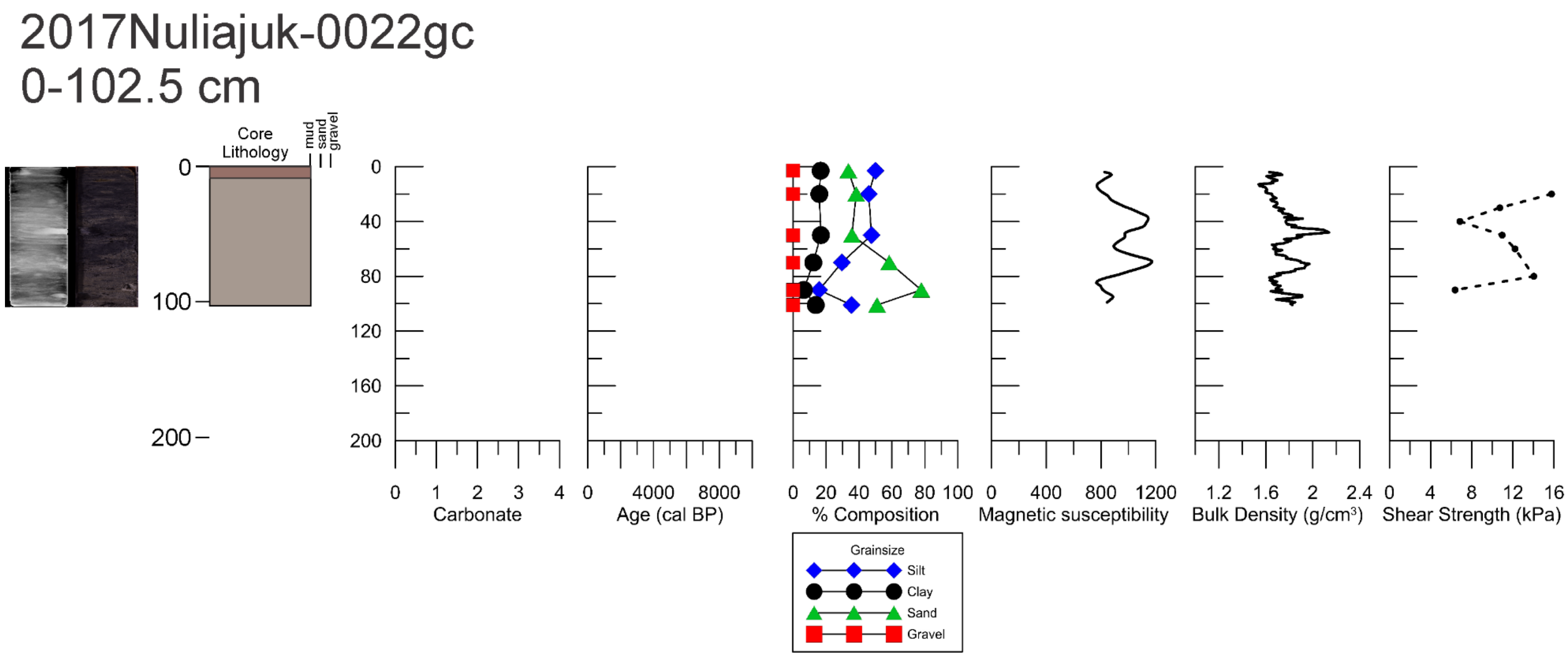

Figure A.50 Core diagram of 2017Nuliajuk-0022

2017Nuliajuk-0023gc
0-65 cm

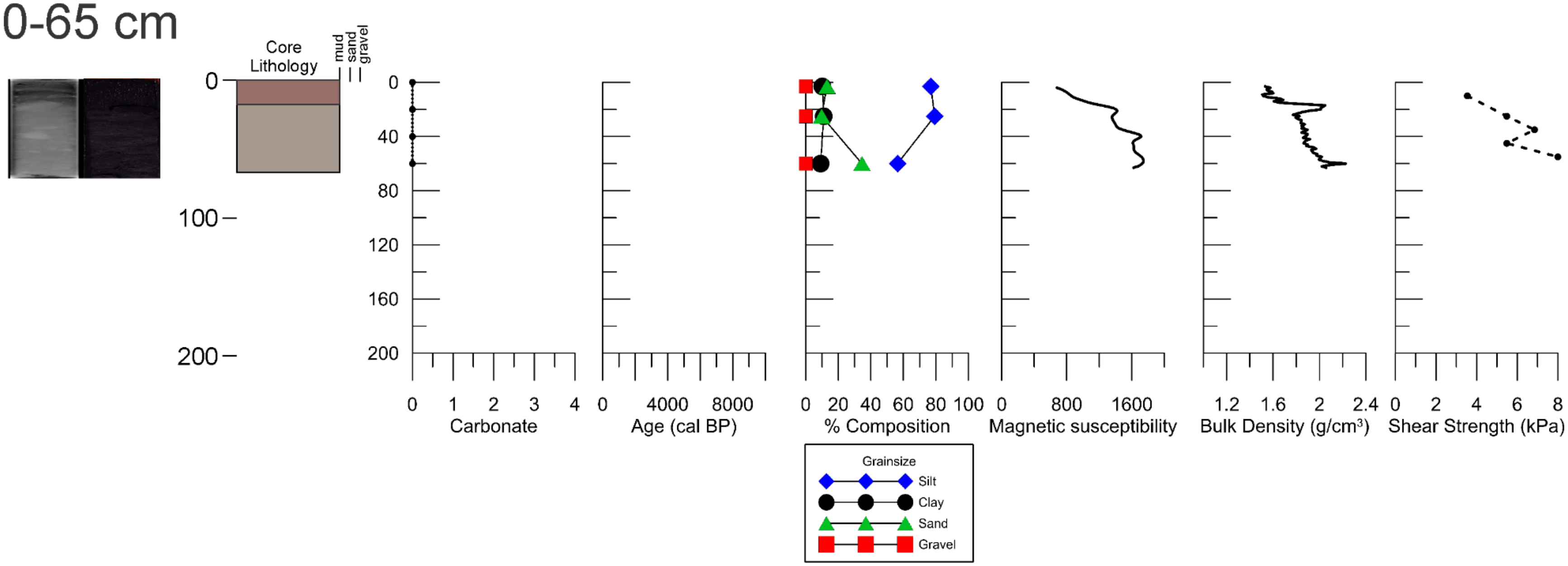

Figure A.51 Core diagram of 2017Nuliajuk-0023

A.3 References

Campbell D.C., Jenner K.A., Higgins J. and Piper D.J.W. (2017). Analysis of piston cores and high-resolution sub-bottom profiler data, Baffin Bay slope, Nunavut; Geological Survey of Canada, Open File 8135, 179 p.

NRCan (2022). Expedition Database; website, Natural Resources Canada, Dartmouth, NS, URL https://ed.gdr.nrcan.gc.ca/index_e.php

Appendix B: Morphometric Parameters of SSFs

Morphometric analysis was completed on 246 SSFs in IFB as described in Chapter 3. The following table of values is the raw morphometric measurements and calculated values.

Table B.1 Description of morphometric parameters measured and calculated for SSFs in IFB. This is a reproduction of Table 3.1, placed here to ease the use of Table B.2.

Parameter		Description
Measured		
Area	A	Area of feature in square kilometres
Perimeter	P	Perimeter of feature in kilometres
Direction of transport	DoT	Cardinal direction of sediment transport
Maximum run-out	R_m	Maximum run-out length in metres
Maximum width	W_m	Maximum width of the feature in metres
Headwall length (curvilinear)	HL_r	Length of the headwall in metres, following the exact path of the headwall
Headwall length (straight line)	HL_s	Length of the headwall in metres, measured as a straight line between two end points
Run-out 1/2	$R_{1/2}$	Run-out in metres as measured by a straight line perpendicular to W_m at 1/2 W_m
Initiation depth	D_i	Water depth at the top of the slope failure feature in metres
Termination depth	D_t	Water depth at the bottom of the slope failure feature in metres
Depth at base of headwall	D_{bhw}	Water depth at the bottom of the headwall in metres
Maximum slope in feature (°)	α_{bathy}	Maximum slope in the feature, as measured from the bathymetry raster
Calculated		
Headwall curvature	CRV	HL_r/HL_s: measure of the convolution of the headwall (1 = straight)
Vertical extent	V	$D_t - D_i$: change in water depth along the run-out of the slope failure in metres
Headwall height	H_{hw}	$D_{bhw} - D_i$: height of the headwall in metres
Compactness	C	4π area/perimeter^2: measure of the similarity to a circle (1 = circular)
Regional slope (°)	α	Angle from D_i to D_t at 1/2 W_m (calculated as in Pinet *et al.* 2015)
Regional slope (maximum) (°)	α_{max}	Angle from D_i to D_t (calculated as in Pinet *et al.* 2015)
Elongation	E	$R_m/R_{1/2}$

Table B.2 Unique Ids (FID; Corresponds to SSF #'s in Chapter 4), locations (Note: Latitude and Longitude may be the same for different features where overlap occurred; See Figs. 4.2-4.5), and morphometric values for 246 SSFs in IFB. Column headers refer to Table 3.1 (reproduced as table B.1) above. Note: Not all SSF footprint were completely mapped, so not all parameters could be measured for every SSF. Missing values are denoted by *.

FID	Longitude	Latitude	DoT	A (km^2)	P (km)	Rm (m)	Wm (m)	HLr (m)	HLS (m)	CRV	$R_{1/2}$ (m)	Di (m)	Dt (m)	$Dbhw$ (m)	V (m)	Hhw (m)	C	E	α_{max} (°)	α_{bathy} (°)	α (°)
0	-68.266	63.338	NNE	0.13	1.52	*	*	*	*	*	*	*	*	*	*	*	0.71	*	*	*	*
1	-68.269	63.339	NNE	0.07	1.08	*	*	*	*	*	*	*	*	*	*	*	0.73	*	*	*	*
2	-68.274	63.341	N	0.47	3.40	*	*	*	*	*	*	*	*	*	*	*	0.52	*	*	*	*
3	-68.270	63.314	NE	0.03	0.70	121.59	68.11	92.04	67.34	1.37	74.87	55.0	57.7	55.6	2.7	0.6	0.76	1.10	1.27	12.6	2.07
4	-68.250	63.341	SW	0.06	1.19	*	*	*	*	*	*	*	*	*	*	*	0.57	*	*	*	*
5	-68.282	63.349	N	2.15	6.00	805.07	623.34	591.69	591.69	1.00	480.81	93.6	122.4	112.9	28.8	19.3	0.75	0.77	2.05	28.3	3.43
6	-68.253	63.350	N	0.04	0.78	156.54	73.66	142.34	48.93	2.91	142.63	35.1	45.3	37.7	10.2	2.6	0.78	1.94	3.73	12.6	4.09
7	-68.252	63.351	N	0.02	0.51	107.72	67.03	58.66	53.86	1.09	88.44	40.6	51.4	44.8	10.8	4.2	0.83	1.32	5.73	16.7	6.96
8	-68.242	63.361	W	0.02	0.57	90.53	67.26	14.06	10.67	1.32	62.98	27.2	30.7	28.7	3.5	1.5	0.71	0.94	2.21	19.5	3.18
9	-68.245	63.362	S	0.03	0.77	116.25	59.30	46.19	34.21	1.35	116.25	32.4	39.3	35.7	6.9	3.3	0.63	1.96	3.40	24.1	3.40
10	-68.255	63.371	SW	0.02	0.71	86.60	29.53	69.09	25.02	2.76	83.59	36.9	48.2	41.8	11.3	4.9	0.62	2.83	7.43	23.3	7.70
11	-68.255	63.371	SW	0.01	0.45	95.10	36.95	72.94	25.37	2.88	87.39	32.9	52.4	37.3	19.5	4.4	0.60	2.37	11.59	24.1	12.58
12	-68.256	63.372	WSW	0.01	0.50	98.46	24.99	57.06	25.02	2.28	90.17	38.5	55.2	40.1	16.7	1.6	0.45	3.61	9.63	28.3	10.49
13	-68.328	63.373	SE	1.51	4.89	683.35	629.79	771.81	629.79	1.23	487.78	36.3	86.5	47.1	50.2	10.8	0.79	0.77	4.20	38.3	5.88
14	-68.325	63.405	NE	0.03	0.68	102.76	78.16	80.78	72.36	1.12	101.91	39.0	48.3	44.8	9.3	5.8	0.85	1.30	5.17	24.1	5.21
15	-68.290	63.407	NE	0.23	2.68	351.16	284.67	167.67	114.24	1.47	186.87	82.9	111.7	88.1	28.8	5.2	0.40	0.66	4.69	28.3	8.76
16	-68.280	63.403	NE	0.07	1.45	306.42	73.73	21.08	21.08	1.00	299.13	68.0	126.7	71.1	58.7	3.1	0.42	4.06	10.84	35.3	11.10
17	-68.276	63.400	NE	0.03	0.75	146.75	41.94	49.07	25.43	1.93	126.13	55.3	105.8	62.0	50.5	6.7	0.58	3.01	18.99	26.6	21.82
18	-68.269	63.404	SW	0.09	1.38	269.19	97.01	73.01	42.72	1.71	251.69	93.1	126.1	94.8	33.0	1.7	0.62	2.59	6.99	24.1	7.47
19	-68.252	63.405	NE	0.03	0.86	166.69	69.38	39.45	22.78	1.73	156.56	105.3	136.8	108.2	31.5	2.9	0.54	2.26	10.70	34.9	11.38
20	-68.257	63.407	NE	0.06	1.34	281.81	85.31	86.23	60.54	1.42	252.49	96.9	133.8	101.5	36.9	4.6	0.44	2.96	7.46	32.5	8.31
21	-68.205	63.381	SW	0.20	2.58	356.75	160.41	31.12	21.49	1.45	311.35	109.3	135.1	112.7	25.8	3.4	0.37	1.94	4.14	42.6	4.74
22	-68.198	63.375	NW	0.10	1.68	268.89	147.12	147.12	147.12	1.00	94.37	86.8	137.9	93.3	51.1	6.5	0.43	0.64	10.76	59.7	28.43
23	-68.139	63.373	NE	0.07	0.98	119.79	138.40	96.62	55.17	1.75	109.64	49.3	62.9	51.1	13.6	1.8	0.87	0.79	6.48	35.3	7.07
24	-68.200	63.401	NE	0.03	0.70	95.71	45.97	59.88	39.07	1.53	80.44	83.9	108.1	86.7	24.2	2.8	0.67	1.75	14.19	22.9	16.74
25	-68.195	63.402	SW	0.02	0.56	76.05	44.15	40.79	34.03	1.20	68.71	89.5	106.5	92.0	17.0	2.5	0.76	1.56	12.60	35.4	13.90
26	-68.191	63.400	SE	0.06	1.48	239.88	45.73	55.74	35.52	1.57	239.88	95.1	99.3	97.6	4.2	2.5	0.36	5.25	1.00	24.1	1.00
27	-68.193	63.399	NW	0.03	0.93	135.14	56.57	43.48	30.55	1.42	135.14	97.5	99.4	98.5	1.9	1.0	0.43	2.39	0.81	12.6	0.81
28	-68.178	63.431	NE	0.06	1.16	216.12	74.61	101.33	55.15	1.84	177.21	127.3	190.4	130.2	63.1	2.9	0.53	2.38	16.28	26.6	19.60
29	-68.347	63.459	NE	0.42	3.74	691.11	178.41	20.55	20.55	1.00	651.60	70.5	149.7	74.5	79.2	4.0	0.37	3.65	6.54	29.7	6.93
30	-68.350	63.448	E	0.01	0.54	79.07	22.86	13.15	13.15	1.00	79.07	36.7	45.3	37.2	8.6	0.5	0.46	3.46	6.21	22.9	6.21
31	-68.349	63.448	NE	0.01	0.41	72.23	14.04	12.71	12.71	1.00	72.23	34.9	44.3	36.2	9.4	1.3	0.53	5.14	7.41	12.6	7.41

Table B.2 Cont.

FID	Longitude	Latitude	DoT	A (km^2)	P (km)	Rm (m)	Wm (m)	HLr (m)	HLS (m)	CRV	$R_{1/2}$ (m)	Di (m)	Dt (m)	$Dbhw$ (m)	V (m)	Hhw (m)	C	E	α_{max} (°)	α_{bathy} (°)	α (°)
32	-68.322	63.421	E	0.02	0.69	*	*	*	*	*	*	*	*	*	*	*	0.56	*	*	*	*
33	-68.322	63.419	E	0.04	0.94	*	*	*	*	*	*	*	*	*	*	*	0.55	*	*	*	*
34	-68.390	63.488	NE	0.50	4.15	*	*	*	*	*	*	*	*	*	*	*	0.36	*	*	*	*
35	-68.380	63.482	E	0.45	3.54	627.61	146.72	177.51	127.69	1.39	190.81	75.1	128.1	77.3	53.0	2.2	0.45	1.30	4.83	28.3	15.52
36	-68.280	63.496	ESE	0.06	1.30	264.65	64.53	53.70	38.15	1.41	264.65	109.9	144.8	112.4	34.9	2.5	0.42	4.10	7.51	19.5	7.51
37	-68.275	63.491	NE	0.03	0.93	202.77	45.08	44.81	32.83	1.36	195.54	110.3	141.4	112.0	31.1	1.7	0.48	4.34	8.72	23.3	9.04
38	-68.269	63.488	NNE	0.06	1.12	194.54	109.68	101.35	87.23	1.16	81.86	107.1	129.6	110.4	22.5	3.3	0.63	0.75	6.60	26.6	15.37
39	-68.235	63.477	NE	1.19	5.20	909.69	375.52	382.08	336.93	1.13	909.69	62.2	261.3	66.9	199.1	4.7	0.55	2.42	12.35	59.2	12.35
40	-68.119	63.458	NW	0.08	1.13	*	*	*	*	*	*	*	*	*	*	*	0.81	*	*	*	*
41	-68.157	63.474	N	0.08	1.45	*	*	*	*	*	*	*	*	*	*	*	0.47	*	*	*	*
42	-68.166	63.476	NE	0.03	0.87	130.79	81.27	39.02	21.95	1.78	95.04	64.7	79.3	65.1	14.6	0.4	0.52	1.17	6.37	33.8	8.73
43	-68.235	63.503	SW	0.27	3.14	584.67	187.19	152.84	108.29	1.41	424.15	64.4	156.1	65.9	91.7	1.5	0.35	2.27	8.91	35.3	12.20
44	-68.222	63.505	E	0.04	0.96	188.69	53.80	93.08	38.49	2.42	188.69	60.9	87.6	63.4	26.7	2.5	0.50	3.51	8.05	30.9	8.05
45	-68.235	63.512	WSW	0.05	1.00	185.48	67.99	121.93	51.79	2.35	185.48	100.7	130.1	102.6	29.4	1.9	0.64	2.73	9.01	49.0	9.01
46	-68.230	63.509	NW	0.07	1.25	212.25	78.75	149.14	81.99	1.82	212.25	72.6	91.8	73.7	19.2	1.1	0.60	2.70	5.17	33.1	5.17
47	-68.238	63.509	NW	0.43	4.24	596.42	360.35	199.07	121.50	1.64	190.06	95.7	159.7	99.3	64.0	3.6	0.30	0.53	6.12	33.7	18.61
48	-68.280	63.522	SW	0.19	2.40	309.11	364.75	165.46	73.33	2.26	226.18	104.9	144.7	108.3	39.8	3.4	0.42	0.62	7.34	32.6	9.98
49	-68.265	63.523	SW	0.17	1.59	255.26	177.82	123.64	99.53	1.24	140.80	104.7	143.2	107.6	38.5	2.9	0.82	0.79	8.58	28.3	15.29
50	-68.394	63.517	NW	0.47	2.91	484.96	252.84	204.49	151.23	1.35	484.96	44.6	105.9	44.8	61.3	0.2	0.70	1.92	7.20	55.5	7.20
51	-68.447	63.516	N	0.05	1.05	177.93	100.82	127.16	111.53	1.14	80.00	46.3	67.9	51.8	21.6	5.5	0.59	0.79	6.92	33.9	15.11
52	-68.449	63.516	N	0.03	0.86	162.77	53.49	97.90	97.90	1.00	46.21	54.9	75.3	58.1	20.4	3.2	0.59	0.86	7.14	33.7	23.82
53	-68.451	63.520	N	0.08	1.39	413.99	125.26	130.71	88.97	1.47	413.99	90.9	112.7	92.4	21.8	1.5	0.55	3.31	3.01	12.6	3.01
54	-68.453	63.520	N	0.14	1.92	544.40	129.15	199.90	115.67	1.73	544.40	87.8	115.1	88.9	27.3	1.1	0.48	4.22	2.87	12.6	2.87
55	-68.444	63.518	NE	0.05	1.21	166.26	77.88	125.75	115.41	1.09	85.00	66.3	90.9	70.3	24.6	4.0	0.47	1.09	8.42	24.1	16.14
56	-68.498	63.535	NNE	0.65	5.52	705.19	115.61	165.64	38.52	4.30	467.42	31.1	130.9	33.5	99.8	2.4	0.27	4.04	8.06	26.6	12.05
57	-68.511	63.539	NE	0.43	3.33	*	*	*	*	*	*	*	*	*	*	*	0.49	*	*	*	*
58	-68.511	63.545	N	0.55	3.19	440.63	367.29	159.24	45.38	3.51	350.76	81.6	139.2	84.5	57.6	2.9	0.69	0.95	7.45	56.0	9.33
59	-68.517	63.550	NE	0.74	4.16	482.89	372.39	370.33	242.29	1.53	425.41	116.7	138.4	119.7	21.7	3.0	0.53	1.14	2.57	33.1	2.92
60	-68.519	63.553	ENE	0.21	1.77	203.46	183.43	204.78	148.41	1.38	196.37	115.8	137.4	117.5	21.6	1.7	0.84	1.07	6.06	33.9	6.28
61	-68.523	63.557	ENE	0.49	3.26	427.76	203.98	184.61	162.85	1.13	402.52	74.1	142.2	77.2	68.1	3.1	0.59	1.97	9.05	33.9	9.60
62	-68.543	63.562	NE	0.11	1.40	*	*	*	*	*	*	*	*	*	*	*	0.72	*	*	*	*
63	-68.560	63.568	E	0.15	3.02	573.56	74.84	31.43	15.72	2.00	573.56	27.5	33.4	28.2	5.9	0.7	0.21	7.66	0.59	28.9	0.59

Table B.2 Cont.

FID	Longitude	Latitude	DoT	A (km^2)	P (km)	Rm (m)	Wm (m)	HLr (m)	HLS (m)	CRV	$R_{1/2}$ (m)	Di (m)	Dt (m)	Dbhw (m)	V (m)	Hhw (m)	C	E	α_{max} (°)	α_{bathy} (°)	α (°)
64	-68.585	63.561	SW	0.03	0.60	100.46	63.91	124.58	57.25	2.18	74.76	40.6	44.1	41.6	3.5	1.0	0.91	1.17	2.00	22.9	2.68
65	-68.583	63.562	NE	0.02	0.56	83.18	52.24	59.46	42.98	1.38	76.79	42.8	45.7	43.7	2.9	0.9	0.82	1.47	2.00	24.1	2.16
66	-68.606	63.560	NNE	0.04	1.13	198.66	65.51	22.99	14.43	1.59	65.10	22.0	52.3	22.6	30.3	0.6	0.40	0.99	8.67	26.6	24.96
67	-68.608	63.561	SSW	0.06	1.20	203.49	65.58	66.74	42.42	1.57	170.01	15.9	53.5	17.2	37.6	1.3	0.56	2.59	10.47	33.7	12.47
68	-68.610	63.558	SW	0.05	1.02	*	*	*	*	*	*	*	*	*	*	*	0.61	*	*	*	*
69	-68.600	63.559	SW	0.06	1.17	154.82	97.88	84.41	68.08	1.24	112.30	41.9	44.4	43.1	2.5	1.2	0.58	1.15	0.93	17.5	1.28
70	-68.643	63.556	NW	0.67	4.12	684.32	245.90	133.66	91.99	1.45	403.48	63.9	103.6	66.5	39.7	2.6	0.50	1.64	3.32	12.6	5.62
71	-68.631	63.518	SE	0.02	0.54	89.98	41.14	33.42	30.14	1.11	89.98	16.3	19.9	16.6	3.6	0.3	0.67	2.19	2.29	23.3	2.29
72	-68.578	63.475	N	0.69	3.67	657.12	298.21	320.79	208.27	1.54	625.05	10.9	44.1	12.0	33.2	1.1	0.64	2.10	2.89	8.9	3.04
73	-68.584	63.477	N	0.47	2.93	533.44	196.40	231.35	162.01	1.43	521.21	6.2	44.2	7.1	38.0	0.9	0.69	2.65	4.07	12.6	4.17
74	-68.591	63.481	NNE	0.14	2.25	452.36	128.85	103.05	38.97	2.64	390.46	5.5	46.0	6.2	40.5	0.7	0.34	3.03	5.12	31.1	5.92
75	-68.591	63.481	NE	0.55	3.30	518.42	294.86	318.01	283.67	1.12	504.24	3.1	48.5	7.9	45.4	4.8	0.64	1.71	5.00	31.1	5.14
76	-68.595	63.483	NE	0.93	3.67	570.54	528.52	255.68	209.65	1.22	513.90	3.5	48.6	4.5	45.1	1.0	0.87	0.97	4.52	29.5	5.02
77	-68.574	63.472	N	0.47	3.33	587.95	373.32	410.21	373.32	1.10	262.92	7.2	39.7	8.4	32.5	1.2	0.53	0.70	3.16	12.6	7.05
78	-68.540	63.485	W	0.20	2.67	*	*	*	*	*	*	*	*	*	*	*	0.35	*	*	*	*
79	-68.553	63.493	SW	0.07	1.13	*	*	*	*	*	*	*	*	*	*	*	0.67	*	*	*	*
80	-68.584	63.498	SW	0.03	0.73	*	*	*	*	*	*	*	*	*	*	*	0.65	*	*	*	*
81	-68.596	63.494	ESE	0.14	1.73	*	*	*	*	*	*	*	*	*	*	*	0.58	*	*	*	*
82	-68.597	63.495	E	0.08	1.30	*	*	*	*	*	*	*	*	*	*	*	0.56	*	*	*	*
83	-68.598	63.496	ENE	0.04	0.91	*	*	*	*	*	*	*	*	*	*	*	0.61	*	*	*	*
84	-68.598	63.497	E	0.11	1.54	*	*	*	*	*	*	*	*	*	*	*	0.56	*	*	*	*
85	-68.672	63.551	N	0.79	3.93	*	*	*	*	*	*	*	*	*	*	*	0.64	*	*	*	*
86	-68.676	63.550	NNW	0.28	2.25	*	*	*	*	*	*	*	*	*	*	*	0.70	*	*	*	*
87	-68.680	63.551	NNE	0.19	1.68	297.71	186.72	139.07	128.62	1.08	267.21	73.9	83.3	74.5	9.4	0.6	0.85	1.43	1.81	12.6	2.01
88	-68.686	63.550	NNE	1.06	4.24	726.03	385.78	298.38	229.47	1.30	534.72	28.9	82.7	32.8	53.8	3.9	0.74	1.39	4.24	45.0	5.75
89	-68.697	63.545	N	1.40	5.21	950.46	395.36	390.09	313.02	1.25	734.74	22.2	65.1	26.2	42.9	4.0	0.65	1.86	2.58	31.3	3.34
90	-68.703	63.546	NE	0.90	4.02	693.33	380.07	233.21	196.14	1.19	587.77	13.5	65.1	15.1	51.6	1.6	0.70	1.55	4.26	33.1	5.02
91	-68.703	63.548	N	1.64	5.56	965.36	546.79	233.21	196.14	1.19	637.54	13.5	68.8	15.1	55.3	1.6	0.67	1.17	3.28	33.1	4.96
92	-68.709	63.548	NNE	0.09	1.27	201.02	115.27	204.95	204.95	1.00	129.62	42.9	56.5	44.9	13.6	2.0	0.71	1.12	3.87	12.6	5.99
93	-68.710	63.548	N	0.69	3.47	520.64	439.69	557.72	373.37	1.49	437.08	22.1	60.9	23.5	38.8	1.4	0.72	0.99	4.26	37.8	5.07
94	-68.713	63.548	NE	0.18	1.85	336.42	172.28	221.32	187.86	1.18	238.71	11.7	50.7	13.4	39.0	1.7	0.67	1.39	6.61	40.4	9.28
95	-68.713	63.550	NE	0.27	1.98	322.70	253.32	199.72	156.73	1.27	297.08	44.7	57.7	45.1	13.0	0.4	0.87	1.17	2.31	12.6	2.51

Table B.2 Cont.

FID	Longitude	Latitude	DoT	*A* (km^2)	*P* (km)	*Rm* (m)	*Wm* (m)	*HLr* (m)	*HLS* (m)	*CRV*	*R* $_{1/2}$ (m)	*Di* (m)	*Dt* (m)	*Dbhw* (m)	*V* (m)	*Hhw* (m)	*C*	*E*	α_{max} (°)	α_{bathy} (°)	α (°)
96	-68.717	63.552	NE	1.80	5.38	833.21	498.10	574.76	523.15	1.10	830.59	21.2	62.8	23.3	41.6	2.1	0.78	1.67	2.86	31.1	2.87
97	-68.720	63.551	NE	0.35	2.36	411.11	183.34	244.07	223.71	1.09	400.95	30.2	56.1	32.4	25.9	2.2	0.80	2.19	3.60	32.3	3.70
98	-68.728	63.555	NE	0.37	3.24	619.56	169.44	236.05	168.42	1.40	572.78	14.9	53.8	17.9	38.9	3.0	0.44	3.38	3.59	24.1	3.89
99	-68.732	63.557	NE	0.50	3.54	658.02	266.44	270.85	247.11	1.10	376.25	12.7	54.7	13.6	42.0	0.9	0.50	1.41	3.65	31.3	6.37
100	-68.733	63.559	ENE	0.16	2.63	521.21	110.94	108.59	48.91	2.22	221.07	13.6	52.9	15.5	39.3	1.9	0.28	1.99	4.31	16.3	10.08
101	-68.737	63.561	NE	0.47	2.86	*	*	*	*	*	*	*	*	*	*	*	0.72	*	*	*	*
102	-68.740	63.564	ENE	0.73	4.25	*	*	*	*	*	*	*	*	*	*	*	0.51	*	*	*	*
103	-68.741	63.565	NE	0.45	3.89	*	*	*	*	*	*	*	*	*	*	*	0.38	*	*	*	*
104	-68.736	63.568	SW	0.23	2.22	*	*	*	*	*	*	*	*	*	*	*	0.58	*	*	*	*
105	-68.739	63.569	SW	0.14	1.58	*	*	*	*	*	*	*	*	*	*	*	0.69	*	*	*	*
106	-68.744	63.573	SW	0.07	1.21	*	*	*	*	*	*	*	*	*	*	*	0.59	*	*	*	*
107	-68.745	63.574	SW	0.02	0.58	*	*	*	*	*	*	*	*	*	*	*	0.78	*	*	*	*
108	-68.746	63.575	SW	0.06	1.11	*	*	*	*	*	*	*	*	*	*	*	0.59	*	*	*	*
109	-68.747	63.576	SW	0.02	0.55	*	*	*	*	*	*	*	*	*	*	*	0.75	*	*	*	*
110	-68.748	63.576	SW	0.03	0.66	*	*	*	*	*	*	*	*	*	*	*	0.82	*	*	*	*
111	-68.749	63.577	SW	0.04	0.78	*	*	*	*	*	*	*	*	*	*	*	0.87	*	*	*	*
112	-68.754	63.573	SE	0.10	1.54	*	*	*	*	*	*	*	*	*	*	*	0.54	*	*	*	*
113	-68.528	63.581	NE	0.52	5.81	751.77	354.67	58.63	41.36	1.42	98.01	105.4	189.3	108.1	83.9	2.7	0.19	0.28	6.37	28.3	40.56
114	-68.561	63.604	NNE	0.09	1.47	239.23	95.38	100.35	84.44	1.19	212.25	49.7	94.9	51.5	45.2	1.8	0.55	2.23	10.70	32.3	12.02
115	-68.554	63.606	NE	0.10	1.30	245.39	87.97	96.99	70.15	1.38	184.01	83.9	203.3	87.6	119.4	3.7	0.76	2.09	25.95	35.3	32.98
116	-68.545	63.607	NE	0.08	1.35	261.25	129.40	140.33	90.95	1.54	261.25	149.7	232.6	151.2	82.9	1.5	0.58	2.02	17.61	70.8	17.61
117	-68.599	63.596	WSW	0.11	1.27	217.27	123.51	67.39	51.95	1.30	209.21	26.3	57.9	28.1	31.6	1.8	0.83	1.69	8.28	39.6	8.59
118	-68.599	63.601	SE	0.32	4.14	501.56	196.87	125.09	49.05	2.55	456.01	46.1	79.3	49.3	33.2	3.2	0.24	2.32	3.79	34.9	4.16
119	-68.588	63.600	NE	0.18	1.98	270.16	289.58	68.56	30.44	2.25	195.94	64.6	136.9	67.7	72.3	3.1	0.59	0.68	14.98	35.0	20.25
120	-68.592	63.599	NE	0.07	1.55	*	*	*	*	*	*	*	*	*	*	*	0.37	*	*	*	*
121	-68.601	63.606	SE	0.02	0.59	*	*	*	*	*	*	*	*	*	*	*	0.79	*	*	*	*
122	-68.597	63.607	NE	0.03	0.65	*	*	*	*	*	*	*	*	*	*	*	0.76	*	*	*	*
123	-68.593	63.608	NE	0.09	1.37	183.16	152.67	160.33	152.67	1.05	173.23	127.7	146.5	130.2	18.8	2.5	0.59	1.13	5.86	39.6	6.19
124	-68.598	63.608	SE	0.05	0.89	70.25	116.28	89.27	73.46	1.22	70.25	65.6	99.2	67.1	33.6	1.5	0.77	0.60	25.56	26.6	25.56
125	-68.612	63.612	S	0.20	1.87	308.48	173.51	172.46	133.95	1.29	308.48	30.6	62.4	32.4	31.8	1.8	0.73	1.78	5.89	35.3	5.89
126	-68.615	63.624	NE	0.15	1.98	323.83	133.87	52.78	26.05	2.03	263.10	43.8	106.5	47.0	62.7	3.2	0.47	1.97	10.96	20.3	13.40
127	-68.617	63.631	SSE	0.95	4.98	562.75	682.74	1026.04	682.74	1.50	259.87	69.4	139.7	73.3	70.3	3.9	0.48	0.38	7.12	73.9	15.14

Table B.2 Cont.

FID	Longitude	Latitude	DoT	A (km^2)	P (km)	Rm (m)	Wm (m)	HLr (m)	HLS (m)	CRV	$R_{1/2}$ (m)	Di (m)	Dt (m)	Dbhw (m)	V (m)	Hhw (m)	C	E	α_{max} (°)	α_{bathy} (°)	α (°)
128	-68.624	63.633	E	0.17	1.63	252.97	176.92	165.64	140.19	1.18	252.97	44.4	84.4	46.4	40.0	2.0	0.78	1.43	8.99	30.9	8.99
129	-68.629	63.640	ENE	0.07	1.15	*	*	*	*	*	*	*	*	*	*	*	0.69	*	*	*	*
130	-68.618	63.646	SE	0.25	2.17	363.11	292.01	93.69	88.17	1.06	300.51	68.7	94.1	69.8	25.4	1.1	0.67	1.03	4.00	46.7	4.83
131	-68.637	63.651	ENE	0.37	2.42	*	*	*	*	*	*	*	*	*	*	*	0.80	*	*	*	*
132	-68.638	63.654	ENE	0.38	2.52	*	*	*	*	*	*	*	*	*	*	*	0.75	*	*	*	*
133	-68.639	63.655	E	0.23	2.27	*	*	*	*	*	*	*	*	*	*	*	0.56	*	*	*	*
134	-68.643	63.660	N	0.07	1.25	223.56	82.87	58.08	52.99	1.10	184.70	100.9	134.7	104.1	33.8	3.2	0.58	2.23	8.60	33.8	10.37
135	-68.645	63.664	N	1.11	4.19	728.44	396.01	406.56	347.26	1.17	556.82	126.9	144.5	130.9	17.6	4.0	0.80	1.41	1.38	72.3	1.81
136	-68.670	63.741	NE	0.03	0.83	138.03	74.12	86.45	59.03	1.46	126.98	23.6	30.4	24.8	6.8	1.2	0.64	1.71	2.82	12.6	3.07
137	-68.682	63.738	NE	0.33	2.69	405.78	270.09	79.73	57.09	1.40	405.78	23.2	62.9	25.8	39.7	2.6	0.57	1.50	5.59	27.2	5.59
138	-68.677	63.729	SE	0.14	1.78	*	*	*	*	*	*	*	*	*	*	*	0.57	*	*	*	*
139	-68.678	63.731	SSW	0.23	2.57	*	*	*	*	*	*	*	*	*	*	*	0.44	*	*	*	*
140	-68.542	63.693	SE	0.06	1.04	170.83	105.03	176.33	93.49	1.89	162.70	33.6	34.8	35.7	1.2	2.1	0.68	1.55	0.40	22.9	0.42
141	-68.520	63.676	W	0.17	1.78	*	*	*	*	*	*	*	*	*	*	*	0.67	*	*	*	*
142	-68.548	63.660	NW	0.07	1.42	247.41	73.12	46.74	25.32	1.85	174.90	54.7	86.1	57.3	31.4	2.6	0.42	2.39	7.23	28.9	10.18
143	-68.529	63.660	W	0.09	1.46	244.72	111.92	41.99	22.82	1.84	220.02	52.2	69.6	53.1	17.4	0.9	0.51	1.97	4.07	33.7	4.52
144	-68.517	63.666	NW	0.04	0.86	137.81	87.76	81.89	61.87	1.32	92.94	48.7	64.9	50.5	16.2	1.8	0.67	1.06	6.70	23.3	9.89
145	-68.521	63.669	E	0.31	2.58	391.31	168.00	124.65	105.92	1.18	321.56	41.9	79.3	44.1	37.4	2.2	0.58	1.91	5.46	28.3	6.63
146	-68.523	63.667	S	0.03	0.73	98.51	95.82	28.48	28.48	1.00	98.51	53.5	64.0	56.6	10.5	3.1	0.72	1.03	6.08	28.3	6.08
147	-68.530	63.671	SW	0.02	0.67	139.42	51.39	32.41	28.16	1.15	139.42	27.7	42.6	28.1	14.9	0.4	0.51	2.71	6.10	19.8	6.10
148	-68.520	63.665	S	0.05	0.97	150.29	90.73	45.07	39.87	1.13	150.29	43.2	55.8	45.7	12.6	2.5	0.61	1.66	4.79	22.4	4.79
149	-68.526	63.662	NW	0.02	0.53	116.76	48.17	9.68	9.68	1.00	116.76	50.9	62.7	51.9	11.8	1.0	0.72	2.42	5.77	14.3	5.77
150	-68.508	63.647	W	0.08	1.31	262.00	72.72	63.07	37.92	1.66	262.00	84.4	95.0	85.1	10.6	0.7	0.56	3.60	2.32	61.8	2.32
151	-68.512	63.644	N	0.07	1.27	181.52	91.35	54.32	37.11	1.46	164.15	36.2	42.8	37.1	6.6	0.9	0.54	1.80	2.08	28.9	2.30
152	-68.515	63.647	N	0.06	1.16	219.53	103.62	142.82	103.62	1.38	202.99	45.8	79.2	46.5	33.4	0.7	0.56	1.96	8.65	36.4	9.34
153	-68.521	63.646	N	0.07	1.87	360.95	96.73	27.63	21.82	1.27	347.40	41.9	89.5	43.1	47.6	1.2	0.24	3.59	7.51	12.6	7.80
154	-68.506	63.638	NE	0.03	0.90	191.91	76.41	70.35	48.92	1.44	181.93	52.8	72.2	54.9	19.4	2.1	0.47	2.38	5.77	25.4	6.09
155	-68.508	63.639	E	0.08	1.45	181.36	38.88	29.53	23.15	1.28	159.74	43.9	72.2	44.5	28.3	0.6	0.46	4.11	8.87	26.6	10.05
156	-68.486	63.648	SE	0.02	0.57	151.15	63.35	124.87	63.35	1.97	151.15	62.8	67.1	64.2	4.3	1.4	0.77	2.39	1.63	32.6	1.63
157	-68.472	63.634	E	0.03	0.83	155.25	49.56	36.76	34.98	1.05	152.94	53.9	78.2	55.4	24.3	1.5	0.61	3.09	8.90	40.4	9.03
158	-68.481	63.606	SE	0.39	3.28	674.76	166.11	79.67	36.07	2.21	580.94	67.1	114.6	69.7	47.5	2.6	0.45	3.50	4.03	27.0	4.67
159	-68.466	63.615	N	0.05	0.94	118.94	77.85	53.02	35.82	1.48	118.94	56.2	82.0	58.2	25.8	2.0	0.78	1.53	12.24	32.3	12.24

Table B.2 Cont.

FID	Longitude	Latitude	DoT	A (km^2)	P (km)	Rm (m)	Wm (m)	HLr (m)	HLS (m)	CRV	$R_{1/2}$ (m)	Di (m)	Dt (m)	$Dbhw$ (m)	V (m)	Hhw (m)	C	E	α_{max} (°)	α_{bathy} (°)	α (°)
160	-68.466	63.612	SSE	0.21	2.24	369.95	209.27	53.36	35.54	1.50	239.33	52.1	64.6	53.8	12.5	1.7	0.52	1.14	1.94	30.9	2.99
161	-68.453	63.614	NE	0.13	1.50	235.15	150.74	67.95	35.84	1.90	226.71	107.8	124.9	110.7	17.1	2.9	0.74	1.50	4.16	40.3	4.31
162	-68.448	63.601	ESE	0.47	3.11	498.52	320.27	69.88	47.30	1.48	484.59	101.6	146.9	103.6	45.3	2.0	0.61	1.51	5.19	35.3	5.34
163	-68.404	63.606	W	0.17	2.29	434.67	139.82	67.92	40.53	1.68	202.55	86.6	124.6	89.1	38.0	2.5	0.42	1.45	5.00	32.6	10.63
164	-68.395	63.606	ENE	0.24	2.49	466.85	240.48	89.91	86.09	1.04	210.44	60.5	90.5	61.5	30.0	1.0	0.50	0.88	3.68	33.8	8.11
165	-68.408	63.617	SW	0.36	4.23	553.51	168.92	119.94	50.22	2.39	192.51	40.3	132.7	43.0	92.4	2.7	0.25	1.14	9.48	26.6	25.64
166	-68.423	63.624	SW	0.51	3.06	483.17	355.35	48.74	34.27	1.42	467.49	60.6	151.6	63.2	91.0	2.6	0.69	1.32	10.67	35.3	11.02
167	-68.419	63.631	S	0.16	2.44	*	*	*	*	*	*	*	*	*	*	*	0.33	*	*	*	*
168	-68.398	63.623	NE	0.18	2.81	*	*	*	*	*	*	*	*	*	*	*	0.29	*	*	*	*
169	-68.384	63.618	NE	0.04	0.90	*	*	*	*	*	*	*	*	*	*	*	0.67	*	*	*	*
170	-68.385	63.619	SW	0.03	0.78	*	*	*	*	*	*	*	*	*	*	*	0.69	*	*	*	*
171	-68.371	63.614	NE	0.05	0.86	*	*	*	*	*	*	*	*	*	*	*	0.77	*	*	*	*
172	-68.366	63.613	NW	0.04	0.91	132.82	84.37	96.79	69.84	1.39	132.82	53.8	58.1	55.4	4.3	1.6	0.65	1.57	1.85	15.8	1.85
173	-68.359	63.612	W	0.07	1.05	183.21	101.88	55.69	32.94	1.69	183.21	55.7	59.4	56.3	3.7	0.6	0.81	1.80	1.16	12.6	1.16
174	-68.358	63.613	SW	0.04	0.82	*	*	*	*	*	*	*	*	*	*	*	0.84	*	*	*	*
175	-68.360	63.614	W	0.06	0.96	*	*	*	*	*	*	*	*	*	*	*	0.76	*	*	*	*
176	-68.425	63.648	S	0.07	1.37	*	*	*	*	*	*	*	*	*	*	*	0.45	*	*	*	*
177	-68.451	63.659	WSW	0.04	0.77	*	*	*	*	*	*	*	*	*	*	*	0.76	*	*	*	*
178	-68.419	63.656	NE	0.14	1.77	*	*	*	*	*	*	*	*	*	*	*	0.58	*	*	*	*
179	-68.408	63.663	WSW	0.09	1.48	*	*	*	*	*	*	*	*	*	*	*	0.51	*	*	*	*
180	-68.406	63.661	SW	0.06	1.24	*	*	*	*	*	*	*	*	*	*	*	0.48	*	*	*	*
181	-68.427	63.678	SW	0.07	1.10	*	*	*	*	*	*	*	*	*	*	*	0.76	*	*	*	*
182	-68.498	63.658	SW	0.02	0.53	*	*	*	*	*	*	*	*	*	*	*	0.84	*	*	*	*
183	-68.500	63.660	NE	0.13	1.32	184.91	174.08	83.47	83.10	1.00	184.91	37.9	65.2	40.3	27.3	2.4	0.90	1.06	8.40	28.3	8.40
184	-68.499	63.661	NE	0.04	0.78	135.40	77.26	49.21	39.23	1.25	135.40	45.4	67.1	47.2	21.7	1.8	0.76	1.75	9.11	27.2	9.11
185	-68.502	63.665	E	0.05	1.05	198.94	71.71	54.57	30.07	1.81	195.42	50.5	72.3	51.9	21.8	1.4	0.51	2.73	6.25	28.3	6.37
186	-68.501	63.669	SW	0.24	2.03	371.79	189.31	142.73	72.67	1.96	332.33	36.2	74.0	37.7	37.8	1.5	0.73	1.76	5.81	56.3	6.49
187	-68.503	63.674	E	0.06	1.28	222.07	85.11	39.76	34.34	1.16	148.39	27.2	64.4	28.3	37.2	1.1	0.46	1.74	9.51	27.2	14.07
188	-68.471	63.681	SW	0.03	0.90	164.26	55.26	27.02	20.79	1.30	139.90	36.8	52.5	37.7	15.7	0.9	0.54	2.53	5.46	32.5	6.40
189	-68.480	63.678	NE	0.18	1.81	315.40	166.63	132.36	101.24	1.31	220.26	27.6	91.1	29.8	63.5	2.2	0.67	1.32	11.38	46.7	16.08
190	-68.484	63.680	NE	0.17	1.93	322.13	184.76	62.61	45.66	1.37	225.64	43.5	77.0	45.6	33.5	2.1	0.56	1.22	5.94	32.5	8.44
191	-68.443	63.691	SW	0.03	0.77	*	*	*	*	*	*	*	*	*	*	*	0.64	*	*	*	*

Table B.2 Cont.

FID	Longitude	Latitude	DoT	*A* (km^2)	*P* (km)	*Rm* (m)	*Wm* (m)	*HLr* (m)	*HLS* (m)	*CRV*	$R_{1/2}$ (m)	*Di* (m)	*Dt* (m)	*Dbhw* (m)	*V* (m)	*Hhw* (m)	*C*	*E*	α_{max} (°)	α_{bathy} (°)	α (°)
192	-68.452	63.692	NE	0.02	0.73	*	*	*	*	*	*	*	*	*	*	*	0.58	*	*	*	*
193	-68.453	63.693	NE	0.04	0.80	*	*	*	*	*	*	*	*	*	*	*	0.79	*	*	*	*
194	-68.448	63.694	SW	0.03	0.70	99.16	73.25	36.55	36.55	1.00	99.16	44.4	57.6	45.6	13.2	1.2	0.66	1.35	7.58	28.3	7.58
195	-68.454	63.696	E	0.05	1.03	*	*	*	*	*	*	*	*	*	*	*	0.60	*	*	*	*
196	-68.515	63.710	SW	0.09	1.23	224.55	97.07	58.88	37.77	1.56	224.55	11.6	34.4	13.1	22.8	1.5	0.73	2.31	5.80	32.5	5.80
197	-68.513	63.706	N	0.02	0.52	73.96	64.47	45.26	26.97	1.68	73.96	25.2	30.6	25.8	5.4	0.6	0.81	1.15	4.18	24.1	4.18
198	-68.515	63.703	NE	0.04	0.93	146.43	60.47	54.37	26.62	2.04	137.48	21.4	43.3	23.2	21.9	1.8	0.65	2.27	8.51	33.9	9.05
199	-68.512	63.704	SW	0.03	0.81	154.23	57.42	35.58	27.90	1.28	154.23	15.5	40.1	15.9	24.6	0.4	0.61	2.69	9.06	24.1	9.06
200	-68.499	63.704	E	0.05	1.05	*	*	*	*	*	*	*	*	*	*	*	0.58	*	*	*	*
201	-68.498	63.705	E	0.04	1.03	*	*	*	*	*	*	*	*	*	*	*	0.53	*	*	*	*
202	-68.498	63.713	S	0.03	0.74	*	*	*	*	*	*	*	*	*	*	*	0.70	*	*	*	*
203	-68.517	63.722	ENE	0.05	0.96	*	*	*	*	*	*	*	*	*	*	*	0.70	*	*	*	*
204	-68.467	63.714	SW	0.05	0.96	*	*	*	*	*	*	*	*	*	*	*	0.74	*	*	*	*
205	-68.468	63.716	SW	0.02	0.70	*	*	*	*	*	*	*	*	*	*	*	0.63	*	*	*	*
206	-68.262	63.569	SW	0.04	0.87	*	*	*	*	*	*	*	*	*	*	*	0.62	*	*	*	*
207	-68.240	63.553	NNW	0.06	1.03	*	*	*	*	*	*	*	*	*	*	*	0.71	*	*	*	*
208	-68.236	63.554	NNW	0.08	1.05	*	*	*	*	*	*	*	*	*	*	*	0.86	*	*	*	*
209	-68.230	63.554	N	0.04	0.86	*	*	*	*	*	*	*	*	*	*	*	0.73	*	*	*	*
210	-68.210	63.554	NE	0.18	1.80	309.28	204.64	79.66	40.58	1.96	279.26	52.3	69.3	53.3	17.0	1.0	0.71	1.36	3.15	60.9	3.48
211	-68.169	63.550	NNE	0.09	1.20	*	*	*	*	*	*	*	*	*	*	*	0.82	*	*	*	*
212	-68.172	63.565	SE	0.14	1.98	*	*	*	*	*	*	*	*	*	*	*	0.45	*	*	*	*
213	-68.163	63.568	S	0.03	0.81	141.31	65.05	59.14	47.61	1.24	141.31	52.5	57.3	53.7	4.8	1.2	0.65	2.17	1.95	12.6	1.95
214	-68.162	63.570	S	0.09	1.48	208.40	145.05	100.72	85.46	1.18	145.92	37.8	65.3	40.0	27.5	2.2	0.52	1.01	7.52	33.9	10.67
215	-68.168	63.591	ESE	0.04	0.81	*	*	*	*	*	*	*	*	*	*	*	0.75	*	*	*	*
216	-68.168	63.593	S	0.03	0.69	97.16	87.33	49.54	29.62	1.67	83.60	35.1	40.1	37.2	5.0	2.1	0.72	0.96	2.95	12.6	3.42
217	-68.161	63.596	S	0.06	1.53	*	*	*	*	*	*	*	*	*	*	*	0.34	*	*	*	*
218	-68.090	63.595	E	0.08	1.21	*	*	*	*	*	*	*	*	*	*	*	0.65	*	*	*	*
219	-68.082	63.589	W	0.07	1.29	*	*	*	*	*	*	*	*	*	*	*	0.55	*	*	*	*
220	-68.081	63.584	W	0.10	1.57	*	*	*	*	*	*	*	*	*	*	*	0.49	*	*	*	*
221	-68.087	63.583	ENE	0.10	1.62	*	*	*	*	*	*	*	*	*	*	*	0.49	*	*	*	*
222	-68.080	63.576	W	0.09	1.75	*	*	*	*	*	*	*	*	*	*	*	0.38	*	*	*	*
223	-68.087	63.571	E	0.06	1.03	*	*	*	*	*	*	*	*	*	*	*	0.66	*	*	*	*

Table B.2 Cont.

FID	Longitude	Latitude	DoT	*A* (km^2)	*P* (km)	*Rm* (m)	*Wm* (m)	*HLr* (m)	*HLS* (m)	*CRV*	*R* $_{1/2}$ (m)	*Di* (m)	*Dt* (m)	*Dbhw* (m)	*V* (m)	*Hhw* (m)	*C*	*E*	α_{max} (°)	α_{bathy} (°)	α (°)
224	-68.078	63.503	E	0.03	0.66	*	*	*	*	*	*	*	*	*	*	*	0.91	*	*	*	*
225	-68.058	63.502	NNW	0.06	1.11	211.64	68.46	119.54	66.39	1.80	211.64	89.6	126.3	92.0	36.7	2.4	0.63	3.09	9.84	31.1	9.84
226	-68.619	63.640	SW	0.61	3.22	485.21	292.49	413.44	291.66	1.42	485.21	108.5	138.1	112.6	29.6	4.1	0.75	1.66	3.49	40.8	3.49
227	-68.613	63.641	SSE	0.57	3.27	569.72	282.12	376.54	219.57	1.71	528.23	90.1	124.1	93.2	34.0	3.1	0.66	1.87	3.42	51.9	3.68
228	-68.473	63.531	NE	1.81	10.66	1692.24	557.17	71.39	44.07	1.62	765.73	38.1	198.6	41.6	160.5	3.5	0.20	1.37	5.42	19.8	11.84
229	-68.465	63.531	NE	0.25	3.67	718.38	114.52	117.66	53.93	2.18	350.87	137.2	156.6	139.5	19.4	2.3	0.24	3.06	1.55	11.9	3.16
230	-68.470	63.527	NE	1.31	6.47	1208.75	300.81	36.92	36.92	1.00	1043.16	14.6	149.1	18.7	134.5	4.1	0.39	3.47	6.35	29.7	7.35
231	-68.467	63.523	NE	0.74	5.39	939.91	285.84	49.34	49.34	1.00	814.31	22.5	141.7	23.4	119.2	0.9	0.32	2.85	7.23	24.1	8.33
232	-68.463	63.523	NE	0.77	4.75	869.25	289.28	294.19	249.49	1.18	726.98	49.5	141.6	55.8	92.1	6.3	0.43	2.51	6.05	26.6	7.22
233	-68.375	63.394	NE	0.68	3.34	*	*	*	*	*	*	*	*	*	*	*	0.76	*	*	*	*
234	-68.331	63.595	SW	0.54	4.02	699.69	259.21	88.19	61.08	1.44	410.76	47.9	103.5	49.8	55.6	1.9	0.42	1.58	4.54	34.9	7.71
235	-68.331	63.599	WNW	0.22	1.83	297.50	190.71	168.58	154.71	1.09	297.50	55.7	93.0	58.1	37.3	2.4	0.82	1.56	7.15	21.8	7.15
236	-68.331	63.601	WNW	0.11	1.29	195.25	145.69	82.43	75.48	1.09	195.25	68.1	91.1	69.9	23.0	1.8	0.84	1.34	6.72	21.8	6.72
237	-68.332	63.602	NW	0.06	0.98	166.99	94.79	79.72	46.88	1.70	149.79	75.1	89.1	77.6	14.0	2.5	0.73	1.58	4.79	20.8	5.34
238	-68.330	63.603	NW	0.05	0.92	154.77	123.46	39.33	39.33	1.00	154.77	54.1	87.3	58.8	33.2	4.7	0.73	1.25	12.11	30.1	12.11
239	-68.392	63.616	SW	0.01	0.48	86.69	49.39	40.83	28.85	1.42	80.90	62.4	71.8	63.4	9.4	1.0	0.81	1.64	6.19	19.8	6.63
240	-68.393	63.611	SE	0.04	0.79	139.15	77.33	60.90	53.76	1.13	136.19	58.3	68.2	59.1	9.9	0.8	0.83	1.76	4.07	31.3	4.16
241	-68.299	63.584	ENE	0.08	1.64	296.49	86.33	43.22	15.71	2.75	244.21	40.6	74.6	42.2	34.0	1.6	0.38	2.83	6.54	14.3	7.93
242	-68.169	63.522	NE	0.04	0.78	119.96	103.52	42.94	33.98	1.26	119.96	45.6	64.2	47.6	18.6	2.0	0.89	1.16	8.81	30.9	8.81
243	-68.199	63.538	NE	0.25	2.23	433.24	164.53	114.76	46.63	2.46	395.68	76.4	145.6	77.7	69.2	1.3	0.63	2.40	9.08	28.3	9.92
244	-68.134	63.557	SE	0.74	7.20	944.87	476.69	111.46	51.49	2.16	567.92	60.0	159.8	61.2	99.8	1.2	0.18	1.19	6.03	25.4	9.97
245	-68.095	63.557	SW	0.05	1.13	223.57	70.32	62.66	22.55	2.78	217.01	49.6	72.3	50.7	22.7	1.1	0.53	3.09	5.80	32.6	5.97

Appendix C: Radiocarbon Dates

C.1 Material Collection in Core Lab

Radiocarbon datable material (typically mollusc shells) was extracted from sediment cores during core lab analysis. On extraction, shells were washed in distilled water to remove sediments, air dried, photographed, and stored in labelled glass or plastic vials.

C.2 Species Identification and Pre-AMS Preparation

The samples were then sent to Paleotec labs for species identification, high resolution photography, and further pre-treatment. This proceeded as follows: "Glass vials and plastic containers containing articulated marine valves, single valves, and shell fragments were all treated similarly in preparation for AMS radiocarbon dating. Using a fine mesh sieve (Canadian Standard Tyler 60 sieve; mesh opening 0.25 mm), the shells were initially cleaned in tap water with a gentle spray to remove loose adhering sediment. The shells were further cleaned in an ultrasonic bath. The shells were air-dried and photographed using either a Nikon Coolpix 4500 digital camera for the larger shells or an Infinity 2 digital camera mounted on an Olympus binocular microscope for smaller shells.

After photographing the desired shell for AMS dating, larger bivalves were further cleaned using a Dremel moto-flex, variable speed tool (Model 332) outfitted with an aluminum oxide grinding bit. To avoid cross-contamination of the carbonate material, new grinding bits were used for each shell grinding. Sterile disposable latex gloves were worn during this procedure and disposed after each shell grinding. The outer chalky layer and any secondary carbonates were removed by grinding both the dorsal and ventral surfaces of the shell revealing the inner nacre. The nacreous layer is shiny and hard being composed of platelets of aragonite (calcium carbonate, $CaCO3$ crystals) separated by sheets of an organic matrix (most often proteins) making it strong and resilient. Nacre is the preferred carbonate material when dating shells. The cleaned shell fragments were inspected and wrapped in freshly-cut aluminum tin foil packets and placed in labeled, sterile, plastic petri dishes (3.5 cm in diameter) in preparation for shipment to the dating facility.

In most cases, the entire valve or valve fragment was submitted for AMS dating since most of the identified bivalves were small-sized and relatively short-lived. For larger-sized bivalves, the outer periphery of the valve was subsampled for dating in order to date the death of the clam." (Alice Telka, pers. com., 2018)

C.3 Accelerator Mass Spectrometry (AMS)

Between 2015 and 2017, all samples were analyzed at the W.M. Keck-Carbon Cycle AMS Facility at the University of California (Irvine). In 2018, larger samples (>50 mg) were analyzed at the André E. Lalonde AMS Laboratory at the University of Ottawa, while smaller samples were analyzed at the Keck facility. Final lab reports were compiled by Paleotec Services with lab results summarized in Table C.1.

AMS dating measures the masses of different isotopes of carbon (^{14}C, ^{13}C, ^{12}C). The ratios of these different isotopes can be used to establish an age for an object based on the rate of radioactive decay of ^{14}C (half-life = ~5700 years).

All results have been corrected for isotopic fractionation according to the conventions of Stuiver and Polach (1977), with $\delta^{13}C$ values measured on prepared graphite using the AMS spectrometer (Table C.1). These can differ from $\delta^{13}C$ of the original material, if fractionation occurred during sample graphitization or the AMS measurement, and are not shown. Standard uncertainty (1-sigma probability) is also provided.

Fraction Modern (Table C.1) is a measurement of the deviation of the $^{14}C/^{12}C$ ratio of a sample from "Modern." Modern is defined as 95% of the radiocarbon concentration (in AD 1950) of NBS Oxalic Acid I (SRM 4990B, OX-I) normalized to δ^{13}CVPDB=-19 per mil (Olsson, 1970). Standard uncertainty (1-sigma probability) is also provided.

$D^{14}C$ (Table C.1) is defined in Stuiver and Pollach (1977) as the relative difference between the absolute international standard (base year 1950) and sample activity corrected for age and $\delta^{13}C$. Standard uncertainty (1-sigma probability) is also provided.

^{14}C age (Table C.1) corresponds to the conventional radiocarbon age BP (before present; AD 1950). Standard uncertainty (1-sigma probability) is also provided. Dates were normalized to -25 ppm following standard practice

C.4 Radiocarbon Calibration

Radiocarbon ages for this dissertation were calibrated using CALIB 8.2 (http://calib.org/calib/; rev. 8, Stuiver and Reimer 1993) and the Marine20 calibration curve ($\Delta R = 41 \pm 21$; Heaton et al. 2020). Prior to the publishing of that curve the Marine13 calibration curve had been used ($\Delta R = 179 \pm 22$). There were minimal changes in the age ranges between the two curves (mean difference 38 ± 5 years for midpoint ages). Sedimentation rates derived using radiocarbon ages differed by <13% (<3.3% for ages >500 years).

The ΔR value used for the Marine13 analysis is based on four samples taken from around outer Frobisher Bay; none are available from inner Frobisher Bay (Coulthard et al. 2010). For the Marine20 analysis, ΔR was generated using the same sample data and the 14CHRONO Marine20 Reservoir Database (http://calib.org/marine/; Reimer and Reimer 2017).

The developers of the Marine20 calibration curve specified that it is applicable in latitudes <50° and may be inappropriate in polar regions. This is because the variability of sea ice cover, upwelling, and air-sea gas exchange at high latitudes may cause additional changes in old carbon concentration. This could have an impact on our marine radiocarbon ages in inner Frobisher Bay. Radiocarbon studies focused in Canadian Arctic waters suggest that regional ΔR values for southeastern Baffin Island and Hudson Strait range up to approximately 210 years (Coulthard et al. 2010), although much higher values pertain further north and west in Foxe Basin and the Arctic Archipelago. In outer Frobisher Bay, measured values of ΔR are lower, perhaps reflecting the bay's location and orientation, open to the North Atlantic.

Table C.1 Accelerator mass spectrometry lab results for radiocarbon dated material in inner Frobisher Bay. Lab ID corresponds to reference number assigned to each sample by W.M. Keck-Carbon Cycle AMS Facility at the University of California (Irvine; UCIAMS) or André E. Lalonde AMS Laboratory at the University of Ottawa (UOC). Core ID corresponds to the sediment core from which the radiocarbon sample was originally collected. Depth downcore is the sample's position in the core. $\delta^{13}C$ is the measured ratio of ^{13}C:^{12}C in parts per thousand. "Fraction modern" is a measurement of the deviation of the ^{14}C:^{12}C of a sample from "Modern". $D^{14}C$ represents the normalized $d^{14}C$ value. ^{14}C age corresponds to the conventional radiocarbon age BP (before present; AD 1950). Standard uncertainties (1-sigma probability) are also provided for $\delta^{13}C$, $D^{14}C$, "Fraction modern" and ^{14}C measurements All values are reported following the conventions in Stuiver and Polach (1977).

Lab ID	Core ID	Depth downcore (cm)	$\delta^{13}C$ (‰)	±	Fraction modern	±	$D^{14}C$ (‰)	±	^{14}C age (BP)	±
UCIAMS-155830	2014805-0004	292-293			0.5078	0.0013	-492.2	1.3	5445	25
UCIAMS-155831	2014805-0004	331-332			0.4416	0.001	-558.4	1	6565	20
UCIAMS-155832	2014805-0004	400-401			0.4213	0.0012	-578.7	1.2	6945	25
UCIAMS-155833	2014805-0004	511-512			0.4059	0.001	-594.1	1	7245	25
UCIAMS-169710	2015805-0006	210-212			0.3194	0.0008	-680.6	0.8	9165	25
UCIAMS-169711	2015805-0007	103-104			0.7472	0.0012	-252.8	1.2	2340	15
UCIAMS-169712	2015805-0007	296-298			0.5721	0.001	-427.9	1	4485	15
UCIAMS-169713	2015805-0007	364-367			0.5342	0.001	-465.8	1	5035	15
UCIAMS-169714	2015805-0007	469-470			0.4419	0.0009	-558.1	0.9	6560	20
UCIAMS-169715	2015805-0008	240-242			0.6055	0.0011	-394.5	1.1	4030	15
UCIAMS-169716	2015805-0008	426-327			0.4955	0.0009	-504.5	0.9	5640	15
UCIAMS-169717	2015805-0008	388-389			0.4506	0.0009	-549.5	0.9	6405	20
UCIAMS-169718	2015805-0008	436-437			0.4384	0.0008	-561.6	0.8	6625	20
UCIAMS-169719	2015805-0008	501-502			0.4248	0.0009	-575.2	0.9	6880	20
UCIAMS-169720	2015805-0009	264-265			0.6746	0.0011	-325.4	1.1	3160	15
UCIAMS-169721	2015805-0009	361-362			0.4907	0.0009	-509.3	0.9	5720	15
UCIAMS-169722	2015805-0009	402-403			0.4584	0.0009	-541.6	0.9	6265	20
UCIAMS-169723	2015805-0009	489-490			0.4413	0.001	-558.7	1	6570	20
UCIAMS-169724	2015805-0009	526-527			0.4324	0.0009	-567.6	0.9	6735	20
UCIAMS-169725	2015805-0009	571-572			0.4222	0.0008	-577.8	0.8	6925	20
UCIAMS-187012	2016Nuliajuk-0021	121-122			0.5352	0.001	-464.8	1	5020	15
UCIAMS-187013	2016Nuliajuk-0021	177-178			0.5005	0.001	-499.5	1	5560	20
UCIAMS-187014	2016Nuliajuk-0024	63-64			0.8668	0.0013	-133.2	1.3	1150	15
UCIAMS-187015	2016Nuliajuk-0026	85-86			0.3294	0.0007	-670.6	0.7	8920	20
UCIAMS-187016	2016Nuliajuk-0028	44-45			0.6492	0.001	-350.8	1	3470	15
UCIAMS-187017	2016Nuliajuk-0029	23-24			0.8756	0.0013	-124.4	1.3	1065	15
UCIAMS-187018	2016Nuliajuk-0029	66-67			0.3803	0.0008	-619.7	0.8	7765	20
UCIAMS-187019	2016Nuliajuk-0029	119-120			0.3579	0.0007	-642.1	0.7	8255	20
UCIAMS-187020	2016Nuliajuk-0030	113-114			0.3855	0.0008	-614.5	0.8	7660	20
UCIAMS-187021	2016804-0001	200-201			0.412	0.0007	-588	0.7	7125	15
UCIAMS-187022	2016804-0001	289-290			0.4062	0.0007	-593.8	0.7	7235	15
UCIAMS-187023	2016804-0001	388-389			0.3727	0.0007	-627.7	0.7	7935	20
UCIAMS-187024	2016804-0002	166-167			0.4216	0.0008	-578.4	0.8	6940	20
UCIAMS-187025	2016804-0002	294-295			0.4033	0.001	-596.7	1	7295	25
UCIAMS-187026	2016804-0002	473-474			0.3839	0.0007	-616.1	0.7	7690	20
UCIAMS-187027	2016804-0007	153-154			0.5093	0.0008	-490.7	0.8	5420	15
UCIAMS-187028	2016804-0007	186-187			0.5053	0.001	-494.7	1	5485	20
UCIAMS-187029	2016804-0007	273-274	-12.1	0.1	0.6018	0.0009	-398.2	0.9	4080	15
UCIAMS-187030	2016804-0007	331-335			0.5249	0.0009	-475.1	0.9	5180	15
UCIAMS-187031	2016804-0007	452-453			0.4786	0.0008	-521.4	0.8	5920	15
UCIAMS-187032	2016804-0008	230-232			0.5278	0.0008	-472.2	0.8	5135	15
UCIAMS-187033	2016804-0008	364-365			0.478	0.0008	-522	0.8	5930	15
UCIAMS-187034	2016804-0008	395-396			0.4643	0.0008	-535.7	0.8	6165	15
UCIAMS-187035	2016804-0008	519-520			0.4139	0.0008	-586.1	0.8	7085	20
UCIAMS-187036	2016804-0009	189-190			0.5814	0.001	-418.6	1	4355	15
UCIAMS-187037	2016804-0009	320-321			0.4213	0.0008	-578.7	0.8	6945	15

Table C.1 Cont.

Lab ID	Core ID	Depth downcore (cm)	$\delta^{13}C$ (‰)	±	Fraction modern	±	$D^{14}C$ (‰)	±	^{14}C age (BP)	±
UCIAMS-187038	2016804-0009	382-383			0.4148	0.0009	-585.2	0.9	7070	20
UCIAMS-187039	2016804-0009	531-532			0.4049	0.0008	-595.1	0.8	7265	20
UCIAMS-187040	2016804-0010	26-27			0.9135	0.0014	-86.5	1.4	725	15
UCIAMS-187041	2016804-0010	330-331			0.4327	0.0008	-567.3	0.8	6730	15
UCIAMS-187042	2016804-0010	482-483			0.4223	0.0008	-577.7	0.8	6925	15
UCIAMS-202065	2015805-0008	283-284			0.5444	0.001	-455.6	1	4885	15
UCIAMS-202066	2015805-0009	281-283			0.6451	0.0013	-354.9	1.3	3520	20
UCIAMS-202067	2016Nuliajuk-0003	59-60			0.5513	0.0011	-448.7	1.1	4785	20
UCIAMS-202068	2016Nuliajuk-0027	59-60			0.3875	0.0008	-612.5	0.8	7615	20
UCIAMS-202069	2016Nuliajuk-0030	33-35			0.6876	0.0013	-312.4	1.3	3010	20
UCIAMS-202070	2016804-0001	43-44			0.8842	0.0016	-115.8	1.6	990	15
UCIAMS-202071	2016804-0007	93-94			0.5441	0.0011	-455.9	1.1	4890	20
UCIAMS-202072	2016804-0007	303-304			0.5464	0.0011	-453.6	1.1	4855	20
UCIAMS-202073	2016804-0007	400-401			0.5127	0.0011	-487.3	1.1	5365	20
UCIAMS-202074	2016804-0008	110-112			0.7898	0.0014	-210.2	1.4	1895	15
UCIAMS-202075	2016804-0008	192-193			0.5579	0.0012	-442.1	1.2	4690	20
UCIAMS-202076	2016804-0009	99-100			0.7176	0.0013	-282.4	1.3	2665	15
UCIAMS-202077	2016804-0010	249-250			0.4565	0.0009	-543.5	0.9	6300	20
UCIAMS-202078	2017Nuliajuk-0009	21-22			0.8202	0.0013	-179.8	1.3	1590	15
UCIAMS-202079	2017Nuliajuk-0009	59-60			0.366	0.0008	-634	0.8	8075	20
UCIAMS-202080	2017Nuliajuk-0015	26-27			0.8941	0.0017	-105.9	1.7	900	20
UCIAMS-202081	2017Nuliajuk-0016	52-53			0.8376	0.0018	-162.4	1.8	1425	20
UCIAMS-202082	2017Nuliajuk-0016	121-122			0.7591	0.0017	-240.9	1.7	2215	20
UCIAMS-202083	2017Nuliajuk-0017	37-38			0.611	0.0011	-389	1.1	3955	15
UCIAMS-202084	2017Nuliajuk-0017	66-67			0.4431	0.0008	-556.9	0.8	6540	15
UCIAMS-202085	2017Nuliajuk-0017	155-156			0.3983	0.0009	-601.7	0.9	7395	20
UCIAMS-202086	2017Nuliajuk-0021	32-33			0.89	0.0018	-110	1.8	935	20
UCIAMS-202087	2017805-0003	114-115			0.4387	0.001	-561.3	1	6620	20
UCIAMS-202088	2017805-0005	53-54			0.6245	0.0014	-375.5	1.4	3780	20
UCIAMS-202089	2017805-0005	160-161			0.3919	0.0009	-608.1	0.9	7525	20
UCIAMS-202090	2017805-0006	180-181			0.3802	0.0008	-619.8	0.8	7770	20
UCIAMS-202091	2017805-0006	289-290			0.3625	0.0008	-637.5	0.8	8150	20
UCIAMS-202092	2017805-0006	466-467			0.3523	0.0009	-647.7	0.9	8380	25
UOC-6795	2016Nuliajuk-0025	73-74			0.5854	0.0019			4301	26
UOC-6796	2016Nuliajuk-0026	48-49			0.3386	0.0013			8699	30
UOC-6797	2016804-0001	132-133			0.7152	0.0023			2692	26
UOC-6798	2017Nuliajuk-0016	16-17			0.8716	0.0028			1104	26
UOC-6799	2017Nuliajuk-0016	88-89			0.7944	0.0025			1849	26
UOC-6800	2017Nuliajuk-0017	128-129			0.4109	0.0015			7145	28
UOC-6801	2017805-0003	79-80			0.4504	0.0015			6407	26
UOC-6802	2017805-0003	296-297			0.4157	0.0014			7051	28
UOC-6803	2017805-0003	361-362			0.4028	0.0016			7305	31
UOC-6804	2017805-0006	55-57			0.6207	0.002			3830	26
UOC-6805	2017805-0006	120-121			0.3905	0.0013			7554	28
UOC-6806	2017805-0006	150-151			0.3868	0.0017			7631	34
UOC-6807	2017Nuliajuk-0022	90-91			0.6325	0.0023			3680	30

Table C.2 New radiocarbon dates from this research in Inner Frobisher Bay. Site # corresponds to references in Chapter 2 and Appendix A. Core Id is the unique signifier assigned by the GSC for each core and is referenced throughout this work. SSF Id indicates the SSF footprint (corresponding to Chapter 4 and Appendix B) from within which the core was collected. Those collected outside of SSF footprints are signified by *. Latitude and Longitude indicate position of the vessel at time of collection. Water depth was measured acoustically at the time of collection. Lab Id indicates processing number assigned by radiocarbon labs. "^{14}C Age (±)" is the uncalibrated age and standard uncertainty measure (1-sigma probability) provided by the lab. "1-sigma Cal Age Range" was determined using the methods described in Chapter 2. Species taxa are provided, where known.

Site #	Core Id	SSF Id	Lat	Long	Water Depth (m)	Lab Id	Depth downcore (cm)	^{14}C Age (±)	1-sigma Cal Age Range	Species
M1	2017805-0006PC	*	63.362	-68.182	118	UOC-6804	55	3830(26)	3640-3460	*Macoma calcarea*
						UOC-6805	120	7554(28)	7870-7700	*Nuculana pernula*
						UOC-6806	150	7631(34)	7940-7790	*Yoldia hyperborea*
						UCIAMS-202090	180	7770(20)	8080-7930	*Yoldia hyperborea*
						UCIAMS-202091	289	8150(20)	8480-8330	*Ennucula tenius*
						UCIAMS-202092	466	8380(25)	8780-8580	*Ennucula tenius*
M2	2017Nuliajuk-0015GC	13	63.373	-68.324	81	UCIAMS-202080	26	900(20)	410-260	Unknown fragment
M3	2017Nuliajuk-0016GC	*	63.378	-68.324	70	UOC-6798	16	1104(26)	560-430	*Clinocardium ciliatum*
						UCIAMS-202081	52	1425(20)	830-690	Unknown fragment
						UOC-6799	88	1849(26)	1280-1140	Snail fragment
						UCIAMS-202082	121	2215(20)	1680-1520	Snail fragment
M4	2017Nuliajuk-0009GC	39	63.478	-68.236	237	UCIAMS-202078	21	1590(15)	1020-860	Unknown fragment
						UCIAMS-202079	59	8075(20)	8400-8260	Unknown fragment
M5	2016Nuliajuk-0030GC	*	63.495	-68.232	153	UCIAMS-202069	33	3010(20)	2680-2500	Unknown fragment
						UCIAMS-187020	113	7660(20)	7970-7820	*Yoldia hyperborea*
M6	2016Nuliajuk-0029GC	43	63.503	-68.235	144	UCIAMS-187017	23	1065(15)	530-410	*Hiatella arctica*
						UCIAMS-187018	66	7765(20)	8080-7920	*Yoldia hyperborea*
						UCIAMS-187019	119	8255(20)	8590-8430	*Portlandia arctica*
M7	2016Nuliajuk-0028GC	47	63.510	-68.241	160	UCIAMS-187016	44	3470(15)	3210-3040	*Macoma calcarea*
M8	2016Nuliajuk-0027GC	48	63.522	-68.280	138	UCIAMS-202068	59	7615(20)	7930-7780	*Yoldia Hyperborea*
M9	2016804-0001PC	*	63.546	-68.475	210	UCIAMS-202070	43	990(15)	470-330	Unknown fragment
						UOC-6797	132	2692(26)	2280-2100	*Hiatella arctica*
						UCIAMS-187021	200	7125(15)	7460-7320	*Portlandia arctica*
						UCIAMS-187022	289	7235(15)	7560-7420	*Portlandia arctica*
						UCIAMS-187023	388	7935(20)	8280-8110	*Nuculana pernula*
M10	2016Nuliajuk-0026GC	224	63.558	-68.138	118	UOC-6796	48	8699(30)	9210-9020	*Yoldia hyperborea*
						UCIAMS-187015	85	8920(20)	9460-9320	*Macoma calcarea*
M11	2016804-0002PC	*	63.564	-68.506	204	UCIAMS-187024	166	6940(20)	7300-7150	*Portlandia arctica*
						UCIAMS-187025	294	7295(25)	7610-7470	*Portlandia arctica*
						UCIAMS-187026	473	7690(20)	8000-7850	*Portlandia arctica*

Table C.2 Cont.

Site #	Core Id	SSF Id	Lat	Long	Water Depth (m)	Lab Id	Depth downcore (cm)	^{14}C Age (±)	1-sigma Cal Age Range	Species
M12	2016Nuliajuk-0025GC	214	63.570	-68.162	46	UOC-6795	73	4301(26)	4270-4080	*Mya truncata*
M13	2016804-0008PC	*	63.582	-68.520	190	UCIAMS-202074	110	1895(15)	1310-1180	*Nuculana pernula*
						UCIAMS-202075	192	4690(20)	4790-4610	*Yoldia hyperborea*
						UCIAMS-187032	230	5135(15)	5330-5140	*Yoldia hyperborea*
						UCIAMS-187033	364	5930(15)	6190-6020	*gastropod*
						UCIAMS-187034	395	6165(15)	6420-6280	*Portlandia arctica*
						UCIAMS-187035	519	7085(20)	7420-7280	*Portlandia arctica*
M14	2016Nuliajuk-0021GC	113	63.582	-68.526	178	UCIAMS-187012	121	5020(15)	5220-5010	*Macoma sp.*
						UCIAMS-187013	177	5560(20)	5770-5600	*Yoldia sp.*
M15	2016804-0007PC	113	63.583	-68.523	190	UCIAMS-202071	93	4890(20)	5010-4830	*Nuculana sp.*
						UCIAMS-187027	153	5420(15)	5620-5470	*Portlandia arctica*
						UCIAMS-187028	186	5485(20)	5710-5550	*Yoldia hyperborea*
						UCIAMS-187029	273	4080(15)	3970-3800	Fish skull fragment
						UCIAMS-202072	303	4855(20)	4970-4810	Unknown fragment
						UCIAMS-187030	331	5180(15)	5410-5230	*Macoma calcarea*
						UCIAMS-202073	400	5365(20)	5580-5430	*Yoldia hyperborea*
						UCIAMS-187031	452	5920(15)	6180-6010	*Yoldia hyperborea*
M16	2016Nuliajuk-0024GC	234	63.594	-68.332	98	UCIAMS-187014	63	1150(15)	600-480	*Nuculana pernula*
M17	2017805-0005PC	*	63.598	-68.524	180	UCIAMS-202088	53	3780(20)	3570-3410	Unknown fragment
						UCIAMS-202089	160	7525(20)	7830-7680	*Portlandia arctica*
M18	2017Nuliajuk-0017GC	*	63.608	-68.480	103	UCIAMS-202083	37	3955(15)	3810-3640	Unknown fragment
						UCIAMS-202084	66	6540(15)	6850-6680	Unknown valve
						UOC-6800	128	7145(28)	7480-7330	*Portlandia arctica*
						UCIAMS-202085	155	7395(20)	7700-7560	*Portlandia arctica*
M19	2015805-0008PC	226	63.638	-68.611	125	UCIAMS-169715	240	4030(15)	3890-3720	Unknown
						UCIAMS-202065	283	4885(15)	5000-4830	*Nuculana sp.*
						UCIAMS-169716	326	5640(15)	5880-5720	*Macoma sp.*
						UCIAMS-169717	388	6405(20)	6700-6530	*Nuculana pernula*
						UCIAMS 169718	436	6625(20)	6950-6770	*Portlandia arctica*
						UCIAMS-169719	501	6880(20)	7250-7080	*Portlandia arctica*

Table C.2 Cont.

Site #	Core Id	SSF Id	Lat	Long	Water Depth (m)	Lab Id	Depth downcore (cm)	^{14}C Age (±)	1-sigma Cal Age Range	Species
M20	2016804-0010PC	226	63.640	-68.612	115	UCIAMS-187040	26	725(15)	230-60	*Nuculana pernula*
						UCIAMS-202077	249	6300(20)	6580-6410	*Nuculana pernula*
						UCIAMS-187041	330	6730(15)	7080-6900	*Portlandia arctica*
						UCIAMS-187042	482	6925(15)	7290-7140	*Portlandia arctica*
M21	2014805-0004PC	*	63.640	-68.620	135	UCIAMS-155830	292	5445(25)	5660-5490	*Portlandia arctica*
						UCIAMS-155831	331	6565(20)	6890-6710	*Portlandia arctica*
						UCIAMS-155832	400	6945(25)	7300-7150	*Musculus sp.*
						UCIAMS-155833	511	7245(25)	7560-7430	*Portlandia arctica*
M22	2015805-0009PC	227	63.641	-68.615	115	UCIAMS-169720	264	3160(15)	2820-2690	Unknown
						UCIAMS-202066	281	3520(20)	3280-3100	Unknown fragment
						UCIAMS-169721	361	5720(15)	5950-5780	*Nuculana sp.*
						UCIAMS-169722	402	6265(20)	6550-6380	*Nuculana pernula*
						UCIAMS-169723	489	6570(20)	6890-6720	*Portlandia arctica*
						UCIAMS-169724	526	6735(20)	7090-6900	*Portlandia arctica*
						UCIAMS-169725	571	6925(20)	7290-7130	*Ennucula tenius*
M23	2016804-0009PC	*	63.643	-68.619	101	UCIAMS-202076	99	2665(15)	2240-2050	Unknown fragment
						UCIAMS-187036	189	4355(15)	4340-4150	*Nuculana pernula*
						UCIAMS-187037	320	6945(15)	7300-7150	*Portlandia arctica*
						UCIAMS-187038	382	7070(20)	7410-7270	*Portlandia arctica*
						UCIAMS-187039	531	7265(20)	7580-7440	*Portlandia arctica*
M24	2016Nuliajuk-0003GC	145	63.669	-68.520	72	UCIAMS-202067	59	4785(20)	4880-4700	*Nuculana Pernula*
M25	2017805-0003PC	*	63.687	-68.625	146	UOC-6801	79	6407(26)	6710-6530	*Macoma calcarea*
						UCIAMS-202087	114	6620(20)	6950-6770	*Portlandia arctica*
						UOC-6802	296	7051(28)	7400-7260	*Portlandia arctica*
						UOC- 6803	361	7305(31)	7620-7470	*Portlandia arctica*
M26	2017Nuliajuk-0021GC	*	63.711	-68.516	54	UCIAMS-202086	32	935(20)	430-290	Unknown fragment

C.5 References

Coulthard R.D., Furze M.F.A., Pieńkowski A.J., Chantel Nixon F., England J.H. (2010). New marine ΔR values for Arctic Canada. *Quaternary Geochronology,* 5(4), p.419–434.

Heaton T.J., Köhler P., Butzin M., Bard E., Reimer R.W., Austin W.E.N., Ramsey C.B., Grootes, P.M., Hughen K.A., Kromer B., Reimer P.J., Adkins J., Burke A., Cook M.S., Olsen J., and Skinner L.C. (2020). Marine20 – The marine radiocarbon age calibration curve (0-55,000 cal BP). *Radiocarbon*, 62(4), p. 779-820.

Olsson I.U. (1970). The use of Oxalic acid as a Standard. In I.U. Olsson, ed., Radiocarbon Variations and Absolute Chronology, Nobel Symposium, 12th Proc., John Wiley & Sons, New York, p. 17.

Reimer, R. and Reimer, P.J. (2017). An online application for ΔR calculation. *Radiocarbon*, 59, Special Issue 5, p. 1623-627. https://doi.org/10.1017/RDC.2016.117

Stuiver M. and Polach H.A. (1977). Discussion: reporting of 14C data. *Radiocarbon*, 19(3), p. 355-363.

Stuiver, M. and Reimer, P.J. (1993). Extended ^{14}C data base and revised CALIB 3.0 ^{14}C age calibration program. *Radiocarbon*, 35, p. 215-230.

Appendix D: SSF Interpreted Age Rationale

Ages for 12 SSFs were interpreted using data from sediment cores in IFB. This was accomplished using both an extrapolated age and maximum constraint approach, as described in the Methods section of Chapter 4. Briefly, the extrapolated age approach relies on using a range of plausible sedimentation rates for IFB (10-56 cm/ka) and post-SSF sediment thickness to establish a window of time required for the deposition of that sediment following the SSF. The maximum constraint approach uses radiocarbon-dated materials from below or within SSF sediments to constrain the oldest possible age of the feature. The following is a core-by-core breakdown of how these methods were applied to 12 SSFs to establish the interpreted age ranges shown in Table 4.4 and Figure 5.1. The cores appear here in the order in which the SSFs appear in that figure.

SSF 43: Core 43a (2016Nuliajuk-0029; Figure A.33) SSF age range was established using primarily an extrapolated age method. Approximately 4 cm of post-SSF sediment (LF5) overlies transported SSF material (LF5+LF2; ~4-50 cm downcore), an erosional contact, and pre-SSF sediment (LF2). This results in an extrapolated age range of 0.1-0.4 ka cal BP. A shell in transported material at 23 cm downcore (UCIAMS-187017) has a 1-sigma age range of 530-410 cal BP, indicating a maximum age constraint of ~530 cal BP, supporting the extrapolated age range. The interpreted age range of the feature is 0.1-0.4 ka cal BP.

SSF 234: Core 234a (2016Nuliajuk-0024; Figure A.28) SSF age range was established using the maximum constraint method. A shell collected from SSF sediment (LF4+LF3) at 63 cm downcore (UCIAMS-187014) generated a 1-sigma age range of 600-480 cal BP. This results in an interpreted age of 0-0.6 ka cal BP.

SSF 48: Core 48a (2016Nuliajuk-0027; Figure A.31) SSF age range was established using primarily an extrapolated age method. Approximately 9 cm of post-SSF sediment (LF5) overlies transported SSF material (LF4+LF2; ~9-30 cm downcore), an erosional contact, and pre-SSF sediment (LF2). This results in an extrapolated age range of 0.2-0.9 ka cal BP. A shell in pre-SSF material at 59 cm downcore (UCIAMS-202068) has a 1-sigma age range of 7930-7780 cal BP, indicating a maximum age constraint of ~8.0 ka cal BP. The interpreted age range of the feature is 0.2-0.9 ka cal BP.

SSF 29: Core 29a (2016Nuliajuk-0031; No Log) SSF age range was established using the extrapolated age method. This core was ~10 cm long and did not have physical properties logged and so there is no core log. The core surface was LF5 and the base was LF2, implying loss of stratigraphy due to SSF. There were at most 10 cm of post-SSF thickness in this core. Applying the extrapolated age method resulted in the age range of this SSF being 0-1.0 ka cal BP.

SSF 145: Core 145a (2016Nuliajuk-0003; Figure A.16) SSF age range was established using primarily the extrapolated age method. Approximately 10 cm of post-SSF sediment (LF5) overlies transported SSF material (LF4+LF3; ~10-70 cm downcore), and pre-SSF sediment (LF3). This results in an extrapolated age range of 0.2-1.0 ka cal BP. A shell in pre-SSF material at 59 cm downcore (UCIAMS-202067) has a 1-sigma age range of 4880-4700 cal BP, indicating a maximum age constraint of ~4.9 ka cal BP. The interpreted age range of the feature is 0.2-1.0 ka cal BP.

SSF 186: Core 186a (2016Nuliajuk-0002; Figure A.15) SSF age range was established using the extrapolated age method. Approximately 10 cm of post-SSF sediment (LF5) immediately overlies an erosional contact with LF2. This results in an interpreted age range of 0.2-1.0 ka cal BP.

SSF 39: Core 39b (2017Nuliajuk-0009; Figure A.39) SSF age range was established using a combination of maximum constraint and extrapolated age methods. A shell in SSF material at 21 cm downcore (UCIAMS-202078) has a 1-sigma age range of 1020-860 cal BP, indicating a maximum age constraint of ~1.0 ka cal BP. Approximately 15 cm of post-SSF sediment (LF5) overlies transported SSF material (LF4+LF3; ~15-45 cm downcore), and an erosional contact with pre-SSF material (LF3+LF2). This results in an extrapolated age range of 0.3-1.5 ka cal BP. Using the maximum constraint age as an older age limit resulted in an interpreted age range of 0.3-1.0 ka cal BP.

SSF 244: Core 244a (2016Nuliajuk-0026; Figure A.30) SSF age range was established using primarily the extrapolated age method. Approximately 21 cm of post-SSF sediment (LF4+LF5) overlies an erosional contact with pre-SSF material (LF3+LF2). This results in an extrapolated age range of 0.4-2.1 ka cal BP. A shell in pre-SSF material at 48 cm downcore (UOC-6796) has a 1-sigma age range of 9210-9020 cal BP, indicating a maximum age constraint of ~9.2 ka cal BP. The interpreted age range of the feature is 0.4-2.1 ka cal BP.

SSF 227: Core 227a (2015805-0009; Figure A.4) SSF age range was established using a combination of maximum constraint and extrapolated age methods. A shell in SSF material at 264 cm downcore (UCIAMS-169720) has a 1-sigma age range of 2820-2690 cal BP, indicating a maximum age constraint of ~2.8 ka cal BP. Approximately 100 cm of post-SSF sediment (LF5+LF4) overlies transported SSF material. This results in an extrapolated age range of 2.3-10 ka cal BP. Using the maximum constraint age as an older age limit resulted in an interpreted age range of 2.3-2.8 ka cal BP.

SSF 113: Core 113a (2016804-0007; Figure A.7) SSF age range was established using primarily the extrapolated age method. Approximately 40 cm of post-SSF sediment overlies transported SSF material (LF4; ~40-200 cm downcore). This results in an extrapolated age range of 0.7-4.0 ka cal BP. A fish skull fragment in pre-SSF material at 273 cm downcore (UCIAMS-187029) has a 1-sigma age range of 3970-3800 cal BP, indicating a maximum age constraint of ~4.0 ka cal BP, supporting the extrapolated age range. The interpreted age range of the feature is 0.7-4.0 ka cal BP.

SSF 230: Core 230a (2016Nuliajuk-0022; Figure A.26) SSF age range was established using the extrapolated age method. Approximately 42 cm of post-SSF sediment (LF5) overlies an erosional contact with LF3. This results in an interpreted age range of 0.8-4.2 ka cal BP.

SSF 226: Core 226a (2015805-0004; Figure A.2) SSF age range was established using a combination of maximum constraint and extrapolated age methods. A shell in SSF material (LF4; ~210-310 cm downcore) at 292 cm downcore (UCIAMS-155830) has a 1-sigma age range of 5660-5490 cal BP, providing a maximum age constraint of ~5.6 ka cal BP. Approximately 210 cm of post-SSF sediment overlies transported SSF material. This results in an extrapolated age range of 3.8-21 ka cal BP. Using the maximum constraint age as an older age limit resulted in an interpreted age range of 3.8-5.7 ka cal BP.